Nanoporous Thermosetting Membranes using Reactive Block Polymer Templates

A DISSERTATION
SUBMITTED TO THE FACULTY OF THE GRADUATE SCHOOL
OF THE UNIVERSITY OF MINNESOTA
BY

Mark A. Amendt

IN PARTIAL FULFILLMENT OF THE REQUIREMENTS
FOR THE DEGREE OF
DOCTOR OF PHILOSOPHY

Marc A. Hillmyer, Advisor

August 2010

Acknowledgements

Regardless of the accomplishment when an individual gets to stand in front “on their own” it is rarely the result of just their efforts. As such, I would like to thank those who helped me get to this point. First, I would like to thank the Air Force for the opportunity. I would also like to thank my advisor Professor Marc Hillmyer for being willing to work with my condensed timeline and providing guidance, encouragement and motivation along the way.

To use an Air Force term, my many collaborators have been a tremendous “force multiplier,” and I would be remiss if I did not thank them. I would like to thank membrane collaborators including Bill Phillip, and Professor Ed Cussler for the flux and MWCO work, Bethany Brinkman and Professor Ray Hozalski for the fouling work, and Justin Weaver and Professor Ranil Wickramasinghe for the virus filtration work. Collaborators in the Hillmyer group were also tremendous. Liang Chen was instrumental in getting me started with the crosslinking DCPD system; Louis Pitet taught me everything I know about ROMP, and Sarah Moench’s second pair of hands this last year was great. Other Hillmyer group members both past and present: John, Carolyn, Naohiko, Monique, Jennifer, Chun, Yang, Megan, Dave, Josh, Grayce, Liz, Marc Jr., Can, and Will reviewed papers, discussed issues or just made life in the office/lab more fun and entertaining.

Finally, the love and support my family has provided has been incredible. Thank you Melissa for your love, support and understanding. I know this has not been an easy three years, and I am grateful for all you’ve done. I would also like to thank Joseph for being a bright spot at the end of my day. Mom and Dad A and O thanks your constant encouragement and for making me take breaks too. Thank you for being our home away from home Aunt Bridie and Uncle Jim.

Philippians 4:13

For Alex who didn't get to experience this world &

Joseph who I get to watch learn about it every day.

Abstract

Pressure driven membrane filtrations are a facile means of performing aqueous separations. The efficiency of these processes depends on the permeability and selectivity of a membrane, which is determined by its structure. This dissertation describes research investigating nanoporous thermosets templated by reactive block polymers as alternatives to current ultrafiltration membranes. The goal of the research was to develop materials with narrow pore size distributions and high void fractions for forming membranes with increased selectivity and permeability.

The flux, filtration and fouling characteristics of membranes formed by selective removal of poly(lactide) from crosslinked films of dicyclopentadiene (DCPD) and the reactive block polymer poly(norbornenylethyl styrene-*s*-styrene)-*b*-poly(lactide) (PNS-PLA) were first explored. The results suggest that thin film composite membranes could achieve permeabilities and selectivities greater than current ultrafiltration membranes without excessive fouling characteristics. Additionally, hydrophilic and stimuli responsive membranes templated by reactive triblock terpolymers exhibited environmentally dependent fluxes demonstrating the ease of creating functionalized membranes using reactive triblock terpolymers.

Further investigation into the compositional influences on the morphology of nanostructured PNS-PLA/PDCPD materials revealed that nanoporous bicontinuous structures form over a wide composition range and that different pore sizes are achievable by varying the PLA block size. Extension of reactive block polymer templating to vinyl crosslinking systems was demonstrated by crosslinking a poly(lactide)-*b*-poly(cyclooctene-*s*-norbornenylmethacrylate)-*b*-poly(lactide) reactive triblock copolymer with a variety of vinyl monomers. Although the soft nature of the poly(cyclooctene) prevented removal of polylactide due to collapse of the pores, nanoporous vinyl thermosets were realized by crosslinking a polylactide-*b*-poly(styrene-*s*-hydroxyethyl methacrylate-*s*-ethylene glycol dimetacrylate) reactive diblock copolymer with styrene and divinyl benzene.

Table of Contents

List of Tables

List of Figures

Chapter 1.

Background

This chapter first introduces principles of porous polymer membranes for water filtration. A brief introduction to block polymers, block polymer self-assembly, and nanoporous materials from block polymers is then presented before reviewing recent efforts into the formation of block polymer based ultrafiltration membranes. The chapter concludes with an overview of this dissertation focused on developing nanoporous thermosetting membranes using reactive block polymer templates.

1.1. Introduction

An essential aspect for sustaining life is an adequate supply of clean water, but many areas of the world suffer from insufficient water supply or ineffective sanitation as nearly 20% of the world's population does not have safe water,[1] while 40% has unsanitary water.[2] Coupled together, these issues lead to 60% of the world's illnesses,[3] and considering that growth of global water consumption was twice the rate of population growth from 1900–1995,[3] this problem is likely to increase. Efforts aimed at solving the global water crisis using traditional water purification methods depend on chemical treatments that are expensive, difficult to extend to developing countries and can actually increase stress on the environment because of their chemical byproducts.[4, 5]

Membrane based separations have proven to be a facile alternative for water purification capable of removing a variety of impurities including bacteria, viruses, organic molecules and dissolved salts by using the full spectrum of filtration processes[6, 7] as can be seen in Figure 1.1.

Process	Microfiltration	Ultrafiltration	Nanofiltration	Reverse Osmosis
Retentate	Bacteria Red Blood Cells Sediment Algae Plant Pigments	Viruses Small Colloids Proteins Enzymes	Amino Acids Antibiotics Multivalent Ions	Aqueous Salts
Pore Size (nm)	100 - 10,000	2 - 100	0.5 - 2	< 0.5
Pressure (psi)	125 - 15	200 - 70	600 - 100	1000 - 400

Figure 1.1. Diagram depicting the range of filtrations for membrane based separations.

Two classes of membranes often used in filtration processes include phase inversion and track-etched membranes. Phase inversion membranes can be made by casting a thin film of a polymer solution[8] followed by immersing it in a nonsolvent, which causes the polymer to precipitate as a web of fibers. Track-etched membranes are made by exposing a thin polymer film to a beam of radiation.[9] The film is then etched in a chemical bath, which removes the polymer damaged by the radiation. Two critical measures of membrane performance are permeability and selectivity. The permeability of a membrane (L_p) can be defined by[10]

$$L_p = \frac{J_v}{\Delta P} \tag{1.1}$$

where J_v is the volumetric flux (volume of water per time per area) and ΔP is the pressure across the membrane. The volumetric flux can be modeled as[7, 11]

$$J_v = \frac{\varepsilon d^2 \Delta P}{32 \tau \mu l} \tag{1.2}$$

using the Hagen-Pouiseuille relationship or as

$$J_v = \frac{d^2 \Delta P}{150 \mu l} \frac{\varepsilon^3}{(1-\varepsilon)^2} \tag{1.3}$$

using the Blake-Kozeny component of the Ergun equation[12] where ε is the void fraction of the membrane, d is the pore diameter, τ is the pore tortuosity, μ is the liquid's viscosity, and l is the thickness of the membrane. The selectivity of a membrane is then based on its ability to reject a solute of interest which can be defined by the rejection coefficient (R)[13]

$$R = \left(1 - \frac{c_p}{c_f}\right) \tag{1.4}$$

where c_p and c_f are the concentration of the solute in the permeate and feed respectively.

Analysis of the separation efficiencies for a variety of ultrafiltration membranes by Mehta *et al.* illustrated an upper limit of membrane performance based on the tradeoffs between permeability and selectivity for isolating the protein bovine serum albumin (BSA).[10] For example, due to the polydispersity of pore sizes, higher selectivities for BSA are achieved by membranes with smaller pore sizes and hence lower

permeabilities. Alternatively, higher permeabilities are observed with membranes with larger pore sizes leading to lower selectivity. Although this analysis was specific to BSA, it highlights the general limitation of the current state of the art ultrafiltration membranes in terms of their selectivity and permeability. Surpassing this apparent performance barrier would further increase the efficiency of membrane based filtrations while decreasing operating costs.[14]

Materials investigated as alternatives to current ultrafiltration membranes with the potential of breaking through the performance barrier due to their high pore density and narrow polydispersity of pores are nanoporous materials templated by block polymers. [15] The remainder of this chapter discusses recent efforts developing ultrafiltration membranes from block polymers by first introducing block polymers, block polymer self-assembly, and nanoporous materials from block polymers. Next, research into the formation of block polymer based ultrafiltration membranes is reviewed. Finally, an overview of this dissertation focused on developing nanoporous thermosetting membranes from reactive block polymer templates is presented.

1.2. Block Polymer Templated Membranes

1.2.1. Block Polymer Self-assembly

A block polymer is a polymeric chain composed of at least two chemically distinct covalently bound polymer segments.[16] Variations in both the number of segments and their connectivity have resulted in a diverse array of block polymers. Simple AB

diblock copolymers,[17] where A is one component and B the other, have been extended to ABA triblock copolymers, ABC triblock terpolymers,[18,19] ABAB tetrablock copolymers, ABCD quarterblock polymers,[20] and ABCDE pentablock polymers[21,22] to name a few. In addition to linear block polymers, other architectures include star,[23,24] comb or graft,[25,26] and cyclic[27] structures. Figure 1.2 illustrates some block polymer architectures.

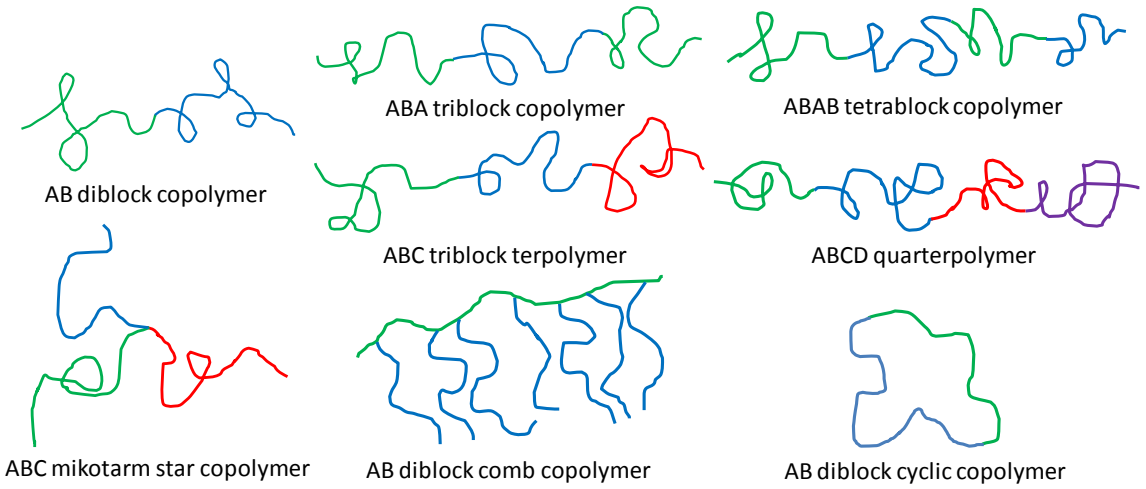

Figure 1.2. Examples of block polymer architectures

An interesting aspect of block polymers is their self-assembly into ordered structures on nanometer length scales.[28] The phase separation of block polymers is driven by the chemically distinct nature of each block and is limited to microphase separation as the two blocks are covalently bound.[29] The final structure formed is a balance of minimizing the interactions between blocks by reducing their interfacial area while avoiding excessive chain stretching. The structure formed depends on the block compositions, degree of polymerization, segment-segment interactions (χ) and temperature, as χ is inversely proportional to temperature.[16, 29, 30] Equilibrium structures

have been observed experimentally[31, 32, 33, 34] and predicted theoretically[31, 35, 36,37] and include lamellar, bicontinuous double-gyroid, hexagonally packed cylinders and spheres on a body centered cubic lattice for AB diblock copolymers. The theoretical phase diagram and equilibrium morphologies for AB diblock copolymers are shown in Figure 1.3.

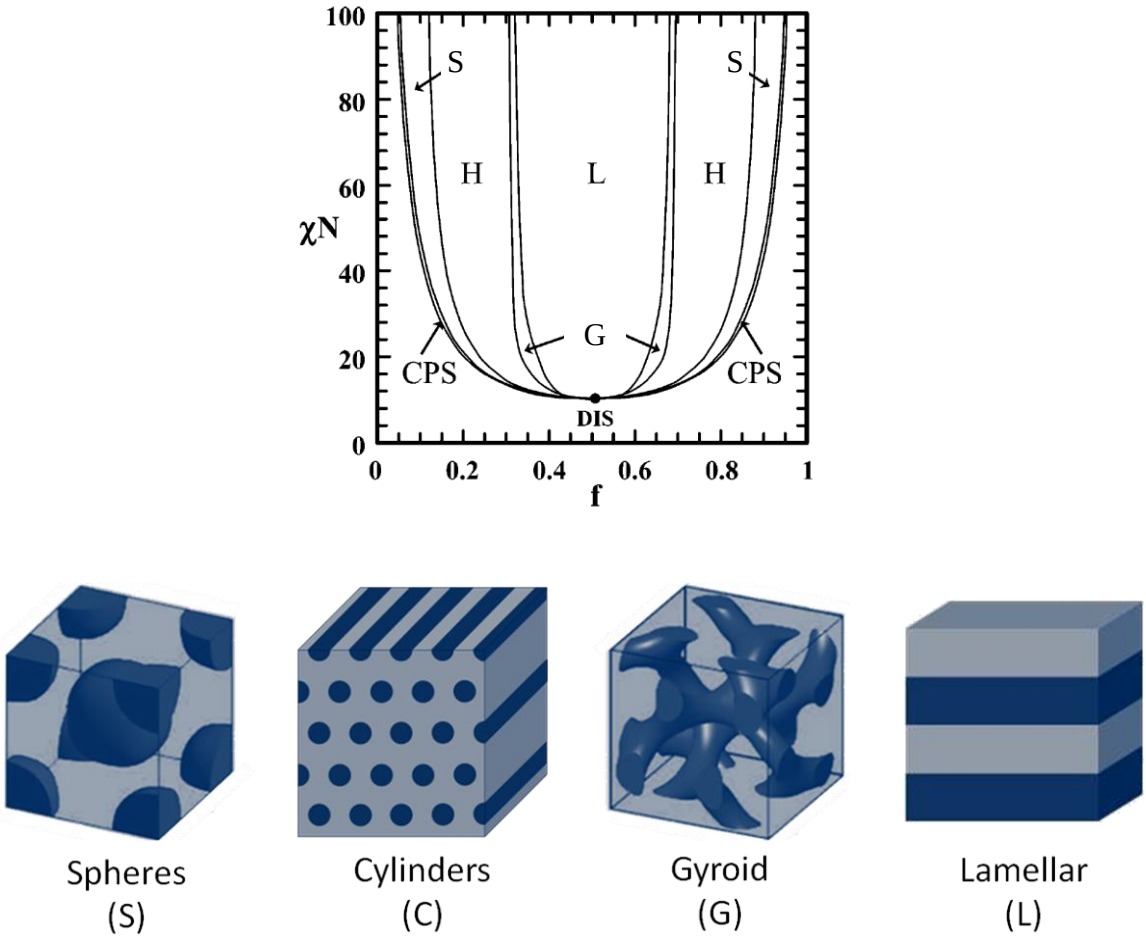

Figure 1.3. Top: theoretical phase diagram for the self-assembly of block copolymers (adapted from Cochran et al.).[37] Bottom: equilibrium morphologies of the phase diagram except for close packed spheres (adapted from Lynd).[38]

1.2.2. Nanoporous Materials from Block Polymers

The self-assembly of block polymers makes them attractive for a variety of technologies requiring structures exhibiting nanometer length scales,[39] and one research area that exploits the nanostructures formed is nanoporous materials from block polymers. The seminal paper in this field described the lamellar self-assembly of an ABA triblock copolymer consisting of two poly((4-vinylphenyl)dimethyl-2-propoxysilane) blocks on either side of a poly(isoprene) (PI) mid-block. Crosslinking the silane block preserved the lamellar microstructure, while subsequent ozonoloysis removed the PI block rendering the material nanoporous.[40]

Since this initial report, the variety of techniques and materials used in block polymer templating of nanoporous materials has grown tremendously, but the same basic methodology remains. After a block polymer containing an etchable block self-assembles into a desired structure, the etchable component is selectively removed. Numerous methods have been employed for selective removal such as ozonolysis,[40] thermal degradation,[41, 42] UV irradiation,[43] chemical etching,[44, 45, 46] reactive ion etching,[47] and single block scission.[48, 49, 50] Figure 1.4 depicts the general scheme for creating a nanoporous material from a cylindrical morphology as an example.

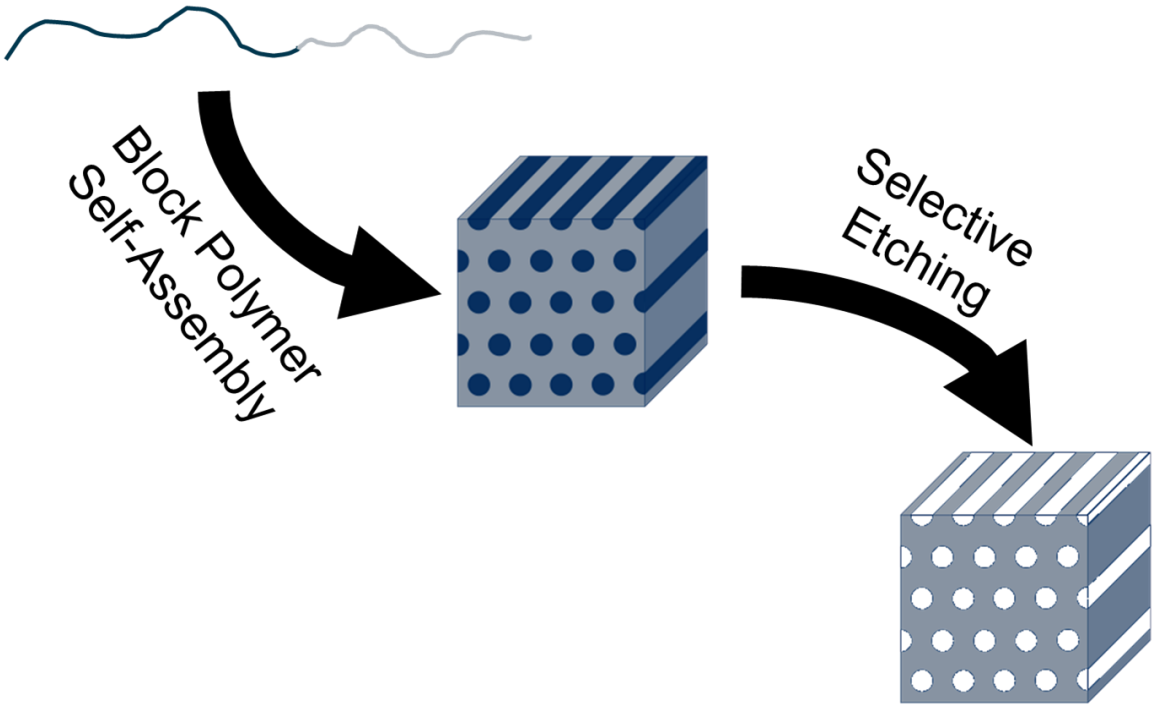

Figure 1.4. Scheme for the formation of nanoporous materials from a diblock copolymer.

Two thorough reviews by Hillmyer et al. and Olson et al. cover the development of nanoporous materials from block polymers.[51, 52] The following section provides a focused review of block polymer membranes broken into sections based on membrane structure. Symmetric membranes have an isotropic structure across the thickness of the membrane. Composite membranes consist of a thin selective layer of one material with smaller pores on a thicker macroporous substructure as a mechanical support.[14] Finally, asymmetric phase inversion membranes are composed of a single material that has a spatially varying morphology. One side of the membrane has a thin selective layer with smaller pores that transitions to a thicker macroporous substructure. Figure 1.5 illustrates the three membrane structures.

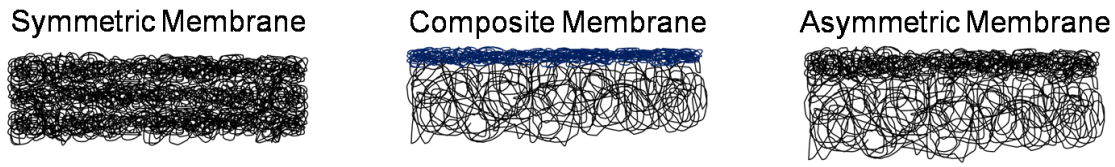

Figure 1.5. Schematic of basic membrane structures.

1.2.3. Symmetric Membranes from Block Polymers

Initial exploration of symmetric membranes templated by block polymers arose from the formation of bulk nanoporous materials and typically focused on thicker polymer monoliths as opposed to thinner membrane structures. While permeability through these bulk materials was lower due to their thicknesses, these initial efforts helped established the potential of nanoporous materials from block polymers as membranes.

In 1999 Liu and coworkers reported the potential application of nanoporous films as membranes using a poly(isoprene)-*b*-poly(cinnamoylethyl methacrylate)-*b*-poly(*tert*-butyl acrylate) PI-PCEMA-PtBA triblock terpolymer.[53] Films 20 to 50 μm thick were prepared by casting a toluene solution with 18 weight percent (wt %) PI-PCEMA-PtBA (204 kg/mol, PI: 12 wt %, PCEMA: 54 wt % and PtBA: 34 wt %) and 2 wt % of a PtBA homopolymer (12.8 kg/mol) on glass. After drying for 2 h, the films were heated at 70 and 100 °C for 5 h and 1 day respectively. Transmission electron microscopy (TEM) indicated the PtBMA formed a tortuous possibly interconnected cylindrical like morphology through the film. UV irradiation crosslinked the PCEMA matrix, and nanochannels were generated by extracting the homopolymer PtBA with methylene chloride. Gas permeation measurements indicated that porosity extended through the

membrane as the permeability was about 6 orders of magnitude greater than for dense polymer films. Water permeability was measured by tracking changes in the height of water in a U shaped tube after a 50 μm thick film had been clamped into the middle of the tube. However, no permeability was observed most likely due to the hydrophobic nature of the pores in the membrane. To examine if this could be overcome, the PtBA was hydrolyzed to poly(acrylic acid) (PAA) by soaking the film in trimethylsilyl iodide for two weeks followed by washing it with a 5/95 (v/v) solution of water/methanol. In addition to making the pore walls hydrophilic, the hydrolysis also increased the porosity in the channels evidenced by a further increase in the gas permeability of the film. Surprisingly, water permeability was still not evident. The authors attribute this to a lack of continuity of the pores across the membranes. They hypothesized that grain boundaries disrupting the continuity are small enough to allow gas molecules to permeate, but too large to allow water permeability. This was supported by achieving permeability through 2 μm thick films obtained by microtoming a thicker sample.

Seeking to improve film's permeability, the authors followed the same basic protocol for the PI-PCEMA-PtBA but instead, cast a PtBA-PCEMA diblock copolymer (220 kg/mol, PCEMA: 77 wt%, PtBMA: 23 wt%) at 20 wt% in toluene.[54] From the bulk sample, thinner films (0.05 and 2 μm) were microtomed for TEM and permeability measurements. Small angle X-ray scattering (SAXS) and TEM indicated the presence of a hexagonally packed cylindrical microstructure with PtBA cylinders in a PCEMA matrix. UV irradiation crosslinked the PCEMA matrix, and hydrolysis of the PtBA to

poly(acrylic acid) (PAA) created porosity within the films. Water permeability as a function of pH was examined. High permeabilities observed at pH 1 and 2 dropped two orders of magnitude at pH 3 before increasing at higher pH. The authors attribute the pH dependent flux to different conformations of the PAA chains in the pores and suggest that these membranes could be employed as valves to modulate flow.

Cooney et al. reported diffusion through nanoporous monoliths templated by block polymers in 2006.[55] The monoliths were prepared from a poly(styrene)-*b*-poly(lactide) (PS-*b*-PLA) copolymer (33 kg/mol, w_{PLA} = 34 wt%) with shear aligned cylinders of PLA in a PS matrix as previously reported protocol.[44,45] SAXS of the monolith revealed a 25 nm domain spacing indicative of PLA cylinders with a 17 nm diameter. The PLA cylinders were selectively etched using base-catalyzed hydrolysis rendering the monolith nanoporous. Porosity was confirmed by measuring diffusion of hydroxide ions through a 2 mm x 2mm x 5mm piece of the monolith. While hydroxide diffusion was observed, the experiment showed the need to pre-wet the samples due to the hydrophobic nature of the pores.

A subsequent paper by Rzayev et al. reported monoliths with hydrophilic pores using a poly(styrene)-*b*-poly(dimethylacrylamide)-*b*-poly(lactide) (PS-*b*-PDMA-*b*-PLA) triblock terpolymer.[56,57] Aligned monoliths exhibited a core-shell cylindrical morphology with a PLA core surrounded by a PDMA shell in a PS matrix. SAXS analysis suggested a 16.8 nm cylinder diameter. Hydrolysis removed the PLA and produced pores with a hydrophilic PDMA brush coating the pore walls. Gas diffusion and hydraulic

permeability through the material were investigated in comparison to a track-etched membrane. Gas diffusion through the monolith exhibited Knudsen diffusion, which is consistent with flow through a nanoporous membrane,[11] and the membrane permeability was 100 times greater than of the track-etched membrane indicative of the increased pore density.

In an effort to make more robust materials, Uehara et al. reported a nanoporous material from a poly(ethylene)-*b*-poly(styrene) (PE-PS) block polymer.[58] By carefully cooling a molten block polymer film to ensure PS vitrification in conjunction with PE crystallization, a bicontinuous material was formed, thereby overcoming the need to align the microstructure for membrane formation. The minority PS domains were subsequently removed by fuming nitric acid leaving behind a semicrystalline nanoporous PE membrane as shown in the scanning electron microscopy (SEM) image in Figure 1.6.

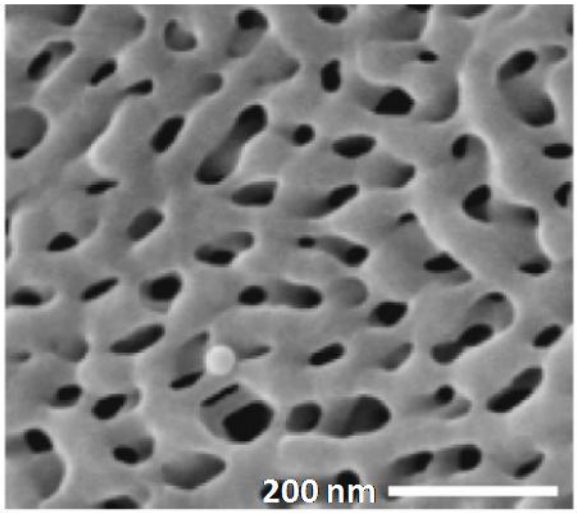

Figure 1.6. SEM micrograph of semicrystalline nanoporous PE (adapted from Uehara et al).[58]

A subsequent paper[59] by Uehara et al. explored controlling the porosity within the material as well as its performance as a size-selective diffusion barrier. Pore sizes were shown to be adjustable from 5 to 30 nm by exposing the membrane to a fuming nitric acid etch for 5 to 30 min respectively. The membranes with variable pore sizes were also tested as a size-selective diffusion barrier for separating glucose and BSA. Membranes were tested by clamping them between two chambers, and after the desired solute(s) had been spiked in one chamber, the solute concentration was monitored overtime in the second chamber. While glucose easily passed through the membranes, BSA was shown to be completely rejected by membranes with 5 and 10 nm pore sizes and rejected up to 88% by a membrane with a 30 nm pore size for a 48 hour hold time. The size selective diffusion performance led the authors to hypothesize that the PE membrane could be of potential interest in biomedical devices such as an implantable glucose sensor.

1.2.4. Composite Membranes from Block Polymers

The formation of composite membranes from block polymers emerged from research into the self-assembly of block polymer thin films. In addition to membrane structures, block polymer thin films have been employed as templates for forming nanodots and nanowires, nanopatterns for high density storage media, lithographic masks and photonic crystals.[39,60] Block polymer thin films are typically formed by spin coating a block polymer solution onto a substrate. After the solvent evaporates, a block polymer coating (50-500 nm) is left on the substrate. The film morphology is determined not only by the polymer characteristics (i.e. size and composition), as for bulk block polymer

samples, but also by interfacial energetics, and film thicknesses leading to more complex phase behavior.[61] Modification of the resulting thin films via selective etching renders them porous thereby creating structures useful as lithographic masks, nanostructured templates or barrier layers for membranes.[60]

One of the first examples of a composite membrane with a selective layer formed from a block polymer template was reported by Yang et al. in 2006.[62] The selective layer was based on previous research into nanoporous thin films templated by poly(styrene)-*b*-poly(methylmethacrylate) (PS-PMMA) block polymers.[63,64,65,66,67] Specifically, a 2 % (w/v) solution of a PS-PMMA block polymer (89 kg/mol; 0.3 volume fraction PMMA) and a PMMA homopolymer (31.8 kg/mol and 10 wt % relative to the PS-PMMA block polymer) were spin coated onto a silicon wafer with neutral brush surface of PS-*r*-PMMA. The resulting 80 nm thin film had a cylindrical microstructure consisting of PMMA cylinders with a perpendicular orientation spanning the thickness of the PS matrix. The thin film was freed from the wafer and deposited onto a porous poly(sulfone) support. Treatment of the film with an acetic acid wash removed the PMMA homopolymer creating a nanoporous layer with 15 nm pores. Figure 1.7 depicts the scheme for the membrane formation.

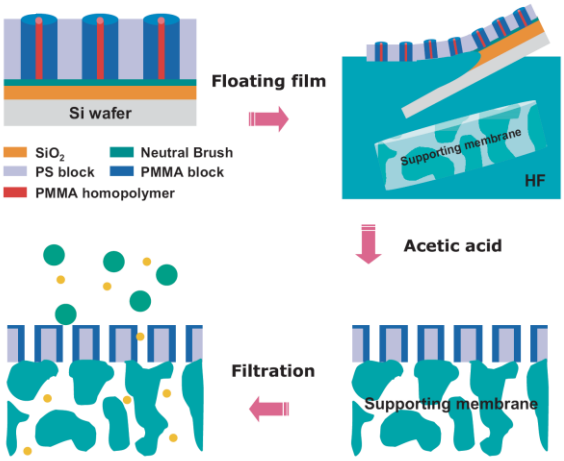

Figure 1.7. Illustration of the composite membrane formation from a thin film of a PS-PMMA block polymer blended with a PMMA homopolymer (adapted from Yang et al.).[62]

The membrane flux and separation performance was evaluated by challenging the membrane with a phosphate buffered solution containing bovine serum albumin (BSA) and human rhinovirus type 14 (HRV 14) at a transmembrane pressure of 0.1 bar. The block polymer membrane exhibited flux values more than 2 orders of magnitude greater than a polycarbonate track-etched membrane. The larger flux of the composite membrane was attributed to differences in the thickness of the barrier layers (80 nm versus 6.5 μm) and the greater pore density of the block polymer membrane (20% versus 2%). Plaque assays of permeate samples for HRV 14 indicated virtually complete rejection of the virus particles. Rejection was further supported by SEM micrographs of the membrane after filtration showing blocked virions on the membrane surface. A graphical comparison of the membrane fluxes as well as the SEM micrograph after filtration are shown in Figure 1.8.

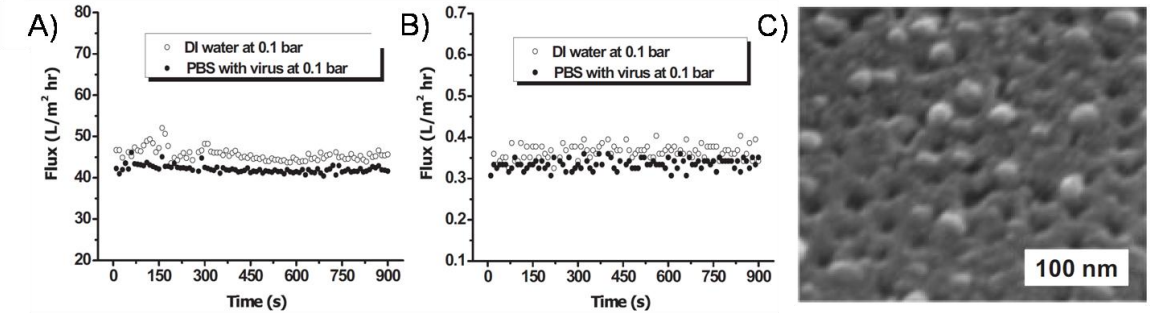

Figure 1.8. Flux of DI water and phosphate buffered solution containing human rhinovirus for a composite membrane with a nanoporous barrier layer derived from a block polymer thin film (A) and a track-etched membrane (B). (C) Depicts the surface of the block polymer composite membrane after filtration and shows blocked virus particles on the surface (lighter spheres) (adapted from Yang et al.).[62]

In a subsequent paper, Yang et al. reported membranes with improved mechanical stability and increased solvent resistance.[68] Following the same basic procedure, a 160 nm thick barrier layer with PMMA cylinders in a PS matrix was formed from a PS-PMMA block polymer (77 kg/mol; 0.25 volume fraction PMMA). The PMMA cylinders were selectively removed by UV irradiation followed by an acetic acid wash. The UV treatment also crosslinked the PS matrix and coupled it to the support membrane. SEM micrographs of the barrier layer show hexagonally packed porous cylinders on the top (Figure 1.9A) and bottom (Figure 1.9B) surfaces, but micrographs of the membrane's cross-section (Figure 1.9C) revealed an un-aligned morphology with both parallel and perpendicular cylindrical pores forming a co-continuous like morphology.

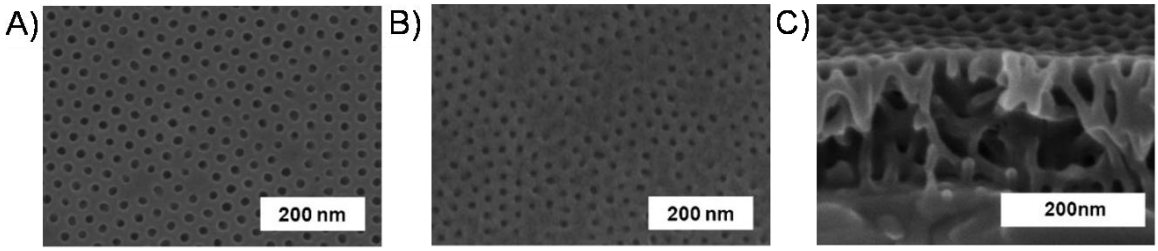

Figure 1.9. SEM micrographs of a nanoporous barrier layer formed by UV irradiation/acetic acid rinse of a PS-PMMA block polymer thin film depicting the top (A) and bottom surface (B) and a cross-sectional image (C) (adapted from Yang et al.).[68]

The membrane permeability and selectivity were evaluated using a similar experimental protocol to their first report. Permeability with DI water was measured at 0.1, 0.5 and 2.0 bar and proportional flux increases were observed with a maximum flux of ~380 L/m^2 hr (LMH) at 2.0 bar. The upper pressure of 2.0 bar was a marked improvement over their previous report as pressures of 0.4 bar or greater caused the previously reported membranes to crack. The authors attribute this improved mechanical stability to the unaligned microstructure of the film. The membrane also retained its selectivity as filtration of solutions of HRV 14 resulted in complete rejection of the virus particles as evidenced by plaque assay. The membrane's solvent stability was demonstrated by immersing the membrane in toluene, DMF, acetic acid and 0.1 M sodium hydroxide solutions. SEM micrographs after each exposure indicated structure preservation. The authors attributed the solvent resistance to crosslinking the PS matrix during UV irradiation. Together these two papers highlight the potential of block polymer composite membranes for achieving high permeability, high selectivity separations for biological and other applications.

In 2007 Sperschneider et al. published a follow-up [69] to their initial communication[70] on efforts to develop nanoporous composite membranes using triblock terpolymers. Spin coating a 5 gL^{-1} solution of a poly(styrene)-*b*-poly(2-vinyl pyridine)-*b*-poly(*tert*-butyl methacrylate) (PS-P2VP-P*t*BMA) terpolymer (140 kg/mol: 16 , 21 and 63 wt % respectively) in chloroform onto either silicon wafers or sodium chloride substrates resulted in height dependent morphologies. At a height of 47 nm a perforated lamellar morphology with a PS core in a P2VP shell and P*t*BMA perforated cylinders formed over large areas after solvent annealing for 100 h with chloroform vapor (Figure 1.10A). Selective etching of the P*t*BMA cylinders could result in porous membranes with an average pore diameter of 35 nm and a porosity of 21%.

Concerned with the brittle nature of PS, a poly(butadiene) (PB) block was substituted to create a more flexible membrane while maintaining the overall molecular weight and composition. Thin films of this polymer cast using the same casting and annealing conditions resulted in a core-shell cylindrical morphology oriented both parallel and perpendicular to the substrate (see Figure 1.10B). By increasing the total molecular weight to 165 kg/mol with only minor compositional variations (PB 14 wt %, P2VP 18 wt %, and P*t*BMA 68 wt %) a core-shell cylindrical morphology with a perpendicular orientation was achieved (Figure 1.10 C). Transfer of the film onto a porous substructure while maintaining its morphology was demonstrated by first spin coating the polymer on a sodium chloride substrate. Next the substrate was dissolved in water, and the free floating membrane could be supported by the desired substrate.

Crosslinking the PB component further improved the mechanical properties while maintaining the core-shell cylindrical morphology. Although porous membranes were not demonstrated, both the perforated-lamella and core-shell cylindrical morphologies reported are appealing structures for triblock terpolymer based membranes, and the process developed for film transfer from a sodium chloride substrate is an attractive methodology for composite membrane fabrication.

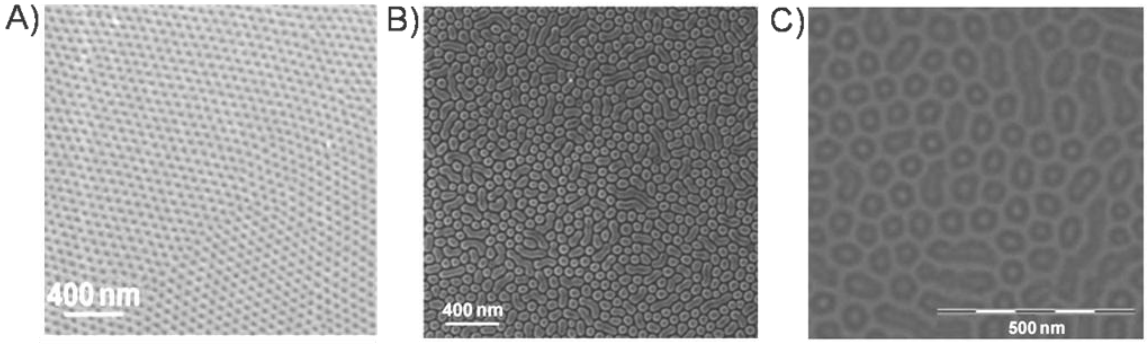

Figure 1.10. A) SEM micrograph of a thin film of the PS-P2VP-P*t*BMA triblock terpolymer with a perforated-lamella morphology. B) SEM micrograph of a 145 kg/mol PB-P2VP-P*t*BMA triblock terpolymer with a core-shell cylindrical morphology with both parallel and perpendicular orientation. C) TEM image of a PB crosslinked 165 kg/mol PB-P2VP-P*t*BMA triblock terpolymer with a core-shell cylindrical morphology with primarily a perpendicular orientation (adapted from Sperschneider et al.).[69]

An example of a composite membrane incorporating both organic and inorganic materials was reported by Nuxoll *et al.* in 2009.[71] In this work, a microporous silicon support was prepared by coating both sides of a 100 µm silicon wafer with 40 nm of Si_3N_4 via chemical vapor deposition. One side of the wafer was then patterned with 20 µm squares 20 µm apart using photolithography, and the square structures were etched through the silicon wafer using reactive ion etching. A poly(styrene)-poly(isoprene)-poly(lactide) (PS-PI-PLA) (69.5 kg/mol: w_{PS} = 0.56, w_{PI} = 0.10 and w_{PLA} =0.34) triblock

terpolymer was then spin coated onto the nonporous Si_3N_4 surface after it had been treated with a 5% solution of (dichloromethyl)-octylsilane to promote polymer adhesion. The resulting 80 nm polymer layer formed a core-shell cylindrical microstructure with PLA cylinders surrounded by a PI shell, which was rendered porous by submerging the composite film in a 0.05 M NaOH solution in a 40 %/60 % (v/v) methanol/water solution for 45 minutes. Tapping-mode atomic force microscopy (AFM) was used to image the surface of the nanoporous block polymer layer and revealed a porous surface with an average pore size of 43 nm. The microporous layer was then extended through the remaining Si_3N_4 layer using a drop of 49% hydrofluoric acid. A schematic of the composite is shown in Figure 1.11.

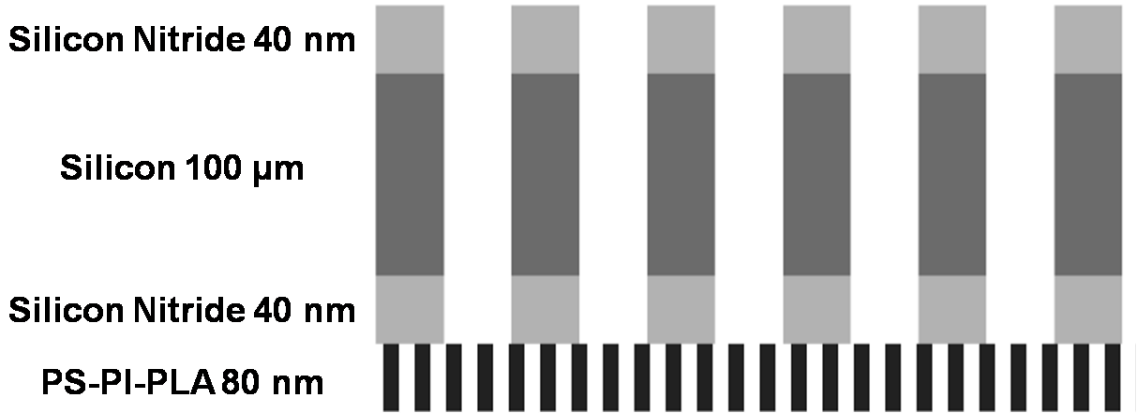

Figure 1.11. Schematic of the final composite membrane showing each of the layers (adapted from Nuxoll et al.).[71]

The size selectivity of the inorganic/organic composite membrane was evaluated by comparing the diffusion of methyl orange and dextran blue through the membrane using a side-by-side diffusion cell. These dyes were introduced into the donor cell and UV/Vis spectroscopy was used to monitor their concentration in the receptor cell. The

flux of the methyl orange increased linearly with time while the flux of the dextran blue remained zero. The exclusion of the dextran blue was attributed to the size selectivity of the membrane as the molar mass of the methyl orange was 327 g/mol but the molar mass of the dextran blue was 2 x 10^6 g/mol. The robust nature of the microporous inorganic support layer makes this composite membrane amendable to more mechanically challenging environments possibly including microelectromechanical devices.

An example of forming a composite membrane by directly casting a block polymer layer onto a microporous support was recently reported by Phillip et al.[72] In this report, a PS-PLA (42 kg/mol: 27 volume % PLA) was directly cast from an 8 wt % solution in 1,1,2-trichloroethane on a prewetted poly(ethersulfone) membrane using a wire-wound rod. After drying, a 4 μm thick polymer layer remained on the membrane surface. The membrane was then exposed to UV irradiation to improve adhesion between the layers as well as crosslink the PS. Crack free composite membranes were produced with areas greater than 100 cm^2.

Pores were introduced in the barrier layer by selectively etching the PLA using dilute sodium hydroxide. SEM micrographs of the membrane surface revealed a cylindrical microstructure with a perpendicular orientation over large areas of the membrane. The membrane permeability and selectivity were evaluated using dead end flow experiments. Flux across the membrane was found to be 1.15 LMH/bar, which was far below the predicted value of 450 LMH/bar. The differences between the observed and predicted flux were attributed to the blockage of pores by the support membrane,

unaligned cylinders in the cross-section of the membrane increasing the tortuosity, and cylinders not spanning the entire thickness of the barrier layer. Although the flux was significantly lower than expected, the selectivity of the membrane was still evaluated by filtering aqueous PEO solutions. PEO rejection was found to be in good agreement with theoretical predictions based on the observed pore size of the selective layer, which is indicative of the monodisperse nature of the pores.

1.2.5. Asymmetric Phase Inversion Membranes with Block Polymers

Anisotropic phase inversion membranes are one of the most commonly used membranes for ultrafiltration.[73] A variety of processes have been employed to produce phase inversion membranes including: non-solvent induced phase separation, thermally induced phase separation, vapor induced phase separation and evaporation induced phase separation.[74] While these processes use different triggers for phase separation, they all result in the formation of a solid, polymer-rich phase that becomes the membrane matrix and a liquid, polymer-poor phase that templates the pores.[13] Of the phase separation processes, non-solvent induced phase separation or immersion precipitation is the most widely employed.[75] Non-solvent induced phase separation involves first casting a film of a polymer solution in a water-miscible solvent; next the film is allowed to stand for a period of time where some of the solvent evaporates before being immersed in a water bath to precipitate the film forming the membrane; finally the membrane is dried and annealed.[73]

A variety of block and graft copolymers have been investigated as casting solution additives for improving the hydrophilic nature and antifouling characteristics of various asymmetric membranes. Examples of this include the modification of poly(sulfone) membranes with poly(ethylene oxide)-*b*-poly(sulfone) block polymers,[76, 77,78] poly(ethersulfone) membranes with poly(ethylene oxide)-*b*-poly(propylene oxide)-*b*-poly(ethylene oxide), [79] poly(vinylidene fluoride) membranes with poly(methyl methacrylate)-*g*-poly(ethylene oxide) [80 , 81] and poly(vinylidene fluoride)-*g*-poly(oxyethylene methacrylate), [82 , 83 , 84] and poly(acrylonitrile) membranes with poly(acrylonitrile)-*g*-poly(ethylene oxide).[85 , 86] These examples highlight how block polymers can introduce new properties to the final membrane when incorporated as additives, but do not take advantage of block polymer self-assembly in templating the porous structures.

In 2007 Peinemann et al. investigated the formation of an assymmetric membrane via the combination of block polymer self-assembly and the phase inversion process.[87] A poly(styrene)-*b*-poly(4-vinylpyridine) (PS-P4VP) copolymer (191 kg/mol and w_{P4VP} = 0.15) was solution cast from tetrahydrofuran (THF) and dimethyl formamide (DMF) using a doctor blade. After the solvent was allowed to evaporate for 10 s, the film was immersed in a water bath for 12 h and then dried. SEM of the resulting membrane structure (Figure 1.12) revealed a 200–300 nm thick layer of aligned cylinders with a pore size of 8 nm over a macroporous layer 150 μm thick. The authors hypothesized that concentration of the block polymer at the surface during evaporation facilitated self-

assembly of the top layer. Upon immersion in water, the polymer precipitated out of solution preserving the self-assembled structure at the surface while forming a sponge like support layer at the bottom due to phase inversion. The flux and selectivity of the membrane was subsequently investigated. A flux of 20 LMH was observed at a pressure of 0.5 bar, while filtration of a solution of albumin (7 nm diameter) resulted in 82% rejection, which is consistent with the estimated pore size of 15 nm.

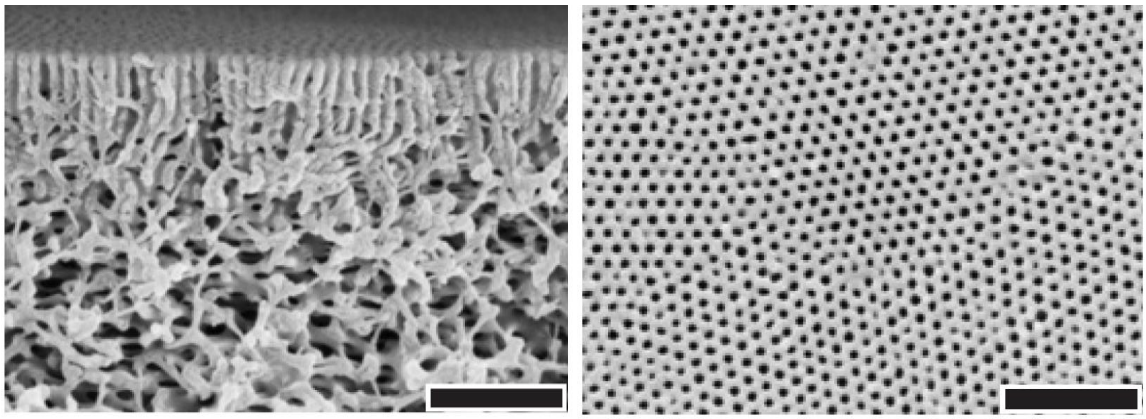

Figure 1.12. SEM micrographs of PS-P4VP membrane. On the left is an image of a cross-section of the membrane, while the right is the surface of the membrane. The scale bars are 500 nm (adapted from Peinemann et al).[87]

1.2.6. Challenges of Block Polymer Membranes

Even with the promise shown by block polymer templated membranes, they are not without their challenges. First, their mechanical toughness is often low as many membranes have an inherently brittle PS matrix,[51] and although microporous membranes are often used for mechanical support, any cracks in the selective layer could significantly impact membrane selectivity. Another major challenge is forming block polymer layers thin enough so that the oft touted theoretical permeabilities can be

realized. Many composite membranes reported have been able to attain permeabilities on order of phase inversion membranes or higher, but forming these membranes requires involved processes that maybe difficult to scale up for membrane production. A final challenge is forming aligned cylindrical domains that span the entire membrane. Many methods have been developed for aligning block polymer structures including shear, e-fields, temperature gradients, solvent evaporation, and neutral surface layers,[39, 88, 89] but the effectiveness of these methods is variable as structures produced often have defects.[44] Additionally, many of these alignment methods add processing steps, which are either cumbersome or unfeasible for forming thin selective layers at larger scales.

Many of these challenges are shared with other applications utilizing nanoporous materials from block polymers, and several methodologies have been employed to address these issues. Increases in mechanical integrity have been achieved by crosslinking the polymer matrix. In two examples, benzocyclobutene was copolymerized with styrene as the matrix block, which subsequently allowed the matrix to be thermally crosslinked prior to removal of the etchable block.[90, 91] Other examples include the crosslinking of PI or PB before removal of a poly(dimethylsiloxane) block.[92, 93]

Efforts aimed at overcoming the challenges associated with domain alignment have focused on developing bicontinuous morphologies. While a bicontinuous structure would have a more tortuous path through the membrane, avoiding often cumbersome alignment procedures might prove pivotal in further development of block polymer templated membranes. For example, Mao et al. accessed the bicontinuous gyroid

morphology for both PS-PLA and poly(styrene)-*b*-poly(ethylene oxide) (PS-PEO) BCPs.[94] The gyroid morphology was kinetically trapped after a lamellar to gyroid order-order transition for PS-PLA and a cylinder to gyroid order-order transition for PS-PEO. Removal of the PLA and PEO respectively led to a bicontinuous nanoporous materials.

The limited region of stability for gyroid structures makes accessing this bicontinuous morphology difficult. Another example of achieving a bicontinuous structure employed a bicontinuous microemulsion.[95] Zhou et al. formed a bicontinuous microemulsion from a ternary blend of PI and PS homopolymers and a PI-*b*-PS diblock copolymer. Subsequently the PI domains were crosslinked using sulfur monochloride, and the PS homopolymer was dissolved in hexanes rendering the material nanoporous. Additionally, the bicontinuous membranes developed by Uehara et al. not only avoided the need to align the structures, but tensile tests of the semicrystalline PE matrix exhibited marked improvements in mechanical toughness over brittle PS matricies.[58]

A final example of an improved nanoporous material was templated by a metathesis reactive block polymer. [96] This material incorporated crosslinked dicyclopentadiene (DCPD) into the matrix to improve both mechanical and thermal stability, and formed a bicontinuous morphology, which prevented the need to align the sample. The material was templated by poly(norbornenylethylstyrene-*s*-styrene)-*b*-poly(lactide) (PNS-PLA) where the PNS block was metathesis reactive. The PNS-PLA block polymer was included during the metathesis polymerization of DCPD in THF using the second generation Grubbs catalyst. The authors hypothesized that metathesis

crosslinking of the DCPD and PNS induced the PLA to phase separate from the forming matrix due to reaction induced phase separation. Phase separation was limited to the nanoscale by incorporation of PNS into the matrix, and removal of PLA using base mediated hydrolysis left a bicontinuous nanoporous structure as seen in Figure 1.13.

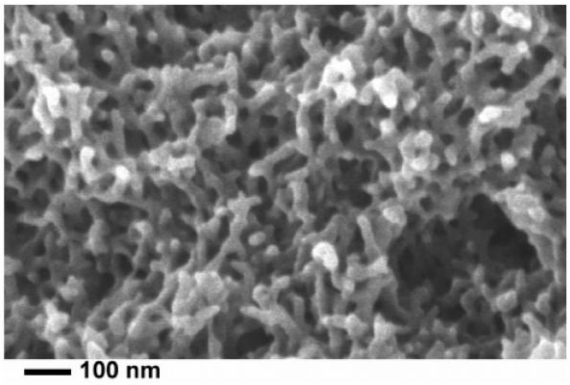

Figure 1.13. SEM micrograph of a fractured surface illustrating the bicontinuous structure.[96]

1.3. Thesis Outline

The goal of my research was to investigate and develop nanoporous thermosetting membranes templated by reactive block polymers as potential alternatives to current water purification membranes. These membranes seek to improve membrane performance by addressing three challenges associated with current ultrafiltration membranes and/or block polymer derived membranes. First, utilizing block polymer self-assembly to template porosity, membranes with narrower pore size distributions could be formed. Achieving narrower pore size distributions with high void fractions should result in a material capable of achieving a high permeability while maintaining a high selectivity. Second, employing materials with a bicontinuous morphology eliminates

the need to align the block polymer domains and the defects often encountered in poorly aligned materials. Finally, forming membranes from thermosetting systems allows for many variables in the system to be "tuned" thereby improving mechanical performance and/or membrane functionality by adjusting the block polymer template or the reactive monomers employed.

Critical to this work is an understanding about the utilization of block polymers in forming nanostructured thermosets, as such this will be reviewed in Chapter 2. Chapter 3 then reports on the flux, filtration and fouling characteristics of membranes formed from the PNS-PLA/DCPD system examined using dead-end flow filtration experiments. Additionally, the expansion of the PNS-PLA/DCPD system to reactive triblock terpolymer templates as a means of imparting functionality to the pores is also reported. By adding and/or varying the mid block employed, hydrophilic and stimuli responsive membranes were formed with the potential for not only improved fouling resistance but also the development of membranes capable of variable flux depending on environmental conditions.

In order to extend the use of reactive block polymer templates beyond metathesis crosslinking, the mechanism of formation of the bicontinuous structure with the PNS-PLA/DCPD system was investigated and is described in Chapter 4. The limit of bicontinuous structure formation was probed by synthesizing a series of PNS-PLA block polymers with varied PLA compositions, which were then used to form an array of films with varied DCPD compositions. Based on the resulting morphologies as determined by

SAXS, SEM, and nitrogen adsorption experiments, conditions necessary for the formation of the bicontinuous morphology are developed.

Finally, expansion of block polymer templating to vinyl crosslinking systems using a poly(lactide)-*b*-poly(cyclooctene-*r*-norbornenylmethacrylate)-*b*-poly(lactide) (PLCNL) triblock copolymer is reported in Chapter 5. The versatility of the vinyl reactive system in forming nanostructured thermosets is proven by using the PLCNL block polymer to impart structure to a several different vinyl reactive monomers including styrene, divinyl benzene, methyl methacrylate, and ethylene glycol dimethacrylate. Although nanoporous thermosets were not generated using this system, the formation of a nanostructured vinyl thermoset as evidenced by SAXS and TEM demonstrates the general applicability of using this reactive block polymer methodology for forming a variety of nanostructured thermosets.

1.4. References

(1) United Nations Educational Scientific and Cultural Organization World Water Assessment Program In Water for People, Water for Life—the United Nations World Water Development Report; Berghahn Books: Barcelona, 2003.

(2) UN Millennium Project Task Force on Water and Sanitation In *Health Dignity and Development: What Will It Take?* Earthscan: London, 2005; Vol. Final Report.

(3) Singh, R. In Hybrid Membrane Systems for Water Purification; Elsevier: Oxford, 2006.

(4) Shannon, M. A.; Semiat, R. *MRS Bulletin* **2008**, *33*, 9–15.

(5) Shannon, M. A.; Bohn, P. W.; Elimelech, M.; Georgiadis, J. G.; Marinas, B. J.; Mayes, A. M. *Nature* **2008**, *452*, 301-310.

(6) Hoek, Eric M. V.; Jawor, A. In "Nanofiltration Separations"; Schwarz, J. A., Contescu, C. I. and Putyera, K., Eds.; *Encyclopedia of Nanoscience and Nanotechnology;* Marcel Dekker: New York, 2004; Vol. 1, pp 2399–2412.

(7) Van Der Bruggen, B.; Vandecasteele, C.; Van Gestel, T.; Doyen, W.; Leysen, R. *Environ. Prog.* **2003**, *22*, 46-56.

(8) Aptel, P.; Buckley, C. A. In "Chapter 2 Categories of Membrane Operations"; Mallevialle, J., Odendaal, P. E. and Wiesner, M. R., Eds.; *Water Treatment Membrane Processes;* McGraw-Hill: New York, 1996; 2.1–2.24.

(9) Eykamp, W. In "Chapter 1 Microfiltration and Ultrafiltration"; Noble, R. D., Stern, S. A., Eds.; *Membrane Separations Technology Principles and Applications;* Elsevier: Amsterdam, 1995; 1–43.

(10) Mehta, A.; Zydney, A. L. *J. Membr. Sci.* **2005**, *249*, 245-249.

(11) Cussler, E. L. In *Diffusion Mass Transfer in Fluid Systems, Second Edition;* Cambridge University Press: New York, 2005.

(12) Bird, R.; Stewart, W. E.; Lightfoot, E. N. In *Transport Phenomena*; J. Wiley & Sons, Inc: New York, 2007;

(13) Baker, R. W. *Membrane technology and applications*, 2nd Ed. John Wiley & Sons Ltd, West Sussex, England, **2004**.

(14) Strathmann, H. *AIChE Journal* **2001** *47*, 1077–1087.

(15) Phillip, W. A.; Rzayev, J.; Hillmyer, M. A.; Cussler, E. L. *J. Membr. Sci.* **2006**, *286*, 144-152.

(16) Bates, F. S. "Polymer-Polymer Phase Behavior", *Science* **1991**, *251*, 898–905.

(17) Hadjichristidis, N.; Pitsikalis, M.; Iatrou, H. *Adv. Poly. Sci.* **2005**, *189*, 1–124.

(18) Hadjichristidis, N.; Iatrou, H.; Pitsikalis, M.; Pispas, S.; Avgeropoulos, A. *Prog. Poly. Sci.* **2005**, *30*, 725–782.

(19) Muller, A. J.; Balsamo, V.; Arnal, M. L. *Adv. Polym. Sci.* **2005**, *190*, 1–63.

(20) Abetz, V.; Simon, Peter F. W. *Adv. Polym.Sci.* **2005**, *189*, 125–212.

(21) Miyaki, Y.; Iwata, M.; Fujita, Y.; Tanisugi, H.; Isono, Y.; Fujimoto, T. *Macromolecules* **1984**, *17*, 1907–1912.

(22) Kim, Y. J.; Sung, Y. K.; Piao, A. Z.; Grainger, D. W.; Okano, T.; Kim, S. W. *J. Appl. Polym. Sci.* **1994**, *54*, 1863–1872.

(23) Ishizu, K.; Uchida, S. *Prog. Polym. Sci.* **1999**, *24*, 1439–1480.

(24) Hadjichristidis, N., *J. Polym. Sci. Part A: Polym. Chem.* **1999**, *37*, 857–871.

(25) Schellekens, M.; Klumperman, B. *J. Macromol. Sci., Rev. Macromol. Chem. Phys.* **2000**, *40*, 167.

(26) Pitsikalis, M.; Pispas, S.; Mays, J. W.; Hadjichristidis, N. *Adv. Polym. Sci.* **1998**, *135*, 1–137.

(27) Hadjichristidis, N.; Pitsikalis, M.; Pispas, S.; Iatrou, H. *Chem. Rev.* **2001**, *101*, 3747–3792.

(28) Lodge, T. P. *Macromol. Chem. Phy.* **2003**, *204*, 265–273.

(29) Bates, F. S.; Fredrickson, G. H. *Phys. Today* **1999**, *52*, 32.

(30) Leibler, L. *Macromolecules* **1980**, *13*, 1602–1617.

(31) Bates, F. S.; Fredrickson, G. H. *Annu. Rev. Phys. Chem.* **1990**, *41*, 525–557.

(32) Bates, F. S.; Schulz, M. F.; Khandpur, A. K.; Forster, S.; Rosedale, J., H.; Almdal, K.; Mortensen, K. *Faraday Discuss.* **1994**, *98*, 7–18.

(33) Khandpur, A. K.; Foerster, S.; Bates, F. S.; Hamley, I. W.; Ryan, A. J.; Bras, W.; Almdal, K.; Mortensen, K. *Macromolecules* **1995**, *28*, 8796–8806.

(34) Hajduk, D. A.; Takenouchi, H.; Hillmyer, M. A.; Bates, F. S.; Vigild, M. E.; Almdal, K. *Macromolecules* **1997**, *30*, 3788–3795.

(35) Matsen, M. W.; Schick, M. *Phys. Rev. Lett.* **1994**, *72*, 2660.

(36) Matsen, M. W.; Bates, F. S. *Macromolecules* **1996**, *29*, 1091–1098.

(37) Cochran, E. W.; Garcia-Cervera, C. J.; Fredrickson, G. H. *Macromolecules* **2006**, *39*, 2449–2451.

(38) Lynd, N. A. *The Effects of Polydispersity on Block Copolymer Self-assembly*, University of Minnesota, Ann Arbor, MI, 2007.

(39) Park, C.; Yoon, J.; Thomas, E. L. *Polymer* **2003**, *44*, 6725–6760.

(40) Lee, J. S.; Hirao, A.; Nakahama, S. *Macromolecules* **1988**, *21*, 274–276.

(41) Hedrick, J.; Labadie, J.; Russell, T.; Hofer, D.; Wakharker, V. *Polymer* **1993**, *34*, 4717–4726.

(42) Du, P.; Li, M.; Douki, K.; Li, X.; Garcia, C. B. W.; Jain, A.; Smilgies, D.; Fetters, L. J.; Gruner, S. M.; Wiesner, U.; Ober, C. K. *Adv. Mater.* **2004**, *16*, 953–957.

(43) Thurn-Albrecht, T.; Steiner, R.; DeRouchey, J.; Stafford, C. M.; Huang, E.; Bal, M.; Tuominen, M.; Hawker, C. J.; Russell, T. P. *Adv. Mater.* **2000**, *12*, 787–791.

(44) Zalusky, A. S.; Olayo-Valles, R.; Taylor, C. J.; Hillmyer, M. A. *J. Am. Chem. Soc.* **2001**, *123*, 1519–1520.

(45) Zalusky, A. S.; Olayo-Valles, R.; Wolf, J. H.; Hillmyer, M. A. *J. Am. Chem. Soc.* **2002**, *124*, 12761–12773.

(46) Ndoni, S.; Vigild, M. E.; Berg, R. H. *J. Am. Chem. Soc.* **2003**, *125*, 13366–13367.

(47) Olayo-Valles, R.; Lund, M. S.; Leighton, C.; Hillmyer, M. A. *J. Mater. Chem.* **2004**, *14*, 2729–2731.

(48) Lee, M.; Park, M.; Oh, N.; Zin, W.; Jung, H.; Yoon, D. K. *Angew. Chem. Int. Ed.* **2004**, *43*, 6465–6468.

(49) Goldbach, J. T.; Lavery, K. A.; Penelle, J.; Russell, T. P. *Macromolecules* **2004**, *37*, 9639–9645.

(50) Zhang, M.; Yang, L.; Yurt, S.; Misner, M. J.; Chen, J.; Coughlin, E. B.; Venkataraman, D.; Russell, T. P. *Adv. Mater.* **2007**, *19*, 1571–1576.

(51) Hillmyer, M. A. *Adv. Polym. Sci.* **2005**, *190*, 137–181.

(52) Olson, D. A.; Chen, L.; Hillmyer, M. A. *Chem. Mater.* **2008**, *20*, 869–890.

(53) Liu, G.; Ding, J.; Stewart, S. *Angew. Chem. Int. Ed.* **1999**, *38*, 835-838.

(54) Liu, G.; Ding, J.; Hashimoto, T.; Kimishima, K.; Winnik, F. M.; Nigam, S. *Chem. Mater.* **1999**, *11*, 2233-2240.

(55) Cooney, D. T.; Hillmyer, M. A.; Cussler, E. L.; Moggridge, G. D. *Crystallogr. Rev.* **2006**, *12*, 13–24.

(56) Rzayev, J.; Hillmyer, M. A. *Macromolecules* **2005**, *38*, 3–5.

(57) Rzayev, J.; Hillmyer, M. A. *J. Am. Chem. Soc.* **2005**, *127*, 13373-13379.

(58) Uehara, H.; Yoshida, T.; Kakiage, M.; Yamanobe, T.; Komoto, T.; Nomura, K.; Nakajima, K.; Matsuda, M. *Macromolecules* **2006**, *39*, 3971–3974.

(59) Uehara, H.; Kakiage, M.; Sekiya, M.; Sakuma, D.; Yamonobe, T.; Takano, N.; Barraud, A.; Meurville, E.; Ryser, P. *ACS Nano* **2009**, *3*, 924-932.

(60) Fasolka, M. J.; Mayes, A. M. *Annu. Rev. Mater. Res.* **2001**, *31*, 323-355.

(61) Krausch, G.; Magerle, R. *Adv. Mater.* **2002**, *14*, 1579-1583.

(62) Yang, S. Y.; Ryu, I.; Kim, H. Y.; Kim, J. K.; Jang, S. K.; Russell, T. P. *Adv. Mater.* **2006**, *18*, 709-712.

(63) Thurn-Albrecht, T.; Steiner, R.; DeRouchey, J.; Stafford, C. M.; Huang, E.; Bal, M.; Tuominen, M.; Hawker, C. J.; Russell, T. P. *Adv. Mater.* **2000**, *12*, 787-791.

(64) Jeong, U.; Kim, H.; Rodriguez, R. L.; Tsai, I. Y.; Stafford, C. M.; Kim, J. K.; Hawker, C. J.; Russell, T. P. *Adv. Mater.* **2002**, *14*, 274-276.

(65) Jeong, U.; Ryu, D. Y.; Kho, D. H.; Lee, D. H.; Kim, J. K.; Russell, T. P. *Macromolecules* **2003**, *36*, 3626-3634.

(66) Jeong, U.; Ryu, D. Y.; Kim, J. K.; Kim, D. H.; Russell, T. P.; Hawker, C. J. *Adv. Mater.* **2003**, *15*, 1247-1250.

(67) Jeong, U.; Ryu, D. Y.; Kim, J. K.; Kim, D. H.; Wu, X.; Russell, T. P. *Macromolecules* **2003**, *36*, 10126-10129.

(68) Yang, S. Y.; Park, J.; Yoon, J.; Ree, M.; Jang, S. K.; Kim, J. K. *Adv. Funct. Mater.* **2008**, *18*, 1371-1377.

(69) Sperschneider, A.; Schacher, F.; Gawenda, M.; Tsarkova, L.; Müller, A. H.; Ulbricht, M.; Krausch, G.; Köhler, J. *Small* **2007**, *3*, 1056-1063.

(70) Gawenda, M.; Sperschneider, A.; Schacher, F.; Krausch, G.; Müller, A.; Ulbricht, M. *Desalination* **2006**, *200*, 29-31.

(71) Nuxoll, E. E.; Hillmyer, M. A.; Wang, R.; Leighton, C.; Siegel, R. A. *ACS Appl. Mater. Interfaces* **2009**, *1*, 888-893.

(72) Phillip, W. A.; O'Neill, B.; Rodwogin, M.; Hillmyer, M. A.; Cussler, E. L. *ACS Appl. Mater. Interfaces* **2010**, 2, 847-853.

(73) van de Witte, P.; Dijkstra, P. J.; van den Berg, J. W. A.; Feijen, J. *J. Membr. Sci.* **1996**, *117*, 1-31.

(74) Ulbricht, M. *Polymer* **2006**, *47*, 2217-2262.

(75) Nunes, S. P.; Peinemann, K. V. In *Membrane Technology in the Chemcial Industry*, Second Edition; Wiley-VCH: Weinheim, Germany, **2006.**

(76) Hancock, L. F. *J. Appl. Polym. Sci.* **1997**, *66*, 1353-1358.

(77) Hancock, L. F.; Fagan, S. M.; Ziolo, M. S. *Biomaterials* **2000**, *21*, 725-733.

(78) Roux, S. P.; Jacobs, E. P.; Reenen, A. J. v.; Morkel, C.; Meincken, M. *J. Membr. Sci.* **2006**, *276*, 8-15.

(79) Wang, Y.; Wang, T.; Su, Y.; Peng, F.; Wu, H.; Jiang, Z. *Langmuir* **2005**, *21*, 11856-11862.

(80) Hester, J. F.; Banerjee, P.; Mayes, A. M. *Macromolecules* **1999**, *32*, 1643-1650.

(81) Hester, J. F.; Mayes, A. M. *J. Membr. Sci.* **2002**, *202*, 119-135.

(82) Hester, J. F.; Banerjee, P.; Won, Y.; Akthakul, A.; Acar, M. H.; Mayes, A. M. *Macromolecules* **2002**, *35*, 7652-7661.

(83) Akthakul, A.; Salinaro, R. F.; Mayes, A. M. *Macromolecules* **2004**, *37*, 7663-7668.

(84) Asatekin, A.; Menniti, A.; Kang, S.; Elimelech, M.; Morgenroth, E.; Mayes, A. M. *J. Membr. Sci.* **2006**, *285*, 81-89.

(85) Kang, S.; Asatekin, A.; Mayes, A. M.; Elimelech, M. *J. Membr. Sci.* **2007**, *296*, 42-50.

(86) Asatekin, A.; Kang, S.; Elimelech, M.; Mayes, A. M. *J. Membr. Sci.* **2007**, *298*, 136-146.

(87) Peinemann, K.; Abetz, V.; Simon, P. F. W. *Nat. Mater.* **2007**, *6*, 992-996.

(88) Hamley, I. W. *J. Phys. Condens. Matter* **2001**, *13*, R643–R671.

(89) Darling, S. B. *Prog. Polym. Sci.* **2007**, *32*, 1152–1204.

(90) Drockenmuller, E.; Li, L. Y. T.; Ryu, D. Y.; Harth, E.; Russell, T. P.; Kim, H.; Hawker, C. J. *J. Polym. Sci., Part A: Polym. Chem.* **2005**, *43*, 1028–1037.

(91) Leiston-Belanger, J. M.; Russell, T. P.; Drockenmuller, E.; Hawker, C. J. *Macromolecules* **2005**, *38*, 7676–7683.

(92) Hansen, M. S.; Vigild, M. E.; Berg, R. H.; Ndoni, S. *Polym. Bull.* **2004**, *51*, 403–409.

(93) Guo, F.; Andreasen, J. W.; Vigild, M. E.; Ndoni, S. *Macromolecules* **2007**, *40*, 3669–3675.

(94) Mao, H.; Hillmyer, M. A. *Soft Mater* **2006**, *2*, 57–59.

(95) Zhou, N.; Bates, F. S.; Lodge, T. P. *Nano Lett.* **2006**, *6*, 2354–2357.

(96) Chen, L.; Phillip, W. A.; Cussler, E. L.; Hillmyer, M. A. *J. Am. Chem. Soc.* **2007**, *129*, 13786-13787.

Chapter 2.

Nanostructured Thermosets using Block Polymers

This chapter reviews the formation of nanostructured thermosets. The first three sections describe nanostructured epoxy thermosets formed by the self-assembly first approach, reaction induced phase separation, or reactive block polymers. The fourth section examines incorporation of different functionalities and structures in epoxies, and the final section reviews nanostructuring of non-epoxy thermosets.

2.1. Introduction

Thermosets are polymers formed by crosslinking multifunctional monomers into a rigid network, and most commonly consist of epoxy, phenolic, unsaturated polyester, and urea-formaldehyde resins.[1] Thermosets make up approximately 15–20% of the total plastics industry[2] and are used in a variety of applications including adhesives, surface coatings, electrical materials, and structural parts.[1, 3] The rigid nature and high use temperature of thermosets have made them useful for many applications where thermoplastics fail.[1]

Thermosets have been modified by creating composite materials to enhance their properties using an assortment of additives and approaches. Though thermosets are thermally stable and rigid, their applications are somewhat limited due to their brittle nature as a consequence of their high crosslink density. The inclusion of rubbers[4] and thermoplastics[5] has been explored as a means of improving the mechanical properties of thermosets. The reaction induced phase separation[6,7] (RIPS) of these additives typically results in structures 0.1 to 10 μm in size. Additionally, the dispersion of preformed polymer particles has also been explored to improve mechanical properties.[1] Macroporous thermosets formed by the RIPS and subsequent removal of volatile liquids have been investigated for not only improving mechanical properties but also reducing the dielectric constant of thermosets.[8]

In addition to macro sized inclusions, nanostructured thermosets have also been investigated. Reducing the particle size at a constant blend composition increases the

number of particles and the interfacial area within the material, while simultaneously decreasing the distance between particles. The increased interfacial area of nanostructured thermosets has been hypothesized to improve their strength by more easily facilitating stress transfer between the matrix and particle.[3] As such, nanostructured thermosets have been an avid area of research not only for improving mechanical properties but also taking advantage of synergistic effects from adding functionalized nanostructures. Carbon nanotubes have been explored for improving the toughness of thermosets while also increasing their conductivity by achieving the electrical percolation threshold.[9,10,11,12,13] Nanoclays have been investigated to improve the flame retardant performance of thermosets.[14,15] A variety of inorganic nanoparticles have been incorporated, and depending on the specific particle impart new properties to the nanocomposite.[16,17,18]

Thermosets have also been nanostructured by taking advantage of the self-assembly behavior of block polymers.[3] While the inclusion of rubber or thermoplastic homo- or copolymers results in structures 0.1 to 10 μm, inclusion of a block polymer with a block that remains miscible with the thermoset before, during, and after the cure and a second block that is either immiscible or becomes immiscible upon curing results in a nanostructured thermosets. Nanostructures are formed using block polymers by either the self-assembly first approach or RIPS. The remainder of this chapter reviews the formation of nanostructured thermosets and is divided into four sections. The first three sections describe nanostructured epoxies formed by the self-assembly first approach,

RIPS and reactive block polymers. The fourth section examines incorporation of different functionalities and structures in epoxies, and the fifth section reviews nanostructuring of other thermosets.

2.2. Nanostructured epoxy thermosets using the self-assembly first approach

Nanostructured thermosets formed by the self-assembly first approach incorporate a block polymer with a thermoset miscible and a thermoset immiscible segment. Upon blending the phase separated block polymer selectively incorporates the thermoset precursors into the thermoset miscible block. The morphology adopted depends both on the block polymer and the blend composition as swelling of the miscible block can result in morphological transitions. [19] Ordered morphologies such as lamellar, gyroid, hexagonally packed cylinders and spheres on a cubic centered lattice[19,20,21] as well as dilute solution morphologies including spherical and wormlike micelles and vesicles[22,23,24,25] have been observed. The self-assembled nanostructures are ultimately immobilized by curing the resin.[19] Figure 2.1 shows the general scheme for forming nanostructured thermosets using the self-assembly first approach.

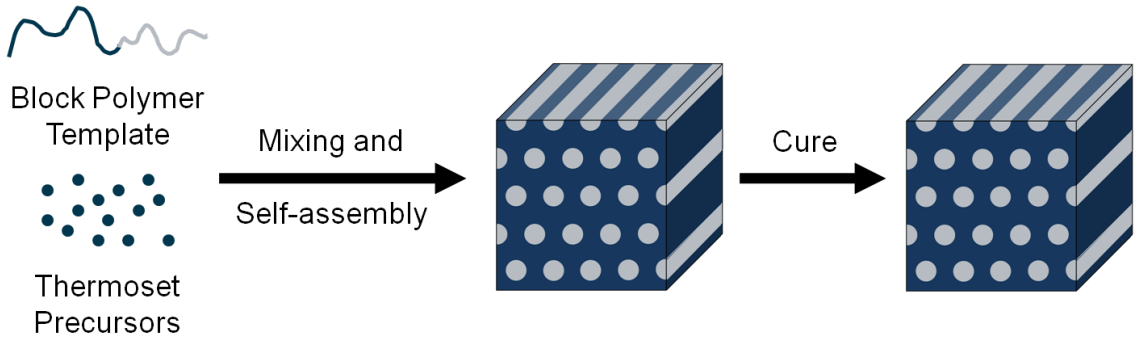

Figure 2.1. General scheme for forming nanostructured thermosets using the self-assembly first approach where mixing of the block polymer template and thermoset precursors results in self-assembly. Subsequent curing of the nanostructured blend locks-in the self-assembled morphology into the thermoset.

2.2.1. Poly(ethylene oxide) (PEO) diblock copolymer templates

PEO has been used in combination with a variety of other blocks to template nanostructures in epoxies as it is miscible with the epoxy both before and after curing.[26,27] The first detailed morphological investigation of a nanostructured epoxy used the diclycidyl ether of bisphenol A (DGEBA) cured with phthalic anhydride (PHTA) as the resin and poly(ethylene oxide)-*b*-poly(ethyl ethylene) (PEO-PEE) or PEO-*b*-poly(ethylene-*alt*-propylene) (PEP) block polymers.[20] Simultaneous small angle neutron scattering and rheological measurements before, during and after curing a blend with PEO-PEP (36 wt %) indicated a transition to a network material without disruption of the cylindrical morphology. Additionally, small angle neutron scattering (SANS) of a blend with 30 wt % PEO-PEE indicated a hexagonally packed cylindrical microstructure with a 14.6 nm domain spacing both before and after curing. Transmission electron microscopy (TEM) exhibited hexagonally packed cylindrical morphologies consistent with the

scattering results as can be seen in Figure 2.2 for a sheer aligned cured DGEBA resin with 25 wt % PEO-PEE.

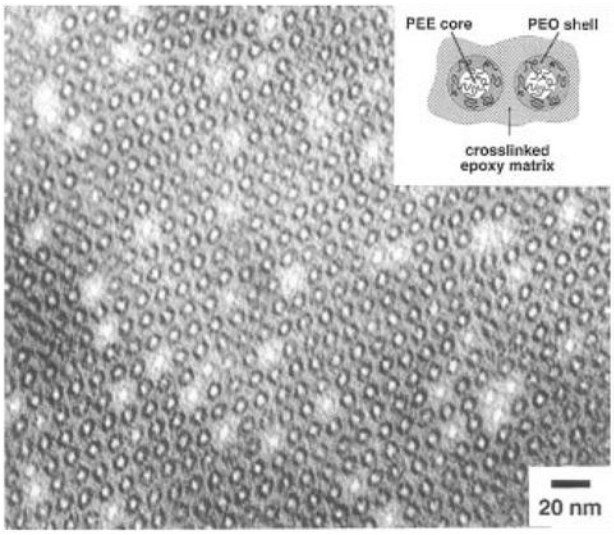

Figure 2.2. TEM of a PEO-PEE block polymer (25 wt %) blended with a DGEBA/PHTA epoxy resin that was shear aligned prior to curing (adapted from Hillmyer et al.)[20]

Lipic et al. further explored nanostructured epoxies blended with a PEO-PEP block polymer [2.7 kg/mol weight fraction of PEO (w_{PEO}) = 0.58].[19] A compositionally dependent phase diagram for uncured blends was developed (Figure 2.3) based on morphologies determined from small angle X-ray scattering (SAXS) and the order-disorder transition temperatures from dynamic mechanical analysis. The full range of bulk ordered morphologies including lamellar, gyroid, cylinders, and spheres were observed. The addition of methylene dianiline (MDA) as the curing agent did not significantly affect the morphologies. Upon curing little morphological variation was observed, but samples with 69 and 35 wt % PEO-PEP underwent gyroid to lamellar and spherical to cylindrical phase transitions respectively as observed by in situ SAXS (see

Figure 2.4 for the 69 wt % sample). The authors hypothesized that expulsion of PEO from the epoxy matrix prior to gelation resulted in a reduction of the interfacial curvature at the PEO-PEP interface, leading to the observed transitions.

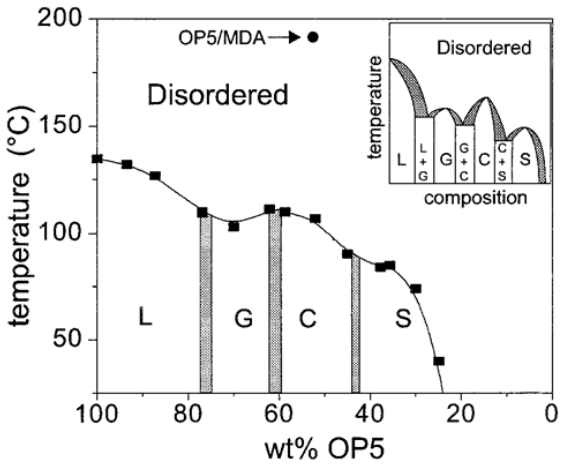

Figure 2.3. Morphological phase diagram for blends of symmetric PEO-PEP block polymer with a DGEBA epoxy resin. The ordered phases are L = lamellar, G = gyroid, C = cylinders, and S = spheres. The inset is a suggested phase diagram indicating two phase regions between the ordered and disordered morphologies (adapted from Lipic et al.).[19]

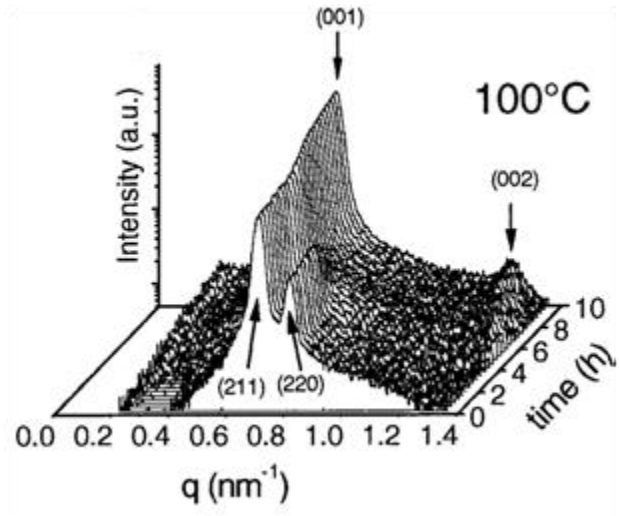

Figure 2.4. Time resolved SAXS during the cure of a PEO-PEP (69 wt %) block polymer blended with a DGEBA/MDA epoxy. The change in scattering peaks from (211) and (220) to (001) and (002) demonstrates a transition from the gyroid to lamellar morphology (adapted from Lipic et al.).[19]

Asymmetric PEO-PEP block polymers [2.1 kg/mol w_{PEO} = 0.32] were also explored as structural templates for DGEBA/MDA epoxies.[28,29] Addition of DGEBA to the pure block polymer resulted in selective swelling of the PEO blocks causing phase transitions from cylindrical to gyroid to lamellar and ultimately vesicular morphologies (Figure 2.5). These phase transitions were driven by increases in the volume fraction of the PEO/DGEBA domain.

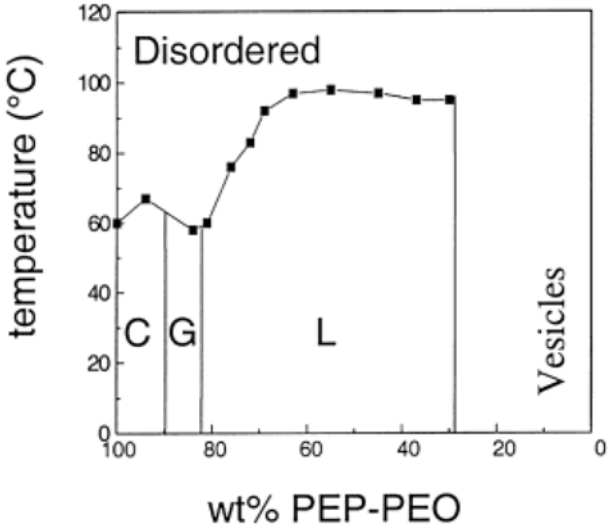

Figure 2.5. Morphological phase diagram for blends of an asymmetric PEO-PEP block polymer (w_{PEO} = 0.32) with a DGEBA epoxy resin. The ordered phases are C = cylinders, G = gyroid, and L = lamellar (adapted from Dean et al.).[29]

Dean et al. further explored dilute solution morphologies of symmetric and asymmetric PEO-PEP block polymers in DGEBA/MDA epoxies.[29] Thermosets modified with 5 wt % or less of a symmetric PEO-PEP block polymer exhibited a spherical micellar morphology both before and after curing as evidenced by SAXS. Increasing the block polymer molecular weight at the same blend composition increased sphere size from 6 to 30 nm. Templating with asymmetric PEO-PEP block polymers resulted in

vesicles of varying size with the number of vesicle layers being controlled by adjusting the PEO-PEP concentration. Differential scanning calorimetry (DSC) revealed that minimal impact on the epoxy glass transition temperature at PEO-PEP concentrations less than 10 wt %. Additionally, ~100% increase in the fracture resistance over neat epoxy thermosets was observed for the spherical morphology independent of micelle size and PEO-PEP concentrations between 5 and 10 wt %. The fracture resistance of the vesicle modified epoxies increased by 177% at a PEO-PEP concentration of 2.5 wt %.

The full range of dilute solution morphologies in DGEBA/MDA epoxy resins was accessed by Dean et al.[30] using a series of PEO-b-poly(butadiene) (PEO-PB) block polymers with w_{PEO} compositions varied from 0.30 to 0.43 at a loading of 2.5 wt %. At w_{PEO} above 0.42, spherical micelles were observed, while below 0.37 vesicles were observed. Wormlike micelles were observed exclusively and in conjunction with vesicles at w_{PEO} of 0.41 and 0.38 respectively. Figure 2.6 illustrates the transition in morphology as a function of block polymer composition. Similar to their previous results, improvement in mechanical properties was the greatest for vesicular modified epoxies, then wormlike micelles and finally spherical micelles.

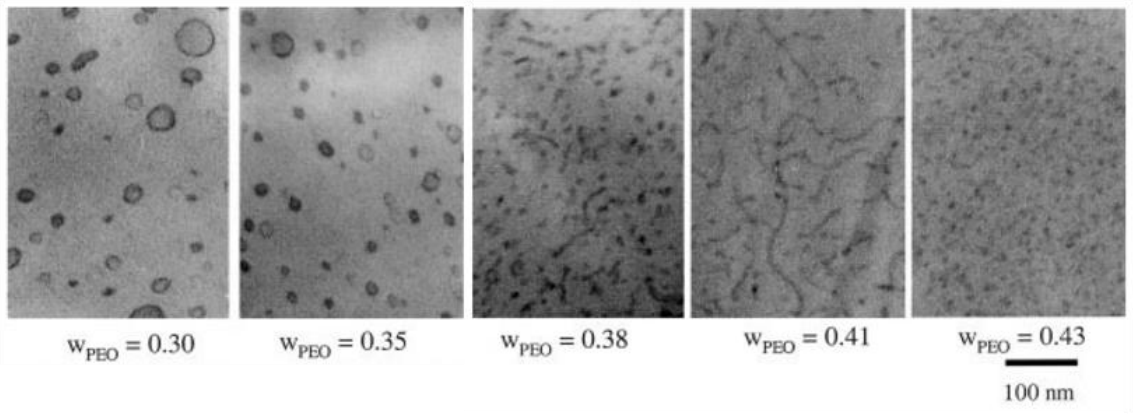

Figure 2.6. TEM micrographs of DGEBA/MDA epoxy modified with 2.5 wt % of a PEO-PB block polymer demonstrating morphological transitions from vesicles to wormlike micelles to spherical micelles upon increasing w_{PEO} in the block polymer template (adapted from Dean et al.).[30]

In addition to DGEBA epoxies, brominated DGEBA (BrDGEBA) has been pursued as a flame retardant epoxy, but these materials are typically too brittle for use.[31] DGEBA epoxies containing between 25 and 50 wt % of BrDGEBA cured with a phenol novolac (PN) curing agent were modified with 5 wt % of two PEO-PEP block polymers. A 40x and 70x improvement in the fracture resistance for 25 wt % BrDGEBA was observed for samples with spherical, and wormlike micelles respectively, while at 50 wt % BrDGEBA, mechanical improvements were maintained for inclusion of wormlike micelles. Changes in the elastic modulus were minimal as reductions of only 10 to 20% were observed. In addition to improving the mechanical properties, the glass transition temperature (T_g) increased by 25 and 55 °C for the spherical and wormlike micellar modified materials respectively thus increasing the operating temperature. Overall, the example shows how nanostructured templates at low loadings can make previously ineffective materials useful for practical applications.

Incorporation of a crystallizable block as the epoxy immiscible block was reported by Guo et al.[32] A DGEBA/MDA epoxy resin was modified with 5 to 82 wt % of a PEO-b-poly(ethylene) (PEO-PE) block polymer [1.4 kg/mol w_{PEO} = 0.5]. Dispersed spherical micelles with crystallized PE cores formed at compositions up to 30 wt % PEO-PE, while aggregated micelles were observed at 40 wt %. Blends with 50 wt % or higher PEO-PE were semicrystalline and exhibited characteristics of a bicontinuous morphology. SAXS confirmed the presence of microphase separation, and fitting of the scattering data assuming spherical micelles indicated the sizes were 8–10 nm in good agreement with the TEM micrographs. DSC was used to probe the melting and crystallization of the PE and PEO blocks to examine the effects of nanoscale confinement on crystallization.

Wu et al. examined the applicability of a commercially available diblock polymer PEO-b-poly(butylene oxide) (PEO-PBO) with a DGEBA/PN resin.[33] A series of PBO-PEO diblock polymers (w_{PEO} from 0.09 to 0.28) were blended with the DGEBA/PN resin at 5 wt %, and the full range of dilute solution morphologies were observed. DSC revealed that the T_g increased from 89–93 °C for clustered vesicles and to 127 °C for wormlike micelles. Mechanical property analysis revealed a 6 to 20 fold increase in toughness depending on the morphology, with the largest increase exhibited by branched wormlike micelles.

Thio et al. explored the strongly segregating PEO-*b*-poly(hexylene oxide) as a template to achieve phase separation at lower molecular weights in DGEBA/PN blends.[34]

Two PEO-PHO diblock copolymers, w_{PEO} = 0.09 and 0.44, formed vesicles and spherical micelles respectively when blended with DGEBA/PN at 5 wt %. Wormlike micelles were formed by blending 5 wt % of an 80/20 blend of the 0.44 and 0.09 w_{PEO} block polymers. While the Young's modulus decreased for the nanostructured thermosets, the fracture toughness increased 4 to 45 fold, with the greatest increase for the wormlike micellar inclusions. The authors hypothesized that the length scale of the resulting nanostructure is critical for toughening. While small spherical micelles did not significantly contribute to plastic deformation and vesicles facilitated premature fracture, the high aspect ratio of the wormlike micelles resulted in a higher toughness by facilitating plastic deformation without premature failure.

An examination of casting solvent, block composition and block molecular weight effects on the morphology of PEO-PEP modified DGEBA/BrDGEBA PN cured resins was reported by Hermel-Davidock et al.[25] Blends with 5 wt % PEO-PEP [10 kg/mol w_{PEO} = 0.33] formed spherical micelles when mixed with the epoxy resin in THF, while mixing in acetone resulted in wormlike micelles. The authors hypothesized that when a poorer PEO solvent is used the corona collapses, which induces the system to minimize the additional interfacial tension by adopting a wormlike micellar morphology. The morphological development was illustrated by comparing the pre/post cure morphologies. THF samples formed spherical micelles almost exclusively before and after curing. Acetone samples had a coexistence of spherical and wormlike micelles before curing, but wormlike micelles were dominant after curing as can be seen in Figure

2.7. The authors attribute this order-order transition to the expulsion of PEO from the epoxy matrix as curing proceeds similar to transitions reported by Lipic.[19] Interestingly the same affect was not observed for a PEO-PEP block polymer with identical composition (w_{PEO} = 0.33) but a lower molecular weight (4.6 kg/mol). Spherical micelles were observed regardless of the mixing solvent, indicating the complex nature of structure formation and transitions.

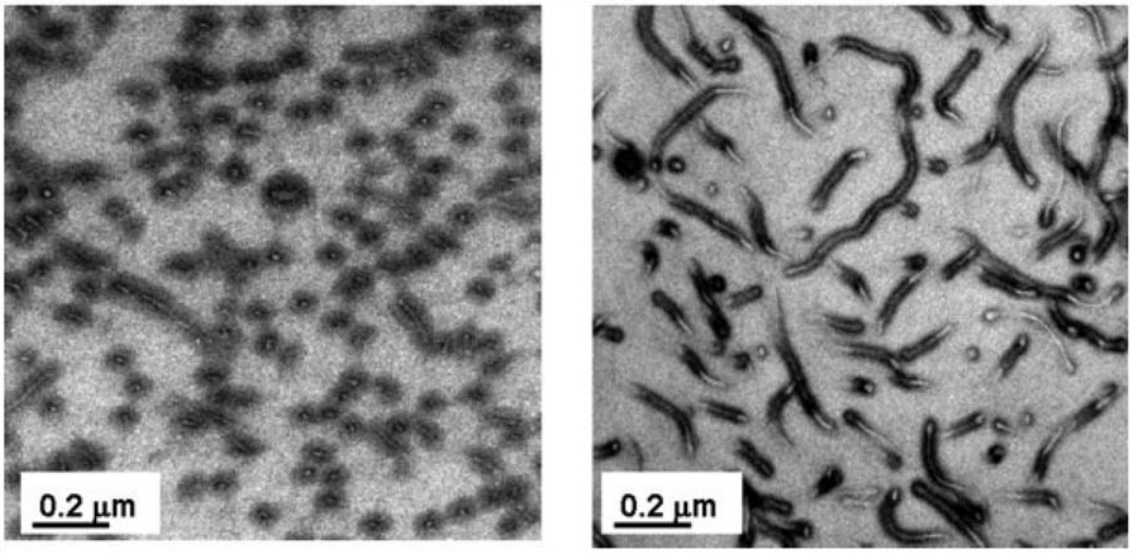

Figure 2.7. TEM of PEO-PEP modified DGEBA/BrDGEBA PN cured epoxy resin both before (left) and after curing (right) showing the phase transition from a mostly spherical to wormlike micelllar morphology (adapted from Hermel-Davidock et al.).[25]

2.2.2. Other block polymer templates

Epoxy miscible blocks other than PEO have also been explored as stabilizers for forming nanostructured thermosets via the self-assembly first approach. Two early examples of block polymer templated thermosets incorporated poly(dimethylsiloxane) (PDMS) using poly(caprolactone) (PCL) as the epoxy miscible block.[35,36] Rifel et al.

incorporated a linear triblock copolymer with PCL at either end of the PDMS midblock into an epoxy resin and cured it with phthalic anhydride without macrophase separation.[35] Buchholz et al. used an H-shaped block polymer with a PDMS backbone and PCL branches.[36] Although not shown, they reported the formation of nanophases 10 to 20 nm in diameter upon inclusion of 5 to 15 weight percent (wt %) of the PDMS. A subsequent paper explored the mechanical properties of the nanostructured material and reported a greater than 2 fold increase in impact strength with 5 wt % of block polymer.[37]

Xu et al. reported a more detailed characterization of PCL-PDMS-PCL nanostructured DGEBA/MOCA [4,4'-methylenebis (2-chloroaniline)] epoxies. Single broad scattering peaks observed during SAXS of cured epoxy blends shifted to lower scattering vectors with increasing triblock polymer composition indicating a decrease in domain size from 25.7 to 19.0 nm for 10 to 40 wt % triblock polymer respectively. TEM and atomic force microscopy (AFM) confirmed the presence of spherical to wormlike micelles depending on the blend composition as can be seen in AFM images shown in Figure 2.8. The epoxy matrix T_g decreased with increasing block polymer composition as observed by DSC and dynamic mechanical thermal analysis (DMTA), suggesting plasticization by the interpenetrating PCL chains.

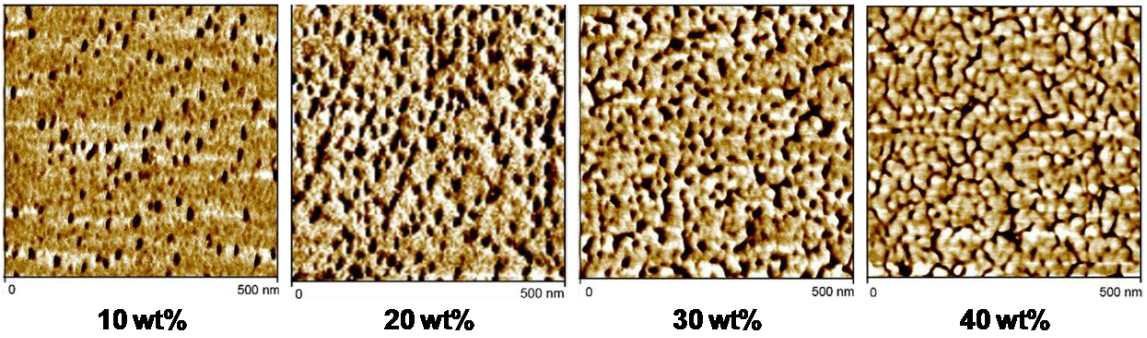

Figure 2.8. AFM images of DGEBA/MOCA epoxy blends with PCL-PDMS-PCL triblock polymers. The wt % values denote the amount of triblock in the blends.

Another epoxy miscible block that has been explored is poly(methyl methacrylate) (PMMA). In a series of papers, Ritzenthaler et al. explored PS-PB-PMMA triblock terpolymers as nanostructure templates.[38,39] Nanostructured epoxy blends were formed using two different PS-PB-PMMA triblock terpolymers [SBM1: 122 kg/mol, w_{PS} = 0.22, w_{PB} = 0.9, w_{PMMA} = 0.69 and SBM2: 123 kg/mol, w_{PS} = 0.12, w_{PB} = 0.18, w_{PMMA} = 0.70], which had small amounts of PS-PB diblock copolymers in them (21 and 10 wt % respectively). Initially, nanostructured blends were observed by TEM in uncured mixtures of SBM1 (50 wt %) with DGEBA and either 4,4'-methylenebis [3-chloro 2,6-diethylaniline] (MCDEA) or 4,4'-diamino diphenyl sulfone (DDS) hardners. However, upon curing the nanostructured morphology was only retained in blends cured with MCDEA. Macrophase separated structures were observed with the DDS hardner due to the phase separation of PMMA from DDS cured epoxies.[38]

Having determined the proper curing agent for achieving nanostructured thermosets, variable composition blends of SBM1 and SBM2 in DGEBA/MCDEA were formed.[39] Blends of SBM1 50 wt % or below exhibited micellar type morphologies

varying from simple spherical micelles to raspberry type micelles to PB cylinders at the PS-PMMA interface as revealed by TEM. Blends with greater than 50 wt % SBM1 had morphologies more comparable to the pure triblock polymer as opposed to micellar structures. In cured blends with 50 wt % SBM2, TEM micrographs revealed micellar morphologies, but because of the increased PB composition, the PB domains covered the PS domains instead of forming the sphere on sphere morphology observed with SBM1. Figure 2.9 shows representative TEM micrographs for blends with both SBM1 and SBM2.

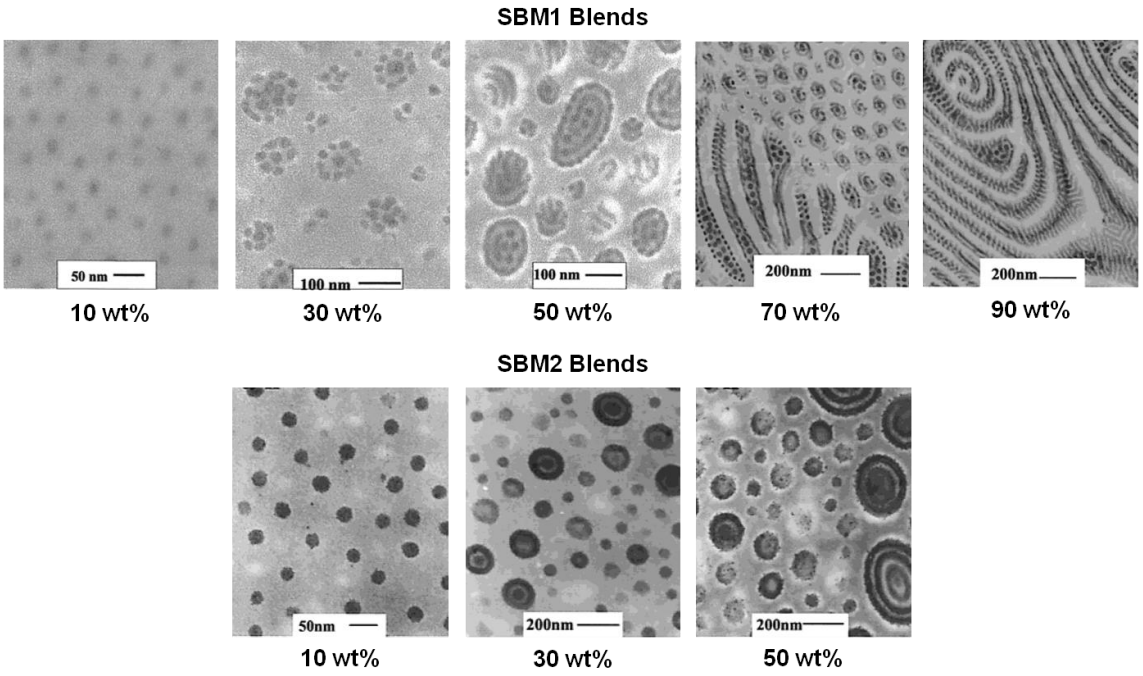

Figure 2.9. TEM micrographs of DGEBA/MCDEA epoxy blends with PS-PB-PMMA triblock terpolymers. The wt % values denote the amount of triblock terpolymer in the blends (adapted from Ritzenthaler et al.).[39]

DMTA of blends with 10 wt % or greater SBM2 revealed a relaxation at -90 °C of the PB domains, a second relaxation of the PS domains at 98 °C, and a third relaxation

at 132 °C corresponding to small amounts of PMMA expelled from the epoxy rich domain near the PB-PMMA interface. A final transition corresponding to the epoxy matrix was observed at variable temperatures depending on the blend composition as increasing amounts of PMMA plasticized the epoxy and decreased the transition temperature. Mechanical testing of 50/50 blends showed improved toughness of the DGEBA/MCDEA from 0.65 to 2 MPa $m^{1/2}$.

2.3. Nanostructured epoxy thermosets using the reaction induced phase separation approach

The formation of nanostructured thermosets using a RIPS approach requires a block polymer template with one block that remains miscible in the thermoset throughout the cure and another block that phase separates upon curing.[40] Phase separation during curing is induced by the decreasing entropic contributions to the free energy of mixing, but since the two blocks are covalently bound, phase separation is limited and nanostructured materials form. The structures attained are trapped by gelation of the thermoset, and include dispersed and fused spherical particles, wormlike structures, bicontinuous structures, lamellae, and cylinders.[14,41,42,43,44] Figure 2.10 shows the general scheme for forming nanostructured thermosets using the RIPS approach.

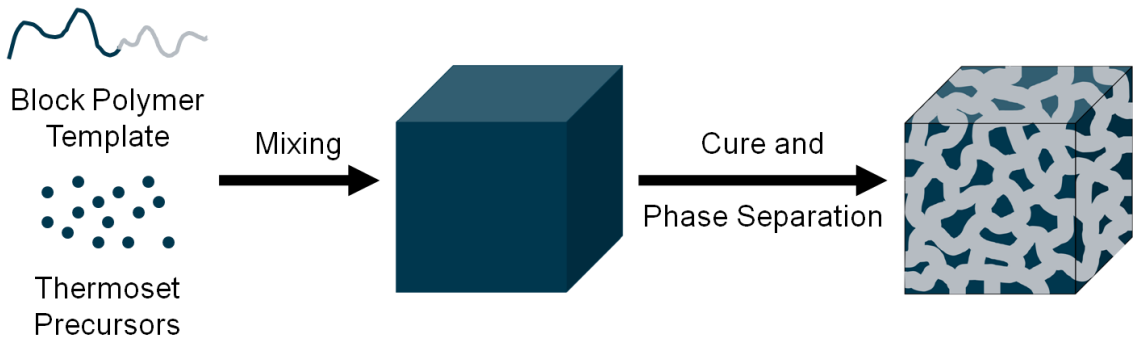

Figure 2.10. AFM phase images of DGEBA/DDM epoxy blends with 10 (A and D), 20 (B and E) and 30 (C and F) wt % PEO-PPO-PEO cured at 80 (A, B and C) and 140 °C (D, E and F).

2.3.1. PEO-PPO-PEO triblock copolymer templates

The commercial availability of PEO-PPO-PEO triblock copolymers has spurred extensive investigation into their use as nanostructure templates for epoxy thermosets. Once blended with the epoxy precursors, the PEO blocks remain miscible throughout the cure, while the initially miscible PPO block phase separates as curing progresses, forming nanostructures via RIPS. Mijovic et al. investigated incorporation of PEO-PPO-PEO into a DGEBA/MDA epoxy thermoset, and used dielectric relaxation spectroscopy (DRS) to track structure development of the PEO-PPO-PEO triblock [4.4 kg/mol w_{PEO} = 0.30] or PEO-PPO diblock [12 kg/mol w_{PEO} = 0.70] modifiers.[45] Optical microscopy of the triblock templated epoxy revealed macrophase separation during curing, which was absent for the diblock templated epoxy. AFM of triblock templated epoxies demonstrated a variety of features over multiple length scales, while the diblock templated epoxies had uniform spherical inclusions 10–30 nm in size. The smaller PEO composition in the PEO-PPO-PEO triblock polymer prevented it from fully stabilizing the PPO blocks upon phase separation leading to the macrophase separated structures.

A subsequent investigation by Guo et al. templated nanostructures using two different PEO-PPO-PEO triblock polymers [5.8 kg/mol, w_{PEO} = 0.3; 8.4 kg/mol w_{PEO} = 0.8] by adjusting the cure conditions. The authors hypothesized that the relative timing of phase separation versus gelation determines the final morphology. Increasing the cure temperature would speed up crosslinking and therefore the onset of gelation, but it could also increase PEO-PPO-PEO mobility and facilitate macrophase separation. To test this hypothesis, thermoset blends were initially cured at 80 °C rather than 120 °C as used previously. TEM micrographs indicated spherical nanostructures formed for the w_{PEO} = 0.3 triblock template at compositions of 10–50 wt %, while macrophase separated structures were observed for 60–80 wt % template compositions. SAXS of the nanostructured samples revealed increased domain spacing with increasing epoxy content, indicating a larger spacing between the micellar inclusions. Compositionally dependent morphological transitions from spherical to wormlike micelles to bicontinuous structures were observed by TEM for the w_{PEO} = 0.8 triblock template.

Thermal properties of the blends were also probed using DSC. The PPO T_g was observed starting at PEO-PPO-PEO compositions of 40 wt % or greater and varied minimally for both templates (−64 °C for w_{PEO} = 0.3 and −56 for for w_{PEO} = 0.8). The PEO melting transition (T_m) was 33 °C for template compositions 60 wt % or greater of the w_{PEO} = 0.3 PEO-PPO-PEO template but decreased with decreasing template composition for w_{PEO} = 0.8 (60 to 50 °C) due to its miscibility with the epoxy matrix. The epoxy T_g decreased significantly upon increasing template composition up to 50 wt %

(170 to 80 °C for w_{PEO} = 0.3 and 170 to 30°C for w_{PEO} = 0.8) due to reductions in the crosslinking density caused by the miscibility of the PEO chains. These results demonstrated how cure conditions influence the final morphology and the importance of controlling the conditions to achieve a nanostructured thermoset.

In a series of papers, Larrañaga et al. further investigated the cure kinetics,[46,47] morphology[48,49] and mechanical properties[50] of DGEBA/DDM epoxies modified with PEO-PPO-PEO block polymers. Initially, the cure kinetics of an epoxy modified with 10–30 wt % PEO-PPO-PEO (2.9 kg/mol, w_{PEO} = 0.38) was probed.[46] DSC temperature scans of epoxy modified blends prior to curing revealed an increase in the polymerization peak temperature with increasing block polymer content. Additionally, isothermal cures using DSC demonstrated a decreasing cure rate with increased block polymer content at all temperatures examined (80, 100, 120, and 140 °C). Retardation of the cure reaction rate was attributed to both dilution effects and hindering of the autocatalytic cure process due to hydrogen bonding between the PEO segments and hydroxyl groups produced *in situ* as shown by infrared spectroscopy.

Phase separation within the blends was examined using DSC, DRS, and cloud point analysis. In addition to the exothermic polymerization peak, DSC dynamic scans indicated a high temperature shoulder in PEO-PPO-PEO containing samples, which became more pronounced with increasing block polymer content. A dynamic temperature scan during measurement of transmitted light suggested the observed shoulder corresponded to phase separation within the blend. DRS indicated macrophase separation

10 minutes into isothermal cures at 140 °C, but at 80 °C macrophase separation was not observed. AFM of epoxy/PEO-PPO-PEO blends cured at 80 °C (Figure 2.11) showed a homogenous morphology for 10 wt % block polymer and nanostructured morphologies for 20 and 30 wt % block polymer samples.[48] In stark contrast, blends cured at 140 °C had macrophase separated morphologies.

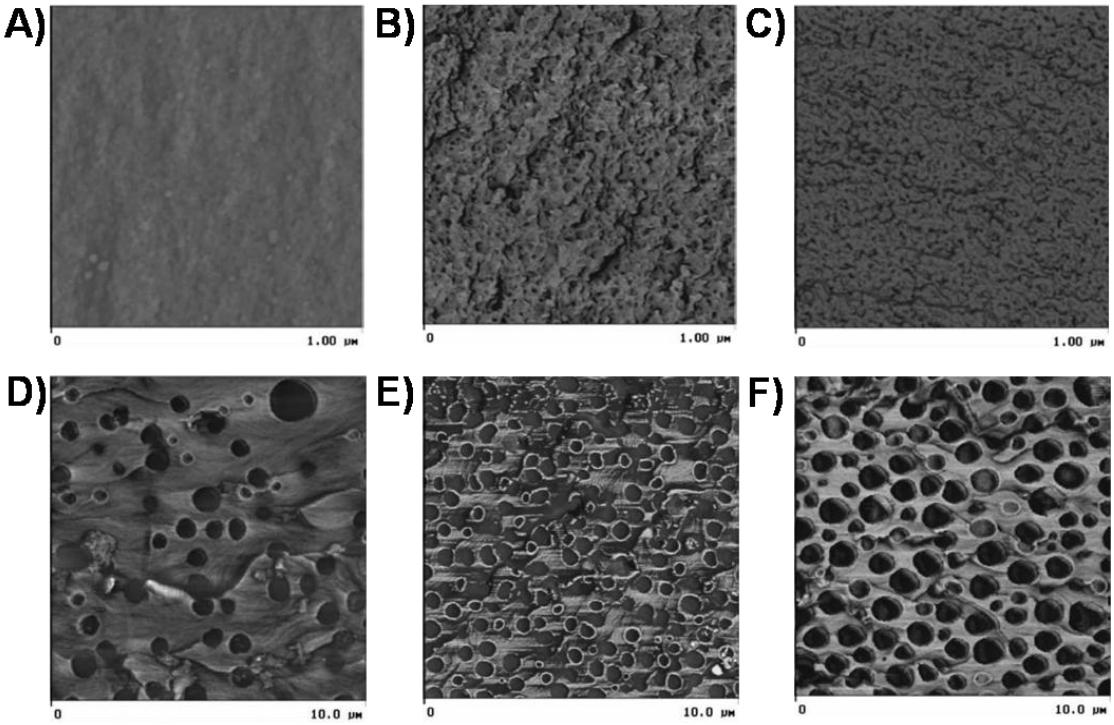

Figure 2.11. AFM phase images of DGEBA/DDM epoxy blends with 10 (A and D), 20 (B and E) and 30 (C and F) wt % PEO-PPO-PEO cured at 80 (A, B and C) and 140 °C (D, E and F) (adapted from Larrañaga et al.).[48]

Thermodynamic analysis of the system revealed χ was directly related to temperature, so upon increasing the curing temperature χ increases, which decreases the extent of reaction necessary to cause phase separation. The competition between the thermodynamics and kinetics of the system explains the temperature dependent

morphologies observed. At lower temperatures, kinetics dominate as gelation occurs before phase separation leading to the homogenous and nanostructure morphologies observed, while at higher temperatures, thermodynamics determines the final morphology as phase separation occurs prior to gelation and formation of macrophase separated morphologies.

Larrañaga et al. then examined the affect of block polymer PEO composition on the cure kinetics and morphologies observed.[47,49] In addition to the block polymer already investigated [2.9 kg/mol, w_{PEO} = 0.38], two additional PEO-PPO-PEO triblock polymers were explored as epoxy modifiers with lower [3.4 kg/mol, w_{PEO} = 0.20] and higher [13.3 kg/mol, w_{PEO} = 0.69] PEO content. As the PEO content in the block polymer and hence total PEO blend content increased, the cure rate decreased in agreement with slowing of the autocatalytic process due to interactions of the PEO segments with the hydroxyl groups. AFM images of blends with 10−30 wt %o f the three block polymers indicated variable morphologies at cure temperatures of 80 and 140 °C. All blends containing the w_{PEO} = 0.69 block polymer resulted in nanostructured morphologies regardless of the cure temperature, while blends with w_{PEO} = 0.20 resulted in macrophase separated morphologies.

The authors attributed the morphological variations to a combination of the kinetics and thermodynamics of the cure and the ability of the PEO segments to prevent macrophase separation during curing. The lower PEO composition in w_{PEO} = 0.20 does not slow the cure rate sufficiently to affect the timing of phase separation relative to

gelation. Additionally, since the chains are too short to stabilize individual micelles, the micelles aggregate and form macrophase separated structures as conversion increases. The large PEO content in w_{PEO} = 0.69 not only slows the cure rate, the interactions between the longer PEO segments and the epoxy matrix are sufficient to stabilize the micellar structures formed thus preventing macrophase separation.

The effect of chain architecture was examined by Guo et al. by investigating DGEBA/MDA cured epoxies blended with two PEO/PPO four-arm star shaped block polymer templates. One template [$(PPO_{core}\text{-}PEO)_4$: 15.0 kg/mol, w_{PEO} = 0.70] consisted of four PPO-PEO blocks connected to an ethylene diamine core via the PPO block, while the second template [$(PEO_{core}\text{-}PPO)_4$: 7.2 kg/mol, w_{PEO} = 0.40] consisted of four PEO-PPO blocks connected to the ethylene diamine core via the PEO block. All $(PPO_{core}\text{-}PEO)_4$/ DGEBA/MDA blends were transparent just above the T_m of the PEO block indicating the blends were not macrophase separated, but $(PEO_{core}\text{-}PPO)_4$/DGEBA/MDA blends with template compositions 60 wt % or greater were cloudy or opaque above the PEO $T_{m,}$ consistent with a macrophase separated structure. DSC of the blends were fairly similar and indicated a suppression of PEO crystallization at block polymer compositions 50 wt % or less due to its miscibility with the epoxy matrix. Additionally, the T_g of the PPO block was only observed at larger block polymer compositions (> 50 wt %). Finally, the epoxy T_g readily decreased with increasing block polymer composition due to plasticization of the matrix with the PEO chains.

TEM micrographs of the 10 to 50 wt % $(PPO_{core}\text{-}PEO)_4$ blends showed a nanophase separated but compositionally dependent morphology consisting of isolated spherical micelles that coalesced at higher compositions until a bicontinuous morphology was observed. TEM micrographs of the 10 to 50 wt % $(PEO_{core}\text{-}PPO)_4$ blends exhibited phase separated structure with features 0.5–1 μm in size. The morphological variations were attributed to the location of the epoxy miscible block. For the $(PPO_{core}\text{-}PEO)_4$ template the epoxy miscible PEO is readily solvated by the epoxy matrix and easily stabilizes the PPO core, but for the $(PEO_{core}\text{-}PPO)_4$ template the epoxy miscible block in the core of the polymer is shielded by the epoxy immiscible block, which leads to macrophase separation.

2.3.2. Other block polymer templates

In addition to PEO-PPO-PEO triblocks, a variety of other block polymer templates have been blended with epoxies to form nanostructures using RIPS. In a series of papers Meng et al. explored various aspects of forming nanostructured epoxy thermosets using RIPS. First, nanostructures formed by blending a PCL-PB-PCL [14.6 kg/mol, w_{PCL} = 0.76] triblock copolymer with a DGEBA/MOCA epoxy were explored.[14] The authors examined the phase behavior of homopolymer chains in the DGEBA/MOCA epoxy, and found that PCL chains are miscible with the DGEBA/MOCA epoxy precursor throughout the cure, while PB homopolymer chains exhibit upper critical solution temperature (UCST) behavior becoming miscible at elevated temperatures before phase separating via RIPS. After establishing the phase behavior of the individual segments,

DGEBA/MOCA blends with 10 to 50 wt % PCL-PB-PCL templates were then cured above the UCST of PB to ensure the structures observed result from RIPS. TEM and AFM of the blends (see Figure 2.12 for TEM) indicated a compositionally dependent microphase separated morphology where individual spheres formed at template compositions of 10 and 20 wt %, while a bicontinuous morphology was observed at 30 and 40 wt %. SAXS also confirmed the presence of microphase separation as broad scattering peaks were observed, which shifted to higher q values with increased block polymer composition. The domain spacings based on these q values were in agreement with those from TEM.

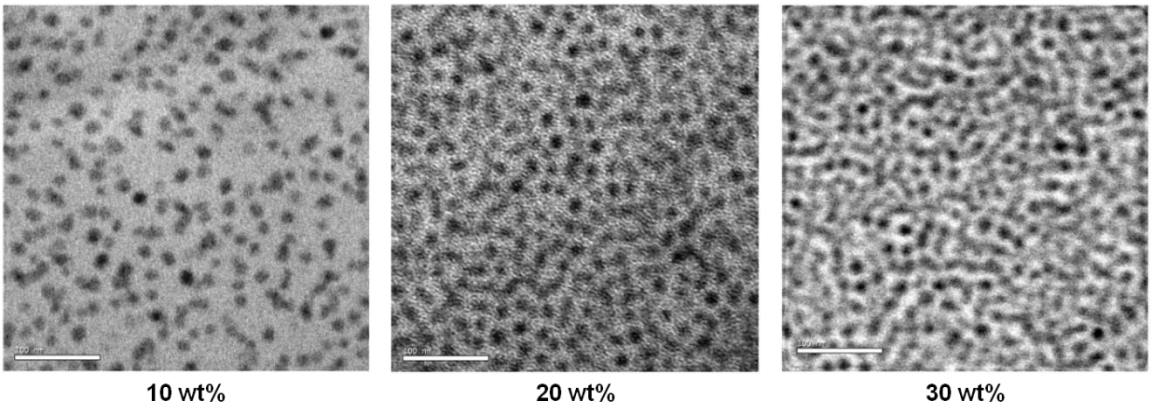

Figure 2.12. TEM micrographs of DGEBA/MOCA epoxy blends with 10, 20 and 30 wt % PCL-PB-PCL block. Samples were microtomed and stained with OsO_4 prior to imaging (adapted from Meng et al).[14]

Building on their initial report, Meng et al. reported the formation of ordered nanostructures using RIPS of a PS-PEO diblock polymer [12.6 kg/mol, w_{PEO} = 0.40] in a DGEBA/MOCA epoxy.[15] Using this template, the PEO block remains miscible throughout the cure, while the PS block exhibits UCST behavior before phase separating during crosslinking. Epoxy blends with 10 to 50 wt % PS-PEO were cured, and their

morphology was investigated by SAXS and AFM. Well-defined scattering peaks with higher order reflections consistent with a spherical or cylindrical morphology on a cubic lattice or a cylindrical morphology on a hexagonally packed lattice were observed in the SAXS patterns. Ordered morphologies were not readily apparent in AFM images of the 10, 20 and 30 wt % PS-PEO blends, but AFM images of a 40 wt % PS-PEO/epoxy blend was consistent with a cubic lattice as can be seen in Figure 2.13.

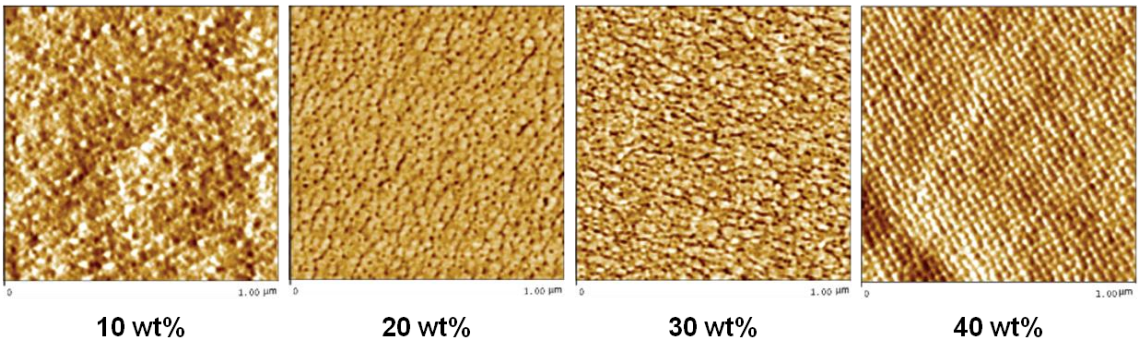

Figure 2.13. AFM phase contrast images of DGEBA/MOCA epoxy blends with 10, 20, 30 and 40 wt % PS-PEO diblock copolymer (adapted from Meng et al.).[15]

Meng et al. also examined the effect of curing agents on nanostructures formed using a PEO-PCL block polymer template (14.3 kg/mol, w_{PEO} = 0.35).[16] Both PEO and PCL homopolymer and PEO-PCL block polymers were blended with a DGEBA epoxy cured with either MOCA or DDS. While the PEO homopolymer remained miscible with the epoxy blend regardless of the curing agent, the PCL homopolymer remained miscible with MOCA cured epoxies, but macrophase separated structures formed when cured with DDS. Block polymer blends exhibited similar phase behavior as homogenous materials were observed when cured with MOCA, but a microphase separated thermoset with spherical PCL nanostructures resulted upon curing with DDS as evidenced by AFM,

TEM, DSC, and SAXS. The results demonstrate the impact of the curing agent on phase separation and potentially provide an avenue for creating phase separated structures with epoxy miscible blocks such as PCL.

Meng et al. also investigated the effect of block polymer architecture by comparing nanostructured DGEBA/MOCA epoxies templated by linear [13.7 kg/mol, w_{PCL} = 0.42] and star shaped [54.6 kg/mol, w_{PCL} = 0.40] PCL-PS block polymers.[51] Blends with block polymer compositions up to 40 wt % were cured. AFM of epoxies with the linear block polymer (Figure 2.14) exhibited microphase separated morphologies that evolved from disordered spherical micelles and fused spherical domains at 10 and 20 wt % to more ordered spherical or cylindrical morphologies packed on a cubic lattice at 30 and 40 wt %. These results were confirmed by SAXS as well-defined scattering peaks were observed with higher order reflections consistent with spherical or cylindrical morphologies on cubic lattices or a cylindrical morphology on a hexagonally packed lattice. AFM of the star template structures indicated microphase separated morphologies as well (Figure 2.14); however, more irregular and less ordered styrene nanophases were observed at compositions up to 30 wt %, while at 40 wt % fairly disordered lamellar nanostructures were apparent. SAXS confirmed microphase separation in the blends with higher order reflections indicating lamellar type lattices. The authors hypothesize that the tethering of PCL-PS chains together in the star template leads to formation of larger "nodules" of PS encased by the PCL when compared to its linear analog. The higher molecular weight of the combined PS chains could lead to a higher UCST, decreased

entropy of mixing, and potentially earlier phase separation, leading to coarsening of the structures and development of the lamellar areas observed. Additionally, the molecular weight differences between the templates would increase the viscosity of the precured blend thereby affecting mobility in the blend.

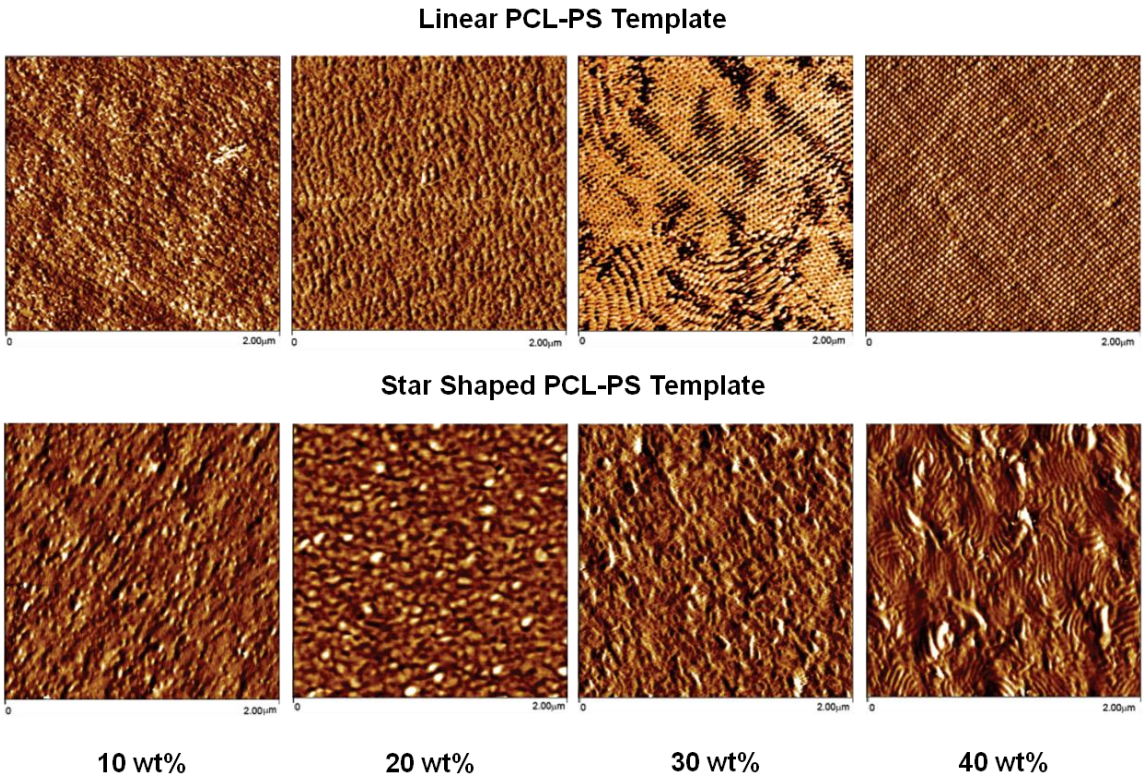

Figure 2.14. AFM phase contrast images of DGEBA/MOCA epoxy blends with 10, 20, 30 and 40 wt % PCL-PS diblock copolymer template with a linear architecture (top) and a star shaped architecture (bottom) (adapted from Meng et al.).[51]

Fan et al. also examined the effects of architecture and sequence on morphology by blending linear PMMA-PS [12.7 kg/mol, w_{PMMA} = 0.58] and tetra-arm star $PMMA_{core}$-PS [57.6 kg/mol, w_{PMMA} = 0.56] and PS_{core}-PMMA [61.6 kg/mol, w_{PMMA} = 0.57] block polymers with DGEBA/MOCA.[18] In these templates, the PMMA block remained

miscible while the PS block underwent RIPS. AFM of the 10–30 wt % samples indicated a spherical morphology that evolved into aggregated spheres with increasing block polymer composition. The 40 wt % blend had ~100 nm spheres with a PMMA corona surrounding the PS cores due to local expulsion of the PMMA during the cure. SAXS scattering patterns confirmed microphase separation within the blends, and indications of higher order reflections were observed possibly indicative of cubic type lattices.

The $PMMA_{core}$-PS blends were cloudy and white upon curing indicating a macrophase separated morphology, but the PS_{core}-PMMA blends were transparent. AFM of the PS_{core}-PMMA blends revealed a compositionally dependent microphase separated morphology with irregular PS particles that transitioned to wormlike/lamellar objects at higher template compositions. SAXS confirmed microphase separation as a single broad scattering peak was observed. The morphological variations between the linear and star block polymers were attributed to the variation in template size similar to the case of the PCL-PS linear versus star architectures by Meng et al.[51] A star block polymer template essentially consists of four linear PMM-PS templates tied together, so the molecular weight of each star would be four times that of a linear chain. The increased molecular weight decreases the entropy of mixing, and shifts the UCST to higher temperatures. The topological changes coupled with the changes in the mixing thermodynamics could lead to the lamellar structures observed. Structural differences between the PS_{core}-PMMA and the $PMMA_{core}$-PS star templates would be due to the sequencing of the individual blocks. When on the periphery, the PMMA block can effectively screen and stabilize the PS

block and mix with the epoxy matrix, but when forming the core, the PMMA block is effectively prevented from mixing with the epoxy matrix, which leads to macrophase separation. Figure 2.15 schematically depicts effects of both architecture and sequencing on the resulting cured templates.

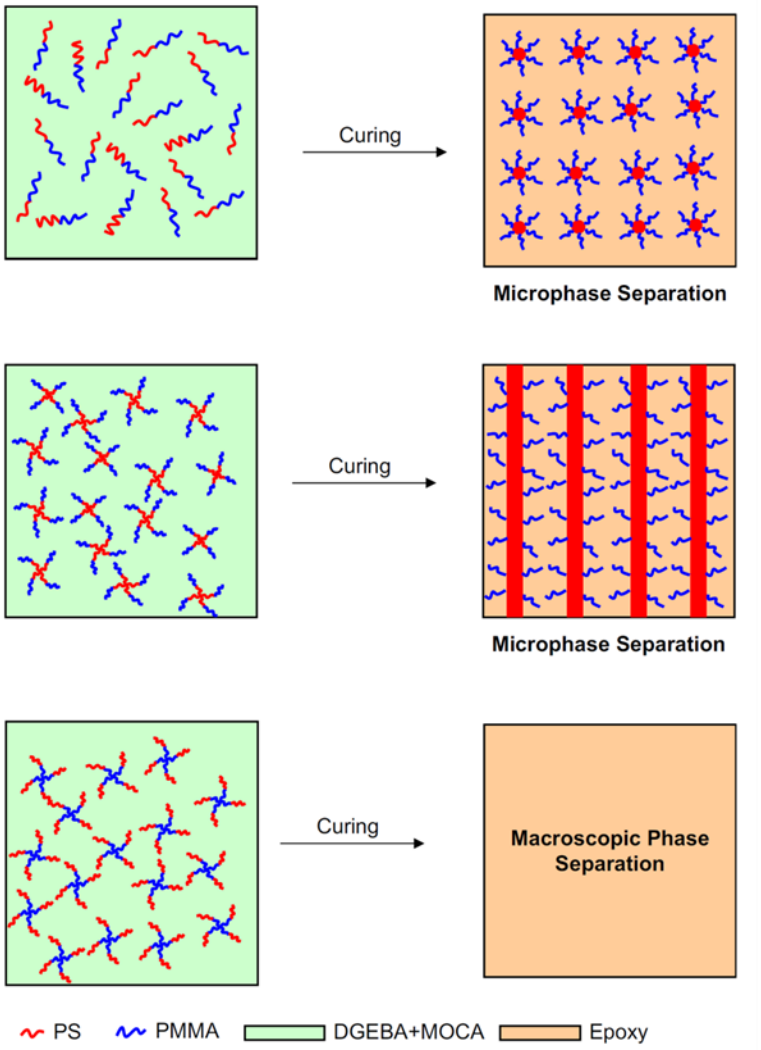

Figure 2.15. Schematic of the various phase separated morphologies for PMMA-PS block polymers depending both on the architecture and sequencing (adapted from Fan et al.).[18]

Xu and coworkers reported the formation of spherical and lamellar nanostructured DGEBA/MOCA epoxies templated by RIPS of a PCL-poly(n-butyl acrylate) (PBA) [12.7 kg/mol, w_{PMMA} = 0.58] block polymer.[17] Cured blends with 10 to 40 wt % PCL-PBA were transparent to transluscent. AFM showed evolution of the blend morphology 10 wt %: spheres, 20 wt %: coalesced spheres, 30 wt %: spheres and worms, and 40 wt % worms and lamellae. Well defined scattering peaks indicative of microphase separation were observed by SAXS, and higher order reflections indicated a cubic lattice for blends ≤ 30 wt % PCL-PBA, and a combination of lamellar and cubic symmetries for 40 wt % PCL-PBA.

2.4. Nanostructured epoxy thermosets using reactive block polymers

A variety of reactive block polymers have also been investigated as nanostructure templates for epoxy resins. The use of reactive block polymers allow the nanostructured morphologies to be further fixed in the blends, increase the variety of curing agents that can be used, and could also facilitate block polymer incorporation at higher concentrations as a means to more functional epoxy resins.

Grubbs et al. investigated both epoxidized isoprene (PIx) and glycidyl methacrylate (GMA) as reactive components for templating in DGEBA/MDA epoxies.[52,53] Templating with PIx-PB block polymers after the selective epoxidiation of PI showed that conversion of 85% or greater is necessary to prevent macrophase

separation. Compositionally dependent morphologies similar to PEO-PEP/epoxy blends observed by TEM (see Figure 2.16) and confirmed by SAXS included lamellae, cylinders, spheres and spherical micelles.

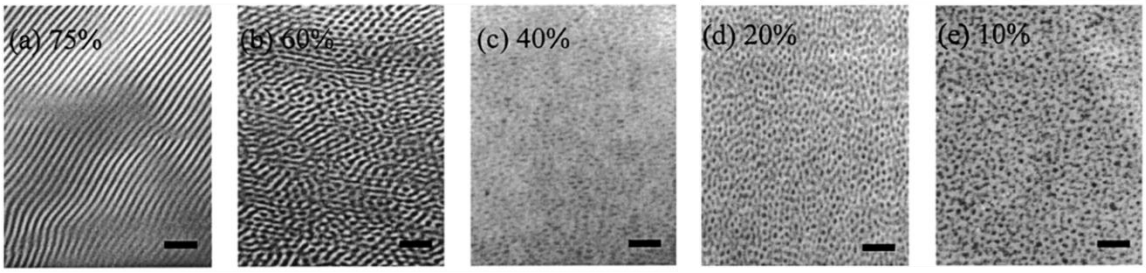

Figure 2.16. TEM of DGEBA/MDA epoxy blends with 75, 60, 40, 20 and 10 wt % PIx-PB reactive diblock copolymer template (adapted from Grubbs et al.).[8]

Thermal analysis of curing by DSC showed two distinct exotherms during the first heating, which correspond to reaction MDA with DGEBA first and followed by the reaction of the PIx with MDA. Reactivity of the reactive block was increased by using GMA as in a poly(methyl acrylate-*stat*-glycidyl methacrylate)-*b*-PI polymer (PMAGMA-PI). Morphologies similar to the PIx-PB template structures were observed after curing, but thermal analysis of curing indicated only a single exotherm, corresponding to the concurrent reaction of the DGEBA and GMA with MDA. Variations in the interfacial region between the epoxy and phase separating block were explained as a function of the reactivity of the block polymer template. For an unreactive template, the epoxy miscible block is expelled at very high epoxy conversion, which leads to a ring around epoxy immiscible block. For a slower reacting template, the reactive block is still expelled at high conversion, but the reactive block then cures at the interface. Finally, a more reactive block cures simultaneously with the epoxy and is fully integrated into the epoxy

network, which prevents expulsion at high conversions. These three morphologies can be seen in Figure 2.17.

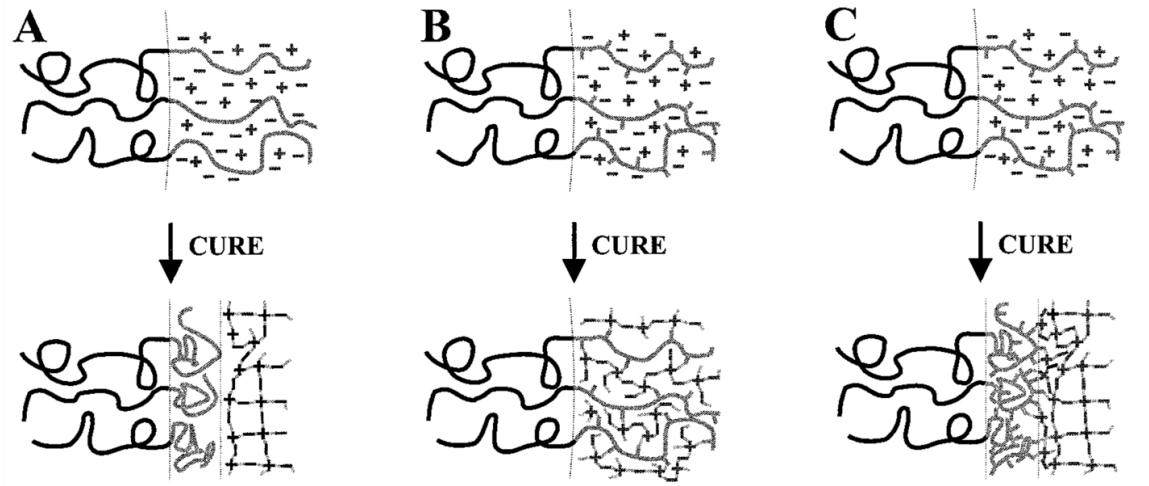

Figure 2.17. Interfacial region near nanostructures for A) unreactive block polymer, B) reactive block polymer that cures simultaneously with the epoxy matrix, and C) reactive block polymer that cures after expulsion from the epoxy matrix (adapted from Grubbs et al.).[8]

Guo et al. extended the work with PMAGMA-PI by comparing templating a novolac/MDA epoxy resin.[54] While nanostructured morphologies such as lamellae, wormlike micelles, and vesicles were observed a large window of macrophase separated structures at intermediate compositions (50–70 wt % PMG-PI) both before and after curing was observed. The macrophase separation was attributed to the inability of the PMAGMA block to adequately incorporate the larger molecular weight novolac resin (2.5 times that of DGEBA) and the possible reduced miscibility of the novolac with the PMAGMA block due to subtle structural differences between the novolac and DGEBA.

Rebizant et al. investigated glycidyl methacrylate as a reactive component for expanding the applicability of PS-PB-PMMA triblocks for templating DGEBA epoxies with other curing agents.[55] Inclusion of 3 wt % GMA effectively prevented macrophase separation from DGEBA/DDS cured epoxies. TEM of PS-PB-PMMA-PGMA blends with a DGEBA/DDS resin before and after curing indicated small structural changes during curing due to coalescence of the templates (see Figure 2.18). Increasing GMA compositon to 8 wt % in the template prevented the tamplates from coalescing resulting in smaller nanostructures (see Figure 2.18).

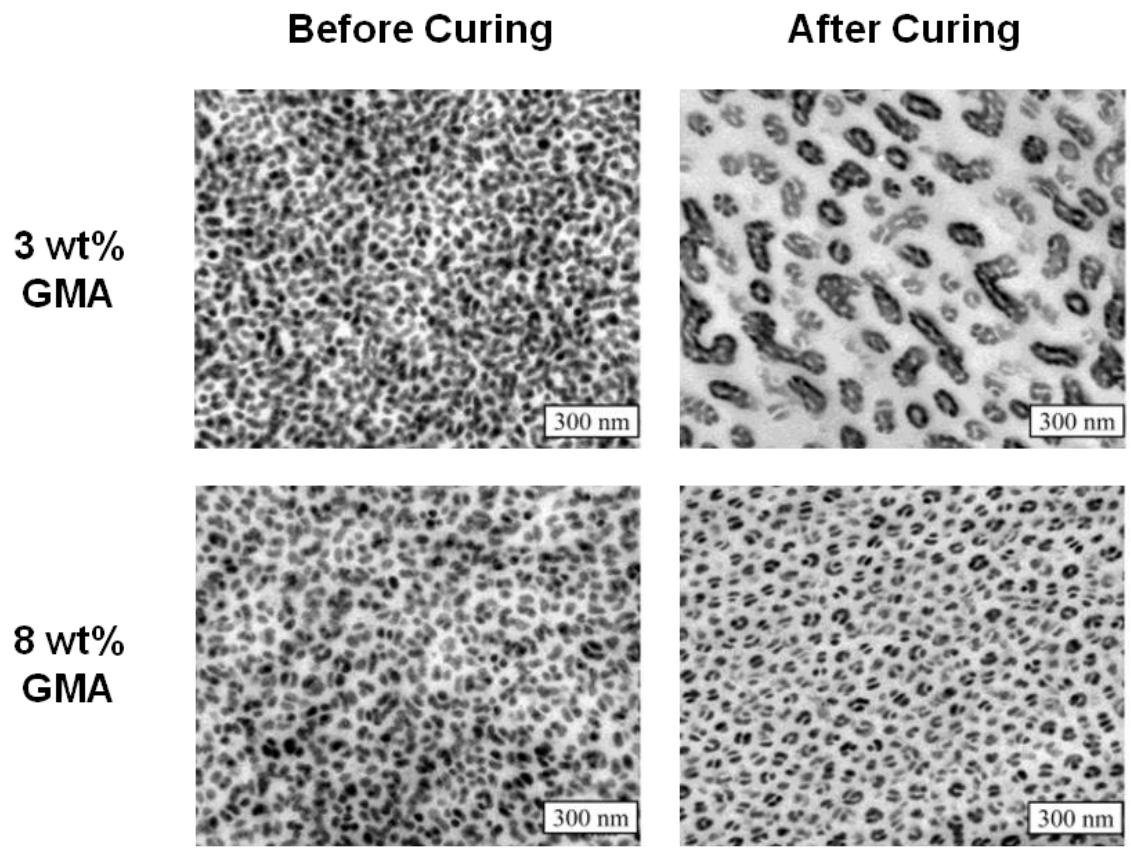

Figure 2.18. TEM micrographs of DGEBA/DDS blends with 30 wt % of PS-PB-PMMA-PGMA both before and after curing (adapted from Rebizant et al.).[55]

Rebizant et al. also showed that an epoxide unit is not required as the reactive component by using statistical copolymers of methyl methacrylate (MMA) and methacrylic acid (MAA) as the reactive block. PS-PB-P(MMA-*stat*-*tert*-butyl methacrylate) [SB(MT)] triblock terpolymers were prepared by sequential anionic polymerization.[56] The *tert*-butyl methacrylate block was subsequently hydrolyzed to MAA [SB(MA)], and both triblock polymers were used as nanostructure templates in DGEBA epoxies cured with MCDEA, MDA, DDS, 2-phenylimidazole (2-PI), methyl tetrahydrophtalic anhydride (MTHPA), and dicyandiamide (DICY). Nanostructured epoxies only resulted for the SB(MT) template epoxy when cured with MCDEA. In stark contrast, nanostructured epoxies resulted for all curing agents except DICY when cured in the presence of the SB(MA) template. The morphological differences observed were ascribed to the ability of the MAA block to react with the epoxy, and the success with a variety of curing agents expands nanostructured templating to a much wider variety of epoxy/hardner combinations.

In a series of papers, Serrano et al. extensively investigated epoxidized butadiene (PexB) as a reactive block in PS-PexB diblock star copolymers.[57,58,59] Epoxidation of a PS-PB star block copolymer (245 kg/mol, w_{PS} = 0.59) with PS end blocks to varying degrees also caused structural rearrangements in the block polymer and resulted in a multicomponent blend of PS-PexB diblock polymers of varying molecular weights and architectures.[57] Cured DGEBA/MCDEA blends with 30 wt % of the PS-PexB diblock templates resulted in transparent epoxy composites for PexB epoxidation degrees of 40%

or greater.[58,59] AFM and TEM images exhibited microphase separated cylindrical morphologies with PS cylinders in the epoxy/PexB matrix (see Figure 2.19 for TEM). SAXS of the blends confirmed microphase separation and higher order reflections were consistent with a hexagonally packed cylindrical microstructure. DMTA analysis of the blends demonstrated thermal transitions associated with the β-relaxation of the epoxy matrix, T_g associated with the PS cylinders, and T_g of the epoxy/PexB matrix.[59] DSC analysis during curing of various blends indicated that the PS-PexB diblock reacts with the MCDEA during the cure likely leading to integration of the PexB in the epoxy matrix.

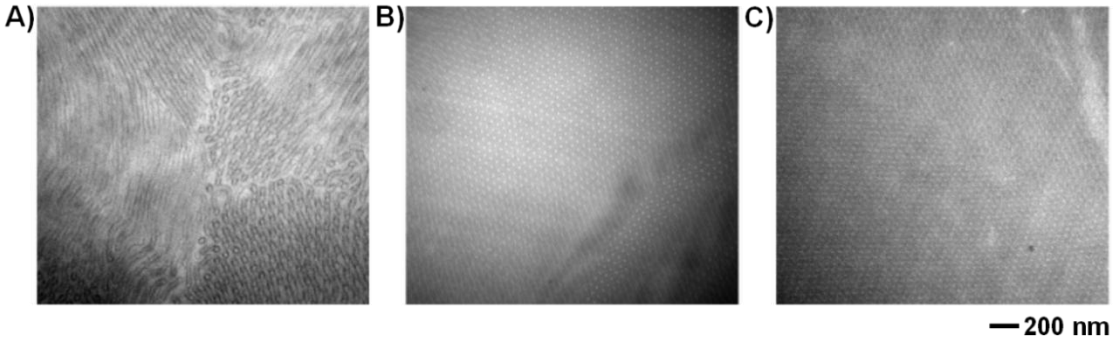

Figure 2.19. TEM micrographs of cured DGEBA/MCDEA blends with 30 wt % of PS-PexB with epoxidation degrees of A) 40%, B) 61% and C) 76% (adapted from Serrano et al.).[59]

Serrano et al. and Ocando et al. also examined DGEBA/MCDEA blends with linear $P^{S\text{-}PexB}$ diblock[60,61] and PS-PexB-PS triblock copolymers.[62] Nanostructured blends were observed when PS-PexB diblock copolymer templates with epoxidation degrees of 22% or greater, but the formation mechanism depended on the percent epoxidation. Nanostructured vesicles (10 wt % template) and worms (30 wt % template) formed via a self-assembly first mechanism at 22% epoxidation as the PexB domains were not

miscible with the epoxy precursors leading to self-assembled structures with a corona of PS chains. Templates with PexB 28% epoxidation and higher formed cylindrical and spherical nanostructures via RIPS, depending on the PS composition in the template.[61] Initial investigations into mechanical properties of the nanostructured blends indicated improved fracture toughness relative to pure epoxy networks, but further investigation is required to better determine the effect of inclusion size and interfacial interactions in the mechanical improvements.[60,61] Similar morphologies and phase behavior were observed with PS-PexB-PS triblock copolymer templates, and analysis of the fraction of epoxidized PexB indicated 4.8 wt % of epoxidized PB in the template was necessary for compatibilizing the PB blocks with the epoxy matrix, in agreement with the PS-PexB diblock work.[62]

Improvement in the thermomechanical properties of DGEBA/MDA epoxies by blending 10 to 40 wt % of a PS-PGMA [14.2 kg/mol, w_{PS} = 0.56] reactive block polymer was reported by Xu et al.[63] Nanostructured morphologies formed by RIPS varied from spherical particles that increased in density within the matrix with increasing PS-PGMA composition until wormlike morphologies formed. Analysis of the thermal properties by DSC indicated an increasing T_g with increasing PS-PGMA composition. DMTA revealed an increase in the storage modulus and a shift in the Tan δ maximum to higher temperatures with increasing template composition (Figure 2.20). These improvements in the thermomechanical properties are counter to the typical performance of nanostructured

blends and are attributed to an increased crosslink density by addition of the PGMA chains.

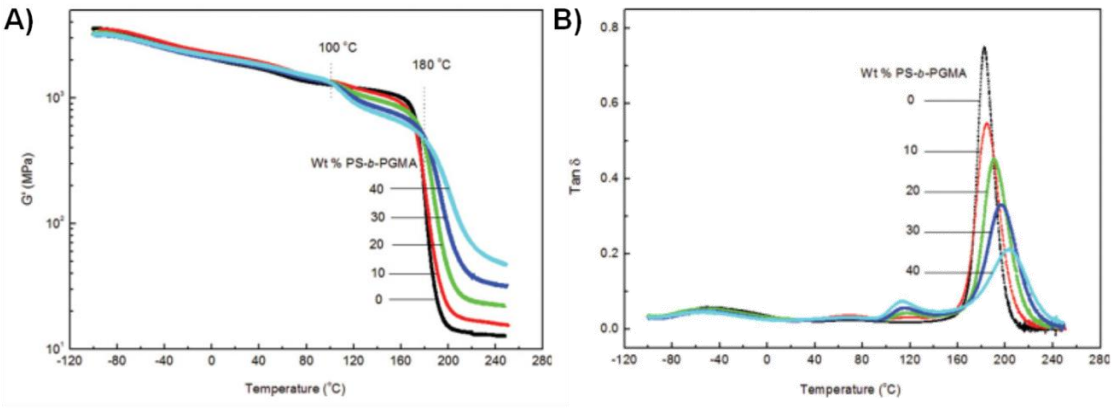

Figure 2.20. A) Storage modulus (G') and B) Tan δ as a function of temperature for nanostructured DGEBA/MDA blends with 0, 10, 20, 30 and 40 wt % PS-PGMA reactive diblock polymer (adapted from Xu et al.).[63]

2.5. Incorporation of different functionalities and structures in epoxy thermosets

Most early reports of nanostructured epoxies have focused on improving the mechanical properties of the resulting composite. More recently, investigations into nanostructured thermosets have examined incorporation of other functionalities or structures in epoxies. Incorporation of block polymers containing fluorinated blocks have been explored as a means of adjusting the epoxy surface properties. Ocando et al. investigated blends of a DGEBA/MCDEA epoxy with a poly(heptadecafluorodecyl acrylate)-b-PCL (PaF-PCL) [19 kg/mol, w_{PCL} = 0.55] block polymer.[64] The composite blends were transparent after curing, and TEM micrographs indicated a nanostructured morphology with wormlike and spherical micelles for a 35 wt % PaF-PCL blend. DSC

and DMTA indicated microphase separation as a T_g associated with the epoxy matrix plasticized by PCL and a T_m corresponding to the melting of the PaF block were observed. Contact angle measurements of the composite indicated increased hydrophobicity and decreased surface energy over a neat epoxy sample due to inclusion of the fluorinated block.

A second example by Yi and coworkers formed DGEBA/MOCA blends with a poly(2,2,2-trifluoroethyl acrylate)-b-PEO (PTFEA-PEO) [9.2 kg/mol, w_{PEO} = 0.54] block polymer.[65] Epoxy blends with 10 to 40 wt % PTFEA-PEO were transparent both before and after curing. SAXS indicated a microphase separated morphology as a broad scattering peak was observed, and AFM revealed an increasing number of homogenously dispersed PTFEA nanoparticles with increasing PTFEA-PEO compositions. Thermal analysis by DSC and DMTA confirmed a phase separated structure as T_gs for both the plasticized epoxy matrix and the PTFEA microdomains were observed. Contact angle measurements (Figure 2.21) indicated decreasing surface energies and increasing hydrophobicity as the PTFEA-PEO composition increased, demonstrating that the surface characteristics could be tailored depending on how much of the PTFEA-PEO block polymer is included in the blend.

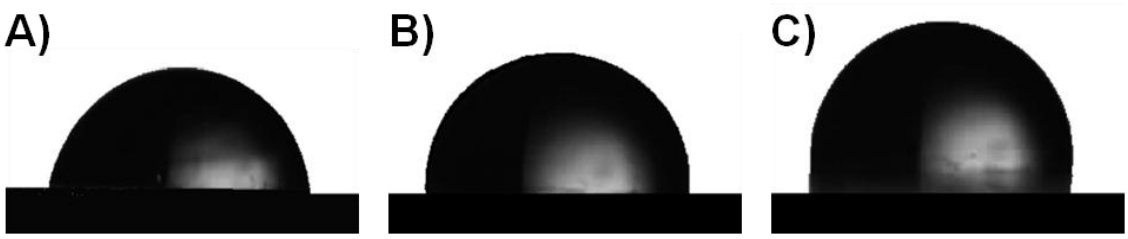

Figure 2.21. Water droplets from contact angle measurements for A) neat epoxy, B) 20 wt % and C) 40 wt % PTFEA-PEO block polymers. (adapted from Yi et al.)[65]

Ni et al. investigated nanostructuring DGEBA/MOCA epoxies with inorganic inclusions by including polyhedral oligomeric silsesquioxane (POSS) capped PCL.[66] AFM and TEM of blends with 10 to 40 wt % POSS capped PCL indicated a nanostructured morphology that evolved from dispersed spheres to interconnected wormlike structures. Since organosilicon materials generally have lower surface energies, contact angle measurements with water and glycol were used to probe the surface characteristics. As the blend fraction of POSS capped PCL increased, hydrophobicity of the material increased while the surface energy decreased. X-ray photoelectron spectroscopy (XPS) indicated enrichment of silicon at the material surface relative to the theoretical composition, suggesting that the changing surface properties are due to increased concentrations of POSS near the surface.

Incorporation of fluorinated inorganic structures with DGEBA/MOCA was investigated by Zeng et al. by blending hepta(3,3,3-trifluoropropyl) polyhedral oligomeric silsesquioxane (HTFPOSS) capped PEO[67] or PCL.[68] In both examples, spherical HTFPOSS nanostructures dispersed in the epoxy evolved into interconnected domains with increasing HTFPOSS composition. AFM micrographs of the surface

clearly showed aggregation of the HTFPOSS capped PEO. Increases in the surface hydrophobicity and decreases in the surface energy were greater than for inclusion of either POSS capped PCL[66] or fluorinated block polymers[64,65] suggesting that fluorinating part of the POSS results in a higher cumulative effect.

In addition to modifying surface properties, porosity has been induced in block polymer modified epoxy composites by selectively removing one of the components. Guo et al. formed nanoporous DGEBA/MDA epoxies from blends with a poly(ispoprene)-b-poly(4-vinyl pyridine) (PI-P4VP) [41.7 kg/mol, w_{PI} = 0.72] block polymer by selectively removing the PI block.[69] SAXS of cured blends with up to 50 wt % PI-P4VP exhibited scattering patterns consistent with a microphase separated morphology, and while higher order reflections suggested a hexagonally packed cylindrical morphology, the broadness of the scattering peaks indicated a lack of long range order in the materials. Ozonolysis of the composites selectively removed the PI component of the blends rendering them nanoporous. TEM of the blends after ozonolysis indicated nanoporous structures dispersed throughout the composite.

2.6. Nanostructured non-epoxy thermosets

While the majority of research into nanostructured thermosets has focused on crosslinked epoxies, more recent investigations have broadened the scope of thermosets investigated to include phenolic and unsaturated polyester resins, polyurethane and poly(dicyclopentadiene) (PDCPD) thermosets.

2.6.1. Phenolic Thermosets

Kosonen et al. investigated blends of a hexamethylentetramine (HMTA) cured phenol novolac resin with a poly(2-vinylpyridien)-*b*-poly(isoprene) (P2VP-PI) block polymer [92 kg/mol, w_{P2VP} = 0.23].[70,71] Crosslinked blends with the total weight fraction of PI equal to 20, 30 and 40 wt % exhibited spherical, disorganized cylindrical and lamellar morphologies as can be seen in Figure 2.22.[70] The phenolic resin is miscible with the P2VP block due to hydrogen bonding interactions as indicated by FITR, while the PI block phase separates. The authors hypothesize that this sort of blending strategy might be useful for improving the mechanical properties of phenolic thermosets similar to the work with nanostructured epoxies.[71]

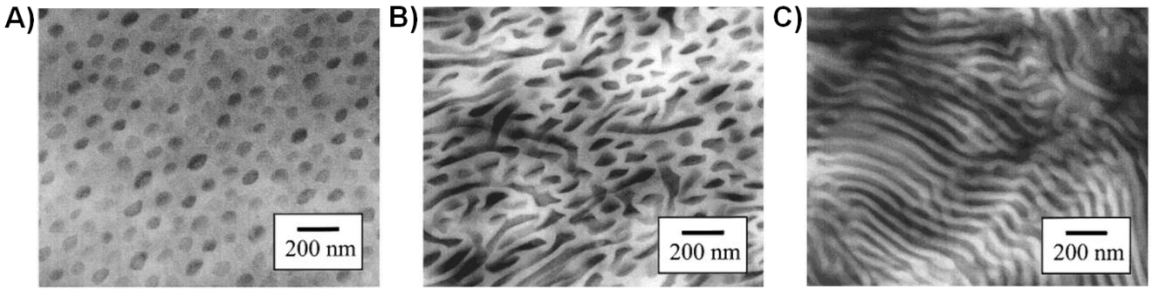

Figure 2.22. TEM micrographs of phenol novolac/HMTA blends with P2VP-PI containing A) 20, B) 30, and C) 40 wt % PI (adapted from Kosonen et al.).[70]

In addition to P2VP-PI block polymers, Kosonen et al. also examined nanostructured blends of phenolic resol resins with PEO-PPO-PEO triblock polymers.[72] Blends with 20 wt % of three different PEO-PPO-PEO triblock polymers (w_{PEO} = 0.4, 0.3 and 0.2) approximately the same molecular weight were formed. When w_{PEO} = 0.4 uniform spherical nanostructures were dispersed throughout the film. At w_{PEO} = 0.3, less

organized nanostructures formed, but at w_{PEO} = 0.2 macrophase separation was observed even for blends with just 6 wt % of PEO-PPO-PEO. Since the nanostructures are stabilized by hydrogen bonding between the PEO segments and the phenolic thermoset, less organized structures are observed as the fraction of PEO decreases in the PEO-PPO-PEO triblock. Eventually, the hydrogen bonding interaction is not strong enough to prevent the macrophase separation of the block polymer. By combining the use of a simply cured resin with the use of the commercially available PEO-PPO-PEO additive, the work demonstrates that value added nanostructured thermosets could be easily transitioned to commercially relevant applications.

Meng et al. further explored the mechanism of structure formation for blends of PEO-PPO-PEO [8.6 kg/mol w_{PEO} = 0.8] with an HMTA cured phenol novolac resin.[73] Nanostructured blends were observed for composites with up to 40 wt % of PEO-PPO-PEO based on AFM and SAXS. Blends of the individual PEO and PPO segments with the resin were also studied using homopolymers with similar molecular weights to the block components. Previous investigations of PEO/phenol novolac blends showed them to be miscible.[74] A single compositionally dependent T_g was observed in DSC for each homopolymer/phenol novolac blend, confirming that prior to cure the components were miscible. During curing, however, the initially transparent blends with PPO became cloudy overtime, indicating phase separation. Based on the phase behavior of the individual block polymer components, the authors concluded that the formation of nanostructures for PEO-PPO-PEO triblocks occurs by RIPS.

Nanostructured phenol thermosets from novolac and resol resins have also been used as precursors to nanoporous carbon. Liang et al. formed nanoporous carbon films from phenolic resorcinol-formaldehyde resin nanostructured by a poly(styrene)-*b*-poly(4-vinyl pyridine) (PS-P4VP) [23.3 kg/mol, w_{P4VP} = 0.49] copolymer.[75]A solution of PS-P4VP (66 wt %) and resorcinol resin in either N,N'-dimethylformamide (DMF) or cyclohexanol was spin or dipcoated onto a variety of substrates. The film was then annealed at 80 °C in an atmosphere of DMF and benzene, leading to a hexagonally packed array of PS cylinders in a matrix of P4VP and resorcinol. The resorcinol resin was then crosslinked by exposing the film to formaldehyde gas to fix the self-assembled structure. Finally, the resorcinol-formaldehyde resin was converted to carbon with concurrent removal of the PS-P4VP by slowly pyrolyzing the film. Nanoporous carbon films with variable thicknesses (nm to μm length scales) covering areas up to 6 cm^2 were formed by this process. Figure 2.23 shows SEM of the surface and cross section of the films.

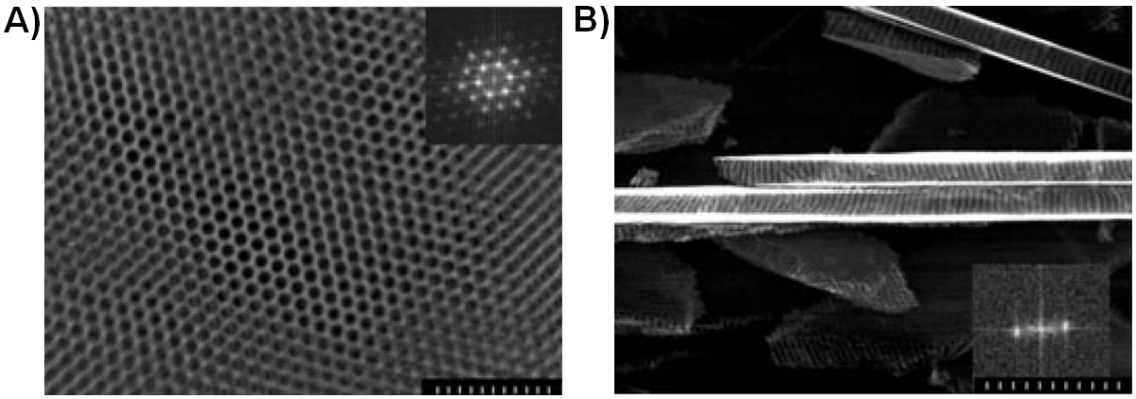

Figure 2.23. SEM micrographs of the surface and cross section of nanoporous carbon films (adapted from Liang et al.).[75]

In a similar work, Kosonen et al. formed a variety of nanoporous structures from carbonized HMTA cured phenol novolac blends with a PS-P4VP template [45.6 kg/mol w_{P4VP} = 0.12].[76] By varying the blend composition spherical, wormlike, cylindrical, and lamellar nanostructures formed as indicated by TEM micrographs. SAXS confirmed microphase separation in the blends and higher order reflections were consistent with the structures observed by TEM. Pyrolysis of the nanostructured blends yielded nanoporous carbon with structures templated by PS-P4VP as can be seen in Figure 2.24. Surface areas were determined using Brunauer-Emmett-Teller analysis of nitrogen sorption data. Surface areas were dependent on the sample morphology and ranged from 340 m^2/g for cylindrical structures to <5 m^2/g for spherical structures. The absorption properties of the porous structures were examined by comparing the uptake of methylene blue and rhodamine 6G dyes from an aqueous solution. UV-Vis spectroscopy overtime indicated virtually complete uptake of the methylene blue due to specific interactions with remaining hydroxyl groups in the material, while rhodamine was only absorbed a small amount. The selective up take of these dyes show the promise of this material for selective sensors or separations.

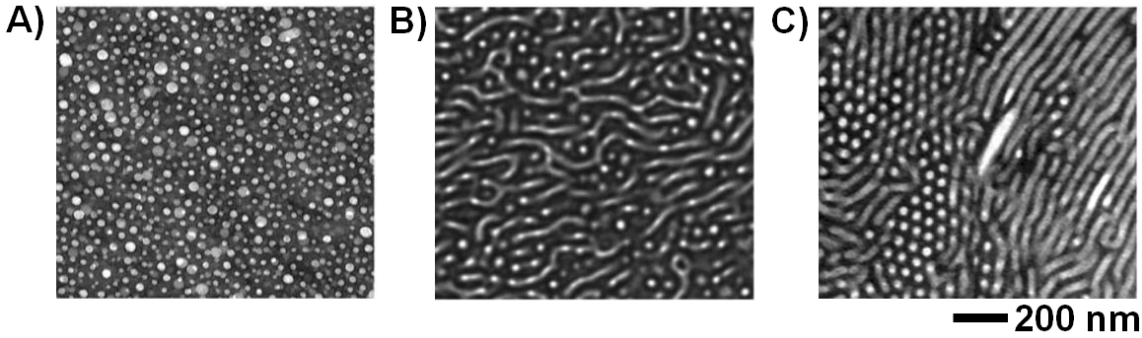

Figure 2.24. TEM micrographs of nanoporous carbon from the pyrolysis of HTMA cured blends of phenolic resin with PS-P4VP containing A) 20, B) 30 and C) 40 wt % PS (adapted from Kosonen et al.).[76]

A final example of nanoporous carbon from a block polymer templated novolac resin was reported by Hu et al.[77] Blends of an HMTA cured phenol novolac resin with 10 to 40 wt % PS-PEO block polymer [15.6 kg/mol, w_{PEO} = 0.32] formed compositionally dependent morphologies that transitioned from spheres on a body-centered cubic lattice to hexagonally packed cylinders with increasing PS-PEO content as evidenced by SAXS and AFM. Controlled pyrolysis at 450 °C for 180 min followed by heating at 800 °C for an additional 180 min resulted in porous carbon with spheres and cylindrical pores. Nitrogen sorption experiments revealed a steep increase in the surface area (<30 m^2/g to 168 m^2/g) upon changing from the spherical to cylindrical morphology, consistent with the cylindrical morphology having an interconnected porous structure.

2.6.2. Unsaturated Polyester Thermosets

Sinturel et al. reported the formation of nanostructured unsaturated polyester (UP) thermosets using a PEO-PE [1.4 kg/mol w_{PEO} = 0.50] block polymer.[78] Uncured blends of the block polymer and UP resin were homogenous and transparent at room temperature,

but exhibit macrophase separation starting at 75 °C, consistent with lower critical solution temperature behavior of PEO oligomers in UP resins. To avoid macrophase separated structures, all blends were cured at 70 °C using lauryl peroxide as a free radical initiator. TEM of the resulting composites revealed lamellar nanoplatelets with semi-crystalline PE cores encased by a layer of PEO. Increasing the block polymer composition from 5 to 25 wt % increased the number of platelets observed and led to their general alignment and aggregation as can be seen in Figure 2.25. SAXS of the blends was consistent with a microphase separated structure, and DSC indicated a depression of the PE crystallization due to confinement within the crosslinked matrix.

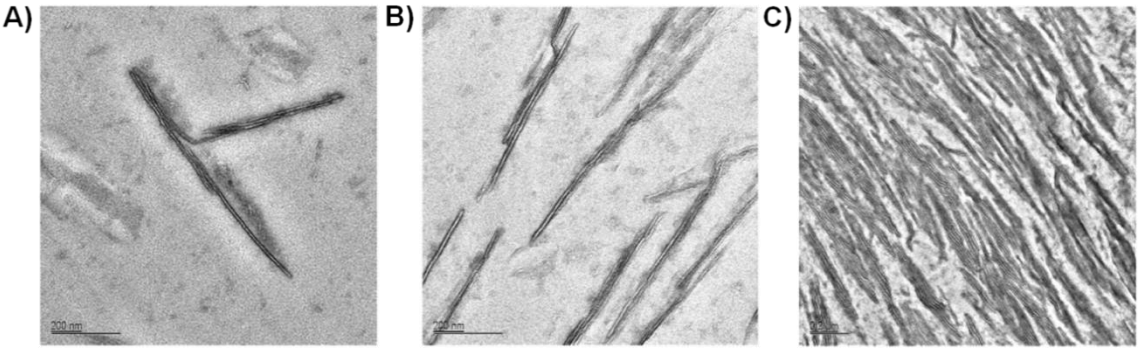

Figure 2.25. TEM micrographs of UP cured thermoset blended with A) 5, B) 10, and C) 25 wt % PEO-PE (adapted from Sinturel et al.).[78]

Serrano et al. also investigated nanostructured UP resins using poly(n-butyl acrylate)-b-poly[(methyl methacrylate)-*stat*-(*N*,*N*-dimethyl acrylamide)] (PBA-P(MMA/DMA)) block polymers.[79] Blends with 10 wt % block polymers with varied DMA composition indicated that 33 and 40 mol % of DMA in the statistical block was necessary to prevent macrophase separation upon curing UP resins with 0 and 22 mol % of orthophthalic acid respectively. Spheres and spherical aggregates were observed by

TEM in the nanostructured blends. Mechanical properties of the blends in comparison to UP resin indicated up to a 50% improvement in the critical stress intensity factor.

2.6.3. Polyurethane thermosets

Nanostructured poly(urethane) blends with PS-PB-PMMA triblock polymer templates were described by Jaffrennou et al.[80] A compositionally diverse array of PS-PB-PMMA triblock polymers were blended with different isocyanates including isophorone diisocyanate (IDI), 1,3-xylylene diisocyanate (XDI), or the trimer of 1,6-diisocyanatohexane (TDI) and oligodiols including oligo(di-propylene oxide) bisphenol A (BPA-PO), oligo(di-ethylene oxide) bisphenol A (BPA-EO), and polycaprolactone triol (PCL-TOH). For linear poly(urethanes) from XDI, and TDI with BPA-PO modified with small amounts (<10 wt %) of pure PS-PB-PMMA triblock polymer, microphase separation with spherical micellar inclusions was observed, but in a few instances aggregation of the spheres led to larger structures and opaque materials. When larger amounts of pure PS-PB-PMMA (> 50 wt %) were included, a cylinder in cylinder structure was observed. Finally, nanostructured network structures were only observed when low amounts (i.e. 20 wt % of the diisocyanate or diol) of either the trifunctional TDI or PCL-TOH were added. When 50 wt % of the diisocyanate or diol were replaced by a trifunctional monomer, macrophase separated structures were observed as the solubility of PS-PB-PMMA is much lower in the multifunctional monomers.

2.6.4. Dicyclopentadiene Thermosets

Nanostructured PDCPD thermosets have been explored for a variety of membrane applications by Hillmyer and coworkers. By employing the metathesis reactive block poly(norbornenylethylstyrene-*s*-styrene) (PNS) to prevent macrophase separation a diverse array of phase separating blocks have been utilized to impart different functionalities and properties to the resulting composites.

Nanoporous PDCPD thermosets have been synthesized by templating with a PNS-polylactide (PLA) block polymer using either the self-assembly first[81] or RIPS approach.[82] SAXS of blends formed using the self-assembly first approach revealed that compositionally dependent morphologies including lamellar and cylindrical structures formed. Crosslinked cylindrical monoliths were produced by curing aligned blends of DCPD and PNS-PLA using the first generation Grubbs catalyst attenuated with triphenyl phosphine. Removal of the PLA by basic hydrolysis resulted in nanoporous monoliths of hexagonally packed aligned cylinders as evidenced by SAXS and SEM (Figure 2.26). The nanoporous monoliths exhibited an average tensile strength of 50 MPa and elongation at break of 10% when examined using tensile testing parallel to the long axis of the cylinders. Additionally, DSC revealed that the monoliths were stable up to 130 °C. These mechanical and thermal properties represent significant improvements in stability when compared with nanoporous PS monoliths.

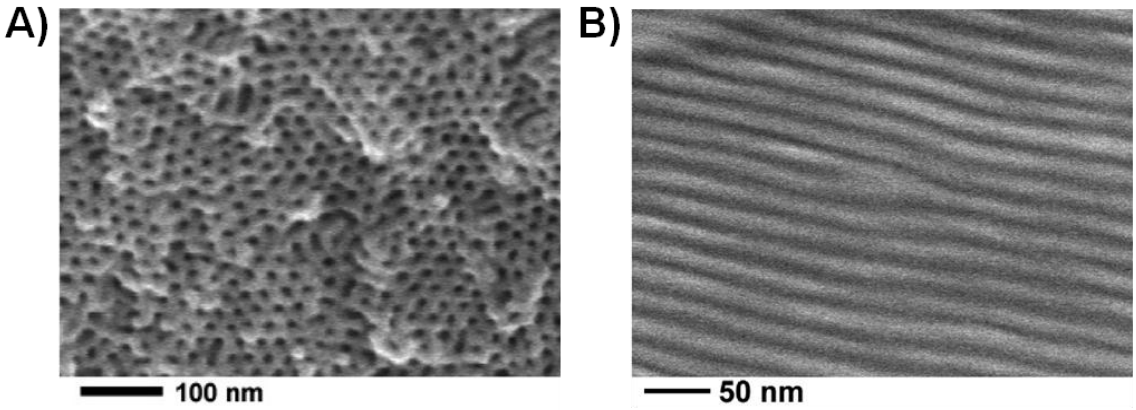

Figure 2.26. SEM micrographs of nanoporous PDCPD cylindrical monoliths templated by a metathesis reactive PNS-PLA block polymer fractured A) perpendicular and B) parallel to the long cylinder axis.

Bicontinuous nanoporous structures were formed by crosslinking the PNS-PLA block polymer with DCPD in a solution of THF using the second generation Grubbs catalyst. During the crosslinking, the PLA block phase separates from the forming matrix by RIPS while the bicontinuous structure is kinetically trapped by gelation of the material. Etching of PLA renders the material nanoporous as in the case for the aligned monoliths. Nanoporous films from these materials have exhibited potential for filtration applications, which are explored further in Chapter 3.

Polyelectrolyte membranes (PEM) have also been templated in crosslinked PDCPD/polycyclooctene (PCOE) films using the RIPS of a PNS-poly(*n*-propyl-*p*-styrenesulfonate (PPSS) block polymer template.[83] Cured films exhibited bicontinuous structures with the PPSS block forming a separate phase from the crosslinked matrix. Hydrolysis of the PPSS to poly(styrenesulfonate) created electrolyte channels that span the thickness of the film. Evaluation of these films as PEMs for direct methanol fuel cells

exhibited lower methanol crossover while maintaining proton conductivities. Additionally, exploration of these membranes for the selective separation of ammonia from hydrogen and nitrogen demonstrated retention of ammonia selectivity for mixed gas experiments, which is typically lost due to swelling of the material by the selective gas.[84] The authors hypothesize that crosslinking the matrix reduces it swelling resulting in a retention of the gas selectivities.

2.7. Conclusions and Outlook

The formation of nanostructured thermosets from block polymers has been an interesting and fruitful area of research over the last 10+ years. Establishment of the self-assembly first, RIPS and reactive block polymer approaches to forming nanostructured thermosets has allowed incorporation of a multitude of block polymers into a variety of thermosets. With the necessary foundation and tools in place, further development of block polymer templated thermosets is well positioned to expand beyond its initial focus on improving mechanical properties in epoxy thermosets, and three specific areas of research are quite intriguing for further study.

First, new block polymers could be explored to synergistically improve a thermosets mechanical properties while imparting new functionality. Inclusion of fluorinated blocks[64,65] and POSS[66,67,68] significantly altered the composite epoxies surface properties. Integration of other blocks such as polyelectrolytes or conducting polymers could open up additional avenues of exploration. Second, investigation of more advanced structures including porous structures could open up new functions for nanostructured

thermosets. The formation of nanoporous carbon from nanostructured phenolic precursors[75,76,77] took advantage of the higher thermal stability of thermosets, which prevented the material from softening and flowing during pyrolysis. Nanoporous thermosets could also be explored as templates for inorganic structures that require temperatures beyond the thermal stability of nanoporous thermoplastics. Moreover the increased thermal stability and solvent resistance could make nanoporous thermosets useful as separation barriers in more harsh environments.

Finally, further exploration of thermosets other than epoxy systems could open up other opportunities for their use. The robust nature of PDCPD made it an excellent candidate for membrane applications, and the variety of phase separating blocks employed demonstrated how a thermosets properties can be tailored to the desired application by changing the phase separating block.[81,82,83,84] Critical to exploring additional epoxy curing agents[55,56] as well as non-epoxy thermosets is the design and synthesis of reactive block polymers to prevent macrophase separation when a suitable nonreactive block cannot be found.

The unique propreties of thermosets have already facilitated their use in areas where traditional thermoplastics cannot operate, and the formation of nanostructured thermosets by incorporation of block polymers has shown to be a facile way to tailor a thermosets properties. By fully exploiting the diverse array of block polymers and thermosets, nanostructured thermosets could become made to order materials with innumerable applications.

2.8. References

(1) Pascault, J.; Sautereau, H.; Verdu, J.; Williams, R. J. J. In *Thermosetting Polymers*; Marcel Dekker: New York, NY, 2002; pp 485.

(2) Biron, M. In *Thermosets and Composites: Technical Information for Plastics Users*; Elsevier: Kidlington, United Kingdom, 2004; pp 501.

(3) Ruiz-Pérez, L.; Royston, G. J.; Fairclough, J. P. A.; Ryan, A. J. *Polymer* **2008**, *49*, 4475-4488.

(4) Bagheri, R.; Marouf, B. T.; Pearson, R. A. *Polym. Rev.* **2009**, *49*, 201.

(5) Hedrick, J. L.; Yilgör, I.; Wilkes, G. L.; McGrath, J. E. *Polym. Bull.* **1985**, *13*, 201-208.

(6) Inoue, T. *Prog. Polym. Sci.*, **1995**, 20, 119-153.

(7) Williams, R. J. J.; Rozenberg, B. A.; Pascault, J. *Adv. Polym. Sci.* **1997**, 128, 95-156.

(8) Kiefer, J.; Hedrick, J. L.; Hilborn, J. G. *Adv Polym Sci* **1999**, *147*, 161-247.

(9) Sandler, J.; Shaffer, M. S. P.; Prasse, T.; Bauhofer, W.; Schulte, K.; Windle, A. H. *Polymer* **1999**, *40*, 5967-5971.

(10) Winey, K. I.; Kashiwagi, T.; Mu, M. *MRS Bull.* **2007**, *32*, 348-353.

(11) Seyhan, A. T.; Gojny, F. H.; Tanoğlu, M.; Schulte, K. *Euro. Polym. J.* **2007**, *43*, 374-379.

(12) Bauhofer, W.; Kovacs, J. Z. *Composites Sci. Technol.* **2009**, *69*, 1486-1498.

(13) Battisti, A.; Skordos, A. A.; Partridge, I. K. *Composites Sci. Technol.* **2010**, *70*, 633-637.

(14) Hunter, D. L.; Kamena, K. W.; Paul, D. R. *MRS Bull.* **2007**, *32*, 323-327.

(15) Zhou, G.; Movva, S.; Lee, L. J. *J Appl. Polym. Sci.* **2008**, *108*, 3720-3726.

(16) González-Campo, A.; Orchard, K. L.; Sato, N.; Shaffer, M. S. P.; Williams, C. K. *Chem. Commun.* **2009**, *27*, 4034-4036.

(17) Henk, P. O.; Kortsen, T. W.; Kvarts, T. *High Perform. Polym.* **1999**, *11*, 281-296.

(18) Nelson, J. K.; Hu, Y. *J. Phys. D* **2005**, *38*, 213-222.

(19) Lipic, P. M.; Bates, F. S.; Hillmyer, M. A. *J. Am. Chem. Soc.* **1998**, *120*, 8963–8970.

(20) Hillmyer, M. A.; Lipic, P. M.; Hajduk, D. A.; Almdal, K.; Bates, F. S. *J. Am. Chem. Soc.* **1997**, *119*, 2749–2750.

(21) Serrano, E.; Tercjak, A.; Kortaberria, G.; Pomposo, J. A.; Mecerreyes, D.; Zafeiropoulos, N. E.; Stamm, M.; Mondragon, I. *Macromolecules* **2006**, *39*, 2254–2261.

(22) Dean, J. M.; Lipic, P. M.; Grubbs, R. B.; Cook, R. F.; Bates, F. S. *J. Polym. Sci., Part B: Polym. Phys.* **2001**, *39*, 2996–3010.

(23) Ritzenthaler, S.; Court, F.; David, L.; Girard-Reydet, E.; Leibler, L.; Pascault, J. P. *Macromolecules* **2002**, *35*, 6245–6254.

(24) Girard-Reydet, E.; Pascault, J.; Bonnet, A.; Court, F.; Leibler, L. *Macromol. Symp.* **2003**, *198*, 309–322.

(25) Hermel-Davidock, T. J.; Tang, H. S.; Murray, D. J.; Hahn, S. F. *J. Polym. Sci., Part B: Polym. Phys.* **2007**, *45*, 3338–3348.

(26) Sixun, Z.; Naibin, Z.; Xiaolie, L.; Dezhu, M. *Polymer* **1995**, *36*, 3609-3613.

(27) Yin, M.; Zheng, S. *Macromol. Chem. Phys.* **2005**, *206*, 929-937.

(28) Grubbs, R. B.; Dean, J. M.; Broz, M. E.; Bates, F. S. *Macromolecules* **2000**, *33*, 9522-9534.

(29) Dean, J. M.; Lipic, P. M.; Grubbs, R. B.; Cook, R. F.; Bates, F. S. *J. Polym. Sci. Part B: Polym. Phys.* **2001**, *39*, 2996-3010.

(30) Dean, J. M.; Grubbs, R. B.; Saad, W.; Cook, R. F.; Bates, F. S. *J. Polym. Sci. Part B: Polym. Phys.* **2003**, *41*, 2444-2456.

(31) Dean, J. M.; Verghese, N. E.; Pham, H. Q.; Bates, F. S. *Macromolecules* **2003**, *36*, 9267-9270.

(32) Guo, Q.; Thomann, R.; Gronski, W.; Staneva, R.; Ivanova, R.; Stuhn, B. *Macromolecules* **2003**, *36*, 3635-3645.

(33) Wu, J.; Thio, Y. S.; Bates, F. S. *J. Polym. Sci. Part B: Polym. Phys.* **2005**, *43*, 1950-1965.

(34) Thio, Y. S.; Wu, J.; Bates, F. S. *Macromolecules* **2006**, *39*, 7187-7189.

(35) Riffle, J. S.; Steckle, W. P., Jr; White, K. A.; Ward, R. S. *Polym. Preprints* **1985**, *26*, 251-252.

(36) Buchholz, U.; Mülhaupt, R. *Polym. Preprints* **1992**, *33*, 205-206.

(37) Könczöl, L.; Döll, W.; Buchholz, U.; Mülhaupt, R. *J. Appl. Polym. Sci.* **1994**, *54*, 815-826.

(38) Ritzenthaler, S.; Court, F.; David, L.; Girard-Reydet, E.; Leibler, L.; Pascault, J. P. *Macromolecules* **2002**, *35*, 6245-6254.

(39) Ritzenthaler, S.; Court, F.; Girard-Reydet, E.; Leibler, L.; Pascault, J. P. *Macromolecules* **2003**, *36*, 118-126.

(40)Meng, F.; Zheng, S.; Zhang, W.; Li, H.; Liang, Q. *Macromolecules* **2006**, *39*, 711–719.

(41)Meng, F.; Zheng, S.; Li, H.; Liang, Q.; Liu, T. *Macromolecules* **2006**, *39*, 5072–5080.

(42) Meng, F.; Zheng, S.; Liu, T. *Polymer*, **2006**, *47*, 7590–7600.

(43) Xu, Z.; Zheng, S. *Macromolecules* **2007**, *40*, 2548–2558.

(44) Fan, W.; Zheng, S. *Polymer*, **2008**, *49*, 3157–3167.

(45) Mijovic, J.; Shen, M.; Sy, J. W.; Mondragon, I. *Macromolecules* **2000**, *33*, 5235-5244.

(46) Larrañaga, M.; Martín, M.; Gabilondo, N.; Kortaberria, G.; Corcuera, M.; Riccardi, C.; Mondragon, I. *Polym. Int.* **2004**, *53*, 1495-1502.

(47) Larrañaga, M.; Martin, M.; Gabilondo, N.; Kortaberria, G.; Eceiza, A.; Riccardi, C.; Mondragon, I. *Colloid Polym. Sci.* **2006**, *284*, 1403-1410.

(48) Larrañaga, M.; Gabilondo, N.; Kortaberria, G.; Serrano, E.; Remiro, P.; Riccardi, C. C.; Mondragon, I. *Polymer,* **2005**, *46*, 7082-7093.

(49) Larrañaga, M.; Arruti, P.; Serrano, E.; de la Caba, K.; Remiro, P.; Riccardi, C.; Mondragon, I. *Colloid Polym. Sci.* **2006**, *284*, 1419-1430.

(50) Larrañaga, M.; Serrano, E.; Martin, M. D.; Tercjak, A.; Kortaberria, G.; de la Caba, K.; Riccardi, C. C.; Mondragon, I. *Polym. Int.* **2007**, *56*, 1392-1403.

(51) Meng, F.; Xu, Z.; Zheng, S. *Macromolecules* **2008**, *41*, 1411-1420.

(52) Grubbs, R. B.; Dean, J. M.; Broz, M. E.; Bates, F. S. *Macromolecules* **2000**, *33*, 9522-9534.

(53) Grubbs, R. B.; Dean, J. M.; Bates, F. S. *Macromolecules* **2001**, *34*, 8593-8595.

(54) Guo, Q.; Dean, J. M.; Grubbs, R. B.; Bates, F. S. *J. Polym. Sci. Part B: Polym. Phys.* **2003**, *41*, 1994-2003.

(55) Rebizant, V.; Abetz, V.; Tournilhac, F.; Court, F.; Leibler, L. *Macromolecules* **2003**, *36*, 9889-9896.

(56) Rebizant, V.; Venet, A.; Tournilhac, F.; Girard-Reydet, E.; Navarro, C.; Pascault, J.; Leibler, L. *Macromolecules* **2004**, *37*, 8017-8027.

(57) Serrano, E.; Larrañaga, M.; Remiro, P. M.; Mondragon, I.; Carrasco, P. M.; Pomposo, J. A.; Mecerreyes, D. *Macromol. Chem. Phys.* **2004**, *205*, 987-996.

(58) Serrano, E.; Martin, M. D.; Tercjak, A.; Pomposo, J. A.; Mecerreyes, D.; Mondragon, I. *Macromol. Rapid Commun.* **2005**, *26*, 982-985.

(59) Serrano, E.; Tercjak, A.; Kortaberria, G.; Pomposo, J. A.; Mecerreyes, D.; Zafeiropoulos, N. E.; Stamm, M.; Mondragon, I. *Macromolecules* **2006**, *39*, 2254-2261.

(60) Serrano, E.; Tercjak, A.; Ocando, C.; Larrañaga, M.; Parellada, M. D.; Corona-Galván, S.; Mecerreyes, D.; Zafeiropoulos, N. E.; Stamm, M.; Mondragon, I. *Macromol. Chem. Phys.* **2007**, *208*, 2281-2292.

(61) Ocando, C.; Tercjak, A.; MartiÌn, M. D.; Ramos, J. A.; Campo, M.; Mondragon, I. *Macromolecules* **2009**, *42*, 6215-6224.

(62) Ocando, C.; Tercjak, A.; Serrano, E.; Ramos, J. A.; Corona-Galván, S.; Parellada, M. D.; Fernández-Berridi, M. J.; Mondragon, I. *Polym. Int.* **2008**, *57*, 1333-1342.

(63) Xu, Z.; Hameed, N.; Guo, Q.; Mai, Y. *J. Appl. Polym. Sci.* **2010**, *115*, 2110-2118.

(64) Ocando, C.; Serrano, E.; Tercjak, A.; Pena, C.; Kortaberria, G.; Calberg, C.; Grignard, B.; Jerome, R.; Carrasco, P. M.; Mecerreyes, D.; Mondragon, I. *Macromolecules* **2007**, *40*, 4068-4074.

(65) Yi, F.; Zheng, S.; Liu, T. *J. Phys. Chem. B* **2009**, *113*, 1857-1868.

(66) Ni, Y.; Zheng, S. *Macromolecules* **2007**, *40*, 7009-7018.

(67) Zeng, K.; Zheng, S. *J. Phys. Chem. B* **2007**, *111*, 13919-13928.

(68) Zeng, K.; Wang, L.; Zheng, S.; Qian, X. *Polymer* **2009**, *50*, 685-695.

(69) Guo, Q.; Liu, J.; Chen, L.; Wang, K. *Polymer* **2008**, *49*, 1737-1742.

(70) Kosonen, H.; Ruokolainen, J.; Nyholm, P.; Ikkala, O. *Macromolecules* **2001**, *34*, 3046-3049.

(71) Kosonen, H.; Ruokolainen, J.; Nyholm, P.; Ikkala, O. *Polymer*, **2001**, *42*, 9481-9486.

(72) Kosonen, H.; Ruokolainen, J.; Torkkeli, M.; Serimaa, R.; Nyholm, P.; Ikkala, O. *Macromol. Chem. Phys.* **2002**, *203*, 388-392.

(73) Meng, F.; Yi, F.; Zheng, S. *J. Macromol. Sci. Part B Phys.* **2008**, 47, 450-462.

(74) Zhong, Z.; Guo, Q. *Polymer* **1998**, *39*, 517-523.

(75) Liang, C.; Hong, K.; Guiochon, G. A.; Mays, J. W.; Dai, S. *Angew. Chem. Int. Ed.* **2004**, *43*, 5785-5789.

(76) Kosonen, H.; Valkama, S.; Nykänen, A.; Toivanen, M.; ten Brinke, G.; Ruokolainen, J.; Ikkala, O. *Adv. Mater.* **2006**, *18*, 201-205.

(77) Hu, D.; Xu, Z.; Zeng, K.; Zheng, S. *Macromolecules* **2010**, *43*, 2960-2969.

(78) Sinturel, C.; Vayer, M.; Erre, R.; Amenitsch, H. *Macromolecules* **2007**, *40*, 2532-2538.

(79) Serrano, E.; Gerard, P.; Lortie, F.; Pascault, J.; Portinha, D. *Macromol. Mater. Eng.* **2008**, *293*, 820-827.

(80) Jaffrennou, B.; Portal, J.; Méchin, F.; Pascault, J. *Eur. Polym. J.* **2008**, *44*, 3439-3455.

(81) Chen, L.; Hillmyer, M. A. *Macromolecules* **2009**, *42*, 4237-4243.

(82) Chen, L.; Phillip, W. A.; Cussler, E. L.; Hillmyer, M. A. *J. Am. Chem. Soc.* **2007**, *129*, 13786-13787.

(83) Chen, L.; Hallinan, D. T.; Elabd, Y. A.; Hillmyer, M. A. *Macromolecules* **2009**, *42*, 6075-6085.

(84) Phillip, W. A.; Martono, E.; Chen, L.; Hillmyer, M. A.; Cussler, E. L. *J. Membr. Sci.* **2009**, *337*, 39-46.

Chapter 3.

Poly(dicyclopentadiene) membranes templated by reactive AB diblock and ABC triblock polymers

This chapter reports on the flux, filtration and fouling characteristics of PNS-PLA/DCPD membranes examined using dead-end flow filtration experiments. Additionally, it explores expansion of the PNS-PLA/DCPD system to reactive triblock terpolymer templates as a means of imparting functionality to the pores. By adding and/or varying the mid-block employed, hydrophilic and stimuli responsive membranes were formed with the potential for not only improved fouling resistance but also the development of membranes capable of variable flux depending on environmental conditions.

3.1. Introduction

The self-assembly of a block polymer[1] into a microphase separated morphology followed by selective removal of one block is a facile method for forming nanoporous materials.[2,3] The high pore density and tailorable pore size of these materials have made them useful in nanolithographic and inorganic templating applications,[4,5] while the narrow pore size distribution imparts the potential for achieving narrower selectivities at higher permeabilities than current ultrafiltration membranes.[6]

Reports of block polymer membranes have included symmetric,[6,7,8] asymmetric,[9] and composite membrane structures[10,11] employing a hexagonally packed cylindrical morphology. Critical in these examples is aligning the cylinders such that they traverse the entire thickness of the membrane, and although many alignment techniques have been developed such as shear,[12,13,14] electric field application,[15,16] solvent evaporation,[17,18,19,20] or tuning the interfacial interactions,[21,22,23] the success of these often laborious techniques is typically limited by block polymer choice or film thickness.

An alternative approach to avoiding morphological alignment has been the recent development of membranes with bicontinuous structures.[24,25,26,27] By carefully controlling crystallization of a poly(styrene)-*b*-poly(ethylene) (PS-PE) block polymer Uehara et al. formed a bicontinuous morphology, which was rendered nanoporous by selective removal of the PS using fuming nitric acid.[24,25] Further development of thin film composite membranes by Yang et al. utilized an unaligned but continuous cylindrical morphology to realize improved mechanical properties as evidenced by filtrations

performed at pressures four times greater than their original report.[26] Chen et al. also reported robust bicontinuous membranes formed by the reaction induced phase separation (RIPS) during the crosslinking of a block polymer template with dicyclopentadiene (DCPD).[27] Specifically, the crosslinking of DCPD with a metathesis reactive block polymer: poly(norbornenylethylstyrene-*s*-styrene)-*b*-poly(lactide) (PNS-PLA) in a solution of THF using the second generation Grubbs catalyst (GII) caused the phase separation of the PLA block and formed a bicontinuous morphology. Subsequent removal of PLA using mild basic hydrolysis resulted in a nanoporous bicontinuous structure. The formation of this material is outlined in Figure 3.1.A below.

The facile preparation and remarkable mechanical properties of the nanoporous bicontinuous PNS-PLA/poly(DCPD) (PDCPD) spurred investigation of its potential as an ultrafiltration membrane. This chapter first reports the flux, filtration and initial investigations into the fouling performance of PNS-PLA/PDCPD membranes. The flux and filtration work was done in collaboration with Bill Phillip in Professor Ed Cussler's research group and has been previously reported both in ACS Applied Materials and Interfaces[28] and in Bill's dissertation.[29] The fouling work was done in collaboration with Bethany Brinkman in Professor Ray Hozalski's research group.

In addition to overcoming the challenge of pore alignment, developing functionalized membranes could improve their performance and expand their applications. A critical limitation to membrane performance is fouling by organic matter and particulates, and increasing a hydrophilicity of a membrane has the potential to

reduce membrane fouling.[30] Additionally, the development of "smart" membranes capable of responding to environmental stimuli could further expand the scope of membrane applications to more advanced systems.[31] Thus far only a few examples of block polymer templated functionalized nanoporous materials[32,33,34,35,36] or membranes[6,7,9] have been reported.

This chapter also explores the formation of hydrophilic and responsive membranes using ABC reactive triblock terpolymer templates where A is the chemically etchable block (PLA), B is the functional mid-block and C is the metathesis reactive block (PNS). After PLA removal, the functional mid-block B is exposed on the membrane pore walls (Figure 3.1.B) similar to core-shell morphologies of self-assembled triblock terpolymer systems.[37]

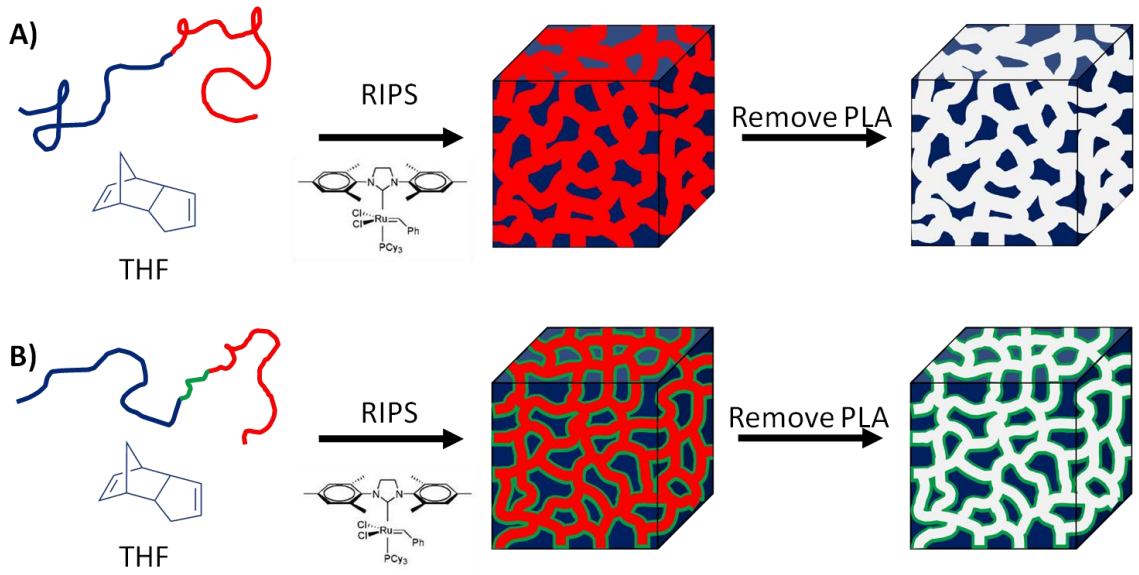

Figure 3.1. Formation of nanoporous PDCPD membranes using a A) PNS-PLA reactive diblock polymer, and B) a reactive triblock polymer where the blue block is PNS, the red block is PLA, and the green block is the functional PX block.

3.2. Experimental

3.2.1. Materials.

Unless specifically noted, all chemicals were used as received from Aldrich. D,L-lactide (99%) purchased from Purac was recrystallized twice from ethyl acetate and stored under N_2 atmosphere. Styrene and tert-butyl methacrylate (Aldrich) were purified by passing through a basic alumina column. *p*-norbornenylethylstyrene was synthesized following a published procedure.[27] 2,2*'*-azobis(isobutyronitrile) (AIBN) from Aldrich was purified by recrystallization from methanol. The radical addition fragmentation transfer (RAFT) chain transfer agent (CTA) *s*-1-dodecyl-*s'*-(*α*,*α'*-dimethyl- *α''*-acetic acid) trithiocarbonate was synthesized following a published procedure.[38] Degassed THF and toluene was purified by passage over an activated alumina column, to remove protic impurities and oxygen prior to use.

3.2.2. Characterization.

^{1}H NMR spectroscopy was performed on a Varian Inova 500 instrument operating at 500 MHz. Solutions were prepared in $CDCl_3$ (Cambridge Isotope Laboratories) at approximately 10 mg/mL. All spectra were obtained at 20 °C after 64 transients using a relaxation delay of 5 s with chemical shifts reported as δ (ppm) relative to the ^{1}H signals from hydrogenous solvent (7.26 ppm for $CHCl_3$).

Size exclusion chromatography (SEC) was used to evaluate the molecular weight evolution and polydispersity indicies (PDIs) of all the samples. Samples were prepared at

concentrations near 1 mg/mL in $CHCl_3$. The SEC instrument operates at 35 °C with $CHCl_3$ as the mobile phase through three PLgel 5μm Mixed-C columns in series with molecular weight range 400–400000 g mol^{-1}. The columns are housed in a Hewlett-Packard (Agilent Technologies) 1100 series liquid chromatograph equipped with a Hewlett-Packard 1047A refractive index detector. PDIs are reported with respect to polystyrene standards obtained from Polymer Laboratories.

FT-IR data was obtained using a Nicolet Magna-IR spectrometer 550. All spectra were recorded using a total of 32 scans and compiled with automatic background subtraction.

Small angle X-ray scattering (SAXS) profiles were recorded on a custom-built beam line at the University of Minnesota. CuKα X-rays (λ=1.542 Å) were generated through a Rigaku RU-200BVH rotating anode fitted with a 0.2 x 2 mm^2 microfocus cathode and Franks mirror optics. Two-dimensional (2-D) diffraction patters were recorded for 300 s using a Siemens area detector and corrected for detector response before analysis. 2-D images were azimuthally integrated to a 1-D plot of intensity versus the scattering vector, *q*.

Scanning electron microscope (SEM) images were obtained on a Hitachi S-900 FE-SEM instrument using a 3.0 kV accelerating voltage. Prior to SEM analysis, samples were coated with a 1.5 nm thick platinum layer via direct platinum sputtering using a VCR Ion Beam Sputter Coater.

3.2.3. Synthesis.

Synthesis of PNS-PLA diblock polymers. A detailed experimental description of the synthesis of PNS-PLA diblock polymers by the anionic copolymerization of styrene and norbornenylethylstyrene followed by the ring opening polymerization of lactide is included in Chapter 4.

Synthesis of PLA-PX-PNS triblock polymers. Hydroxyl group terminated PLA was prepared by the ring-opening polymerization (ROP) of D,L-lactide using a triethyl aluminum catalyst and a benzyl alcohol initiator. The hydroxyl terminated PLA was coupled to the CTA following a reported procedure.[33] This macro-CTA was then used to synthesize the triblock terpolymers as described.

PLA-PtBMA. *tert*-butyl methacrylate (0.21 mL, 1.3 mmol), PLA-CTA (0.88 g 0.033 mmol), and AIBN (1.0 mg, 0.0061 mmol) were dissolved in 2.0 mL of DMF in an air-free flask. The flask was heated in an oil bath at 60 °C for 40 minutes. The polymer was then precipitated in pentane, collected and dried under vacuum overnight.

PLA-PNIPAM. *N*-isopropylacrylamide (0.90 g, 7.9 mmol), PLA-CTA (2.00 g, 0.074 mmol), and AIBN (4.9 mg, 0.030 mmol) were dissolved in 11.0 mL of DMF in a pressure vessel with a side arm. The solution was degassed for 10 minutes and then 3 freeze-pump-thaw cycles were performed. The flask was then heated at 85°C for 20 minutes. The polymer was precipitated in pentane, redissolved in THF and precipitated in pentane again before being dried under vacuum overnight.

PLA-PX-PNS. The PNS block was grown from the PLA-PX diblock copolymers using a solution polymerization procedure as outlined here for PLA-PNIPAM-PNS. PLA-PNIPAM (1.51 g, 0.049 mmol), styrene (2.24 g, 21.5 mmol), p-norborneneylethyl styrene (0.52 g, 2.3 mmol) and AIBN (2.9 mg, 0.018 mmol) were dissolved in 6.0 mL of toluene. The polymerization solution was degassed with argon for 10 minutes before 3 freeze-pump-thaw cycles were performed. The solution was then heated in an oil bath at 70 °C for 17 hours. After removal from the oil bath, the solution was diluted with THF and precipitated in methanol. The polymer was recovered by filtration and reprecipitated in pentane from methylene chloride.

3.2.4. Membrane preparation.

Membranes were prepared by dissolving the desired block polymer template, and DCPD in one vial and GII in a second vial in THF (75 to 85 wt %). The two vials were then combined, stirred for 10 seconds and cast on glass using a doctor blade. The film was covered and left to crosslink for 18 hours. Immersion of the films in methanol solution facilitated their removal from the substrate. The films were then immersed in a 0.5 M NaOH solution (60/40 by volume of water/methanol), and heated at 70 °C for 3 days to remove the PLA. Resultant membranes were washed with methanol and dried under vacuum for 24 hours. Hydrolysis of PtBMA chains was performed by exposing the PNS-PtBMA/PDCPD membrane to a 90/10 by volume solution of formic acid and trifluoroacetic acid room temperature for 24 hours. Finally, prior to liquid flow

measurements the membranes were exposed to an oxygen reactive-ion etch (O_2 RIE) for 3 to 5 minutes to remove a thin PDCPD skin layer that forms on the film surface.

3.2.5. Liquid flow measurements.

Liquid flow measurements were performed using an Amicon 8010 stirred filtration cell (Millipore Co, Billerica, MA). 2.5 cm circular disks were cut from the dry nanoporous films, and sealed in the cell using a silicone O-ring. The membranes were first wetted with either methanol or isopropanol followed by flushing with pure water for 1 hour to remove any remaining alcohol. To establish baseline flux values, the cell was then filled with distilled water and a pressure difference (from 0.3 to 1.4 bar) was applied using N_2 gas. The permeating water was collected for at least a half an hour to ensure a constant flow rate, and then the permeate mass was recorded over time. For the flux measurements at variable pH, dilute solutions of NaOH and HCl in distilled water were used as the permeate, and the membrane was flushed with the new solution for an hour to allow equilibration prior to measuring the flow. For variable temperature measurements, the entire stirred cell was heated in a water bath for two hours at each temperature prior to any measurements.

Flow through the membranes was modeled using the Hagen-Pouiseuille relationship:[39,40]

$$J_v = \frac{\varepsilon d^2 \Delta P}{32 \tau \mu l} \tag{3.1}$$

and the Blake-Kozeny component of the Ergun equation:[41]

$$J_v = \frac{d^2 \Delta P}{150 \mu l} \frac{\varepsilon^3}{(1-\varepsilon)^2} \tag{3.2}$$

where J_v is the volumetric flux, ε is the void fraction, d is the pore diameter in the Hagen Pouiseuille relationship and a characteristic length scale associated with the pore size in the Ergun equation, ΔP is the pressure drop across the membrane, μ is the viscosity, l is the membrane thickness and τ is the membrane tortuosity.

3.2.6. Molecular Weight Cutoff (MWCO) Measurements.

All experiments evaluating the MWCO were performed in an Amicon 8010 stirred cell pressurized at 0.9 bar. The MWCO of PNS-PLA/PDCPD membranes was evaluated using two approaches. The membranes were initially challenged with 1.5 g/L aqueous solutions of poly(ethylene oxide) (PEO) chains. Individual solutions for each PEO molecular weight (0.8, 3.0, 9.0, 14.0, 23.0, 35.0, 59.0, 100.0 and 400.0 kg/mol) were passed through the membrane. PEO concentrations in the feed and permeate solutions were determined from the total organic carbon content measured using a Sievers 900 portable TOC analyzer. The total organic carbon content was converted into concentration based on calibration curves for each PEO stock solution. The percent rejection for each PEO molecular weight was then calculated based on the PEO concentrations using equation 3.3:[42]

$$R = \left(1 - \frac{c_p}{c_f}\right) \times 100\% \tag{3.3}$$

where c_p and c_f are the concentration of the solute in the permeate and feed respectively.

A continuous MWCO curve was determined based on ASTM 1343 [43] by challenging the membranes with a solution of polydisperse dextrans ranging from 10^{-1} to 10^6 kg/mol. An SEC trace of the feed solution is shown in Figure 3.2. After the filtration, the concentration of the feed and permeate solutions was measured using SEC, and the percent rejection was determined for each molecular weight using equation 3.3.

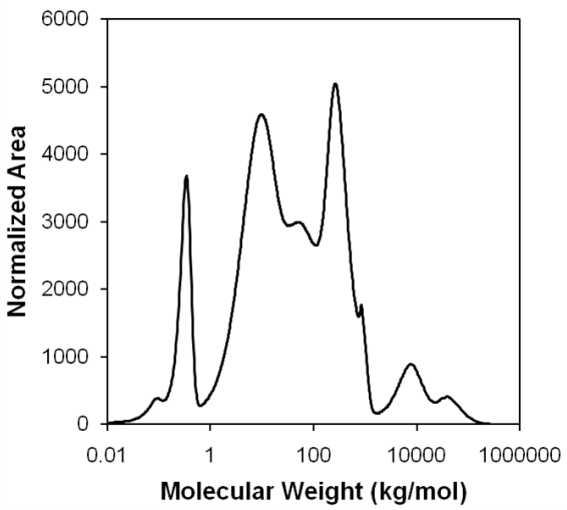

Figure 3.2. SEC trace of dextran feed solution showing the molecular weight distribution of chains.

3.2.7. Fouling Experiments.

Fouling experiments were performed using an Amicon 8200 stirred filtration cell (Millipore Co, Billerica, MA). 6.2 cm diameter circular disks were cut from the dry nanoporous films, and sealed in the cell using a silicone O-ring. A pressure of 1.5 bar and a constant stirring speed of 120 rpm was maintained during all experiments. Flux through the membrane was first measured for 75 mL of ultrapure water to establish the initial

pure water flux. Then 200 mL of test water was placed in the stirred cell. The test water consisted of three carbonate buffer solutions containing Suwannee River whole natural organic matter (NOM), fulvic acid, or humic acid. The whole NOM, fulvic and humic acids were purchased as powders from the International Humic Substances Society (IHSS). Flux through the membrane was then measured for approximately 150 mL of the test solution. The remaining test solution was carefully removed and replaced with 75 mL of ultrapure water, and the clean water flux of the fouled membrane was measured.

3.3. Flux, filtration and fouling performance of diblock templated membranes

3.3.1. Diblock polymer characterization and membrane formation

A number of PNS-PLA block polymers were formed by the anionic copolymerization of styrene and norbornenylethyl styrene followed by the ring opening polymerization of lactide. A more detailed discussion of the synthesis of PNS-PLA block polymers is included in Chapter 4. The molecular weight of the polymers was determined by ^{1}H NMR end group analysis, and the PDI of the polymers was determined using SEC and is based on poly(styrene) standards. The polymer PDIs are larger than what is expected for controlled polymerizations due to the presence of residual homopolymer PNS. The presence of homopolymer PNS most likely arises from incomplete end capping of the PNS block with ethylene oxide, so the chain does not have a hydroxyl group to serve as an initiator for subsequent polymerization of lactide. Table 3.1 provides a

summary of the polymers used. Each polymer is labeled PNS-PLA (X-Y) where X is the molecular weight of the PNS block and Y is the molecular weight of the PLA block.

Table 3.1 Molecular characteristics of PNS-PLA block polymers

Polymer[a]	$M_{n,\ PNS}$ (kg/mol)[b]	x_N[c]	$M_{n,\ PLA}$ (kg/mol)[b]	PDI[d]	w_{PLA}[e]
PNS-PLA (27-32)	27	0.14	32	1.27	0.54
PNS-PLA (27-42)	27	0.14	42	1.31	0.61
PNS-PLA (27-65)	27	0.14	65	1.43	0.71
PNS-PLA (23-20)	23	0.14	20	1.55	0.47
PNS-PLA (27-66)	27	0.08	66	1.75	0.71

[a]Polymers are labeled PNS-PLA (X-Y) where X is the molecular weight of the PNS block and Y is the molecular weight of the PLY block. [b]Molecular weights were determined by ^{1}H NMR end group analysis. [c]Mole fraction of N in the PNS block as determined by ^{1}H NMR spectroscopy. [d]PDI determined by size exclusion chromatography based on poly(styrene) standards. [e]Weight fraction of PLA ($w_{PLA} = M_{n,\ PLA}/(M_{n,\ PNS} + M_{n,\ PLA})$).

Using the PNS-PLA block polymers a series of membranes were prepared by solution casting the respective PNS-PLA diblock polymer with dicyclopentadiene and GII in THF on a glass plate using a doctors blade. The cast solutions were covered and cured overnight under ambient conditions yielding transparent cross-linked films with thicknesses ranging from 50 to 100 μm depending on the concentration of the casting solution and the height set on the doctors blade. Multiplying the wt % of PNS-PLA/PDCPD in the casting solution by the casting height provides an estimate of the final dry height of the membrane. For example a solution with 25 wt % PNS-PLA and DCPD cast at 500 μm would result in a membrane around 125 μm thick. Table 3.2 outlines the composition and characteristics of the membranes formed.

Table 3.2. Composition and characterization data for PNS-PLA/PDCPD membranes

Membrane[a]	PLA-PNS (wt %)	DCPD (wt %)	GII (wt %)	PLA (wt %)	Mass Loss[b] (wt %)	Domain Spacing (nm)[c]	
						BE	AE
NSLD (27-32)	79	21	0.6	43	62	-[d]	-[d]
NSLD (27-42)	78	22	0.4	48	49	48	47
NSLD (27-65)	67	33	0.5	47	49	56	50
NSLD (23-20)[e]	67	33	0.1	31	37	-[d]	-[d]
NSLD (27-66)[f]	67	33	0.1	47	49	-[d]	52

[a]All membranes were cast from 75–85 wt % THF solutions. [b]Mass loss corresponds to the total percentage of mass loss upon etching the sample. [c]Domain spacings where determined from SAXS at room temperature using the Teubner-Strey microemulsion model. [d]A peak was not observed in the scattering pattern of these samples. [e]Three different membranes were cast at this composition and the average mass loss is shown. [f]Nine different membranes were cast at this composition and the average mass loss is shown.

The films were rendered porous by etching them in a 0.5 M water/methanol (60/40 by volume) solution of sodium hydroxide at 70 °C for 3 days. A comparison of the mass loss to the initial wt % of PLA indicated loss of an equivalent amount of mass. Removal of PLA was confirmed by FT-IR of the membranes. Figure 3.3 shows the IR spectrum for NSLD (27-65) and is representative of the other membranes. The absence of the lactide carbonyl peak at 1750 cm^{-1} after etching indicates removal of the PLA block.

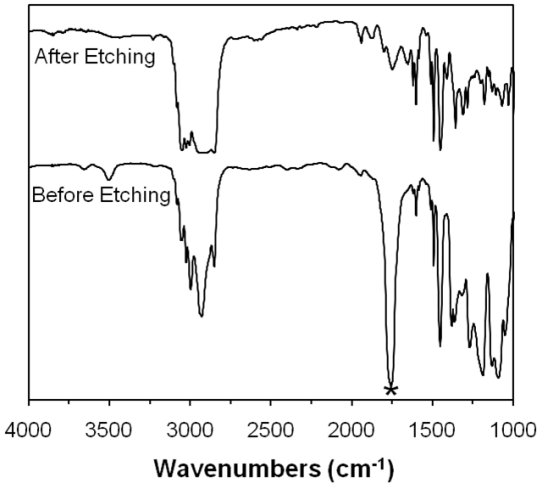

Figure 3.3. IR of membrane NSLD (27-65) both before and after etching. The loss of the lactide carbonyl stretch at ~1750 cm^{-1} (*) indicates removal of the PLA block.

SAXS patterns for the samples before etching exhibited a single broad scattering peak, which is indicative of a microphase separated but disordered structure. After etching, the scattering pattern shape was similar, but the scattering intensity significantly increased indicating both preservation of the nanostructure and increased contrast due to removal of the PLA component. Figure 3.4 shows the SAXS pattern for NSLD (27-42) and is representative of other membranes where scattering was observed. Scattering was not observed for all membranes possibly due to the thickness of the material. In all cases when scattering was not observed, further characterization by SEM confirmed the presence of a microphase separated morphology.

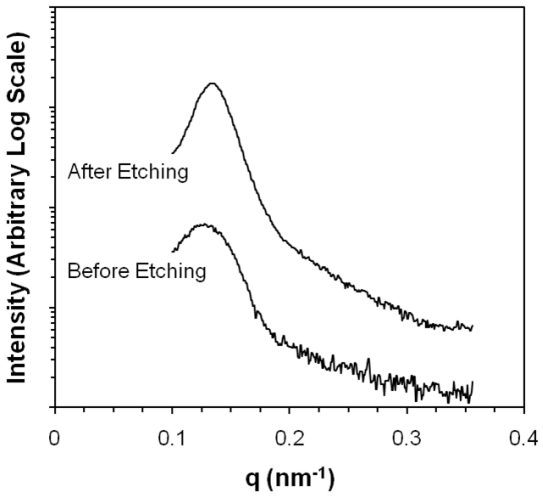

Figure 3.4. One-dimensional SAXS profiles for NSLD (27-42) before and after etching.

Prior to permeability experiments, both surfaces of the membranes were exposed to an oxygen-reactive ion etch (O_2-RIE) for 3 to 5 minutes to remove a thin nonporous PDCPD "skin" layer[27] and expose the underlying pores. SEM was used to confirm skin layer removal and characterize the porous substructure. Typically, greater than 80% of the surface has exposed pores after the O_2-RIE, but the surface is not homogenous throughout. Figure 3.5 demonstrates two regions for membrane NSLD (27-32) after etching. Figure 3.5A and Figure 3.5B exhibit exposed pores, which account for greater than 80% of the surface, while Figure 3.5C and Figure 3.5D show a region with more obscured pores.

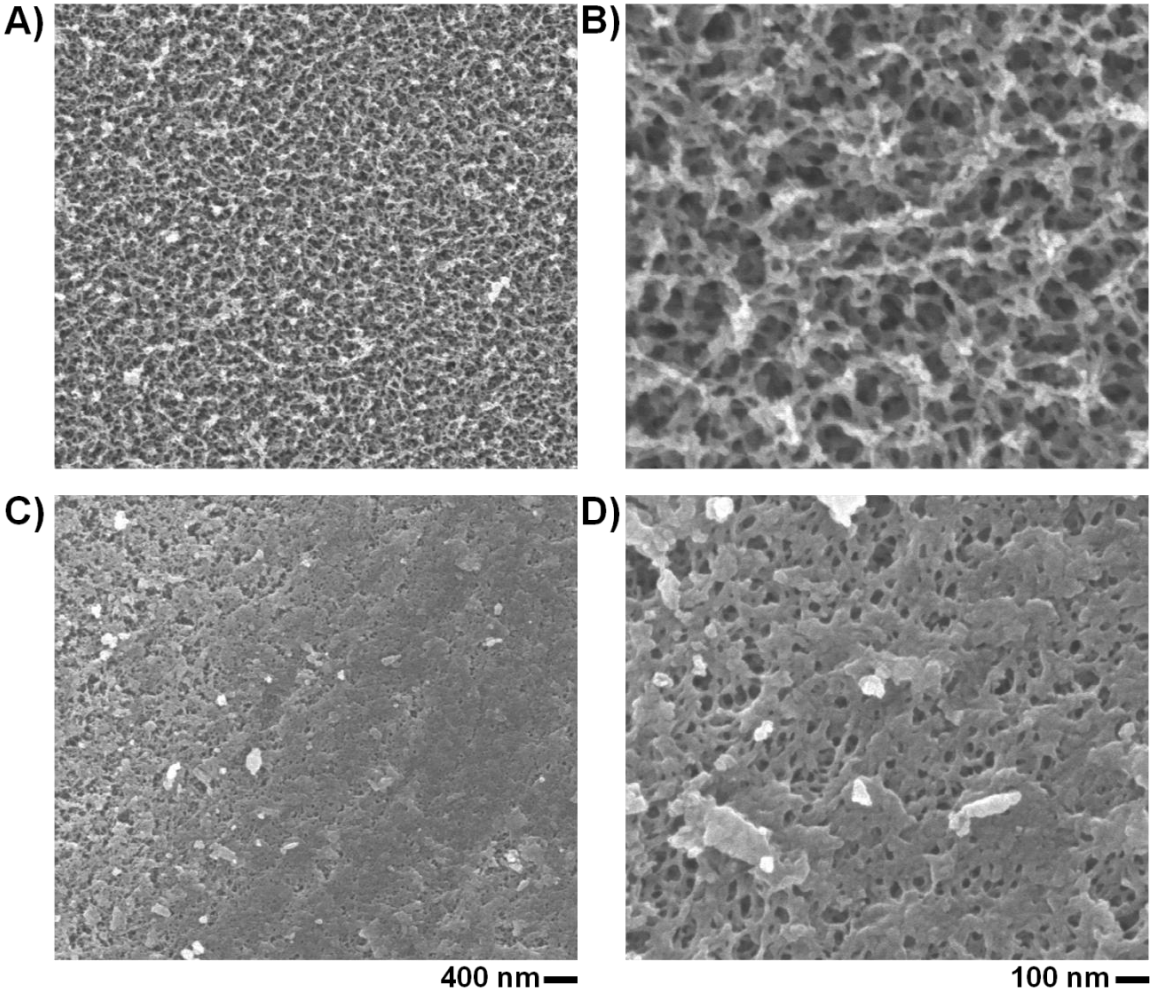

Figure 3.5. SEM micrographs of the surface of NSLD (27-32) after the O_2-RIE illustrating two regions on the surface with exposed pores (A and B) and obscured pores (C and D). The scale bars on the bottom apply to the images in that column. The surfaces were coated with 1.5 nm of platinum prior to imaging to prevent charging.

3.3.2. Pure water flux.

The pressure dependent flux of the NSLD (27-42) membrane was evaluated at 0.5, 0.7, 0.9, 1.1 and 1.4 bar using a dead end filtration stirred cell. After wetting the membrane, the appropriate pressure was applied, and water flowed for half an hour before recording the flux over time. Two separate measurements were performed for each

pressure, and Figure 3.6 shows the observed flux values plotted as a function of pressure. A linear response to pressure was observed in agreement with both the Hagan Pouiseulle and Ergun relationships.

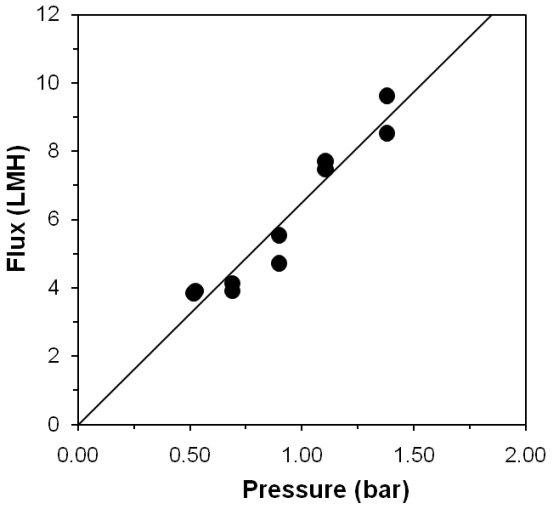

Figure 3.6. Pressure dependent water flux for NSLD (27-42) membrane as a function of pressure (circles), and the best fit linear regression line, which corresponds to a pressure dependent flux of 6.5 LMH/bar.

The overall pressure dependent flux from the slope of the linear regression of the data was 6.5 LMH/bar. Based on this value, apparent pore sizes of 13.7 and 24.0 nm were calculated using the Hagan Pouiseulle and Ergun relationships, respectively. Estimated pore sizes from SEM are approximately 20 to 25 nm, which is in good agreement with the result of the Ergun equation. The flux of 6.5 LMH/bar is quite low when compared to commercially available ultrafiltration membranes, which typically fall between 150 and 1750 LMH/bar.[44] However, if the PNS-PLA/PDCPD membrane could be applied as a coating on top of a microfiltration membrane to achieve a selective layer of 500 nm, the

theoretical flux would be 3250 LMH/bar, which is greater than the flux range of current ultrafiltration membranes.

3.3.3. Filtration performance.

The potential for achieving superior fluxes is only a worthwhile pursuit if the membrane selectivity is also high. The selectivity of PNS-PLA/PDCPD membranes was investigated by two different ultrafiltration experiments. First, single solute rejection experiments were performed with solutions of PEO. A NSLD (27-42) membrane was challenged with nine aqueous PEO solutions (1.5 g/L) with PEO molecular weights of 0.8, 3.4, 8.9, 14.0, 23.5, 35.0, 59.0, 100.0 and 400.0 kg/mol. The percent rejection of each PEO chain was determined using the concentration of PEO in the feed and permeate and is plotted in Figure 3.7.

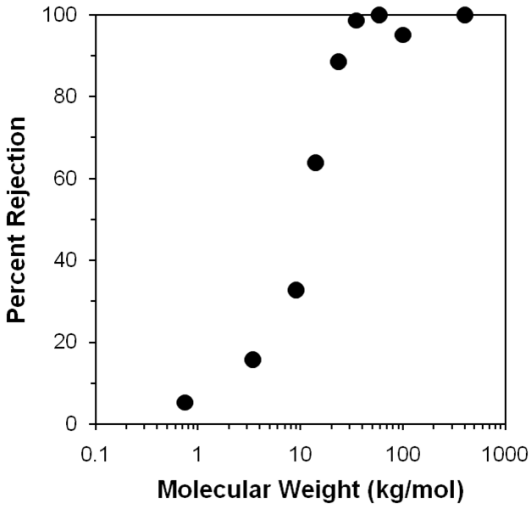

Figure 3.7. Percent rejection as a function of PEO molecular weight for single solute aqueous solutions of PEO chains with molecular weights of 0.8, 3.4, 8.9, 14.0, 23.5, 35.0, 59.0, 100.0 and 400.0 kg/mol.

Figure 3.7 shows a fairly steep increase in rejection with increasing molecular weight achieving virtually complete rejection of PEO chains 35.0 kg/mol or greater. Previous modeling by Phillip et al. showed that the observed rejection was in agreement with predictions based on the ratio of the size of the PEO chain to the apparent pore diameter from the Hagan Pouiseuille relationship.[28,29] Agreement between the rejection and modeling based on the estimated pore size suggests a uniform pore structure across the membrane.

In addition to the single solute rejection experiments, the selectivity of PNS-PLA/PDCPD membranes was explored using the ASTM standard for evaluating the MWCO performance of ultrafiltration membranes[43] in collaboration with GE Water.[45] Two PNS-PLA/PDCPD membranes were tested, NSLD (27-32) and NSLD (27-65), to show the effect of changing the PLA block size on the selectivity of the membrane, and a phase inversion membrane under development by GE Water was also tested to confirm the consistency of the results. Under this protocol the membranes were challenged with a feed solution of mixed dextrans with a molecular weight range from 0.5 to 10,000 kg/mol (see Figure 3.2 for SEC trace of the molecular weight distribution). The percent rejection was determined from the dextran concentration in the feed and permeate solutions from SEC. The respective MWCO curves for the phase inversion membrane, NSLD (27-32) and NSLD (27-65) are shown in Figure 3.8.

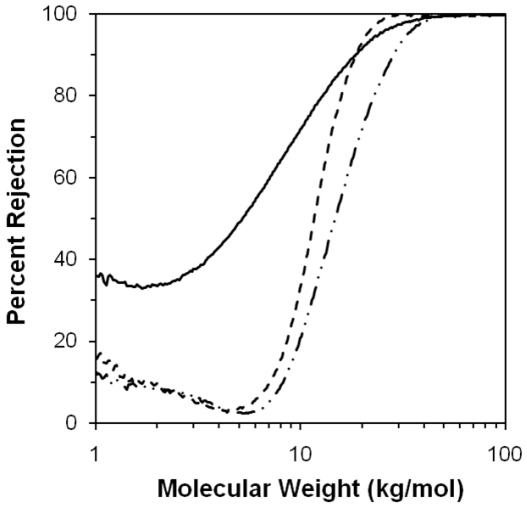

Figure 3.8. Rejection curves of mixed dextrans for the GE Water phase inversion membrane (solid), NSLD (27-32) (dash) and NSLD (27-65) (dash-dot-dot).

Two key features are in Figure 3.8. First, the MWCO curves for both NSLD (27-32) and NSLD (27-65) are steeper than the phase inversion membrane. In order to achieve 95% rejection of a 35 kg/mol solute, the phase inversion membrane would also be rejecting significant fractions of lower molecular weight species, but the PNS-PLA/PDCPD membranes would not. The increased selectivity of the PNS-PLA/PDCPD membranes would permit more selective separations by preventing unnecessary exclusion of other solutes of interest from the permeate stream. Second, the difference between the NSLD (27-32) and NSLD (27-65) MWCO curves. Qualitatively the NSLD (27-65) MWCO curve shifts to higher molecular weights for achieving the same rejection. Quantitatively, the NSLD (27-32) achieves 95% rejection for solutes 24.1 kg/mol or larger, while NSLD (27-65) 95% rejection is at 33.4 kg/mol. The change in rejection signifies an increased pore size as expected for increasing the PLA block size,

and suggests that the membrane pore structure can be specifically tailored by controlling the molecular weight of the PLA.

3.3.4. Membrane Fouling.

The reduction in membrane flux due to binding of matter retained during filtration, such as NOM, is called fouling.[30] Fouling is of critical concern to membrane performance as a reduction in flux decreases the both productivity and efficiency of the process. Therefore, investigation of the fouling performance of PNS-PLA/PDCPD membranes is important as any potential gains in membrane flux could be eliminated if the membranes exhibit significant fouling. The fouling of PNS-PLA/PDCPD membranes was explored by exposing NSLD (23-20) membranes to a test water solutions containing whole NOM, fulvic acid or humic acid as the foulant. Figure 3.9 shows the flux overtime of the membrane during the fouling experiments. The initial pure water fluxes were similar to the previous flux measurements considering the membranes were thinner (~30 μm vs 100 μm). The one exception is the membrane fouled with whole NOM, which was a factor of 5 greater. This could be due to a small crack in the membrane. Fouling measurements on this membrane may be skewed due to the crack, but still give an indication of how the material may stick to the membrane.

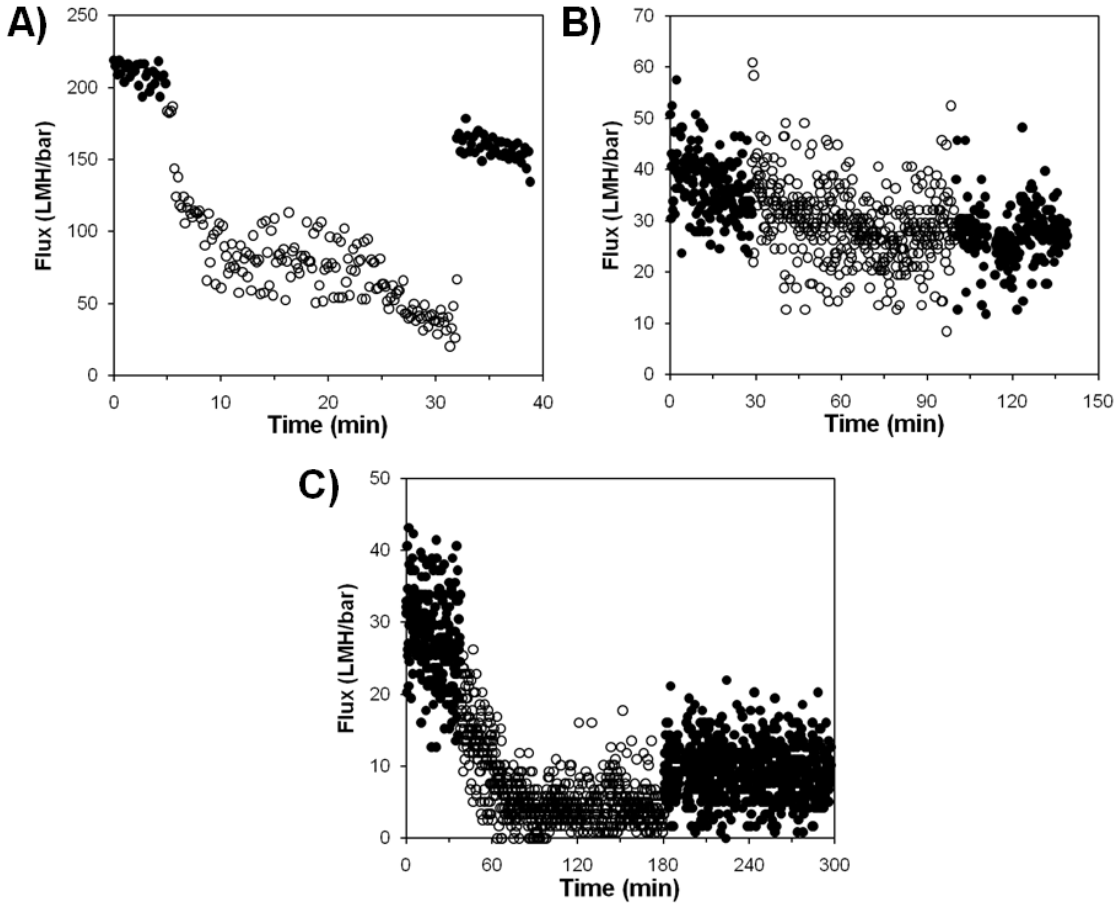

Figure 3.9. Fouling performance of three NSLD (23-20) membranes exposed to A) whole NOM, B) fulvic acid and C) humic acid. The filled circles are the permeability measurements for clean water both before and after fouling, while the open circles are the permeability measurements during the flux of the test water fouling solutions.

The flux decline due to fouling with whole NOM and fulvic acid was rapid and significant as declines of 62 and 84% were observed, but fouling with humic acid was somewhat less as only a decline of 27% was observed. Since fulvic and humic acid are components of whole NOM it is possible that the fouling observed with whole NOM primarily arises from interactions of fulvic acid with the membrane. Relative to humic acid, fulvic acid is composed of lower molecular weight species,[46] so the increased

fouling due to fulvic acid could be indicative of fouling within the pores. Interestingly the recovery of flux during the final clean water flux measurement for the whole NOM and fulvic acid fouled membranes suggests that the NOM is not strongly bound to the surface of the membrane and could be easily removed by physical methods without the need for chemical cleaning. While these results are preliminary, they indicate that the PNS-PLA/PDCPD membranes exhibit interesting fouling behavior with regard to the permanent binding of foulants, and additional experiments are warranted to further investigate this behavior.

3.4. Hydrophilic and responsive membranes from reactive triblock terpolymers

3.4.1. Synthesis of Triblock Polymers and Their Membrane Formation.

A series of controlled free-radical polymerizations by reversible addition-fragmentation chain transfer (RAFT) using a trithiocarbonate end-capped polylactide[33] were performed to prepare triblock terpolymers consisting of a chemically etchable block, PLA, a functional mid-block and a metathesis reactive statistical copolymer of styrene and norbornenylethyl styrene (Figure 3.10). The mid blocks used included *tert*-butyl methacrylate (tBMA), and *N*-isopropylacrylamide (NIPAM).

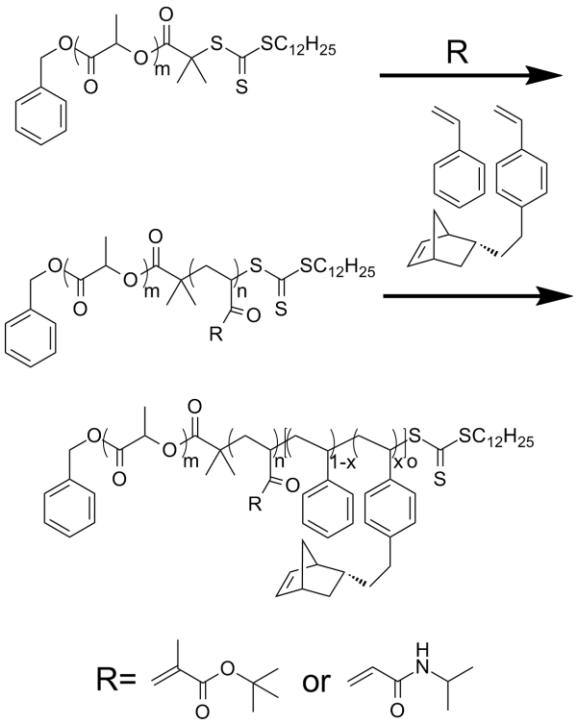

Figure 3.10. Synthetic scheme for the formation of PLA-PX-PNS triblock terpolymers.

Efficient reinitiation in the consecutive polymerization steps was confirmed by ^{1}H-NMR spectroscopy (Figure 3.11) and size exclusion chromatography (Figure 3.12) of the polymers resulting in triblock terpolymers with polydispersities between 1.2 and 1.6. Table 3.3 includes the molecular characteristics of the three triblock terpolymers used in formation of the membranes.

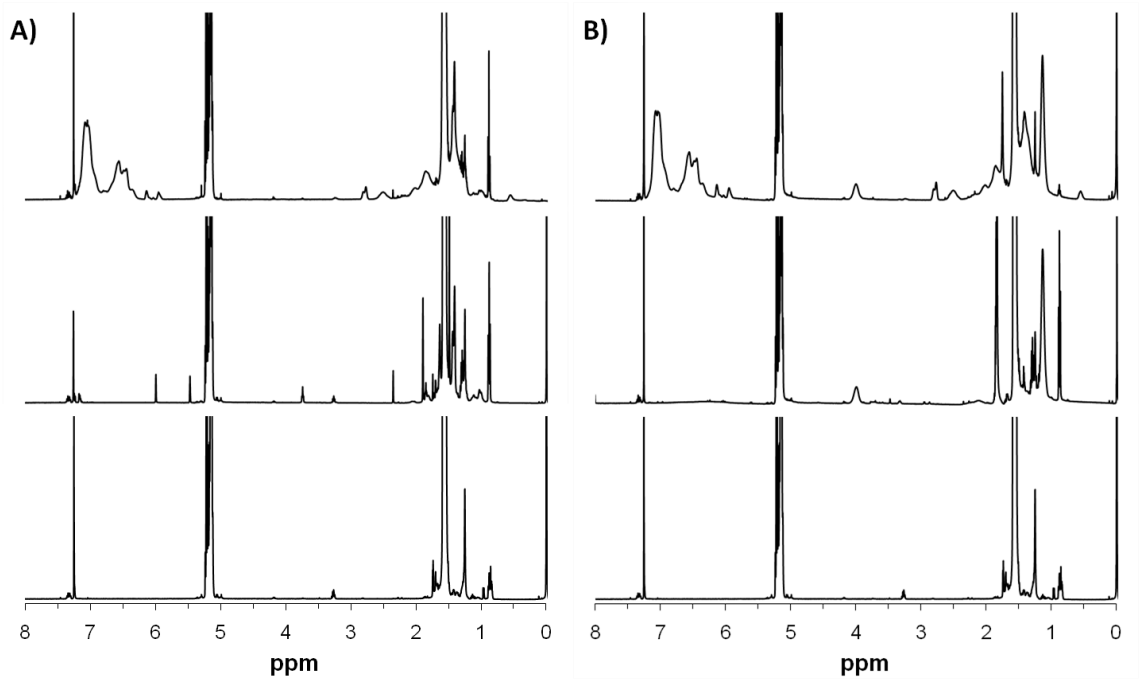

Figure 3.11. ^{1}H NMR spectra showing the progressive addition of blocks starting with PLA functionalized with the RAFT agent (bottom), PLA-PX (middle) and PLA-PX-PNS (top) for the synthesis of A) PLA-PtBMA-PNS and B) PLA-PNIPAM-PNS triblock polymers.

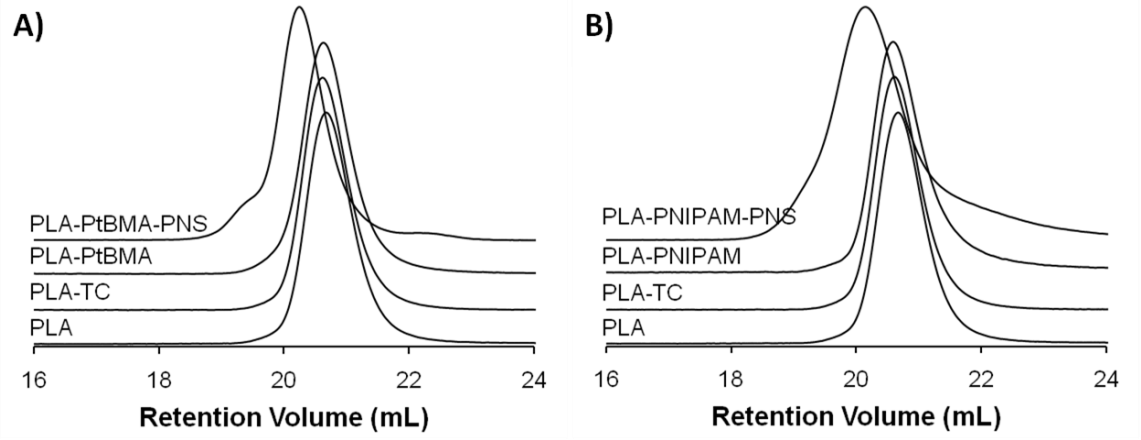

Figure 3.12. SEC showing the progressive addition of blocks in synthesizing the triblock polymers for A) PLA-PtBMA-PNS and B) PLA-PNIPAM-PNS.

Table 3.3. Molecular characteristics of PLA-P*X*-PNS triblock terpolymers.

Polymer	$M_{n,\ PLA}$ (kg/mol) [a]	$M_{n,\ PX}$ (kg/mol) [a]	$M_{n,\ PNS}$ (kg/mol)[a], x_N [b]	PDI[c]	w_{PLA} [d]
PLA-PtBA-PNS	28	1	12, 0.07	1.20	0.68
PLA-PNIPAM-PNS	28	4	15, 0.12	1.54	0.60

[a]Molecular weights were determined by ^{1}H NMR end group analysis. [b]Mole fraction of N in the PNS block as determined by ^{1}H NMR spectroscopy. [c]PDI determined by size exclusion chromatography based on poly(styrene) standards. [d]Weight fraction of PLA ($w_{PLA} = M_{n,\ PLA}/(M_{n,\ PLA} + M_{n,\ PX} + M_{n,\ PNS})$).

Membranes were prepared from these triblock terpolymers by casting a solution of the respective triblock terpolymer (13 wt%), dicyclopentadiene (7 wt%), and GII (0.02 wt%) in THF (80 wt%) on a glass plate using a doctors blade. The cast solutions were covered and cured overnight under ambient conditions yielding transparent cross-linked films with thicknesses between 20 and 50 μm. The films were rendered porous by etching them in a 0.5 M water/methanol solution of sodium hydroxide at 70 °C for 3 days. Table 3.4 outlines the composition and characteristics of the membranes formed.

Table 3.4. Composition and characterization data for PLA-PX-PNS/PDCPD membranes.

Membrane[a]	PLA-PX-PNS (wt %)	DCPD (wt %)	PLA (wt %)	Mass Loss[b] (wt %)	Domain Spacing (nm)[c]	
					BE	AE
LTNS	67	33	45	56	25	25
LNNS	67	33	40	47	36	36
NSLD (27-66)[d]	67	33	48	57	-[e]	52

[a]All membranes were cast from 80 wt % THF solutions with 0.1 wt % of GII relative to the polymer and DCPD mass. [b]Mass loss corresponds to the total percentage of mass loss upon etching the sample. [c]Domain spacings were determined from SAXS at room temperature using the Teubner-Strey microemulsion model. [d]NSLD (27-66) membrane was templated by PNS-PLA (27-66) to be a control to compare with the triblock templated membranes. [e]Scattering was not observed for this sample.

FT-IR spectroscopy (Figure 3.13) confirmed PLA removal based on the absence of the PLA carbonyl stretch at 1750 cm^{-1} after etching. Additionally, preservation of the mid blocks through the hydrolysis was confirmed by the presence of peaks at 1720, and

1650 cm^{-1} after etching, which correspond to the carbonyl stretches of the PtBA and PNIPAM respectively.

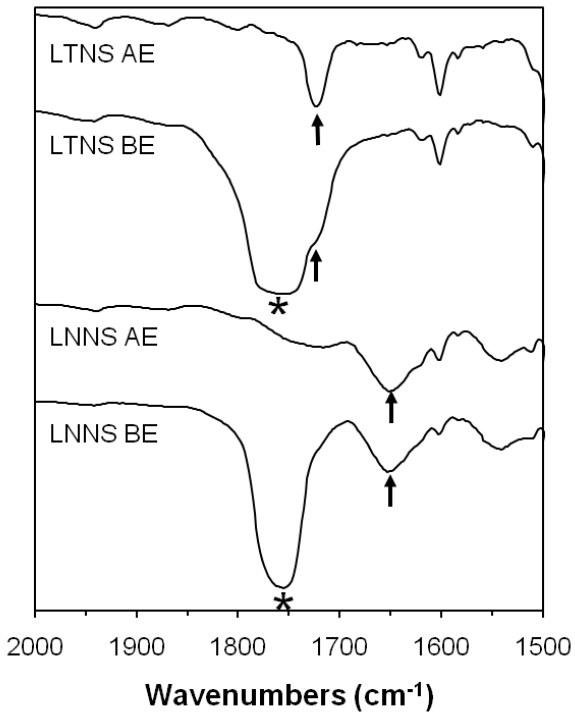

Figure 3.13. FT-IR spectra of the membranes both before (BE) and after (AE) etching. The asterisk (*) denotes the location of the PLA carbonyl stretch (~1750 cm^{-1}), which is virtually absent in each sample after etching. The arrow indicates the location of the amide or ester carbonyl stretch of PtBMA (1720 cm^{-1}) or PNIPAM (1650 cm^{-1}), which is preserved during the hydrolysis.

Morphologies were characterized using SAXS and SEM. SAXS patterns (Figure 3.14) for the samples before etching exhibited a single broad scattering peak, which is indicative of a microphase separated but disordered structure. In both cases, the scattering pattern was retained after etching, but the scattering intensity significantly increased, indicating both preservation of the nanostructure and increased contrast due to removal of the PLA component. The scattering patterns for the samples were modeled using using

the Teubner-Strey microemulsion model[47,48] to estimate the principle domain spacing. The LTNS membrane had a domain spacing of 25 nm, and the LNNS membrane had a domain spacing of 36 nm.

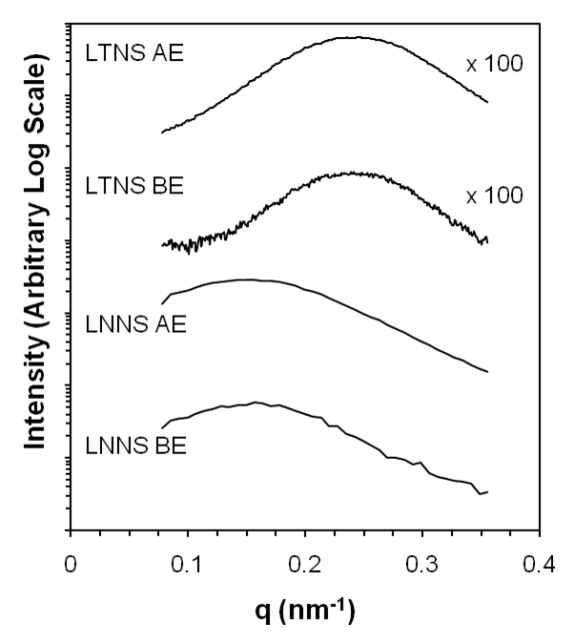

Figure 3.14. One-dimensional SAXS profiles for the LTNS and LNNS membranes both before (BE) and after etching (AE). The LTNS patterns were both vertically shifted by a 100x multiplier for clarity.

SEM micrographs of etched samples (Figure 3.15) revealed that the membranes had a nanoporous bicontinuous structure with pore sizes of approximately 20 nm for LNTS and 25 nm for LNNS, which is consistent with the domain spacing from SAXS.

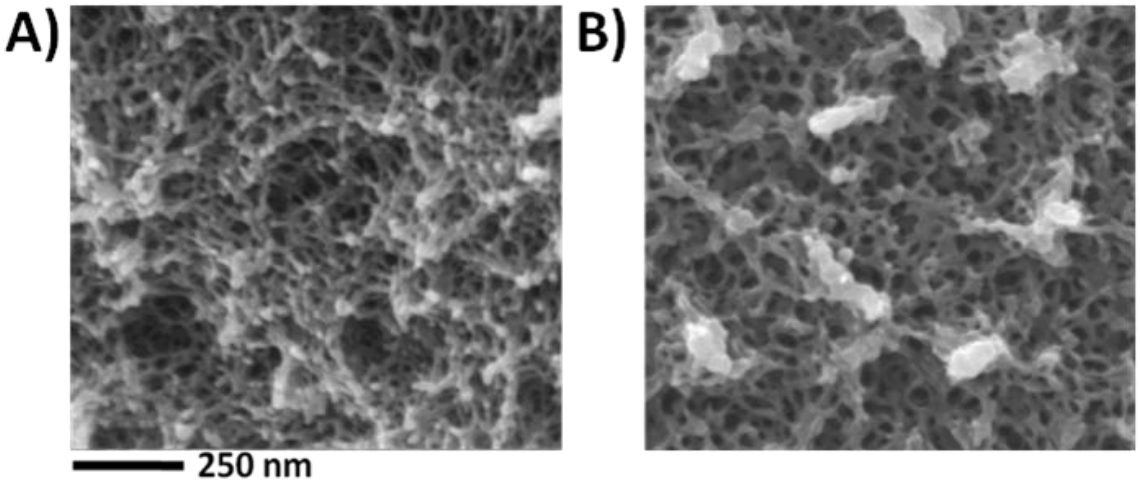

Figure 3.15. SEM micrographs of A) LTNS membrane and B) LNNS membrane after etching. The scale bar applies to both images. All samples were coated with 1.5 nm of platinum prior to imaging to prevent charging.

3.4.2. pH responsive membranes using PLA-PtBMA-PNS.

Initial investigations into forming a pH responsive membrane focused on hydrolyzing a PDMA mid-block to poly(acrylic acid) (PAA), but attempts to hydrolyze the PDMA chains using 6M hydrochloric acid[33] resulted in low conversions.[49] As an alternative route, PtBMA is readily hydrolyzable to poly(methacrylic acid) using a variety of approaches,[50,51,52,53] so it was used as a precursor to PMAA for making pH responsive membranes.

The pressure dependent flux of a LTNS membrane was evaluated at 0.7, 1.0 and 1.4 bar. Figure 3.16 shows the observed flux values for the membranes plotted as a function of pressure. A linear response to pressure was observed in agreement with both the Hagan Pouiseuille and Ergun relationships. The slope from the best fit of the data indicates that the overall pressure dependent flux was 5.6 LMH/bar. Based on the flux

data, apparent pore sizes can be calculated. Pore sizes of 7.1 and 13.9 nm were determined using the Hagan Pouiseuille relationship and the Ergun equation, respectively. The values determined using the Ergun equation are in better agreement with the pore sizes observed in SEM and domain spacings from SAXS for the LTNS membrane but are lower possibly due to incomplete removal of the PDCPD skin layer, which would reduce the overall flux and apparent pore size.

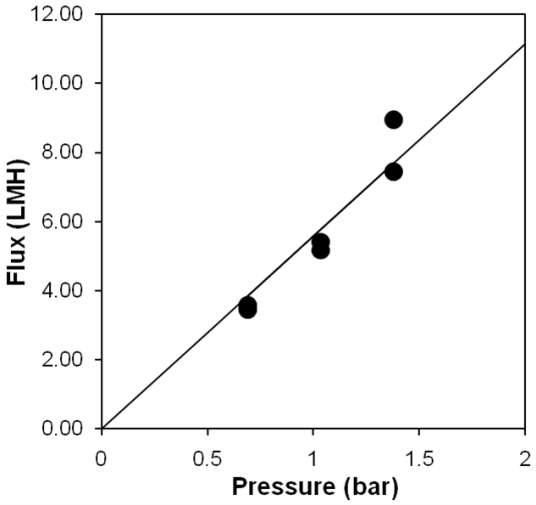

Figure 3.16. Water flux for LTNS membrane as a function of pressure (circles), and the best fit linear regression (line) corresponding to a pressure dependent flux of 5.6 LMH/bar.

After establishing the flux, flux through the LTNS membrane at 1.0 bar was examined at different pH values. Two flux measurements were performed upon increasing pH from 1 to 3, 6, 9, 12, and 14. Figure 3.17 shows the change in flux with pH.

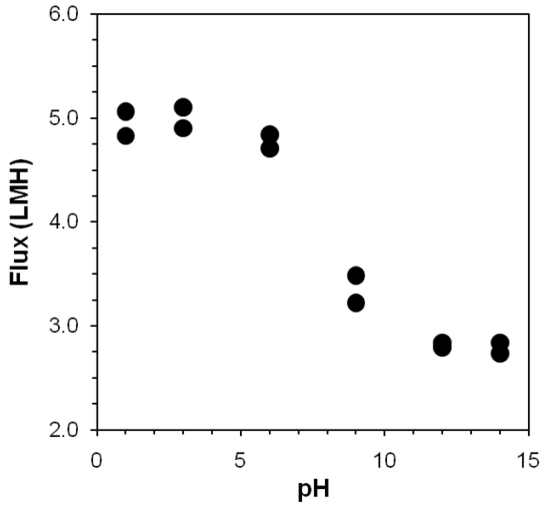

Figure 3.17. Observed flux as a function of pH for a LTNS membrane at a pressure drop of 1.0 bar.

Approximately a 45 % flux decline was observed upon increasing the pH from 1 to 14 centered around pH 7. Decreasing the pH back to 1 resulted in a return of the flux to the original value with a small hysteresis. A variable flux for the LTNS membrane was not expected, but one possible explanation was that the membrane was hydrolyzed during flux measurements at low pH. To check this, the membrane was examined by FT-IR (Figure 3.18) in comparison to a different piece of membrane that had been hydrolyzed using a formic acid/trifluoroacetic acid (90/10) solution.

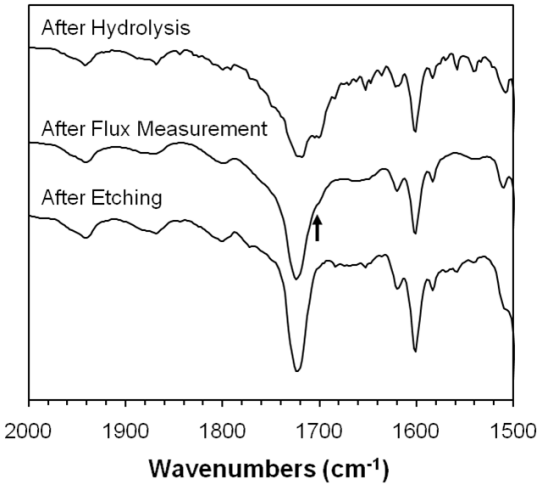

Figure 3.18. FT-IR spectra of the LTNS membrane after etching, after the flux measurements at variable pH and a different LTNS membrane after being hydrolyzed.

As can be seen in Figure 3.18, FT-IR indicates that the membrane was not significantly hydrolyzed during the flux measurements. Since the 1720 cm^{-1} peak appears to be slightly broader after the flux measurement and a slight shoulder appears at 1700 cm^{-1} where the PMAA carbonyl would appear, a very small amount of the PtBMA might have been hydrolyzed to PMAA, but a majority of the PtBMA remains.

To further probe the origin of the pH dependent flux, a PNS-PLA/PDCPD membrane was tested as a control following the same protocol. As can be seen in Figure 3.19, the NSLD (27-66) control membrane also exhibited a pH dependent flux very similar to that for the LTNS membrane, except only a 20% flux decline was observed. Additionally, the flux remains constant or slightly increases through pH 6, drops at pH 9 and remains level at pH 12 unlike the LTNS membrane, which exhibited a slight flux decline at pH 6, a significant drop to pH 9 and then another slight decrease in flux to pH 12. A pH dependent of flux was previously observed and reported for other PNS-

PLA/PDCPD membranes, but a flux decline linearly dependent on pH of approximately 40% was observed.[28]

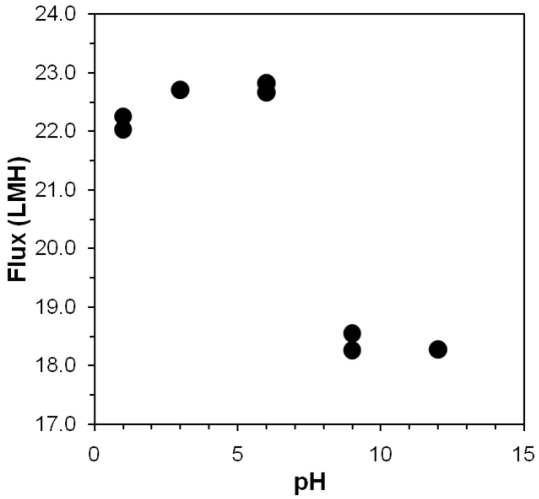

Figure 3.19. Observed flux as a function of pH for the NSLD (27-66) control membrane at a pressure drop of 1.0 bar.

In order to further compare the observed flux dependence on pH, the apparent change in pore size was determined for both membranes using the Ergun equation. For the LTNS membrane the apparent pore size dropped from 13.3 to 9.9 nm, while the apparent pore size of the NSLD (27-66) control membrane changed from 24.0 to 21.6 nm. The origin of the flux decline due to pH in the LNS control membrane is unknown at this time, but could be due reaction in the pores that creates some other pH responsive functionality.

Although the change in apparent pore size for both membranes is close possibly indicating that the same process is affecting both membranes, the change of the LTNS membrane is greater. In an attempt to decouple the effect of hydrolysis of the LTNS

membrane from any inherent flux dependence of the control membrane, two LTNS membranes were hydrolyzed prior to any flux measurements, but after hydrolysis the membranes were not permeable to water due to some sort of blockage of the pores. Repeated attempts to obtain a hydrolyzed membrane were unsuccessful, possibly indicating a structural change within the membrane preventing water permeability.

3.4.3. Thermoresponsive membranes using PLA-PNIPAM-PNS.

Numerous investigations[54] into the aqueous solution behavior of PNIPAM have established its LCST at 32 °C, making it useful for thermoresponsive materials such as micelles,[55] surfaces,[56] and hydrogels.[57] The incorporation of PNIPAM into membranes via grafting approaches has also been an avid area of research for forming thermoresponsive membranes.[58] Here we sought to exert additional control on the chain length and location of the PNIPAM brush layer by incorporating it into the block polymer template to create a thermoresponsive membrane.

Pure water flux through the LNNS membranes was measured at pressures of 0.7, 1.0 and 1.4 bar two times for three different membranes. Figure 3.20 shows the observed flux values for the membranes plotted as a function of pressure. A linear response to pressure was observed in agreement with both the Hagan Pouiseuille and Ergun relationships. From the slope of the best fit of the data the overall pressure dependent flux was 7.4 LMH/bar. Based on the flux data, apparent pore sizes of 8.8 and 21.2 nm were determined using the Hagan Pouiseuille relationship and the Ergun equation respectively. The values determined using the Ergun equation are in better agreement with the pore

sizes observed in SEM and domain spacings from SAXS for the LNNS membrane, so the Ergun equation will be used for any further pore size estimates from flux data for the LNNS membrane.

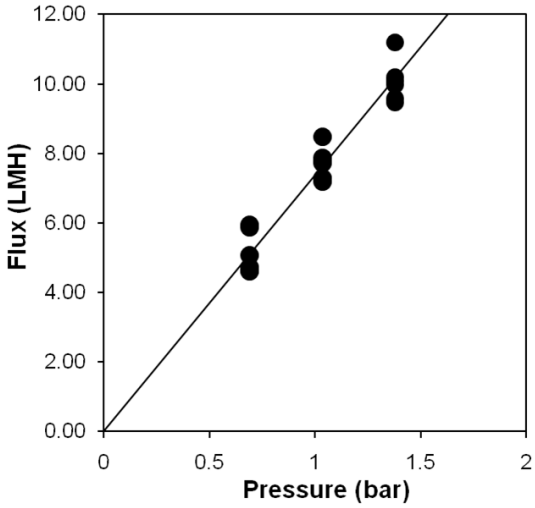

Figure 3.20. Water flux for PNS-PNIPAM/PDCPD membranes at room temperature as a function of pressure (circles), and the best fit linear regression (line) corresponding to a pressure dependent flux of 7.4 LMH/bar.

The transmembrane flux was then measured at 25 and 52°C for one membrane and 25, 40, 45 and 50°C for two other membranes under a constant pressure of 1.0 bar. The system was equilibrated for two hours after each temperature change prior to measuring the flux. Figure 3.21A shows the viscosity corrected flux normalized to the viscosity corrected flux at 25 °C for three LNNS membranes and the LNS control membrane. An average flux increase of approximately 25% from 25°C to 50°C for the three LNNS membranes was observed relative to no significant change for the LNS control membrane clearly indicating a thermally induced change in flux. The reversibility of the flux change is demonstrated in Figure 3.21B, as it shows the viscosity corrected

flux for a membrane upon heating and cooling. The agreement between the observed fluxes at a temperature whether during a heating or cooling cycle clearly indicate the reversibility of the flux change.

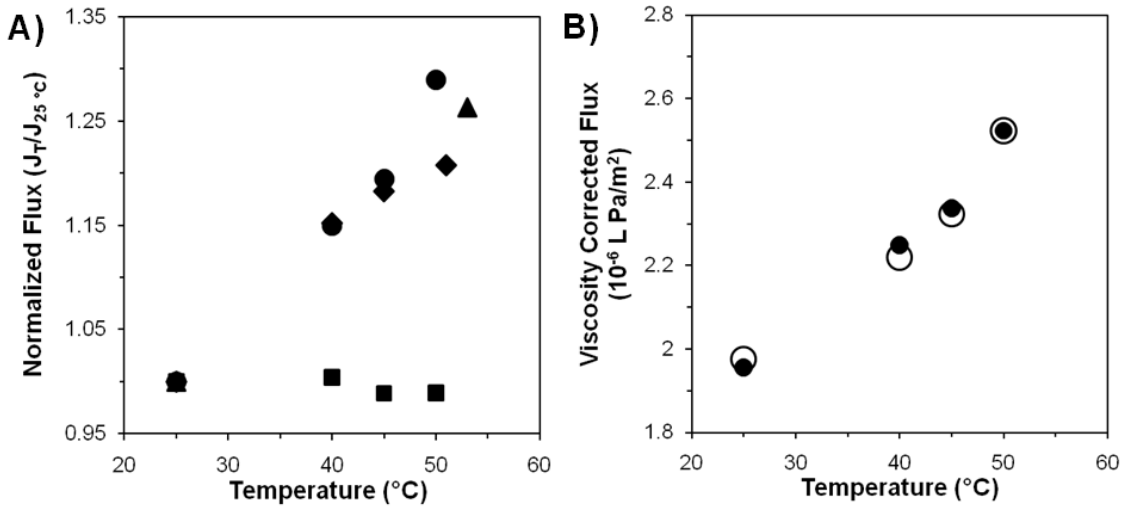

Figure 3.21. A) Viscosity corrected flux normalized to the viscosity corrected flux at 25°C for three LNNS membranes (filled circle, diamond and triangle) and the LNS control membrane (filled squares) as a control. **B)** Viscosity corrected flux as a function of temperature upon heating (filled circles) and cooling (open circles) for a LNNS membrane.

Since the LCST of PNIPAM is 32°C,[54] it was expected that changes in flux would be resolved within 5–10 degrees of the LCST consistent with previous results,[59,60] but flux increases were observed out to 50°C. This change in flux over a broader range of higher temperatures is consistent with an increase and broadening of the PNIPAM LCST with decreasing molecular weight as reported by Xia et al.[61] Specifically, the phase transition of a 2.8 kg/mol PNIPAM chain was observed from 36.3 to 43.0°C and 43.3 to 47.0°C based on turbidity and differential scanning calorimetry measurements, respectively, while the LCST of a 5.0 kg/mol PNIPAM chain was 37.5. to 38.9 and 39.7

to 41.7°C. Although the exact onset of the flux change was not observed, the continued increase in flux out to 50°C is consistent with the broadening of the LCST considering the PNIPAM molecular weight is 4 kg/mol.

Based on the flux data, pore dimensions calculated using the Ergun equation were 21.9 and 24.8 nm. The increase in flux and hence pore size should be equatable to the collapse of the PNIPAM brush upon transitioning above the LCST. The height of a dry brush (h_{dry}) can be estimated using equation 3.3:[62]

$$h_{dry} = \frac{\sigma N M_0}{N_{Av}\rho} \tag{3.4}$$

while the height of a wet PNIPAM brush (h_{wet}) can be estimated using equation 3.5:[62]

$$h_{wet} = 0.153 N \sigma^{1/3} \tag{3.5}$$

where σ is the grafting density of the chains, which was estimated based on the surface area (181 m^2/g) of a LNS sample with a similar PLA block size and composition (see Chapter 4 sample: PNS-PLA (11-26) D33), N is the total number of repeat units, M_0 is the monomer molecular weight (113.2 g/mol), N_{Av} is Avagadro's number, and ρ is the density of PNIPAM (1.070 g/cm^3).[63] The calculated height of the dry brush is 0.6 nm, while the wet height of the brush is 2.5 nm. Since the pore should be lined on all sides with the brush layer, the corresponding change in pore size would be two times the difference between the wet and dry height, which is 3.8 nm. This change in pore size is in

reasonable agreement with the estimated difference in pore sizes at 25 and 50°C of 2.9 nm supporting the conclusion that the collapse of the PNIPAM brush layer due to increasing the temperature above the LCST is the likely cause of the increased flux.

3.5. Conclusions

Overall, the flux and filtration characteristics of PNS-PLA/PDCPD membranes examined exhibit potential as alternatives to current ultrafiltration membranes, and warrant further exploration as composite membrane structures. By forming composite structures with a thin PNS-PLA/PDCPD selective layer over a macroporous support the superior fluxes might be realized. A second aspect for further consideration is the fouling of the membrane. Although initial investigations indicate a lack of permanent fouling, these results must be further explored and confirmed with additional experiments. Finally, the formation of membranes using a reactive triblock terpolymer provides a facile avenue for developing functional membranes as shown here for thermal and potentially pH responsive membranes with a PNIPAM and PtBMA mid-block, respectively.

3.6. Acknowledgements

This work was largely supported by CIE Polymers. M. A. A. acknowledges financial support from the U. S. Air Force. Parts of this work were carried out in the College of Science and Engineering Characterization Facility, University of Minnesota, a member of the NSF-funded Materials Research Facilities Network (www.mrfn.org).

3.7. References

(1) Bates, F. S. *Science* **1991**, *251*, 898-905.

(2) Hillmyer, M. A. *Adv. Polym. Sci.* **2005**, *190*, 137-181.

(3) Olson, D. A.; Chen, L.; Hillmyer, M. A. *Chem. Mater.* **2008**, *20*, 869-890.

(4) Fasolka, M. J.; Mayes, A. M. *Annu. Rev. Mater. Res.* **2001**, *31*, 323-355.

(5) Hawker, C. J.; Russell, T. P. *MRS Bull.* **2005**, *30*, 952-966.

(6) Phillip, W. A.; Rzayev, J.; Hillmyer, M. A.; Cussler, E. L. *J. Membr. Sci.*, **2006**, *286*, 144-152.

(7) Liu, G.; Ding, J.; Hashimoto, T.; Kimishima, K.; Winnik, F. M.; Nigam, S. *Chem. Mater.* **1999**, *11*, 2233-2240.

(8) Cooney, D. T.; Hillmyer, M. A.; Cussler, E. L.; Moggridge, G. D. *Crystallogr. Rev.* **2006**, *12*, 13-24.

(9) Peinemann, K.; Abetz, V.; Simon, P. F. W. *Nat. Mater.* **2007**, *6*, 992-996.

(10) Yang, S. Y.; Ryu, I.; Kim, H. Y.; Kim, J. K.; Jang, S. K.; Russell, T. P. *Adv. Mater.* **2006**, *18*, 709-712.

(11) Nuxoll, E. E.; Hillmyer, M. A.; Wang, R.; Leighton, C.; Siegel, R. A. *ACS Appl. Mater. Interfaces* **2009**, *1*, 888-893.

(12) Koppi, K. A.; Tirrell, M.; Bates, F. S. *Phys. Rev. Lett.* **1993**, *70*, 1449.

(13) Winter, H. H.; Scott, D. B.; Gronski, W.; Okamoto, S.; Hashimoto, T. *Macromolecules* **1993**, *26*, 7236-7244.

(14) Zalusky, A. S.; Olayo-Valles, R.; Wolf, J. H.; Hillmyer, M. A. *J. Am. Chem. Soc.* **2002**, *124*, 12761-12773.

(15) Morkved, T. L.; Lu, M.; Urbas, A. M.; Ehrichs, E. E.; Jaeger, H. M.; Mansky, P.; Russell, T. P. *Science* **1996**, *273*, 931-933.

(16) Thurn-Albrecht, T.; Schotter, J.; Kastle, G. A.; Emley, N.; Shibauchi, T.; Krusin-Elbaum, L.; Guarini, K.; Black, C. T.; Tuominen, M. T.; Russell, T. P. *Science* **2000**, *290*, 2126-2129.

(17) Kim, G.; Libera, M. *Macromolecules* **1998**, *31*, 2569-2577.

(18) Fukunaga, K.; Elbs, H.; Magerle, R.; Krausch, G. *Macromolecules* **2000**, *33*, 947-953.

(19) Hahm, J.; Sibener, S. J. *Langmuir* **2000**, *16*, 4766-4769.

(20) Kim, S. .; Misner, M. .; Xu, T.; Kimura, M.; Russell, T. *Adv. Mater.* **2004**, *16*, 226-231.

(21) Mansky, P.; Liu, Y.; Huang, E.; Russell, T. P.; Hawker, C. *Science* **1997**, *275*, 1458-1460.

(22) Huang, E.; Rockford, L.; Russell, T. P.; Hawker, C. J. *Nature* **1998**, *395*, 757-758.

(23) Kim, S. O.; Solak, H. H.; Stoykovich, M. P.; Ferrier, N. J.; de Pablo, J. J.; Nealey, P. F. *Nature* **2003**, *424*, 411-414.

(24) Uehara, H.; Yoshida, T.; Kakiage, M.; Yamanobe, T.; Komoto, T.; Nomura, K.; Nakajima, K.; Matsuda, M. *Macromolecules* **2006**, *39*, 3971-3974.

(25) Uehara, H.; Kakiage, M.; Sekiya, M.; Sakuma, D.; Yamonobe, T.; Takano, N.; Barraud, A.; Meurville, E.; Ryser, P. *ACS Nano* **2009**, *3*, 924-932.

(26) Yang, S. Y.; Park, J.; Yoon, J.; Ree, M.; Jang, S. K.; Kim, J. K. *Adv. Funct. Mater.* **2008**, *18*, 1371-1377.

(27) Chen, L.; Phillip, W. A.; Cussler, E. L.; Hillmyer, M. A. *J. Am. Chem. Soc.* **2007**, *129*, 13786-13787.

(28) Phillip, W. A.; Amendt, M.; O'Neill, B.; Chen, L.; Hillmyer, M. A.; Cussler, E. L. *ACS Appl. Mater. Interfaces* **2009**, *1*, 472-480.

(29) Phillip, W. A. *Block Polymer Membranes for Selective Separations*, University of Minnesota, Ann Arbor, MI, 2009.

(30) Rana, D.; Matsuura, T. *Chem. Rev.* **2010**, 110, 2448-2471.

(31) Ulbricht, M. *Polymer* **2006**, *47*, 2217-2262.

(32) Liu, G.; Ding, J.; Stewart, S. *Angew. Chem. Int. Ed.* **1999**, *38*, 835-838.

(33) Rzayev, J.; Hillmyer, M. A. *J. Am. Chem. Soc.* **2005**, *127*, 13373-13379.

(34) Mao, H.; Arrechea, P. L.; Bailey, T. S.; Johnson, B. J. S.; Hillmyer, M. A. *Faraday Discuss.* **2005**, *128*, 149-162.

(35) Bailey, T. S.; Rzayev, J.; Hillmyer, M. A. *Macromolecules* **2006**, *39*, 8772-8781.

(36) Guo, F.; Jankova, K.; Schulte, L.; Vigild, M. E.; Ndoni, S. *Macromolecules* **2008**, *41*, 1486-1493.

(37) Hadjichristidis, N.; Iatrou, H.; Pitsikalis, M.; Pispas, S.; Avgeropoulos, A. *Prog. Polym. Sci.* **2005**, *30*, 725-782.

(38) Lai, J. T.; Filla, D.; Shea, R. *Macromolecules* **2002**, 35, 6754-6756.

(39) Cussler, E. L. In *Diffusion Mass Transfer in Fluid Systems Second Edition;* Cambridge University Press: New York, 2005.

(40) Van Der Bruggen, B.; Vandecasteele, C.; Van Gestel, T.; Doyen, W.; Leysen, R. *Environ. Prog.* **2003**, *22*, 46-56.

(41) Bird, R.; Stewart, W. E.; Lightfoot, E. N. In *Transport Phenomena*; J. Wiley & Sons, Inc: New York, 2007;

(42) Baker, R. W. *Membrane technology and applications*, 2nd Ed. John Wiley & Sons Ltd, West Sussex, England, **2004**.

(43) Standard Test Method for Molecular Weight Cutoff Evaluation of Flat Sheet Ultrafiltration Membranes; ASTM-ASTM International, 2001; ASTM E 1343-90 (reapproved 2001).

(44) Mehta, A.; Zydney, A. L. *J. Membr. Sci.* **2005**, *249*, 245-249.

(45) Trent Biniek and Andrew Back of GE Water were especially helpful with the dextran MWCO work.

(46) Thurman, E. M. In *Organic Geochemistry of Natural Waters;* Martinus Nighoff/Dr. W. Junk: Hingham, MA, 1985; pp 497.

(47) Lichterfeld, F.; Schmeling, T.; Strey, R. *J. Phys. Chem.* **1986**, *90*, 5762-5766.

(48) Teubner, M.; Strey, R. *J. Chem. Phys.* **1987**, *87*, 3195.

(49) Roerdink, M. unpublished results.

(50) Liu, G.; Ding, J.; Stewart, S. *Angew. Chem. Int. Ed.* **1999**, *38*, 835-838.

(51) Storey, R. F.; Scheuer, A. D.; Achord, B. C. *Polymer* **2005**, *46*, 2141-2152.

(52) Meng, F.; Zheng, S.; Liu, T. *Polymer*, **2006**, *47*, 7590-7600.

(53) Guo, F.; Jankova, K.; Schulte, L.; Vigild, M. E.; Ndoni, S. *Macromolecules* **2008**, *41*, 1486-1493.

(54) Schild, H. G. *Prog. Polym. Sci.* **1992**, *17*, 163-249.

(55) Alarcon, C. d. l. H.; Pennadam, S.; Alexander, C. *Chem. Soc. Rev.* **2005**, *34*, 276-285.

(56) Mendes, P. M. *Chem. Soc. Rev.* **2008**, *37*, 2512-2529.

(57) Klouda, L.; Mikos, A. G. *Eur. J. Pharm. Biopharm.* **2008**, 68, 34-45.

(58) Kumar, A.; Srivastava, A.; Galaev, I. Y.; Mattiasson, B. *Prog. Polym. Sci.* **2007**, *32*, 1205-1237.

(59) Shtanko, N. I.; Kabanov, V. Y.; Apel, P. Y.; Yoshida, M.; Vilenskii, A. I. *J. Membr. Sci.* **2000**, *179*, 155-161.

(60) Lue, S. J.; Hsu, J.; Chen, C.; Chen, B. *J. Membr. Sci.* **2007**, *301*, 142-150.

(61) Xia, Y.; Yin, X.; Burke, N. A. D.; Stover, H. D. H. *Macromolecules* **2005**, *38*, 5937-5943.

(62) Wang, S.; Zhu, Y. *Langmuir* **2009**, *25*, 13448-13455.

(63) Coover, H. W.,Jr.; Shields, D. J. *J. Polym. Sci.* **1959**, *39*, 532-533.

Chapter 4.

Formation of nanostructured poly(dicyclopentadiene) thermosets using reactive block polymers

This chapter explores the compositional influences on the morphology of nanostructured poly(dicyclopentadiene) (PDCPD) thremosets prepared by the reaction induced phase separation (RIPS) of a metathesis reactive block polymer template. A series of films containing poly(norbornenylethyl styrene-*s*-styrene)-*b*-poly(lactide) (PNS-PLA) block polymers with varied PLA block lengths and different DCPD compositions were crosslinked using the second generation Grubbs catalyst. The film morphologies were interrogated by small angle X-ray scattering, scanning electron microscopy and nitrogen absorption measurements, and the results demonstrate that a majority of the films exhibited a bicontinuous nanoporous structure upon selective etching of the PLA component. A general mechanism for the formation of nanostructured DCPD using this protocol is proposed, and critical conditions for the formation of bicontinuous structures based on the extent of overlap of the block polymer is developed.

4.1. Introduction

The formation of nanostructured ceramics, polymers and composite materials has been at the forefront of numerous research endeavors. In particular, nanostructured thermosets have received attention as the thermal,[1] dielectric,[2] diffusion[3] and mechanical[3,4] properties of these materials can be systematically tuned depending on the components incorporated. Thermosets are formed by the coupling reactions of multifunctional monomers into a network structure, and the nanostructuring of thermosets can be accomplished through the incorporation of an additive that is integrated into the final structure upon curing. Examples of such additives include nanoparticles,[1,2] liquid crystals,[3] nanotubes,[4] and block polymers.[5]

Block polymers self-assemble into nanometer-sized morphologies that minimize unfavorable contact between the chemically distinct monomers and avoid excessive stretching of the component blocks.[6] When incorporated into thermosetting systems, nanostructured materials can be formed. An early example of this was demonstrated by Hillmyer et al.[5] using an amphiphilic block polymer and an epoxy resin. Since that report, many examples of nanostructured epoxies using block polymers have been reported.[5,7,8,9,10,11,12,13] In most of these cases, the block polymer contains an epoxy-philic segment and an epoxy-phobic segment. The morphology adopted in the uncured state depends on the nature of the block polymer and the blend composition as incorporation of the thermosetting monomers into the epoxy-philic block compatible domains leads to predictable morphological transitions.[7] Typical bulk block polymer morphologies such as

lamellar, gyroid, cylindrical and spherical,[5,7,8,9] and dilute solution morphologies, including spherical and wormlike micelles and vesicles,[10,11,12,13] have been observed. These morphologies can be frozen into the final structure upon curing often with minimal changes to the nanostructure.[7]

Seeking to expand the scope of block polymers to include polymers where both blocks are miscible in the thermoset precursors, Meng et al. demonstrated that self-assembly of the block polymer prior to curing was not always necessary. To create a nanostructured thermoset using this approach, a block polymer with one segment that remained miscible in the thermoset throughout the cure and another block that phase separated upon curing was employed.[14] Phase separation during curing is induced by the decreasing entropic contributions to the free energy of mixing. Since the two blocks are covalently bound, phase separation is limited and nanostructured materials are formed. The final morphologies formed via this reaction induced phase separation (RIPS) approach are microphase separated, and the typical structures attained are trapped by gelation of the thermoset. Morphologies observed using this approach include dispersed and fused spherical particles, wormlike structures, bicontinuous structures, lamellae, and cylinders.[14,15,16,17,18]

Variations in the chemical composition,[14,17] number of blocks[7,11] and architecture[9,18] of the block polymer additives have been explored. Additionally, reactive block polymers have been investigated as a means of fixing the morphologies of the block polymer and expanding the choice of precursors used in the thermoset.[19,20,21,22]

[,23,24,25,26,27,28] The scope of thermosets investigated in these studies remains fairly narrow as epoxy thermosets [5,7,9,10,11,12,13,14,15,16,17,18,29, 30,31,32,33,34,35,36,37,38] have received the bulk of the attention with only limited studies of phenolic[8, 39 , 40] and unsaturated polyester resins.[4142] Finally, applications of nanostructured thermosets using block polymers has primarily focused on their potential to improve the mechanical properties of the thermoset[10,12,36,38] leaving a range of applications unexplored.

Our interest in the formation of nanostructured thermosets was motivated by the search for tough nanoporous membranes. We recently reported the formation of nanostructured poly(dicyclopentadiene) (PDCPD) by a RIPS process using a metathesis reactive block polymer: poly(norbornenylethylstyrene-*s*-styrene)-*b*-poly(lactide) (PNS-PLA).[43] In that example a tetrahydrofuran (THF) solution of PNS-PLA and DCPD was crosslinked using the second generation Grubbs catalyst (GII) and a nanostructured bicontinuous morphology resulted.[43] Alternatively, by incorporating the first generation Grubbs catalyst and evaporating the solvent, an ordered cylindrical morphology formed that could be fixed by crosslinking to create a nanostructured thermoset by a "self-assembly first" approach. [44] Both of these nanostructured thermosets were rendered nanoporous by selectively removing the PLA component. These two distinct approaches to nanoporous PDCPD are depicted schematically in Figure 4.1.

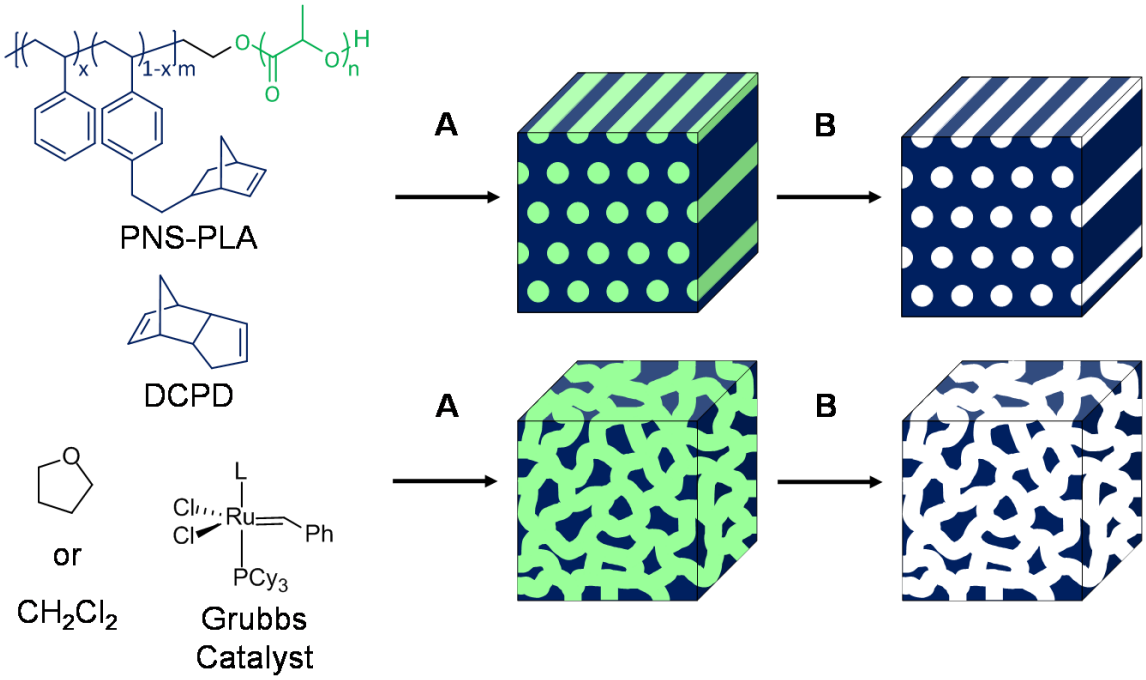

Figure 4.1. Pathways to nanoporous PDCPD via either self-assembly first (top) or RIPS (bottom). During step A of the self-assembly first approach the block polymer, DCPD and the first generation Grubbs catalyst are dissolved in CH_2Cl_2, the CH_2Cl_2 is evaporated, the block polymer structure is aligned, and then the material is crosslinked. During step A of the RIPS approach a THF solution containing the block polymer and DCPD is crosslinked using the second generation Grubbs catalyst followed by evaporation of the solvent. During step B for both methods, the PLA component is removed by basic hydrolysis.

The reactive block polymer RIPS approach to nanostructured materials holds a great deal of promise for the formation of membranes with particularly attractive technological applications. Applications demonstrated include the ultrafiltration of water[45] as discussed in Chapter 3, the separation of N_2 and NH_3[46] and polymer electrolyte membranes for direct methanol fuel cells.[47] Therefore, a detailed mechanistic understanding will enable the systematic tuning of the nanostructures and will be beneficial for the future development of these systems. Herein additional insight into the mechanism of nanostructure formation in the RIPS protocol using DCPD and PNS-PLA

is provided. This includes how PLA block size and DCPD composition affected the final morphology of the material by a combination of small angle X-ray scattering (SAXS), scanning electron microscopy (SEM) and nitrogen adsorption experiments.

4.2. Results

4.2.1. Synthesis and Characterization of PNS-PLA Block Polymers.

PNS-PLA block polymers were previously synthesized by controlled radical polymerization using a PLA homopolymer functionalized with a chain transfer agent appropriate for controlled reversible addition fragmentation transfer (RAFT) polymerization.[43,44] Various PLA block polymers[48,49,50] have also been prepared through the controlled ring-opening polymerization of lactide from a hydroxyl-terminated polymer.[51] This latter approach was adopted for the formation of PNS-PLA as shown in Figure 4.2.

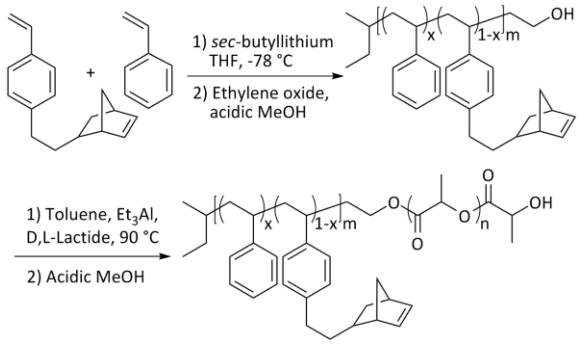

Figure 4.2. Synthetic scheme for the formation of PNS-PLA.

Living anionic copolymerization of a mixture of styrene and norbornenylethyl styrene (N) followed by the addition of ethylene oxide produced a hydroxyl functionalized PNS copolymer in 90% recovered yield. By ^{1}H NMR spectroscopy

(Figure 4.3) it was determined that 14 mol% of N units were incorporated in the PS block, and the number average molecular weight (by end group analysis) was 11 kg/mol. This number average molecular weight was in good agreement with the value (11 kg/mol) determined by size exclusion chromatography using a light scattering detector. A polydispersity index (PDI) of 1.09 for this sample is consistent with the controlled nature of the polymerizations. The molecular weight and level of N incorporation compare favorably to the theoretical values of 10 kg/mol and 15 mol% respectively. The slightly larger experimental molecular weight is attributed to potential contaminants in the N monomer that terminate some of the initiator or propagating chain ends. A comparison of the hydroxyl end groups to the sec-butyl lithium end groups indicates 89% of the chains were successfully terminated with ethylene oxide. Although the copolymerization statistics were not investigated, it is expected that the norbornenylethyl substituent would be electron donating, which would decrease the stability of N-derived carbanion relative to styrene.[52] The difference in stability of styrene (M_1^-) relative to N (M_2^-) could lead to reactivity ratios of $r_1 > 1$ and $r_2 < 1$ similar to those observed for anionic polymerizations of styrene (M_1) and *p*-methylstyrene (M_2), $r_1 = 1.3$ and $r_2 = 0.9$,[53] or styrene (M_1) and *p-t*-butylstyrene (M_2), $r_1 = 1.34$ and $r_2 = 0.86$.[54] In any case, the reactivity ratios for styrene and N are likely close to 1 and thus a near random distribution of N units in the backbone is expected.

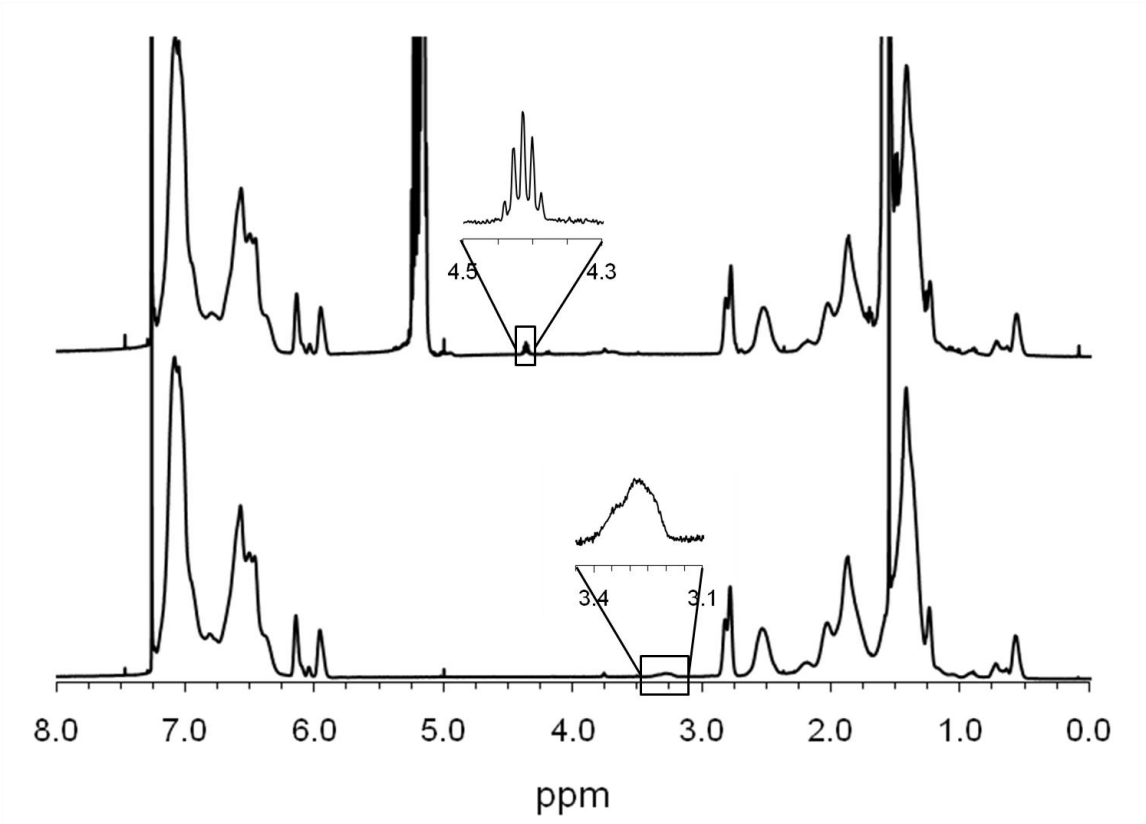

Figure 4.3. ^{1}H NMR spectra for the PNS (11) homopolymer (bottom) and the PNS-PLA (11-26) block polymer above.

d,l-Lactide was polymerized using triethyl aluminum and the above hydroxy-terminated PNS to give a series of PNS-PLA block polymers. Molar masses of the PLA blocks were determined using ^{1}H NMR spectroscopy (Figure 4.3) based on end group analysis. SEC data exhibited a clear shift to lower elution volumes (Figure 4.4) with increasing PLA molecular weight. A small amount of PNS homopolymer due to the incomplete end capping with ethylene oxide (see above) was evident in the SEC data.

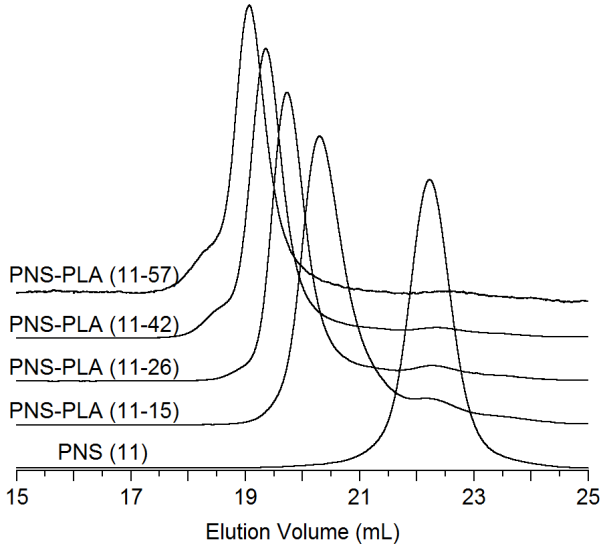

Figure 4.4. SEC chromatograms for the PNS-PLA (11-Y) series of block polymers.

Molecular characteristics of the polymers are listed in Table 4.1. All polymers are labeled PNS-PLA (X-Y) where X is the molar mass of the PNS block and Y is the molar mass of the PLA block in kg/mol. In addition to the PNS-PLA (11-Y) series a PNS-PLA (15-30) sample with only 2 mol % N in the PNS block was prepared by the same protocol.

Table 4.1. Molecular characteristics of PNS-PLA block polymers

Polymer	M_n (kg/mol) [a] PNS	x_N [b]	M_n (kg/mol) [a] PLA	PDI [c]	w_{PLA} [d]
PNS (11)	11	0.14		1.07	
PNS-PLA (11-15)	11	0.14	15	1.45	0.58
PNS-PLA (11-26)	11	0.14	26	1.54	0.70
PNS-PLA (11-42)	11	0.14	42	1.55	0.79
PNS-PLA (11-57)	11	0.14	57	1.34	0.84
PNS-PLA (15-30)	15	0.02	30	1.21	0.67

[a]Molecular weights were determined by ^{1}H NMR end group analysis. [b]Mole fraction of N in the PNS block as determined by ^{1}H NMR spectroscopy. [c]PDI determined by size exclusion chromatography based on poly(styrene) standards. [d]Weight fraction of PLA ($w_L = M_{n,\,PLA}/(M_{n,\,PNS} + M_{n,\,PLA})$).

4.2.2. Nanoporous Thermoset Formation.

Following the protocol previously reported,[43] crosslinked films were prepared from solutions containing PNS-PLA and between 0 and 83 wt % DCPD (based on the total mass of PNS-PLA + DCPD). Briefly, a 75 wt % THF solution of the PNS-PLA and DCPD were combined with a 5 mg/mL THF solution of GII (0.5 wt % GII based on the total mass of the PNS-PLA and DCPD). In all cases, gelation occurred after approximately 70 s.[55] After curing and drying overnight at room temperature, the samples were annealed at 100 °C for 1 h. The samples had contracted slightly due to the evaporation of the THF and densification. Based on their final mass after annealing, the samples contained 0–14 wt% THF. A list of the samples prepared using this general protocol is given in Table 4.2. All samples are labeled with the PNS-PLA sample code followed by DZ where Z is the DCPD wt % used to prepare the sample.

Table 4.2. Composition and characterization data for the crosslinked films

Film[a]	PLA (wt %)	mass loss[b] (wt %)	D (nm)[c] before etching	D (nm)[c] after etching	BET surface area (m^2/g)
PNS-PLA (11-15) D0	57	62	19	20	315
PNS-PLA (11-15) D17	48	54	21	21	265
PNS-PLA (11-15) D33	38	44	22	22	185
PNS-PLA (11-15) D50	29	8	23	23	3
PNS-PLA (11-15) D67	19	3	23	23	0
PNS-PLA (11-15) D83	10	21	25	[d]	0
PNS-PLA (11-26) D0	70	77	29	24	227
PNS-PLA (11-26) D17	58	66	29	28	253
PNS-PLA (11-26) D33	47	54	31	30	181
PNS-PLA (11-26) D50	35	41	36	36	94
PNS-PLA (11-26) D67	23	12	52	[d]	0
PNS-PLA (11-26) D83	12	29	[d]	[d]	0
PNS-PLA (11-42) D0	79	90	37	37	[f]
PNS-PLA (11-42) D17	66	74	[d]	[d]	167
PNS-PLA (11-42) D33	53	61	[d]	[d]	122
PNS-PLA (11-42) D50	40	49	[d]	[d]	76
PNS-PLA (11-42) D67	27	33	[d]	[d]	34
PNS-PLA (11-42) D83	13	54	[d]	[d]	3
PNS-PLA (11-57) D0	84	90	34	[d]	[f]
PNS-PLA (11-57) D17	70	76	[d]	[d]	131
PNS-PLA (11-57) D33	56	62	[d]	[d]	87
PNS-PLA (11-57) D50	42	48	[d]	[d]	67
PNS-PLA (11-57) D67	28	34	[d]	[d]	31
PNS-PLA (11-57) D83	14	25	[d]	[d]	7

[a]PNS-PLA (11-Y) DZ where Y is the molecular weight of PLA block in the block polymer (kg/mol) and Z is the DCPD wt % used to prepare the sample. All samples were prepared from a 75 wt % solution of THF and the components and were crosslinked with 0.5 wt % of GII. [b]Mass loss corresponds to the total percentage of mass loss upon etching the sample. [c]Domain spacings where determined from SAXS at room temperature using the Treubner-Strey microemulsion model. [d]A peak was not observed in the scattering pattern of these samples. [f]Surface area measurements were not performed on these samples as the samples were too mechanically weak to analyze.

The samples were then subjected to basic hydrolysis to selectively etch the PLA block (see Experimental section). The mass loss post hydrolysis was calculated as a percentage of the original mass of the cured sample (Table 4.2). The mass loss in the samples was generally comparable to the calculated PLA mass in the films based on the

initial composition. Some samples exhibited mass losses less than the initial amount of PLA indicating that some PLA domains were inaccessible to the etching solution during the 72 h etch. In samples with mass losses greater than the initial PLA wt %, we suspect that the loss of any remaining THF or unreacted DCPD in the sample as well as small PDCPD fragments not effectively integrated into the sample was the cause. The biggest discrepancy was observed in samples containing 83 wt % DCPD.

4.2.3. Material Characterization.

One-dimensional SAXS data acquired at room temperature of the crosslinked films are given in Figure 4.5. Most of the samples exhibited a single broad peak characteristic of a nanophase separated but disordered structure. After etching, the scattering intensity increased significantly for all samples consistent with formation of a nanoporous material. The shape of most scattering profiles did not change upon etching consistent with preservation of the nanostructured morphology. The scattering profile for PNS-PLA (11-15) D83 before etching exhibited a broad scattering peak while after etching a scattering peak was not discernable likely due to the disruption of the nanostructure upon etching as the sample lost considerably more mass than the initial PLA wt % leading to macropores near the bottom surface of the sample (see Figure 4.8). Scattering patterns of PNS-PLA (11-26) D83 and the PNS-PLA (11-42) and PNS-PLA (11-57) series (with the exception of the D0 samples before etching) did not exhibit a scattering maxima due to the lack of a nanophase separated structure or because the domain spacing was greater than the range of the SAXS instrument (see below).

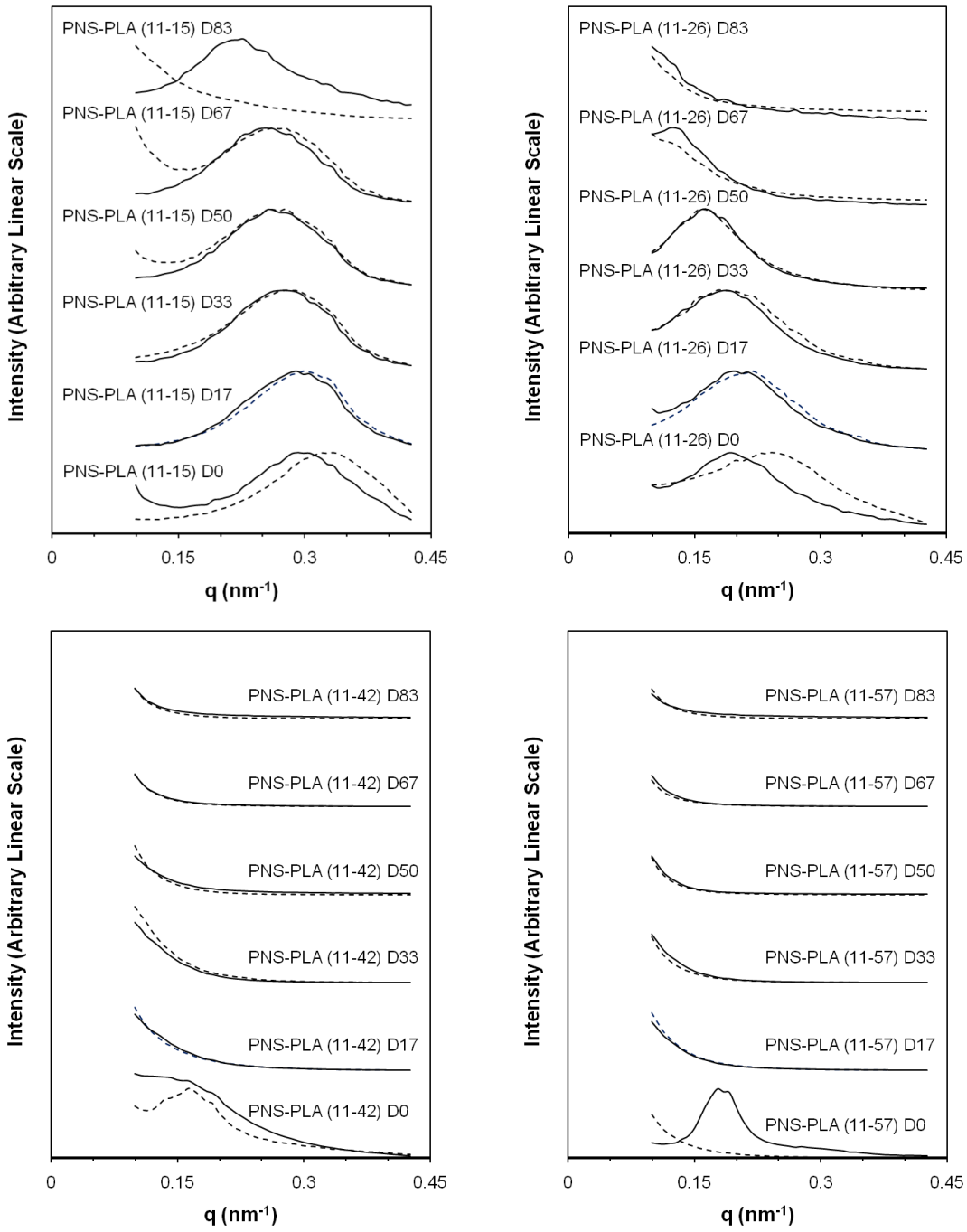

Figure 4.5. One-dimensional SAXS profiles for the PNS-PLA (11-15) (top left), PNS-PLA (11-26) (top right), PNS-PLA (11-42) (bottom left), and PNS-PLA (11-57) (bottom right) series of films acquired at room temperature. The solid and dashed lines are the scattering patterns before and after etching, respectively. Each set of scattering profiles were normalized and shifted vertically for clarity.

The scattering that contained well-defined SAXS peaks were modeled using the Teubner-Strey microemulsion model.[56] Although this model was developed to describe the scattering of microemulsions, fitting the scattering patterns with the model should allow extraction of useful parameters for describing their structure given the bicontinuous structures observed by SEM (see below). The scattering patterns were first fit using equation 3.1.[56]

$$I(q) \sim \frac{1}{a_2 + c_1 q^2 + c_2 q^4} \tag{3.1}$$

In equation 1 *I(q)* is the intensity of the scattering, q the principle scattering vector, and a_2, c_1 and c_2 are fitting constants. The principal domain spacing (D) can be extracted from the fitting constants using equation 3.2.[56]

$$D = 2\pi \left[\frac{1}{2} \left(\frac{a_2}{c_2} \right)^{1/2} - \frac{1}{4} \frac{c_1}{c_2} \right]^{-1/2} \tag{3.2}$$

In the PNS-PLA (11-15) and PNS-PLA (11-26) samples, D increased with increasing fraction of DCPD in the samples (Figure 4.6). This is consistent with trends observed in other nanostructured thermosets formed via RIPS. [14,15,17]

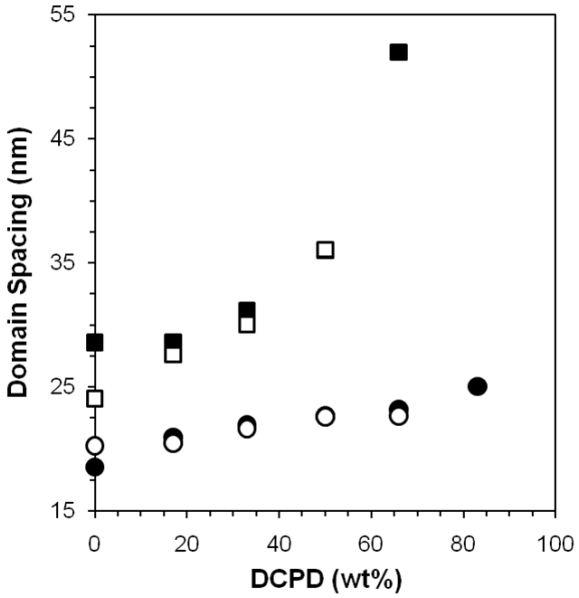

Figure 4.6. Domain spacing by SAXS analysis of the PNS-PLA (11-15) (circles) and PNS-PLA (11-26) (squares) series of films both before (filled) and after (open) etching as a function of DCPD wt %.

In addition to the domain spacing, the correlation length (ξ) of the samples can be calculated from the fitting parameters using equation 3.3.[56]

$$\xi = \left[\frac{1}{2}\left(\frac{a_2}{c_2}\right)^{1/2} + \frac{1}{4}\frac{c_1}{c_2}\right]^{-1/2} \tag{3.3}$$

The correlation length is a measure of the short range order among domains,[57] and the ratio of the correlation length to the domain spacing provides an indication of the domain size polydispersity.[58] The smaller the ratio the larger the domain size polydispersity. A final parameter that can be extracted is the amphiphilicity factor (f_a) (equation 3.4).[59,60,61]

$$f_a = \frac{c_1}{\sqrt{4a_2c_2}} \tag{3.4}$$

The amphiphilicity factor describes the quality of a microemulsion. A microemulsion typically does not result if $f_a < -1$. If $-1 < f_a < 0$, a "good" microemulsion with a well defined structure forms, while if $0 < f_a < 1$, poor micremulsions form. Finally, if $f_a > 1$, then the sample is unstructured.[61] Although the crosslinked films are not microemulsions, the amphiphilicity factor provides a qualitative idea for how strongly structured the films are. Table 4.3 provides the correlation length, ratio of correlation length to domain size, and the amphiphilicity factor for the modeled samples.

Table 4.3. Parameters from Teubner-Strey model fits

Film[a]	Correlation length, ξ (nm) BE, AE	ξ/D BE, AE	Amphiphilicity factor (f_a)
PNS-PLA (11-15) D0	14, 13	0.75, 0.67	−0.91, −0.89
PNS-PLA (11-15) D17	17, 17	0.79, 0.81	−0.92, −0.93
PNS-PLA (11-15) D33	16, 15	0.74, 0.69	−0.91, −0.90
PNS-PLA (11-15) D50	16, 15	0.69, 0.64	−0.90, −0.88
PNS-PLA (11-15) D67	15, 13	0.65, 0.56	−0.89, −0.85
PNS-PLA (11-15) D83	11, -	0.43, -	−0.76, -
PNS-PLA (11-26) D0	11, 10	0.37, 0.41	−0.69, −0.73
PNS-PLA (11-26) D17	14, 14	0.47, 0.49	−0.80, −0.81
PNS-PLA (11-26) D33	14, 13	0.44, 0.43	−0.77, −0.75
PNS-PLA (11-26) D50	16, 15	0.45, 0.43	−0.78, −0.76

The amphiphilicity factor for all samples had values between −1 and −0.65, which is within the region for "good" microemulsions, and thus the samples would be strongly structured. The ratio of the correlation length to the domain spacing was variable among the samples. The ratio for the PNS-PLA (11-15) samples decreased with increasing

DCPD composition suggesting an increase in the domain size polydispersity. The ratio was less variable for the PNS-PLA (11-26) samples but was considerably smaller than the PNS-PLA (11-15) samples indicating the domain size polydispersity of the PNS-PLA (11-26) samples was larger.

SEM micrographs of cryo-fractured surfaces of the samples coated with 1.5 nm of platinum (Figure 4.7) revealed that most of the etched films have a nanoporous bicontinuous morphology including the PNS-PLA (11-42) and PNS-PLA (11-57) containing samples that did not exhibit a peak in the SAXS data. Domain spacings for these samples based on the SEM micrographs were > 65 nm, and such large domain spacings would be difficult to discern given the range of the SAXS instrument. The micrographs also reveal that increasing PLA block size at fixed DCPD composition leads to increasing pore size (consistent with the SAXS data), while increasing the DCPD composition at fixed PLA block size leads to a coarsening of the structure. Additionally, unlike the other samples, the PNS-PLA (11-15) D50, PNS-PLA (11-15) D67, and PNS-PLA (11-26) D67 samples exhibited largely nonporous morphologies, which is consistent with the inability to etch all of the PLA based on the mass loss data (Table 4.2).

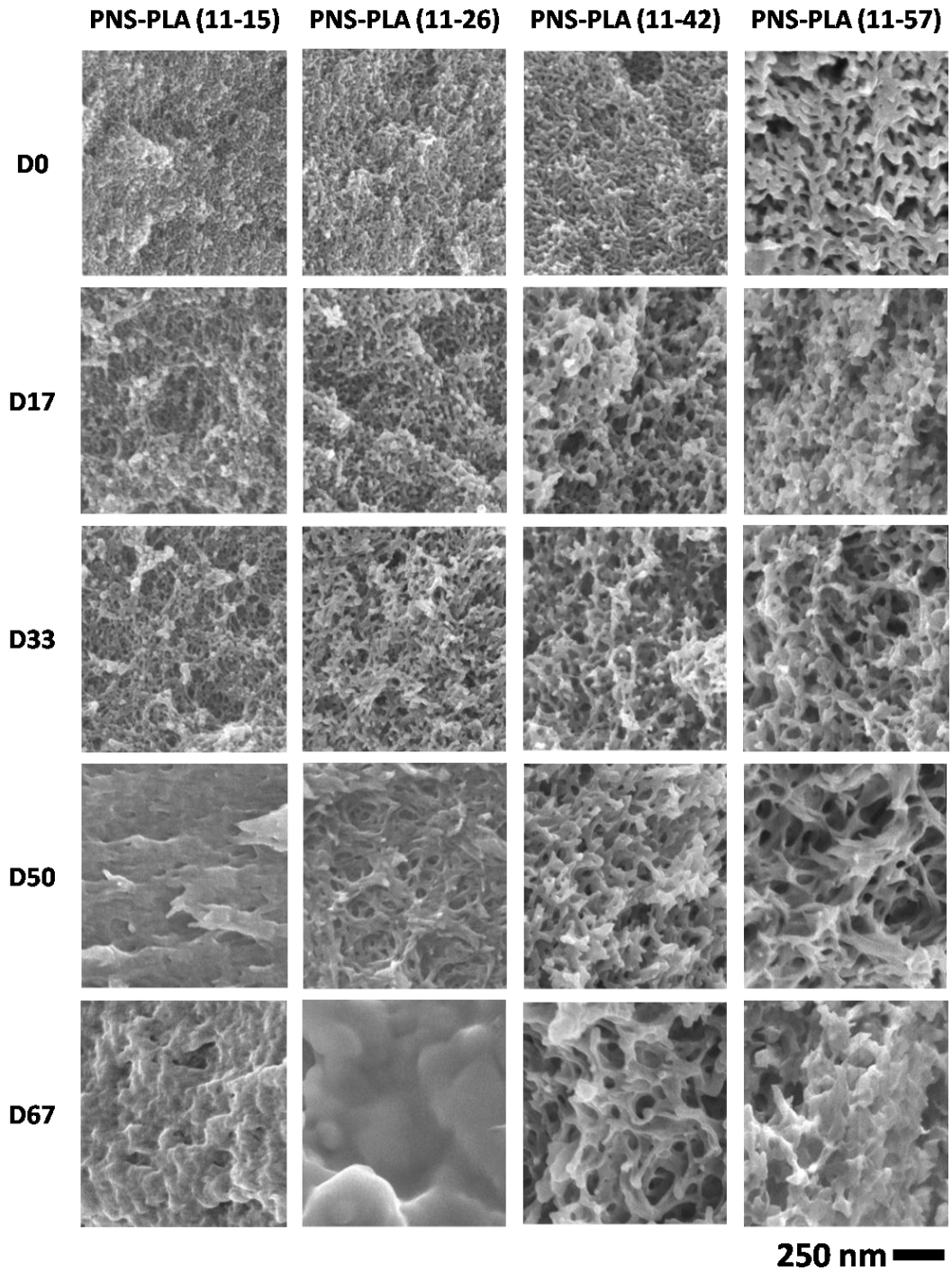

Figure 4.7. Scanning electron micrographs of fractured surfaces of etched films. All samples were cryo-fractured and coated with 1.5 nm of platinum prior to imaging to prevent charging.

The morphology of the PNS-PLA (11-Y) D83 films could not be adequately characterized by a single micrograph. Figures 4.8–4.11 show the cross-sections of the PNS-PLA (11-Y) D83 samples. Region A in each sample was close to the surface of the film exposed to air during crosslinking and was mostly nonporous. Region B in the middle of the film typically contained both porous and nonporous areas. Region C depicts the section of the film in contact with the glass vial used to prepare the sample. This section of the film is quite similar to the bicontinuous morphology observed for the other samples except it has larger pores and a broader pore size distribution. These data indicate that in samples with a large DCPD content, the formation of composite materials is more complicated that in the samples with less DCPD.

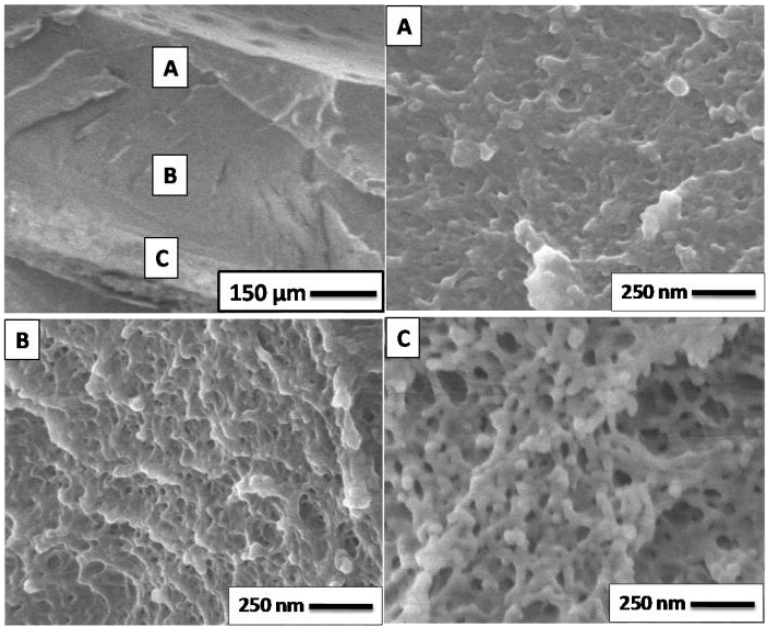

Figure 4.8. Scanning electron micrographs of a fractured surface of the PNS-PLA (11-15) D83 film. Cross section of the entire film (top left), with the three regions highlighted corresponding to the other three micrographs (A, B, and C) shown.

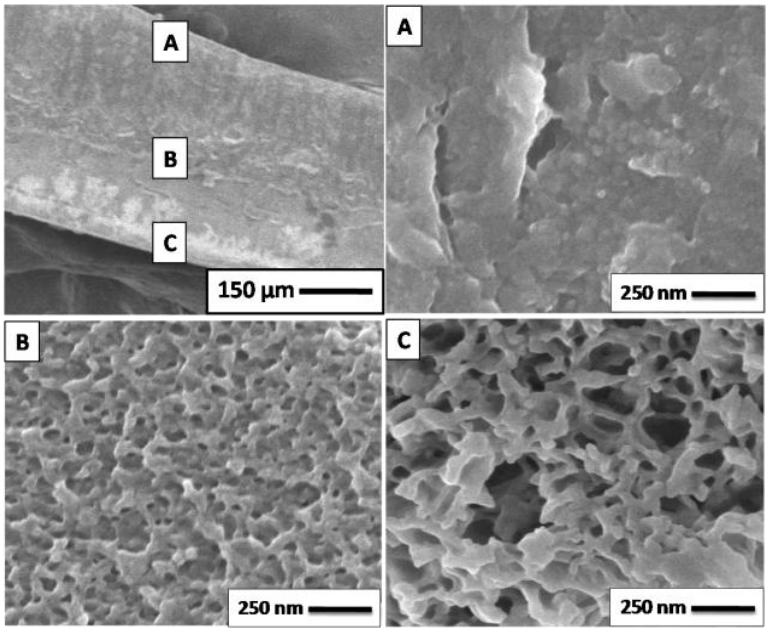

Figure 4.9. Scanning electron micrographs of a fractured surface of the PNS-PLA (11-26) D83 film. Cross section of the entire film (top left), with the three regions highlighted corresponding to the other three micrographs (A, B, and C) shown.

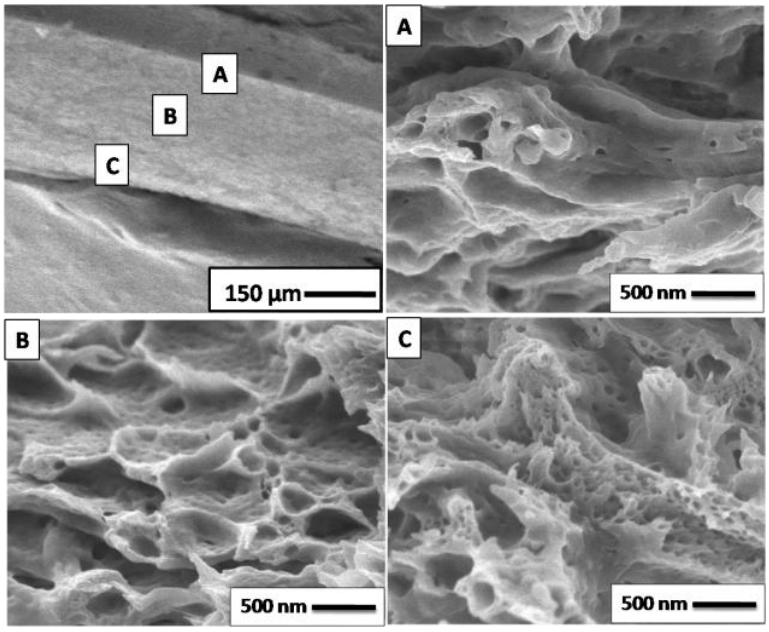

Figure 4.10. Scanning electron micrographs of a fractured surface of the PNS-PLA (11-42) D83 film. Cross section of the entire film (top left), with the three regions highlighted corresponding to the other three micrographs (A, B, and C) shown.

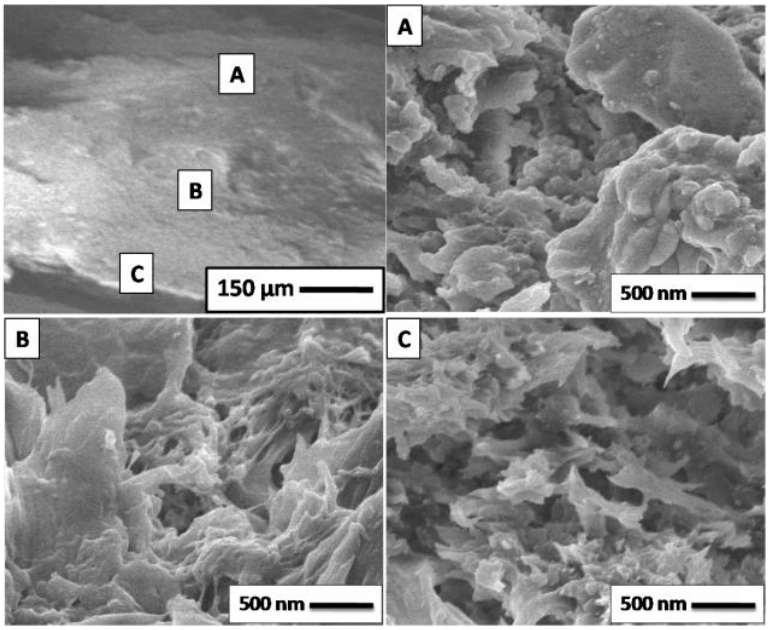

Figure 4.11. Scanning electron micrographs of a fractured surface of the PNS-PLA (11-57) D83 film. Cross section of the entire film (top left), with the three regions highlighted corresponding to the other three micrographs (A, B, and C) shown.

Nitrogen adsorption analysis of the etched samples resulted in isotherms similar to Type IV isotherms typical of mesoporous materials.[62] Surface areas were calculated using the Brunauer-Emmett-Teller (BET) multipoint method[63] (Table 4.2). Pore size distributions were determined using the Barrett-Joyner-Halenda (BJH) approach[64] and are shown for the D33 samples and the PNS-PLA (11-15) containing series in Figure 4.12.

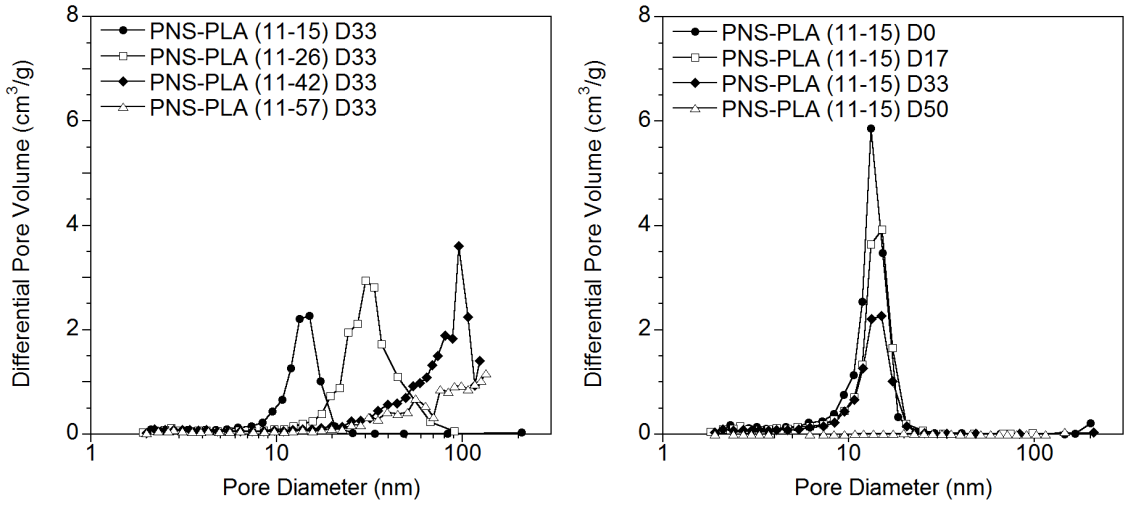

Figure 4.12. BJH Pore size distributions for the D33 series of films (left) and PNS-PLA (11-15) series of films (right). The differential pore volume is defined as the d(incremental pore volume)/d(log pore diameter).

The D33 series of films shows that as the PLA block size increases the pore size distribution shifts to larger diameters, which corroborates trends in both the SAXS and SEM data. Additionally, the BET surface areas decrease from 185 m^2/g to 87 m^2/g (Table 2) upon increasing the PLA molar masses from 15 to 57 kg/mol. Pore sizes for the PNS-PLA (11-15) samples are essentially constant with increasing weight percent of DCPD (up to 33 wt % DCPD). While the single PLA block size led to relatively consistent pore sizes, the BET surface area of these films decreases with increasing DCPD concentration from 315 m^2/g to 185 m^2/g for DCPD concentrations ranging from 0 to 33 wt %. Given the consistent pore size distribution in these samples, the surface area of the films decreases linearly with decreases in the volume fraction of PLA in the composite, as expected for a fixed pore size. At higher DCPD compositions, the PNS-PLA (11-15) samples had very little or immeasurable surface areas, consistent with the SEM micrographs of the D50 and D67 samples.

The trend of a decreasing surface area observed for the PNS-PLA (11-15) samples was also observed for the other block polymer samples at higher DCPD compositions. A surface area was determined for the PNS-PLA (11-26) D50 sample; however surface areas for the D67 and D83 surface areas were not measurable. Surface areas for the PNS-PLA (11-42) and PNS-PLA (11-57) samples decreased linearly with decreases in PLA volume fraction at all DCPD compositions.

4.3. Discussion

The results section demonstrated that the metathesis crosslinking of a THF solution of DCPD in the presence of a PNS-PLA block polymer can yield a nanostructured PDCPD/block polymer composite sample, and the PLA in these samples can be etched to generate nanoporous materials. Pore sizes could be tailored by adjusting the size of the PLA block, and the porosity was controlled by varying the DCPD content in the composites. The balance of this chapter discusses the mechanism of structure formation in these composites. That is, how does a homogeneous solution containing DCPD, PNS-PLA and THF give the observed structures upon addition of a metathesis catalyst?

4.3.1. Mechanism Investigation.

The structures formed using the above approach are kinetically trapped, and thus the influence of gelation time on the final structure was examined in a series of PNS-PLA (11-15) D33 films crosslinked with 5, 0.5 and 0.05 wt % GII. The films gelled almost

instantly (5%), at 70 s (0.5%) and at 13 min (0.05%). SAXS patterns exhibited a single broad scattering peak for all three samples with average domain spacings of 23, 21 and 21 nm for the 5%, 0.5% and 0.05% films respectively. SEM images of etched films revealed bicontinuous structures (Figure 4.13) in all cases. The small changes in domain spacing and lack of variation among the SEM micrographs suggest that the timing of gelation does not significantly impact resultant structures. Thus coarsening of the structure during the RIPS process does not seem to be occurring to a significant extent. An alternative conclusion is that the structure forms via a self-assembly first mechanism. However, as previously reported in reference 32, dynamic light scattering (DLS) analysis of a THF solution of PNS-PLA and DCPD prior to catalyst addition did not indicate any aggregation of the block copolymer chains (i.e., micelle formation) suggesting that the chains were simply dissolved in the solvent mixture prior to crosslinking. From a practical view, using less catalyst to obtain the same structure is desirable. Although the impact of the mechanical properties was not investigated, a decrease in the catalyst concentration could lead to a decrease in the crosslinking density possibly leading to weaker materials.

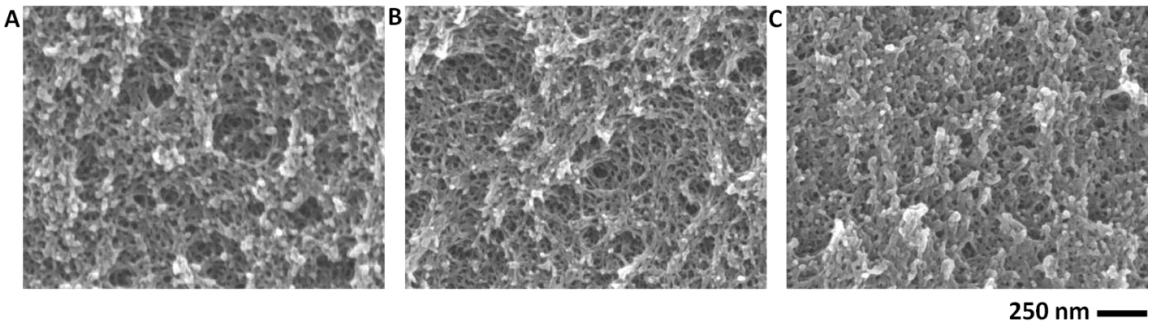

Figure 4.13. Scanning electron micrographs of fractured surfaces of etched PNS-PLA (11-15) D33 films crosslinked with (A) 5, (B) 0.5 and (C) 0.05 wt % of GII.

To track the structure development upon crosslinking the evolution of the SAXS data as a function of crosslinking time was explored. In initial SAXS experiments, structure development was monitored well into the crosslinking and a shift of the principal scattering peak to lower values of q (larger domain spacings) was observed. At longer crosslinking times, electron density contrast was lost and no further information could be gathered. To overcome this limitation, a PNS-PLA (11-15) D33 solution was prepared in benzene and divided among five ampoules. To four ampoules 0.25 wt % of GII was added, and the samples were crosslinked for 10 s, 1 min, 8 min, and 1 h. After the designated times, further structure development was arrested by immersion in a liquid nitrogen bath, and the benzene was removed by sublimation (i.e., freeze dried). In this way, the partially cured samples can be interrogated to get a sense of how and when the nanostructure is formed. In addition to the freeze dried samples, the mixture in the fifth ampoule was crosslinked by the normal solvent evaporation protocol over (24 h) using 0.25 wt % GII. SAXS patterns for all the dried samples are shown in Figure 4.14.

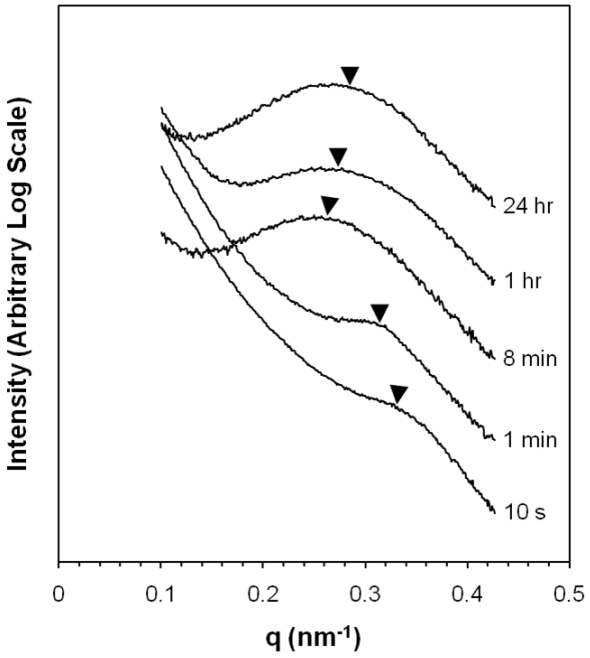

Figure 4.14. One-dimensional SAXS profiles for PNS-PLA (11-15) D33 samples freeze dried after 10 s, 1 min, 8 min, and 1 h, of crosslinking. The 24 h sample was not freeze dried as the solvent had already evaporated. The arrow denotes the peak maximum.

The SAXS patterns show the emergence of a scattering peak at 10 s, which first shifts to low q and then back to high q. These general shifts in the scattering profile qualitatively match changes observed during our original in-situ SAXS experiments. The initial peak observed at 10 s corresponds to a domain spacing of 19 nm and indicates that the sample is already phase separated due to the increasing molecular weight of the crosslinking components. At 1 and 8 min the domain spacings were 20 and 24 nm, respectively. The domain spacing increased as the material further organized until gelation was reached at about 90 seconds. Upon gelation, the material is a swollen network, and the domain spacing decreases to 23 nm as swelling within the material reduces due to concomitant evaporation of solvent. Finally, after 24 h the all the solvent

has evaporated and the scattering vector shifts to slightly higher values resulting in a domain spacing of 22 nm. Figure 4.15 schematically depicts what occurs during crosslinking of the samples.

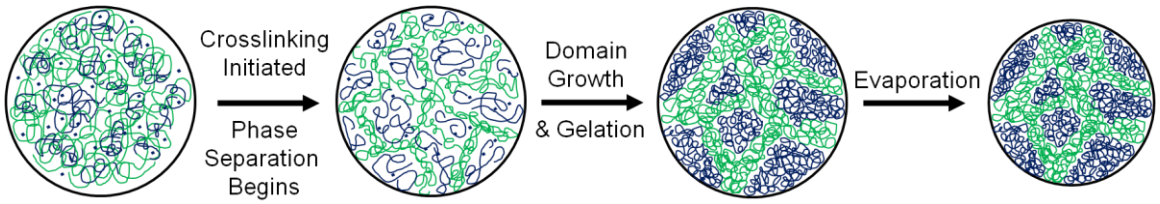

Figure 4.15. Scheme of morphological development during crosslinking.

The change in domain spacing upon solvent evaporation was corroborated by first swelling a crosslinked and dried PNS-PLA (11-26) D50 sample in THF. The swollen sample was then analyzed by SAXS every 10 min over a 40 min span while the THF evaporated. At the beginning of the drying experiment, the sample did not have an observable scattering peak likely due to a lack of electron density contrast, but a broad peak was observed after 10 min of drying at RT that shifted to higher q values at longer times. The unswollen sample originally had a domain spacing of 34 nm which after swelling shifted to 39 nm at 10 min, 38 at 20 min, 37 at 30 min and 36 at 40 min. Qualitatively, the shift in domain spacing observed for the crosslinked swollen sample is in good agreement with the decrease in domain spacing after gelation in the freeze dried samples supporting the conclusion that the change in domain spacings are due to evaporation of the solvent.

4.3.2. Morphological Control.

The SEM micrographs in Figure 4.7 revealed that most samples exhibited bicontinuous nanoporous morphologies, while a few were nonporous. Specifically, films PNS-PLA (11-15) D50, PNS-PLA (11-15) D67 and PNS-PLA (11-26) D67 were largely nonporous indicating possible encapsulation of PLA within the matrix, which was corroborated by the mass loss data for those samples (Table 4.2). These samples illustrate that there is an upper limit to the level of DCPD incorporation in PNS-PLA (11-15) and PNS-PLA (11-26) samples required to access a bicontinuous structure. On the other hand, films templated with PNS-PLA block polymers containing larger PLA blocks retained bicontinuous structures at higher DCPD fractions. For example, in the case of the PNS-PLA (11-42) and PNS-PLA (11-57) templated membranes, bicontinuous structures were observed using up to 67 wt% DCPD.

We examined the effect of PLA block length (composition) on the nature of the reactive solution prior to crosslinking. Previous DLS results suggested that prior to crosslinking the PNS-PLA chains were simply dissolved in the mixture of THF and DCPD.[43] To complement that study, we examined the extent of overlap of the PNS-PLA block polymers in solution as this could influence the final morphology. The overlap concentration (c^*) for the polymer chains can be estimated by Equation (3.5).[65]

$$c^* = \frac{3M}{N_{av} 4\pi {R_g}^3} \tag{3.5}$$

where M is the molecular weight of the block polymer; N_{av} is Avogadro's number, and R_g is the radius of gyration. The radius of gyration was estimated based on the hydrodynamic radius (R_h) measured for the free chains in THF using DLS (see supporting information) and the relationship in Equation (3.6).[66]

$$R_g = \frac{R_h}{0.66} \tag{3.6}$$

Table 4.4 contains the calculated c* for the block polymers in mg/mL and an extent of overlap c/c* for each sample. The transition between non-bicontinuous and bicontinuous structures was within c/c* ranges of 1.8–2.5 for PNS-PLA (11-15), 1.5–2.2 for PNS-PLA (11-26), 1.0–2.0 for PNS-PLA (11-42), and 1.1–2.3 for PNS-PLA (11-57) solutions. From these data, it appears that the critical concentration (i.e., extent of overlap) to achieve a bicontinuous structure is around 2c*.

Table 4.4. Estimated overlap concentration (c*) for the PNS-PLA block polymers and the ratio of c/c* for each of the DCPD solutions prior to crosslinking. Final crosslinked samples that were determined to be bicontinuous are in italics and samples that were non-bicontinuous are in bold.

	PNS-PLA (11-15)	PNS-PLA (11-26)	PNS-PLA (11-42)	PNS-PLA (11-57)
c*[a]	82	68	51	44
c/c* D0	*3.7*	*4.4*	*5.9*	*6.8*
c/c* D17	*3.1*	*3.7*	*4.9*	*5.7*
c/c* D33	*2.5*	*2.9*	*3.9*	*4.5*
c/c* D50	**1.8**	2.2	*3.0*	*3.4*
c/c* D67	**1.2**	**1.5**	*2.0*	*2.3*
c/c* D83	**0.6**	**0.7**	**1.0**	**1.1**

[a] Calculated overlap concentration for the block polymer in mg/mL based on DLS results (see supporting information).

The apparent relation between the morphology and the extent of block polymer overlap sheds light on the structure formation mechanism. Initially, the crosslinking solution contains solvent (i.e., THF), DCPD and PNS-PLA. After adding the catalyst the PNS block and DCPD crosslink, and their increasing molecular weight increases the free energy of mixing with the PLA until the PLA block phase separates from the developing PNS/PDCPD matrix. If the block polymer was well overlapped, a bicontinuous structure forms to best minimize interfacial tension with the matrix material. That is, isolated domains of PLA would have a higher interfacial area with the PNS/PDCPD matrix than a percolating 3-D structure at the same volume fraction.[67] At lower block polymer concentrations the PLA chains are more easily encapsulated and form isolated domains in the developing PNS/PDCPD matrix.

To examine the morphological dependence on the extent of overlap, two PNS-PLA (11-26) D33 samples were crosslinked at 85 and 92 wt % THF instead of the 75 wt % used in all of the above experiments. Dilution of the crosslinking solution caused a delay in gelation from 70 s at 75 wt % to 3 min at 85 wt % while the 92 wt % sample did not form a gel but ultimately solidified as a coating on the sample vial after 16 h. SEM micrographs of freeze-fractured surfaces of etched films are shown in Figure 4.16. The 85 wt % sample appears to have a bicontinuous structure, but the structure is more open than the 75 wt % sample. The 92 wt % sample has some bicontinuous areas, but the structure is more collapsed and less uniform than the other two samples.

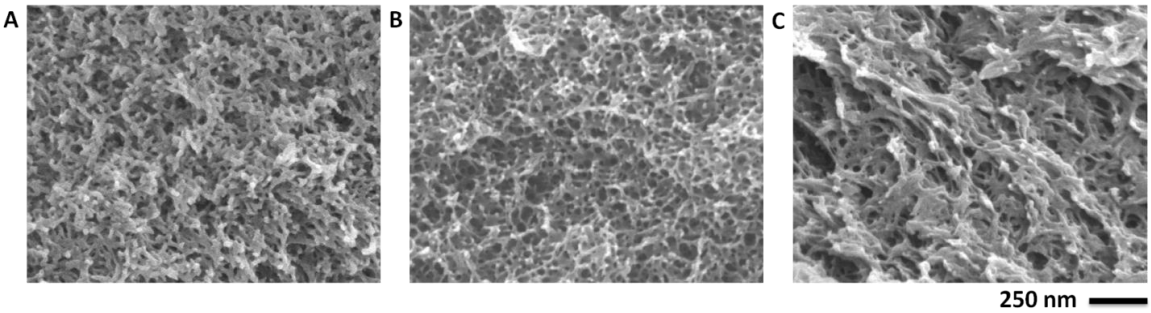

Figure 4.16. Scanning electron micrographs of fractured surfaces of PNS-PLA (11-26) D33 samples cast at (A) 75, (B) 85, and (C) 92 wt % THF.

The c/c* ratio was 2.9, 1.5 and 0.7 for the 75, 85 and 92 wt % samples, respectively. The formation of a bicontinuous structure at a c/c* of 1.5 for the 85 wt% sample is just at the edge of the transition range for the PNS-PLA (11-26) samples (1.5–2.2) as determined above. The c/c* ratio for the 92 wt % sample was 0.7, which is below the range of the bicontinuous structures observed for the PNS-PLA (11-26) samples, and the formation of a more collapsed structure with non-bicontinuous areas is consistent with consistent with the morphological dependence on the extent of overlap.

The above analysis allows for structure predictions based on the block polymer molecular weight and composition of the solution prior to crosslinking. Figure 4.17 shows a phase diagram for the films formed in this study. It also illustrates compositions of the smaller overlapping c/c* range (1.8–2.0) for the four block polymers at a THF composition of 75 wt% (grey areas). Compositions to the upper left of these regions would be more overlapped and likely result in a bicontinuous morphology, while compositions to the lower right would be less overlapped and likely result in encapsulated PLA domains and non-bicontinuous samples.

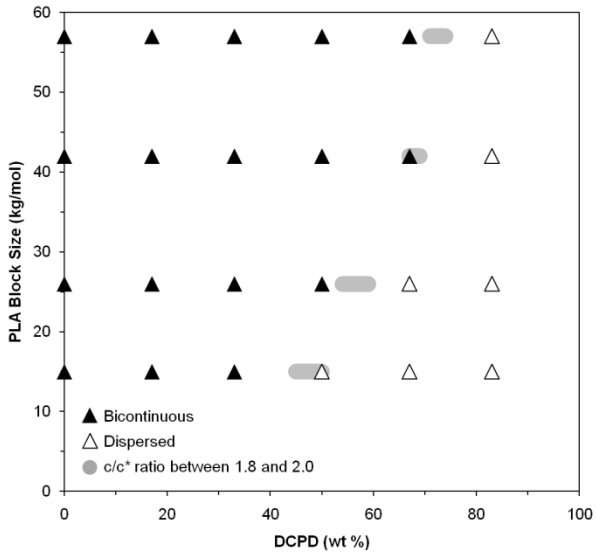

Figure 4.17. Phase diagram of the films formed in this study where the filled triangles represent bicontinuous structures and the empty triangles represent structures with isolated PLA domains (i.e., non-bicontinuous). The grey areas depict compositions with c/c* ratios between 1.8 and 2.0 for the block polymers assuming a THF composition of 75 wt %.

4.4. Conclusions

In this chapter the templating of nanostructures within a DCPD thermoset by a metathesis reactive block polymer, PNS-PLA was explored. Nanophase separated morphologies from homogenous solutions of the components formed via a RIPS mechanism. Mechanistic investigations revealed that crosslinking the PNS block into the thermoset matrix was vital to limiting macrophase separation, and that the morphologies were unaffected by altering the catalyst concentration. Examining a wide range of compositions with multiple PLA block lengths revealed that the pore size and surface area of the materials can be tailored by changing the PLA block size and DCPD composition, respectively. Additionally, a transition from a bicontinuous morphology to

an encapsulated morphology was observed in the samples. The morphology formed was found to depend on the concentration of block polymer relative to the overlap concentration, allowing for morphological control and possibly predictions based on the block polymer size and crosslinking solution composition.

4.5. Experimental

4.5.1. Materials.

Unless specifically noted, all chemicals were used as received from Aldrich. Styrene was first passed through a basic alumina column and then distilled over calcium hydride under reduced pressure. Ethylene oxide was distilled over butyl magnesium chloride under reduced pressure. 4-chloromethylstyrene was passed through a basic alumina column. D,L-lactide (99%) purchased from Purac was recrystallized twice from ethyl acetate and stored under N_2 atmosphere. GII was a gift from Materia and was used as received. Degassed THF was purified by passage over an activated alumina column, while degassed toluene was purified by passage over an activated alumina column and supported copper catalyst column to remove protic impurities and oxygen prior to use.

4.5.2. Characterization.

^{1}H NMR spectroscopy was performed on a Varian Inova 500 instrument operating at 500 MHz. Solutions were prepared in $CDCl_3$ (Cambridge Isotope Laboratories) at approximately 10 mg/mL. All spectra were obtained at 20 °C after 64

transients using a relaxation delay of 5 s with chemical shifts reported as δ (ppm) relative to the ^{1}H signals from hydrogenous solvent (7.27 ppm for $CHCl_3$).

SEC was used to evaluate the molecular weight evolution and polydispersity indicies of all the samples. Samples were prepared at concentrations near 1 mg/mL in $CHCl_3$ or THF depending on the instrument used. The first SEC instrument operates at 35 °C with $CHCl_3$ as the mobile phase through three PLgel 5μm Mixed-C columns in series with molecular weight range 400–400000 g mol^{-1}. The columns are housed in a Hewlett-Packard (Agilent Technologies) 1100 series liquid chromatograph equipped with a Hewlett-Packard 1047A refractive index detector. PDIs are reported with respect to polystyrene standards obtained from Polymer Laboratories. A second SEC instrument is a Waters 150 CALC/GPC instrument using three Phenomenex Phenogel columns of 103, 104 and 105 Å porosities coupled with a Wyatt OPTILAB refractive index detector and a Wyatt DAWN multiangle light-scattering detector. This instrument operates at 40 °C with THF as the mobile phase and a flow rate of 1 mL/min.

SAXS profiles were recorded on a custom-built beam line at the University of Minnesota. CuKα X-rays (λ=1.542 Å) were generated through a Rigaku RU-200BVH rotating anode fitted with a 0.2 x 2 mm^2 microfocus cathode and Franks mirror optics. Two-dimensional (2-D) diffraction patters were recorded for 300 s using a Siemens area detector and corrected for detector response before analysis. 2-D images were azimuthally integrated to a 1-D plot of intensity versus *q*.

SEM images were obtained on a Hitachi S-900 FE-SEM instrument using a 3.0 kV accelerating voltage. Prior to SEM analysis, cryo fractured monoliths were coated with a 1.5 nm thick platinum layer via direct platinum sputtering using a VCR Ion Beam Sputter Coater. Nitrogen adsorption experiments were carried out on a Micromeritics ASAP 2000 V3.00 sorption analyzer, and samples were prepared by degassing under high vacuum at 60 °C for at least 6 hours.

Samples were prepared for DLS by dissolving each block polymer at 2 wt% in THF. The block polymer solutions were then filtered through 0.45 μm microfilters (Millipore) into dust free 0.25 in. diameter glass tubes. Samples were immersed in a temperature-controlled silicon oil bath inside a home built goniometer, and DLS measurements were performed using a Lexel model 75 Ar+ ion laser with a 488 nm operating wavelength. A Brookhaven BI-DS photomultiplier was used to detect the scattered light intensity and the resulting signal was processed using a BI-9000AT digital correlator. The intensity autocorrelation function was measured over an hour for each polymer at 25 °C and angles of 60, 90 and 120 degrees. The measured intensity autocorrelation functions, $g_2(t)$, at each angle for each polymer are converted to the electric field correlation function, $g_1(t)$ via the Siegert relation:

$$g_2(t) = 1 + |g_1(t)|^2 \tag{3.5}$$

The electric field correlation function was the plotted versus time, and the data was fit using the single exponential:

$$g_1(t) = Aexp(-\Gamma \cdot t) \tag{3.6}$$

cumulant, which accounts for the effects of polydispersity:

$$g_1(t) = Aexp(\Gamma \cdot t)(1 + \frac{\mu_2}{2!}t^2 - \frac{\mu_3}{3!}t^3 + \cdots) \tag{3.7}$$

and double exponential, which considers the presence of two dominant sized solutes:

$$g_1(t) = A_1 exp(-\Gamma_1 \cdot t) + A_2 exp(-\Gamma_2 \cdot t) \tag{3.8}$$

where Γ is the mean decay rate. The best fit for each correlation function was determined by examining the residual difference between the measured data and the calculated fits.

The mean diffusion coefficient (D) was extracted from a linear fit of the mean decay rate versus the square of the scattering vector, and the hydrodynamic radius (R_h) was obtained using the Stokes-Einstein relation:

$$R_h = \frac{k_B T}{6\pi\eta_s D} \tag{3.9}$$

where k_B is the Boltzman constant; T is the temperature, and η_s is the solvent viscosity.

In addition to the fitting analysis, REPES was used to evaluate the distribution of relaxation times and ultimately distribution of the sizes using inverse Laplace transformations of the electric field correlation functions for measurements at 60 and 90 degrees.

4.5.3. Synthesis.

Synthesis of Hydroxyl-terminated Poly(norbornenylethyl styrene-s-styrene) (PNS-OH). PNS-OH was prepared in an approach adapted from a previously reported method for the synthesis of hydroxyl-terminated polystyrene.[50] A 1-L round bottom flask adapted with five threaded glass connectors was heated at 250 °C overnight under vacuum. Then a glass stir bar and p-norbornenylethyl styrene (2.02 g, 9.02 mmol), prepared via previously reported methods,[43,44] were added under a positive pressure of argon. Next a buret of purified styrene (4.79 g, 46.1 mmol), a buret of purified ethylene oxide (5.40 g, 123 mmol), and a flask of 0.3 L of purified THF were connected to the reaction flask via threaded glass connectors. Five pump purge cycles with argon were performed on the reaction flask before it was pressurized with argon. THF was added to the reaction flask, which was submerged in an isopropyl alcohol/dry ice bath. The styrene was then added to the reaction flask, followed by the addition of *sec*-butyllithium (0.70 mL, 0.49 mmol). The polymerization was allowed to proceed for 30 min, and then the ethylene oxide was added. The solution was slowly warmed to room temperature over an hour, and allowed to stir overnight. The alkoxy chain end was terminated by the addition of 3 mL of a 1 M hydrochloric acid solution in methanol that had been degassed by bubbling with argon for 15 minutes and allowed to stir for 1 hour before being precipitated methanol. The precipitate was recovered by vacuum filtration and then reprecipitated in methanol from THF. The precipitate was again recovered via vacuum filtration before being dried under vacuum for 48 h. 6.193 g of a white powder was recovered for a yield of 90.1%. Number average molecular weight of the polymer was 11 kg/mol with a 14% mole fraction of

norbornenylethyl styrene as determined by ^{1}H NMR end group analysis. SEC analysis determined a PDI of 1.09.

^{1}H NMR ($CDCl_3$): δ 6.30–7.20 (b, Ar**H**), 5.90–6.20 (b, –C**H**=C**H**–), 3.27 (b, –C**H$_2$**–OH), 2.78–2.81 (–C**H**–CH_2=CH_2–C**H**–), 2.53 (b, Ar-C**H$_2$**–), 2.02 (b, –C**H**–CH_2–CH_2–Ar), 1.86 (b, –CH–C**H$_2$(exo)** –CH–), 1.41 (b, –CH–C**H$_2$**–CH– and –C**H$_2$**–CH_2–Ar), 1.23 (b, –CH–C**H$_2$**–CH), 0.9 (b, –C**H$_2$**– of initiator), 0.7 (b, –C**H$_3$** of initiator), 0.56 (b, CH–CH_2**(endo)**=CH).

Synthesis of Poly(norbornenylethyl styrene-s-styrene)-b-Poly(lactide) (PNS-PLA)

All PNS-PLA block copolymers were synthesized following the same general procedure based on the ROP of lactide using a triethyl aluminum PNS-OH macroinitiator. An example synthesis is described for PNS-PLA (11-15). 2.00 g (0.154 mmol) of PNS (11) and a Teflon stir-bar were added to a 48 mL round bottom pressure vessel capped with a Teflon screw-cap. The pressure vessel was placed in a glove-box under a nitrogen atmosphere and 25 mL of toluene and 75 µL (0.75 mmol) of a 1 M triethyl aluminum solution in heptanes was added via a graduated cylinder and a syringe respectively. The pressure vessel was capped and stirred for 16 h, and then 3.331 g (23.1 mmol) of D,L-lactide was added. The pressure vessel was capped and removed from the glove box, and heated at 105 °C for 5 h. The polymerization was terminated by the addition of 2 mL of a 2 M hydrochloric acid solution in methanol, and the polymerization solution was then precipitated in methanol. The precipitate was recovered via vacuum filtration, and reprecipitated in methanol from THF. The precipitate was once again recovered via

vacuum filtration and dried under vacuum for 48 hours. 4.740 g of a white solid was recovered for a yield of 89.0%. Number average molecular weight of the polymer was 15 kg/mol as determined by ^{1}H NMR end group analysis, while the PDI was 1.45 as determined by SEC.

^{1}H NMR ($CDCl_3$): δ 6.30–7.20 (b, Ar**H**), 5.90–6.20 (b, –C**H**=C**H**–), 5.13-5.24 (m, –C(O)–C**H**(CH_3)–O–), 4.36 (m, –C(O)–C**H**(CH_3)–O– end group), 2.78–2.81 (–C**H**–CH_2=CH_2–C**H**–), 2.53 (b, Ar-C**H$_2$**–), 2.02 (b, –C**H**–CH_2–CH_2–Ar), 1.86 (b, –CH–C**H$_2$(exo)** –CH–), 1.57 (b, –C(O)–CH(C**H$_3$**)–O–), 1.41 (b, –CH–C**H$_2$**–CH– and –C**H$_2$**–CH_2–Ar), 1.23 (b, –CH–C**H$_2$**–CH), 0.9 (b, –C**H$_2$**– of initiator), 0.7 (b, –C**H$_3$** of initiator), 0.56 (b, CH–CH_2**(endo)**=CH).

Preparation of Nanoporous Films Films were formed by dissolving the PNS-PLA template and DCPD in 1.0 mL of THF at the desired compositions followed by the addition of a GII in solution (0.2 mL). After stirring for 10 seconds, the stir bar was removed; the vial was placed under a crystallization dish, and the solution was allowed to crosslink for 18 hours. The film was then uncovered and placed in an oven at 100 °C to anneal the film. Films were then cut into smaller pieces (approximately 5 mm x 3 mm x 1 mm), immersed in a 0.5 M NaOH solution (40/60 by volume of methanol and water), and heated at 70 °C for 3 days to remove the PLA. Resultant monoliths were washed with methanol and dried under vacuum for 24 hours.

4.6. Acknowledgements

This work was largely supported by the U.S. Department of Energy (Grant No. 5-35908). M. A. A. acknowledges financial support from the U. S. Air Force. Parts of this work were carried out in the College of Science and Engineering Characterization Facility, University of Minnesota, a member of the NSF-funded Materials Research Facilities Network (www.mrfn.org).

4.7. References and Notes

(1) Zammarano, M.; Franceschi, M.; Bellayer, S.; Gilman, J. W.; Meriani, S. *Polymer* **2005**, *46*, 9314–9328.

(2) Nelson, J. K.; Hu, Y. *J. Phys. D* **2005**, *38*, 213–222.

(3) Douglas, E. P. *Polym. Rev.* **2006**, *46*, 127–141.

(4) Jeong, W.; Kessler, M. R. *Chem. Mater.* **2008**, *20*, 7060–7068.

(5) Hillmyer, M. A.; Lipic, P. M.; Hajduk, D. A.; Almdal, K.; Bates, F. S. *J. Am. Chem. Soc.* **1997**, *119*, 2749–2750.

(6) Bates, F. S.; Fredrickson, G. H. *Annu. Rev. Phys. Chem.* **1990**, *41*, 525–557.

(7) Lipic, P. M.; Bates, F. S.; Hillmyer, M. A. *J. Am. Chem. Soc.* **1998**, *120*, 8963–8970.

(8) Kosonen, H.; Ruokolainen, J.; Nyholm, P.; Ikkala, O. *Macromolecules* **2001**, *34*, 3046–3049.

(9) Serrano, E.; Tercjak, A.; Kortaberria, G.; Pomposo, J. A.; Mecerreyes, D.; Zafeiropoulos, N. E.; Stamm, M.; Mondragon, I. *Macromolecules* **2006**, *39*, 2254–2261.

(10) Dean, J. M.; Lipic, P. M.; Grubbs, R. B.; Cook, R. F.; Bates, F. S. *J. Polym. Sci., Part B: Polym. Phys.* **2001**, *39*, 2996–3010.

(11) Ritzenthaler, S.; Court, F.; David, L.; Girard-Reydet, E.; Leibler, L.; Pascault, J. P. *Macromolecules* **2002**, *35*, 6245–6254.

(12) Girard-Reydet, E.; Pascault, J.; Bonnet, A.; Court, F.; Leibler, L. *Macromol. Symp.* **2003**, *198*, 309–322.

(13) Hermel-Davidock, T. J.; Tang, H. S.; Murray, D. J.; Hahn, S. F. *J. Polym. Sci., Part B: Polym. Phys.* **2007**, *45*, 3338–3348.

(14)Meng, F.; Zheng, S.; Zhang, W.; Li, H.; Liang, Q. *Macromolecules* **2006**, *39*, 711–719.

(15)Meng, F.; Zheng, S.; Li, H.; Liang, Q.; Liu, T. *Macromolecules* **2006**, *39*, 5072–5080.

(16) Meng, F.; Zheng, S.; Liu, T. *Polymer*, **2006**, *47*, 7590–7600.

(17) Xu, Z.; Zheng, S. *Macromolecules* **2007**, *40*, 2548–2558.

(18) Fan, W.; Zheng, S. *Polymer*, **2008**, *49*, 3157–3167.

(19) Grubbs, R. B.; Broz, M. E.; Dean, J. M.; Bates, F. S. *Macromolecules* **2000**, *33*, 2308–2310.

(20) Grubbs, R. B.; Dean, J. M.; Broz, M. E.; Bates, F. S. *Macromolecules* **2000**, *33*, 9522–9534.

(21) Grubbs, R. B.; Dean, J. M.; Bates, F. S. *Macromolecules* **2001**, *34*, 8593–8595.

(22) Rebizant, V.; Abetz, V.; Tournilhac, F.; Court, F.; Leibler, L. *Macromolecules* **2003**, *36*, 9889–9896.

(23) Rebizant, V.; Venet, A.; Tournilhac, F.; Girard-Reydet, E.; Navarro, C.; Pascault, J.; Leibler, L. *Macromolecules* **2004**, *37*, 8017–8027.

(24) Serrano, E.; Larrañaga, M.; Remiro, P. M.; Mondragon, I.; Carrasco, P. M.; Pomposo, J. A.; Mecerreyes, D. *Macromol. Chem. Phys.* **2004**, *205*, 987–996.

(25) Serrano, E.; Martin, M. D.; Tercjak, A.; Pomposo, J. A.; Mecerreyes, D.; Mondragon, I. *Macromol. Rapid Commun.* **2005**, *26*, 982–985.

(26) Serrano, E.; Tercjak, A.; Kortaberria, G.; Pomposo, J. A.; Mecerreyes, D.; Zafeiropoulos, N. E.; Stamm, M.; Mondragon, I. *Macromolecules* **2006**, *39*, 2254–2261.

(27) Serrano, E.; Tercjak, A.; Ocando, C.; Larrañaga, M.; Parellada, M. D.; Corona-Galván, S.; Mecerreyes, D.; Zafeiropoulos, N. E.; Stamm, M.; Mondragon, I. *Macromol. Chem. Phys.* **2007**, *208*, 2281–2292.

(28) Ocando, C.; Tercjak, A.; Serrano, E.; Ramos, J. A.; Corona-Galván, S.; Parellada, M. D.; Fernández-Berridi, M. J.; Mondragon, I. *Polym. Int.* **2008**, *57*, 1333–1342.

(29) Mijovic, J.; Shen, M.; Sy, J. W.; Mondragon, I. *Macromolecules* **2000**, *33*, 5235–5244.

(30) Guo, Q.; Thomann, R.; Gronski, W.; Thurn-Albrecht, T. *Macromolecules* **2002**, *35*, 3133–3144.

(31) Ritzenthaler, S.; Court, F.; Girard-Reydet, E.; Leibler, L.; Pascault, J. P. *Macromolecules* **2003**, *36*, 118–126.

(32) Larrañaga, M.; Gabilondo, N.; Kortaberria, G.; Serrano, E.; Remiro, P.; Riccardi, C. C.; Mondragon, I. *Polymer,* **2005**, *46*, 7082–7093.

(33) Serrano, E.; Martin, M. D.; Tercjak, A.; Pomposo, J. A.; Mecerreyes, D.; Mondragon, I. *Macromol. Rapid Commun.* **2005**, *26*, 982–985.

(34) Meng, F.; Xu, Z.; Zheng, S. *Macromolecules* **2008**, *41*, 1411–1420.

(35) Meng, F.; Yi, F.; Zheng, S. *J. Macromol. Sci., Part B: Phys.* **2008**, *47*, 450.

(36) Liu, J. ; Sue, H.; Thompson, Z. J.; Bates, F. S.; Dettloff, M.; Jacob, G.; Verghese, N.; Pham, H. *Macromolecules* **2008**, *41*, 7616–7624.

(37) Fan, W.; Wang, L.; Zheng, S. *Macromolecules* **2009**, *42*, 327–336.

(38) Tang, H. S.; Hermel-Davidock, T. J.; Hahn, S. F.; Murray, D. J.; Cieslinski, R. C.; Verghese, N. E.; Pham, H. Q. *J. Polym. Sci., Part B: Polym. Phys.* **2009**, *47*, 393–406.

(39) Kosonen, H.; Ruokolainen, J.; Nyholm, P.; Ikkala, O. *Polymer,* **2001**, *42*, 9481–9486.

(40) Kosonen, H.; Ruokolainen, J.; Torkkeli, M.; Serimaa, R.; Nyholm, P.; Ikkala, O. *Macromol. Chem. Phys.* **2002**, *203*, 388–392.

(41) Sinturel, C.; Vayer, M.; Erre, R.; Amenitsch, H. *Macromolecules* **2007**, *40*, 2532–2538.

(42) Serrano, E.; Gerard, P.; Lortie, F.; Pascault, J.; Portinha, D. *Macromol. Mater. Eng.* **2008**, *293*, 820–827.

(43) Chen, L.; Phillip, W. A.; Cussler, E. L.; Hillmyer, M. A. *J. Am. Chem. Soc.* **2007**, *129*, 13786–13787.

(44) Chen, L.; Hillmyer, M. A. *Macromolecules* **2009**, *42*, 4237–4243.

(45) Phillip, W. A.; Amendt, M.; O'Neill, B.; Chen, L.; Hillmyer, M. A.; Cussler, E. L. *ACS Appl. Mater. Interfaces* **2009**, *1*, 472–480.

(46) Phillip, W. A.; Martono, E.; Chen, L.; Hillmyer, M. A.; Cussler, E. L. *J. Membr. Sci.* **2009**, *337*, 39–46.

(47) Chen, L.; Hallinan, D. T.; Elabd, Y. A.; Hillmyer, M. A. *Macromolecules* **2009**.

(48) Schmidt, S. C.; Hillmyer, M. A. *Macromolecules* **1999**, *32*, 4794–4801.

(49) Wang, Y.; Hillmyer, M. A. *Macromolecules* **2000**, *33*, 7395–7403.

(50) Zalusky, A. S.; Olayo-Valles, R.; Wolf, J. H.; Hillmyer, M. A. *J. Am. Chem. Soc.* **2002**, *124*, 12761–12773.

(51) Hillmyer, M. A.; Bates, F. S. *Macromolecules* **1996**, *29*, 6994–7002.

(52) Hsieh, H. L.; Quirk, R. P. In Chapter 10: Copolymerization; *Anionic Polymerization: Principles and Practical Applications*; Marcel Dekker, Inc.: New York, 1996; pp 237.

(53) Tobolsky, A. V.; Boudreau, R. J. *J. Polym. Sci.* **1961**, *51*, S53–S56.

(54) Chen, J.; Fetters, L. J. *Polym. Bull.* **1981**, *4*, 275–280.

(55) The gelation time for a DCPD solution in THF (75 wt%) using 0.5 wt% catalyst in the absence of block polymer was about 8.5 minutes. This difference in gelation time is consistent with the PNS block acting as a multifunctional crosslinking agent thus decreasing the critical extent of reaction for gelation.

(56) Teubner, M.; Strey, R. *J. Chem. Phys.* **1987**, *87*, 3195.

(57) Morkved, T. L.; Stepanek, P.; Krishnan, K.; Bates, F. S.; Lodge, T. P. *J. Chem. Phys.* **2001**, *114*, 7247-7259.

(58) Chen, S.; Chang, S.; Strey, R. *Prog. Colloid Polym. Sci.* **1990**, 81, 30-35.

(59) Schubert, K.; Strey, R. *J. Chem. Phys.* **1991**, *95*, 8532-8545.

(60) Schubert, K.; Strey, R.; Kline, S. R.; Kaler, E. W. *J. Chem. Phys.* **1994**, *101*, 5343-5355.

(61) Koehler, R. D.; Schubert, K.; Strey, R.; Kaler, E. W. *J. Chem. Phys.* **1994**, *101*, 10843-10849.

(62) Lowell, S. In *Introduction to Powder Surface Area;* John Wiley and Sons: New York, 1979; pp 199.

(63) Brunauer, S.; Emmett, P. H.; Teller, E. *J. Am. Chem. Soc.* **1938**, *60*, 309–319.

(64) Barrett, E. P.; Joyner, L. G.; Halenda, P. P. *J. Am. Chem. Soc.* **1951**, *73*, 373–380.

(65) Duval, M.; Haida, H.; Lingelser, J. P.; Gallot, Y. *Macromolecules* **1991**, *24*, 6867–6869.

(66) Hiemenz, P. C.; Lodge, T. P. In *Polymer Chemistry;* CRC Press: Boca Raton, 2007; Vol. 2nd Edition.

(67) Scriven, L. E. *Nature* **1976**, *263*, 123–125.

Chapter 5.

Nanostructured vinyl thermosets using reactive triblock copolymers

This chapter describes the formation of nanostructured vinyl thermosts using a new vinyl reactive triblock copolymer. The reactive triblock copolymer poly(lactide)-*b*-polycylooctene-*s*-5-norbornene-2-methacrylate)-*b*-poly(lactide) (PLCNL) was synthesized and crosslinked with a variety of vinyl monomers to form nanostructured thermosets. Differential scanning calorimetry, small angle X-ray scattering, and transmission electron microscopy were used to characterize the films, and lamellar, bicontinuous and homogenous structures were observed. Analysis of the crosslinking suggested that the timing of gelation versus phase separation in the films played a critical role in determining the final morphology of the films.

5.1. Introduction

Incorporating additives into thermosets is a useful strategy for improving their mechanical properties.[1] The emergence of the inverse relationship between particle size and mechanical strength[2] has brought nanostructured thermosets to the forefront of many experimental endeavors. Including block polymers in epoxy thermosets is a facile route for forming nanostructured thermosets using either a self-assembly first, or reaction induced phase separation (RIPS) approach.[3] The self-assembly first approach involves incorporation of an amphiphilic block polymer containing both epoxy-philic and epoxy-phobic segments into an appropriate resin. The nanophase separated morphology arising from the block polymer self-assembly can be subsequently trapped through curing.[4,5] Under the RIPS approach both block polymer segments are initially miscible in the epoxy resin, but during the cure, one segment phase separates to form a nanostructured thermoset.[6,7]

Reactive block polymers have also been investigated as templates for nanostructuring epoxy resins. Bates and coworkers investigated epoxidized isoprene and statistical copolymers of either methyl acrylate or methyl methacrylate with glycidyl methacrylate as reactive blocks.[8,9,10,11] Similarly, Leibler and coworkers investigated glycidyl methacrylate and statistical copolymers of methyl methacrylate with acrylic acid as reactive blocks.[12,13] Finally, Mondragon and coworkers have extensively investigated epoxidized butadiene as a reactive block.[14,15,16,17,18,19] These efforts have increased the

variety of suitable curing agents,[13] and could facilitate block polymer incorporation at higher concentrations as a means to functionalized epoxy resins.[8]

The success of reactive block polymers in templating epoxy thermosets spurred us to investigate nanostructuration of other thermosets for potential membrane applications. Our initial efforts focused on the thermosetting monomer dicyclopentadiene (DCPD), which we templated using the metathesis reactive block poly(norbornenylethylstyrene-*s*-styrene) coupled with a variety of phase separating blocks. We first explored the formation of nanoporous poly(DCPD) with the chemically etchable poly(lactide) as the phase separating block using both the self-assembly first[20] and the RIPS[21] approaches. Nanoporous membranes formed using the RIPS approach exhibited improved selectivity when compared to a commercial ultrafiltration membrane. [22] Polymer electrolyte membranes (PEM) using poly(n-propyl-*p*-styrenesulfonate) as the phase separating block were also investigated. Hydrolysis of the n-propyl ester to poly(styrene sulfonate) produced selective PEMs for direct methanol fuel cells [23] and ammonia selective membranes applicable for the separation of ammonia from hydrogen and nitrogen.[24] Finally, the RIPS of a poly(N,N-dimethylaminoethyl methacrylate) block resulted in membranes for the efficient separation of methane from carbon dioxide.[25]

Using the generic approach established in the metathesis crosslinking of DCPD in the presence of metathesis-reactive block polymer approach we aimed to expand the scope of thermosets by exploring the nanostructuration of vinyl thermosetting systems. The diversity of monomers used in vinyl thermosetting systems are attractive for creating

materials with a variety of physical properties, and the ability to cure vinyl thermosets thermally or photochemically increases the range of potential applications. Herein this chapter reports the formation of nanostructured vinyl using a variety of vinyl monomers and a new, reactive poly(lactide)-*b*-poly(cyclooctene-*s*-5-norbornene-2-methylene methacrylate)-*b*-poly(lactide) (PLCNL) block polymer following the RIPS mechanism outlined in Figure 5.1.

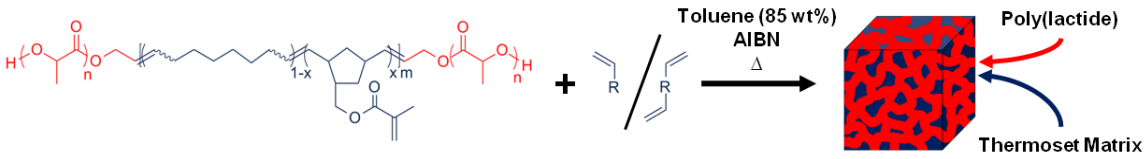

Figure 5.1. Formation of nanostructured vinyl thermosets by crosslinking a PLCNL reactive block polymer template with a variety of vinyl monomers.

5.2. Experimental

5.2.1. Materials.

Unless specifically noted, all chemicals were used as received from Aldrich. All vinyl monomers were passed through a basic alumina column to remove any inhibitors prior to use. d,l-lactide (99%) from Purac was recrystallized twice from toluene and stored under N_2 atmosphere. 2,2'-azobis(isobutyronitrile) (AIBN) from Aldrich was purified by recrystallization from methanol. Degassed tetrahydrofuran (THF), toluene, and methylene chloride were purified by passage over an activated alumina column. Cyclooctene (**C**) was distilled over calcium hydride prior to use. 5-norbornene-2-methylene methacrylate (**N**) was prepared following a reported procedure.[30]

5.2.2. Characterization.

$CDCl_3$ (Cambridge Isotope Laboratories) solutions at approximately 10 mg/mL of sample were analyzed by ^1H nuclear magnetic resonance (NMR) spectroscopy on a Varian Inova 500 instrument operating at 500 MHz. All spectra were obtained at 20 °C after 64 transients using a relaxation delay of 5 s with chemical shifts reported as δ (ppm) relative to the ^1H signals from hydrogenous solvent (7.26 ppm for $CHCl_3$).

Molecular weight evolution and polydispersity indicies of the polymers were determined using size exclusion chromatography (SEC). Samples were prepared at concentrations near 5 mg/mL in $CHCl_3$. The instrument operates at 35 °C with three PLgel 5μm Mixed-C columns in series covering the molecular weight range of 400–400000 g mol^{-1}. The columns are housed in a Hewlett-Packard (Agilent Technologies) 1100 series liquid chromatograph equipped with a Hewlett-Packard 1047A refractive index detector. PDIs are reported with respect to polystyrene standards (Polymer Laboratories).

Small angle X-ray scattering (SAXS) of the block polymer template was performed at the Advanced Photon Source (APS) at Argonne National Laboratories at Sector 5-ID-D beamline. The beamline is maintained by the Dow-Northwestern-Dupont Collaborative Access Team (DND-CAT). The source produces X-rays with a wavelength of 0.729 Å. The sample to detector distance was 5.65 m and the detector radius is 81 mm. Scattering intensity was monitored by a Mar 165 mm diameter CCD detector with a resolution of 2048 x 2048. Small angle X-ray scattering (SAXS) of the crosslinked films

was performed on a custom beam line at the University of Minnesota. X-rays (CuKα, λ=1.542 Å) were generated by a Rigaku RU-200BVH rotating anode with Franks mirror optics and a 0.2 x 2 mm^2 microfocus cathode. Two-dimensional (2-D) diffraction patters were recorded for 300 s using a Siemens area detector and corrected for detector response before analysis. In both cases, the 2-D images were azimuthally integrated to a 1-D plot of intensity versus scattering vector, $q = 4\pi \sin(\theta/2)/\lambda$ [θ is scattering angle; λ is wavelength].

Differential scanning calorimetry (DSC) was performed on a TA instruments DSC Q-1000 calorimeter calibrated with an internal indium standard. Samples were sealed inside hermetic aluminum pans and were heated to and annealed at 120 °C for 5 minutes prior to being cooled to -120 °C to standardize the thermal history. The samples were then analyzed by heating at 10 °C /min to 120 °C.

Samples were microtomed using a Reichert UltraCut S Ultramicrotome with a Model FC-S addition and then stained with OsO_4 vapor for 15 min from a 4% aqueous solution in preparation for transmission electron microscopy (TEM). TEM images were obtained using a Gatan Multiscan CCD camera on a JEOL JEM-1210 microscope operating at 120 kV.

5.2.3. Synthesis.

Synthesis of poly(cyclooctene-s-5-norbornene-2-methylene methacrylate) (PCN). The synthesis of PCN was adapted from the synthesis of telechelic poly(cyclooctene)

using cis-2-butene-1,4-di(oligolactide) (**1**) as a chain transfer agent[26] and is described as follows. A 250 mL round bottom flask with a standard tapered neck and a side arm connected to a flow of argon was flame-dried. To the flask second generation Grubbs catalyst (5 mg, 5.9 μmol), 0.50 g (2.3 mmol) of BHT, 0.51 g (1.1 mmol) **1**, and 100 mL of dry THF were added. The flask was placed in an oil bath at 40 °C and fitted with a drop funnel that was fire dried and filled with 8.07 g (73.2 mmol)of **C** and 2.00 g (10.4 mmol) of **N**. After stirring the catalyst and chain transfer agent together for 30 min, one drop of the monomer solution was added. The polymerization solution was stirred for an additional 30 min and then the remaining monomer solution was added dropwise over 2 h. The solution was stirred for 16 h at 40 °C, and then the polymer was precipitated in methanol before being dried under vacuum for 24 h. 9.03 g was recovered for a 90% yield. The number average molecular weight from ^{1}H NMR analysis was 11 kg/mol and the polymer contained 11 mol% of **N**. SEC analysis indicated a PDI of 1.83 and a number average molecular weight of 16 kg/mol based on polystyrene standards.

^{1}H NMR ($CDCl_3$): δ 6.08 (s, C**H$_2$**=C(CH_3)CO_2–), 5.74–5.83 (m, CH_2–C**H**=CH–CH_2-O-), 5.53 (s, C**H$_2$**=C(CH_3)CO_2–), 5.32–5.40 (m, –CH_2–C**H**=C**H**–CH_2– C backbone and –CH–C**H**=C**H**–CH– N backbone), 4.64–4.74 and 4.52–4.62 (m, =CH–C**H$_2$**–O–), 4.24–4.30 and 4.32–4.38 (m, –CO_2–C**H(**CH_3)–O–), 3.96–4.00 and 4.10–4.13 (m, –CH–C**H$_2$**–O–), 1.91–2.05 (m, –C**H$_2$**–CH=CH–C**H$_2$**– C backbone and –C**H**–CH=CH–C**H**– N backbone), 1.48–1.55 (d, –CO2–CH(C**H$_3$**)–O–), 1.23–1.38 (m, =CH–CH_2–C**H$_2$**– C backbone).

Synthesis of poly(lactide)-b-poly(cyclooctene-s-5-norbornene-2-methylene methacrylate)-b-poly(lactide) (PLCNL). The synthesis of PLCNL was based on the ring opening polymerization of lactide by 1,5,7-triazabicyclo[4.4.0]dec-5-ene (TBD).[27] A pressure vessel was loaded with a Teflon stirbar and 8.51 g of PCN and taken into an inert atmosphere glovebox. To the pressure vessel 24.02 g (0.17 mol) of lactide and 170 mL of dry methylene chloride was added. Once the lactide and PCN had dissolved 25.7 mg (0.18 mmol) of TBD was added. The solution was stirred for 30 s and then 57.0 mg (0.47 mmol) of benzoic acid was added to terminate the polymerization. The polymer was precipitated in methanol and dried under vacuum for 24 h. Recovered yield was 31.79 g (98%). The number average molecular weight of the polylactide was 32 kg/mol based on ^{1}H NMR analysis. SEC analysis indicated a PDI of 1.41 and a number average molecular weight of 55 kg/mol based on polystyrene standards.

^{1}H NMR ($CDCl_3$): δ 6.08 (s, C**H$_2$**=C(CH_3)CO_2–), 5.74–5.83 (m, CH_2–C**H**=CH–CH_2-O-), 5.53 (s, C**H$_2$**=C(CH_3)CO_2–), 5.32–5.40 (m, –CH_2–C**H**=C**H**–CH_2– C backbone and –CH–C**H**=C**H**–CH– N backbone), 5.12–5.25 (m, –CO_2–C**H(**CH_3)–O– L backbone), 4.64–4.74 and 4.52–4.62 (m, =CH–C**H$_2$**–O–), 4.30–4.40 (m, –CO_2–C**H(**CH_3)–O– L end group), 3.96–4.00 and 4.10–4.13 (m, –CH–C**H$_2$**–O–), 1.91–2.05 (m, –C**H$_2$**–CH=CH–C**H$_2$**– C backbone and –C**H**–CH=CH–C**H**– N backbone), 1.55–1.59 (d, –CO2–CH(C**H$_3$**)–O–), 1.23–1.38 (m, =CH–CH_2–C**H$_2$**– C backbone).

Preparation of Nanostructured Films. Films were formed by dissolving the PLCNL block polymer and vinyl monomer (s) (300 mg in total) at the desired

composition in 2 mL of toluene containing 1 mg of AIBN. The solution was then placed in an oven initially at room temperature that was warmed to 100 °C typically over 2 h. The samples were cured in the oven at 100 °C for 16 hours, before being placed under vacuum for 2 h. The resulting transparent films were colorless to amber in color depending on the monomer used. To remove the PLA, the films were etched in a 0.5 M NaOH solution (40/60 methanol/water by volume) at 70, 40 and 25 °C for 3, 7 and 14 d respectively. After etching, the films were rinsed with methanol and dried for 16 hours under vacuum.

5.3. Results and Discussion

5.3.1. Synthesis and Characterization of PLCNL Block Polymers.

Initial attempts to form nanostructured vinyl thermosets focused on crosslinking a solution of a poly(butadiene)-poly(lactide) block polymer in either styrene or styrene and divinyl benzene. A number of trials yielded opaque brittle materials suggesting that macrophase separation occurred. We hypothesized that a block with a more reactive functionality as opposed to the pendant unsaturation in polybutadiene might facilitate incorporation into the developing matrix sooner, thereby preventing macrophase separation similar to our previous results for nanostructured poly(DCPD) thermosets.[28] Search for an orthogonally polymerizable difunctional monomer led us to investigate 5-norbornene-2-methylene methacrylate **(N)** since the norbornene group can be polymerized by ring opening metathesis polymerization (ROMP) without reaction of the pendant methacrylate.[29,30,31,32]

Telechelic polymers can be generated by including an acyclic monounsaturated chain transfer agent (CTA) during the ROMP of cyclic olefins,[33] and an array of ABA triblock copolymers are accessible by using appropriately functionalized CTAs. For example, CTAS with functionalities appropriate for atom-transfer radical polymerization (ATRP),[34,35] reversible addition-fragmentation chain transfer (RAFT)[36] and hydroxy telechelic olefin macroinitiators[37,38,39,40,41,42] for ring-opening polymerization (ROP) of cyclic esters[26,43,44] have been reported. Wanting to avoid crosslinking of the pendent methacrylate groups during polymerization of the second block, hydroxy telechelic olefin macroinitiators for the ROP of lactide were pursued. As such, the ROMP of **C** and **N** with the CTA cis-2-butene-1,4-di(oligolactide) (**1**) followed by the ROTEP of lactide was chosen as the synthetic scheme (Figure 5.2).

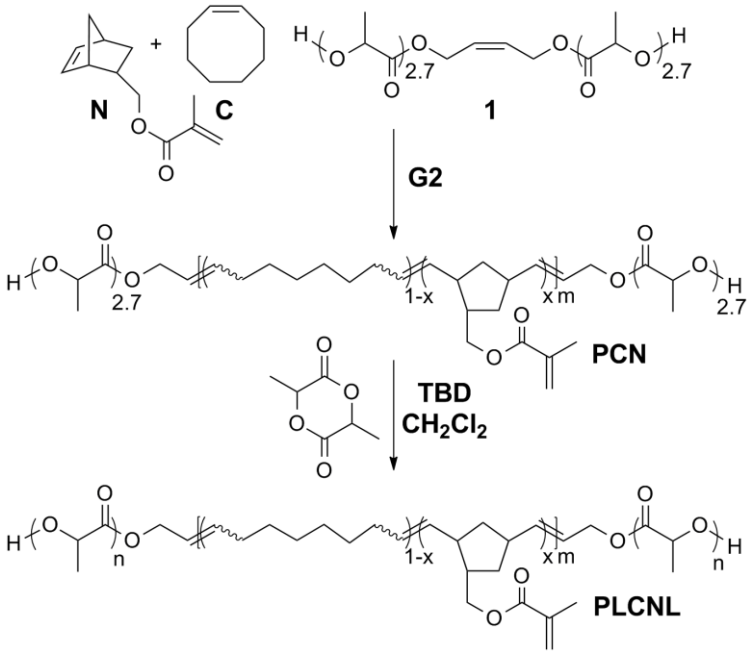

Figure 5.2. Synthesis of PCN copolymer and PLCNL block polymer using ROMP and ROTEP.

ROMP of **C** and **N** using the second generation Grubbs catalyst in the presence of **1** yielded a hydroxy telechelic PCN copolymer (90% recovered yield). ^{1}H NMR end group analysis (Figure 5.3) indicated a number average molecular weight (M_n) of 11 kg/mol assuming exactly two end groups per chain. The experimental molecular weight is slightly greater than the theoretical M_n of 9 kg/mol based on the ratio of the initial monomer to CTA concentration and suggests incomplete incorporation of the CTA. Based on the difference between the experimental and theoretical molecular weights, CTA incorporation during polymerization was 82%. Lower incorporation of the CTA could be due to its isomerization to trans-2-butene-1,4-di(oligolactide), which would not be active as a CTA.[26]

The ^{1}H NMR spectrum is consistent with preservation of the methacrylate group of **N** based on persistence of the signals at δ = 6.08 and 5.53 ppm, which correspond to the methacrylate vinyl protons. The equivalent intensity of the vinyl signals with the protons of the methylene linking the ester and norbornene (δ = 4.24, 4.38 ppm) suggest the methacrylate groups were retained on each **N**. The relative integration of these signals to the **C** olefin hydrogen signals at δ = 5.32–5.40 ppm indicate 11 mol % **N** was incorporated into the polymer, which is close to the feed loading of 12 mol %. Extensive intra- and inter-chain metathesis throughout the polymerization should scramble the distribution of the two monomers along the backbone and result in a statistical PCN copolymer. The PCN polymer is designated as PCN[11], where the number in brackets refers to the molecular weight in kg/mol.

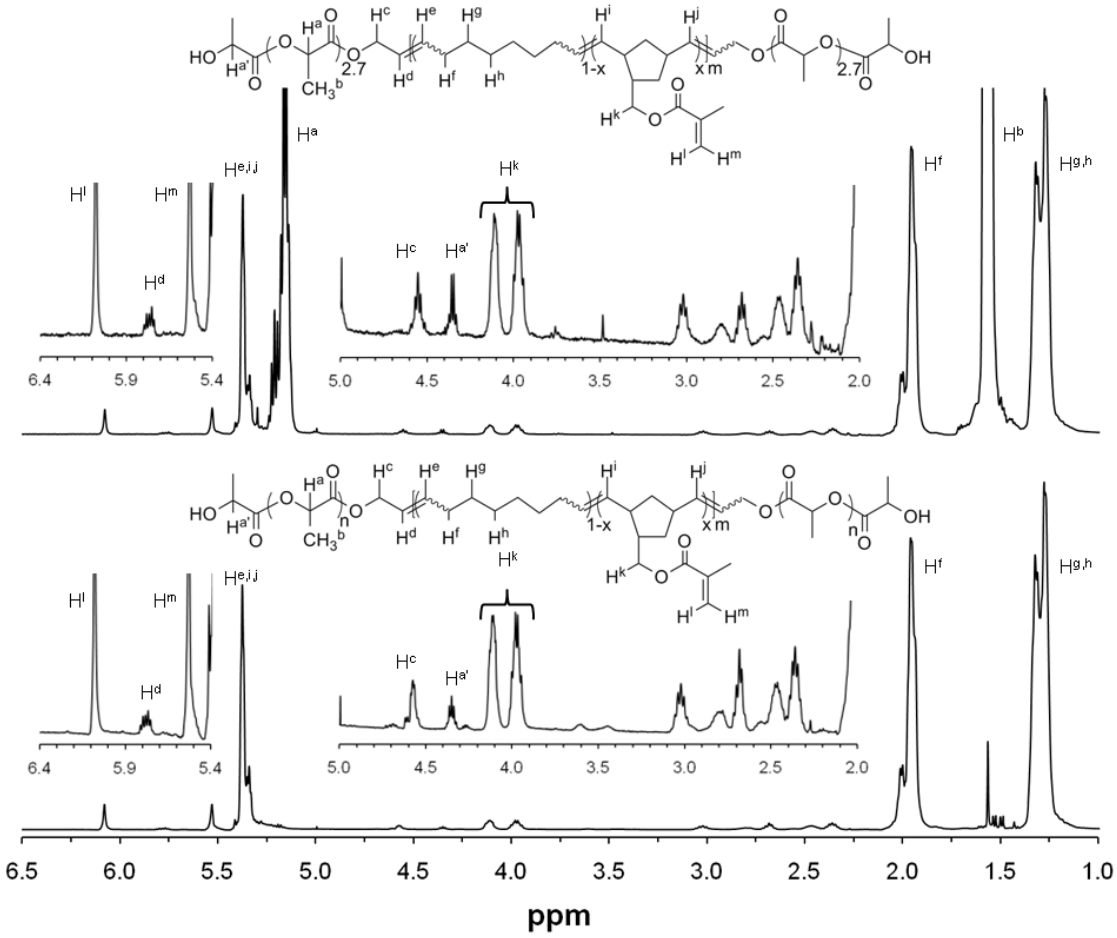

Figure 5.3. ^{1}H NMR for the PCN[11] copolymer (bottom) and PLCNL[16-11-16] block polymer (top).

The hydroxy telechelic PCN[11] copolymer was then used to initiate the ROP of d,l-lactide catalyzed by 1,5,7-triazabicyclo[4.4.0]dec-5-ene (TBD).[45] The ^{1}H NMR spectrum clearly demonstrates polylactide addition based on the appearance of the methyl (δ = 1.55–1.59 ppm) and methine (δ = 5.12–5.25 ppm) proton signals. Importantly, retention of the methacrylate vinyl signals (δ = 5.53 and 6.08 ppm) and protons of the methylene linking the ester and norbornene (δ = 4.24, 4.38 ppm) indicate no transesterification of the methacrylate ester (Figure 5.3). The total M_n of the polylactide

was calculated to be 32 kg/mol based on the relative integration of repeat unit signals and the PCN M_n originally determined by ^1H NMR spectroscopy. The PLCNL block polymer is designated as PLCNL[16-11-16], where the numbers in brackets refer to the molecular weight of the L, CN and L blocks in kg/mol.

SEC chromatographs of the PCN[11] copolymer and PLCNL[16-11-16] block polymer are shown in Figure 5.4. The PDI value for PCN[11] was 1.83, and the broad low molecular weight tail present in the PCN[11] chromatograph is likely due to a small level of low molecular weight cyclic oligomers that formed during the polymerization. The PLCNL[16-11-16] chromatograph has clearly shifted to lower elution volumes consistent with the increased molecular weight from addition of the polylactide blocks. The PDI value of PLCNL[16-11-16] was 1.41.

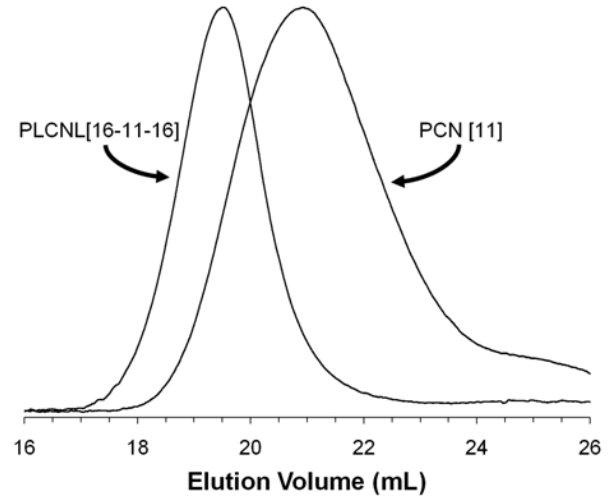

Figure 5.4. SEC chromatograms for the PCN [11] copolymer and the PLCNL [16-11-16] block polymer.

DSC was performed on both the PCN[11] copolymer and PLCNL[16-11-16] block polymer to investigate their thermal properties (Figure 5.5). The thermogram for PCN[11] indicates a glass transition temperature (T_g) of −55 °C and a melting transition temperature (T_m) of 49 °C for the semicrystalline portions of consecutive **C** repeat units. These transitions occur at –66 and 27 °C, respectively, for the PLCNL[16-11-16] block polymer. Additionally, the emergence of an additional T_g characteristic of polylactide at 52 °C is consistent with microphase separation of the blocks.

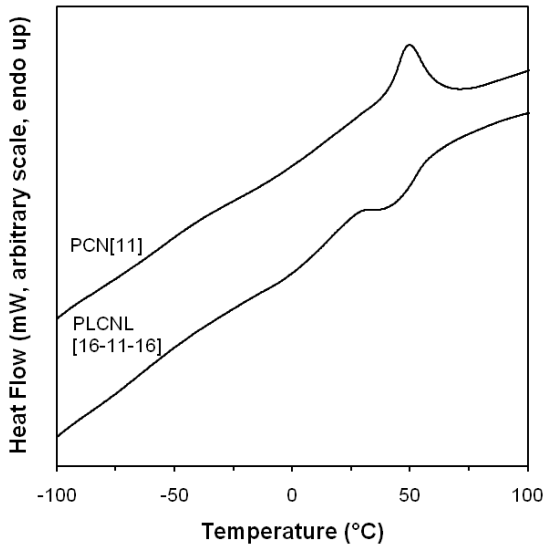

Figure 5.5. DSC traces of PCN[11] copolymer and PLCNL[16-11-16] block polymer. Traces represent the second heating at a rate of 10 °C/min after annealing at 120 °C for 5 min before cooling to -120 °C. The traces have been vertically shifted for clarity.

Microphase separation was corroborated by SAXS of PLCNL[16-11-16] at 25 °C (Figure 5.6). The position of the principle scattering peak indicated a domain spacing of 24 nm, and higher order reflections suggested a hexagonally packed cylindrical morphology.

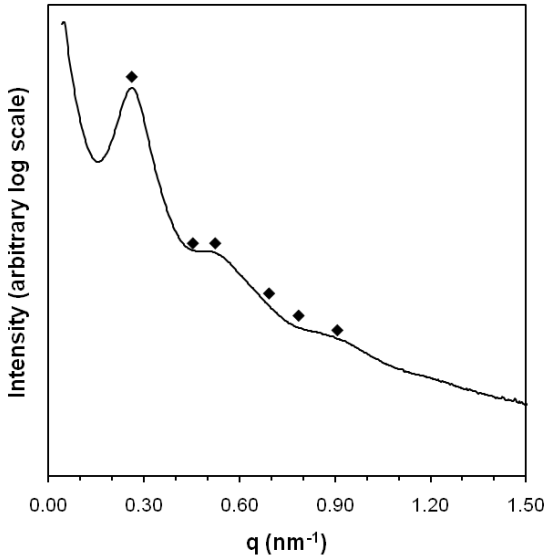

Figure 5.6. One dimensional SAXS profile of LCNL [16-11-16] block polymer measured at 25 °C. The black diamonds indicate the predicted positions of higher order reflections for a hexagonally packed cylindrical morphology based on the principal scattering peak.

5.3.2. Formation of Nanostructured Films.

Initial crosslinking attempts with PLCNL[16-11-16] were attempted by heating PCN[11] (9.9 wt %) with styrene (5 wt %), divinyl benzene (5 wt %) and AIBN (0.1 wt %) in toluene (80 wt %) at 100 °C. After 16 hours a transparent slightly yellow film was recovered unlike the opaque yellowish materials from crosslinking trials with polybutadiene suggesting that the increased reactivity of the pendent methacrylate leads to crosslinking of PCN into the thermoset earlier, which prevents macrophase separation

After this initial result, a series of films (Table 5.1) with PLCNL [16-11-16] were then crosslinked with styrene (S), methyl methacrylate (M), or either a mixture of styrene and divinyl benzene (D) or methyl methacrylate and ethylene glycol dimethacrylate (E) at varying compositions by first dissolving the block polymer and vinyl monomer(s) in

toluene (85 wt %) along with AIBN (0.05 wt %) inside a capped vial. The mixtures were heated for 16 h at 100 °C to give transparent films ranging from colorless to amber, depending on the vinyl monomer(s) employed. Table 1 contains molecular and thermal characteristics for the series of thermosets labeled as R X, where R indicates the vinyl monomer(s) used and X represents the wt % of vinyl monomer(s) in the feed solution.

Table 5.1. Composition and characterization data for crosslinked films.

Sample[a]	% Mass remaining post curing	Gel fraction	D[b] (nm)	T_{gCN} (°C)	T_{gL} (°C)	T_g[f] (°C)
PLCNL 100	100	76	26	−67	54	
S 34	85	81	26	−69	54	
S 50	67	77	28	−75	52	
S 66	67	63	39	−64	53	82
S 84	45	57	42	−65	47	82
SD 34	93	90	25	−59	57	
SD 50	90	98	27	[d]	53	
SD 66	89	100	[c]	[d]	53	
SD 84	87	100	[c]	[d]	42	
M 34	94	75	21	−59		57
M 50	77	73	20	−62		60
M 66	73	67	[c]	[d]		64
M 84	69	3	[c]	[d]		73
ME 34	100	83	23	−66	55	
ME 50	91	97	[c]	[d]	54	
ME 66	88	97	[c]	[d]	55	
ME 84	91	100	[c]	[d]	[e]	

[a]LCNL 100 only contains block polymer; the remaining film samples are labeled as R X where R denotes the monomer cured (S: styrene, D: divinyl benzene, M: methyl methacrylate, and E: ethylene glycol dimethacrylate) and X denotes total monomer wt % in the feed solution. Samples with both a monofunctional and difunctional monomer had equal masses of each monomer. All samples were crosslinked in toluene (85 wt %) with 0.05 wt % AIBN. [b]Principal domain spacing determined from SAXS at room temperature using the Teubner Strey microemulsion model. [c]A scattering reflection was not observed in these samples. [d]The T_g of the CN block was not observed in these samples. [e]A T_g of the L block was not observed in this sample. [f]Glass transition temperature for the vinyl monomer (S) or a combination of the vinyl monomer and L for films that included M.

The film mass after curing indicated some degree of mass loss during crosslinking (Table 5.1). The percent mass loss increased with increased monomer loadings, was greater for styrenic monomers than methacrylic monomers and decreased when difunctional monomers were included. This mass loss is likely due to a loss of vinyl monomers because of their volatility, so the actual monomer content in the cured film is presumably less than the initial monomer loadings.

To further investigate crosslinking over time, feed solutions of S 34, SD 34, M 34 and ME 34 were divided among 10 vials each, which were then heated to 100 °C. Each hour during curing a sample was removed from the oven, and SEC was performed on the samples until the solution could no longer be filtered by a 200 nm filter. S 34 samples were analyzed by SEC for up to 5 h and gelation occurred between 9–10 hours. SD 34 samples were analyzed by SEC for up to 3 h and gelation occurred between 5–6 h. M 34 samples were analyzed by SEC for up to 2 h and gelation occurred between 3–4 h. ME 34 samples were analyzed by SEC for up to 1 h and gelation occurred between 2–3 h. Chromatograms for each series are shown in Figure 5.7. Chromatograms for S 34 indicate a broadening of the PLCNL[16-11-16] peak at 2 h, which evolves into a higher molecular weight shoulder (3 h) before becoming bimodal at 4 h and multimodal at 5 h. The broadening at 2 h indicates that the PLCNL[16-11-16] polymerizes with styrene early during the cure, and the development of bi and multimodal peaks reveals that multiple PLCNL[11-16-11] chains couple together. Of note is that even at 5 h the largest peak in the chromatogram appears to be unreacted PLCNL[11-16-11], but although

further changes in the chromatograms could not be observed, continued polymerization of styrene and additional chain couplings should continue throughout the cure until the final network structure develops.

Chromatograms for the SD 34, M 34 and ME 34 series (Figure 5.7) were similar to the traces for S 34, but bimodal and multimodal peaks were observed earlier. According to the relative timing of gelation and changes in the chromatographs over time, samples with difunctional monomers cured faster than just monofunctional monomers as expected, and the methacrylic monomers cured faster than the styrenic monomers. The lower reactivities of the styrenic monomers and the monofunctional versus difunctional monomers coincides with the relative mass losses during crosslinking indicating that the longer reaction times coupled with the monomer volatility lead to the greater losses during crosslinking.

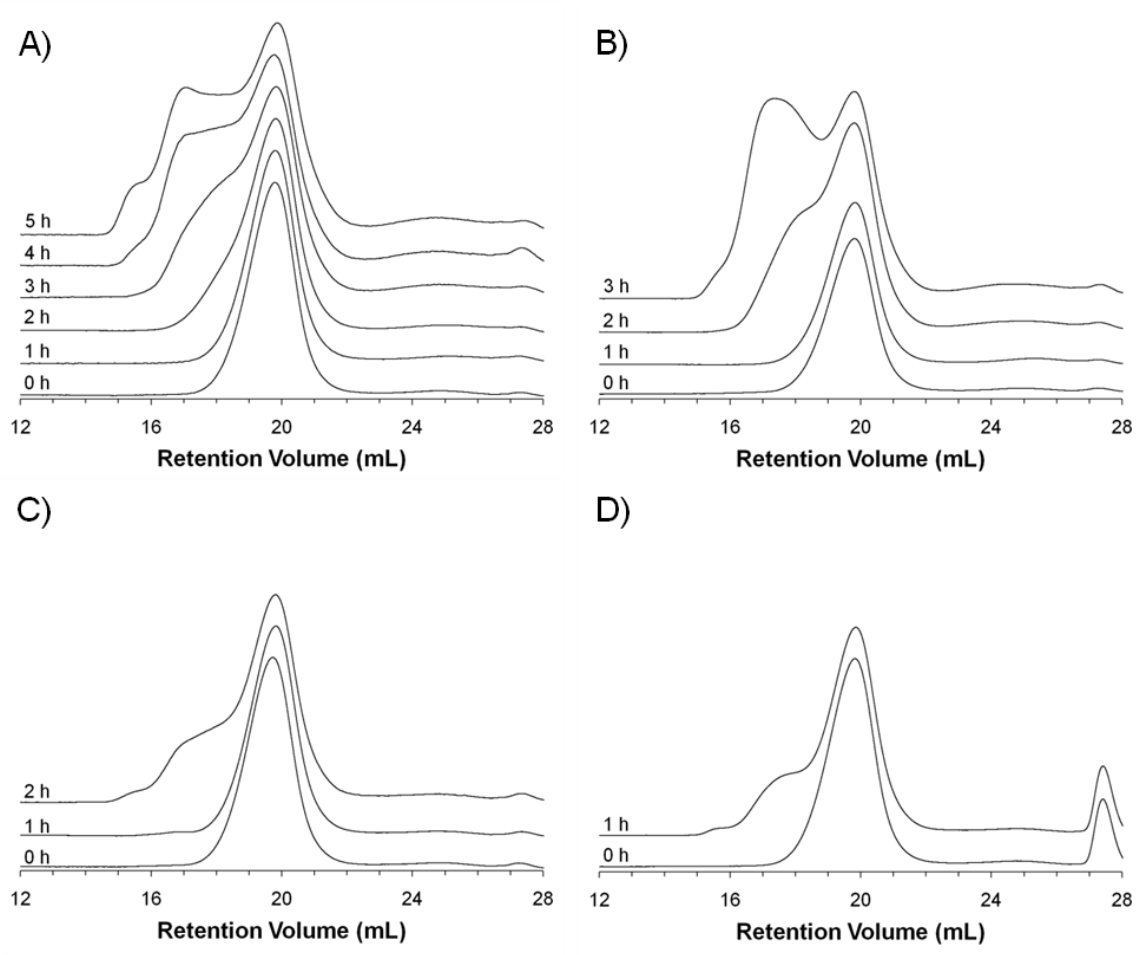

Figure 5.7. Size exclusion chromatograms showing the evolution of crosslinking for A) S 34, B) SD 34, C) M 34 and D) ME 34 films over time.

5.3.3. Characterization of Nanostructured Films.

The crosslinked films were first characterized by determining the gel fraction. A small portion of each film (20–30 mg) was swollen in 2 mL of toluene at room temperature. After 24 h the toluene solution was removed; the remaining polymer was dried, and the gel fraction was determined based on the mass remaining relative to the initial mass. Gel fractions of films containing only monofunctional monomers were typically lower and decreased with increasing monomer content. This is expected as the

ratio of multifunctional crosslinking agent (PLCNL [16-11-16]) decreases with increasing monomer composition, and hence the crosslink density should be lower. Contrary to the monofunctional vinyl monomers, gel fractions for films containing difunctional monomers were typically higher and increased with increasing monomer content. Difunctional monomers are also crosslinking reagents, so increases in the number of crosslinking reagents should lead to higher crosslink density, and thus higher gel fraction.

The thermal properties of the crosslinked films were analyzed by DSC. T_gs observed for the samples during the second heating cycle are recorded in Table 5.1 and heating traces for the second heating cycle all films are shown in Figure 5.8. In comparison to the uncrosslinked PLCNL [16-11-16], two glass transitions consistent with the PCN (−67 °C) and polylactide blocks (54 °C) were observed in PLCNL 100 indicative of microphase separation, but a melting transition was absent suggesting that crosslinking the block polymer suppressed crystallization.

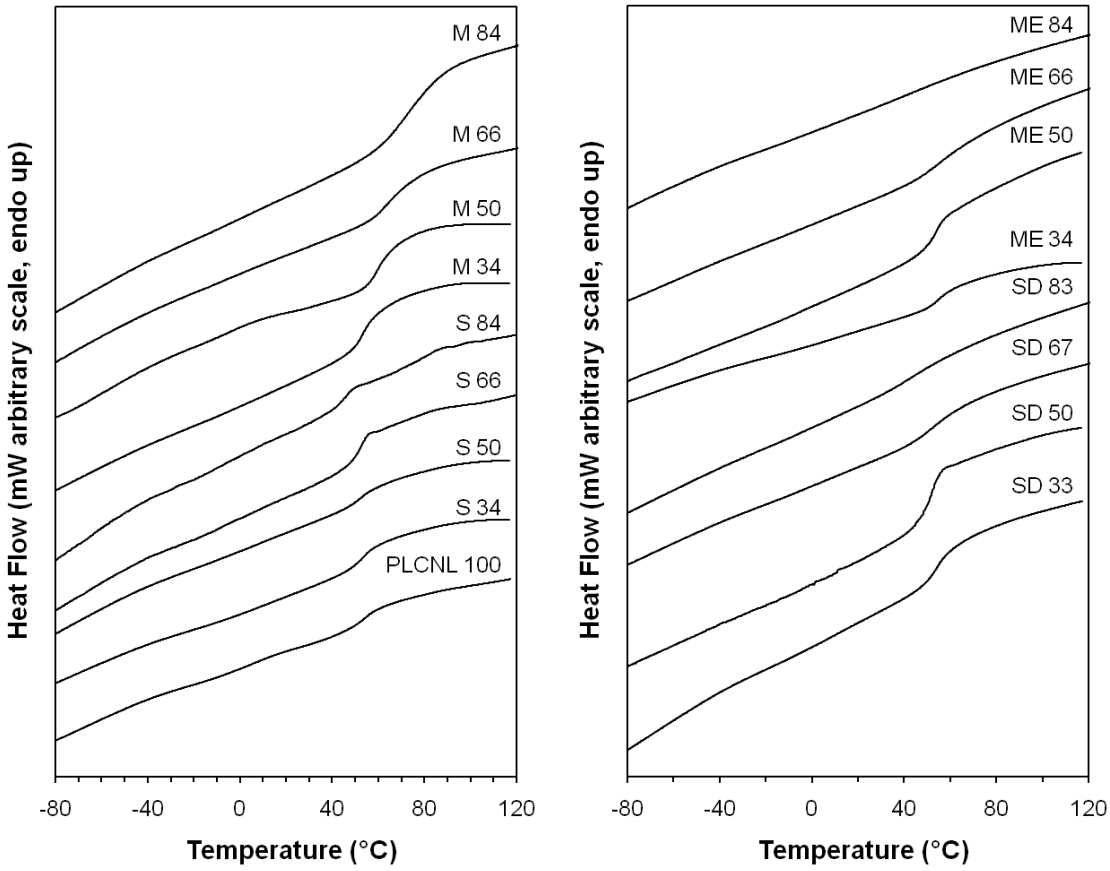

Figure 5.8. DSC traces for crosslinked films. Traces represent the second heating at a rate of 10 °C/min after annealing at 120 °C for 5 min before cooling to -120 °C. The traces have been vertically shifted for clarity.

Transitions in the other films varied with both the amount and type of monomer included. Two T_gs corresponding to the PCN and polylactide blocks were observed in the S X series (-75– -64 °C for CN and 47– 54 °C for L) indicative of a microphase separated morphology in the samples. Additionally, a third T_g observed at 82 °C for S 66 and S 84 was attributed to longer polystyrene segments within the samples, given the larger percentage of the monomer included in crosslinking. Two T_gs corresponding to the PCN and polylactide blocks were also observed in the SD 34 film, while only the polylactide

T_g was observed in the remaining samples. The loss of the PCN T_g is possibly due to the greater extent of crosslinking upon increasing D composition, which limits segmental motion of the CN backbone/matrix.

Glass transitions of the M X series were distinct from the S X series. Glass transitions for the CN backbone were observed at −59 °C and −62 °C for the M 34 and M 50 films, but were absent in the M 66 and M 84 films. Additionally, the T_g initially associated with polylactide steadily increased with increasing methyl methacrylate composition (57–73 °C). The increasing T_g likely results from the miscibility of polylactide and poly(methyl methacrylate),[46,47] so the observed T_g depends on the composition of the film and increases with increasing methacrylate. This was further confirmed by DSC of a polylactide-*b*-poly(methyl methacrylate) (28-14 $kgmol^{-1}$) block polymer, which was formed by the polymerization of methyl methacrylate in the presence of a trithiocarbonate functionalized polylactide RAFT macro-chain transfer agent.[48] This block polymer exhibited a single broad T_g at 61 °C. The ME X series of films was similar to the SD X series as glass transitions for the PCN and polylactide components were observed in the ME 34 film, but were absent at higher ME compositions. Specifically, a polylactide T_g was observed in the ME 50 and ME 66 films, but no T_gs were observed for the ME 84 film.

One dimensional SAXS profiles of the PLCNL 100 and all films with 34 wt % vinyl monomer exhibited a single broad scattering peak characteristic of a microphase separated morphology consistent with the DSC analysis; however scattering among

higher monomer composition films was monomer dependent as can be seen for the S X, SD X, M X and ME X series shown in Figure 5.9. Since TEM micrographs of the R 34 samples (see below) indicated they had bicontinuous morphologies, SAXS patterns where scattering was observed were modeled using the Teubner-Strey microemulsion model[49] to determine the domain spacings reported in Table 5.1.

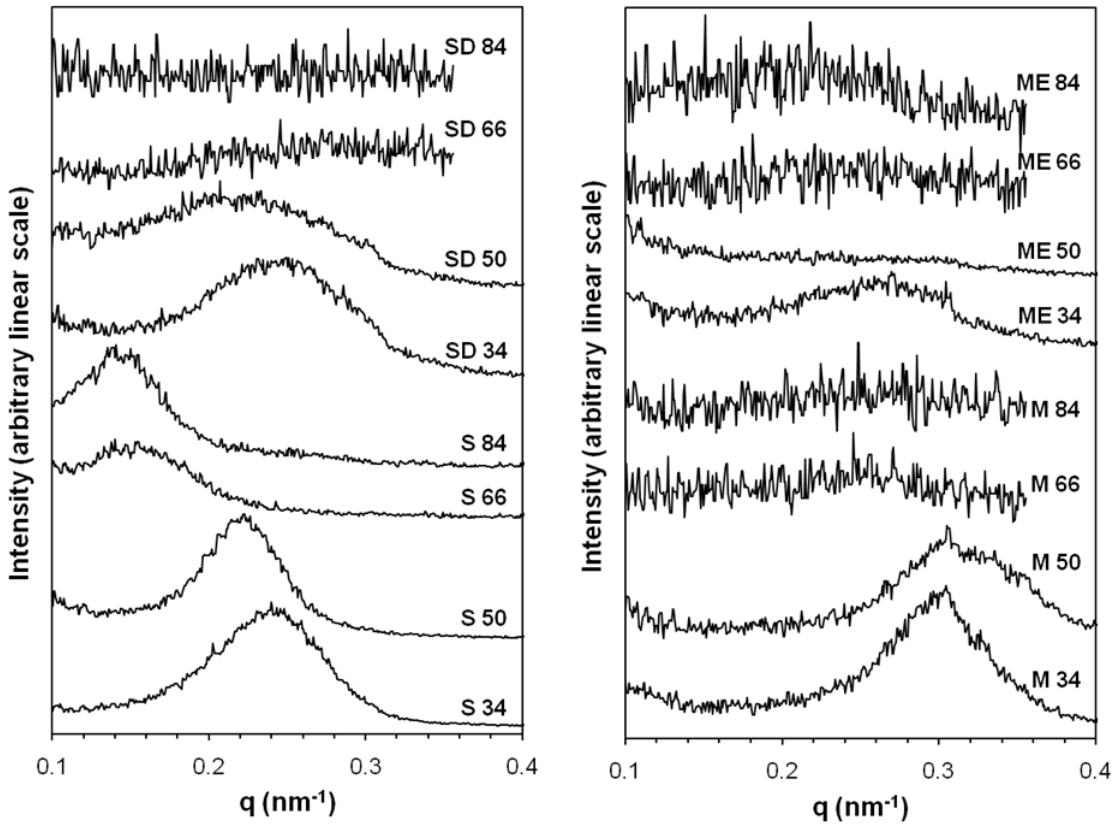

Figure 5.9. One-dimensional SAXS profiles for the crosslinked PLCNL films at room temperature. The profiles have been vertically shifted for clarity.

The S X series of films exhibited broad scattering peaks for all compositions indicating microphase separation. Additionally, the increases in domain spacing with increasing monomer content are consistent with growth of the matrix. This observation is

consistent with previous examples of nanostructured thermosets with varied compositions formed by RIPS.[6,7,28,50] For the SD X series, scattering broadened in SD 50 but was absent in SD 66 and SD 84. The larger peak breadth for SD 50 suggests a broader distribution of domain sizes. No scattering was observed for SD 66 and SD 84 signifying a lack of microphase separation in the material.

A similar comparison could be made between the M and ME series of films as the M 34 and M 50 films exhibit a scattering peak, while ME 50, ME 66 and ME 84 films did not exhibit any scattering. Scattering peaks observed in the M 34 and M 50 samples suggest that there is phase separation within the film, but in contrast to the S series, the M 66 and M 84 samples did not exhibit scattering peaks. The SAXS signal is lost in the M 66 and M 84 samples since M is presumably distributed throughout the material leading to the loss of phase separation in the films. This is also consistent with the DSC data as the PCN T_g was not observed in the M 66 and M 84 possibly indicating a lack of phase separation.

TEM was used to further probe film morphology by imaging ultrathin sections of the films. Prior to imaging, the samples were microtomed and the PCN block was selectively stained with osmium tetroxide. Micrographs of the PLCNL 100 and R 34 films shown in Figure 5.10 revealed a microphase separated bicontinuous morphology consistent with DSC and SAXS. The dark regions in the micrographs correspond to the stained PCN segments, while the lighter regions likely correspond to the polylactide domains. Domain spacings of 21 nm determined for the PLCNL 100 and 23 nm for ME

34 were in reasonable agreement with that from SAXS (26 and 23 nm), but domain spacings for the S 34 (13 nm), SD 34 (17 nm), M 34 (11 nm) and ME 34 (20 nm) films were smaller than the SAXS domain spacings S 34 (26 nm), SD 34(25 nm), and M 34 (23 nm).

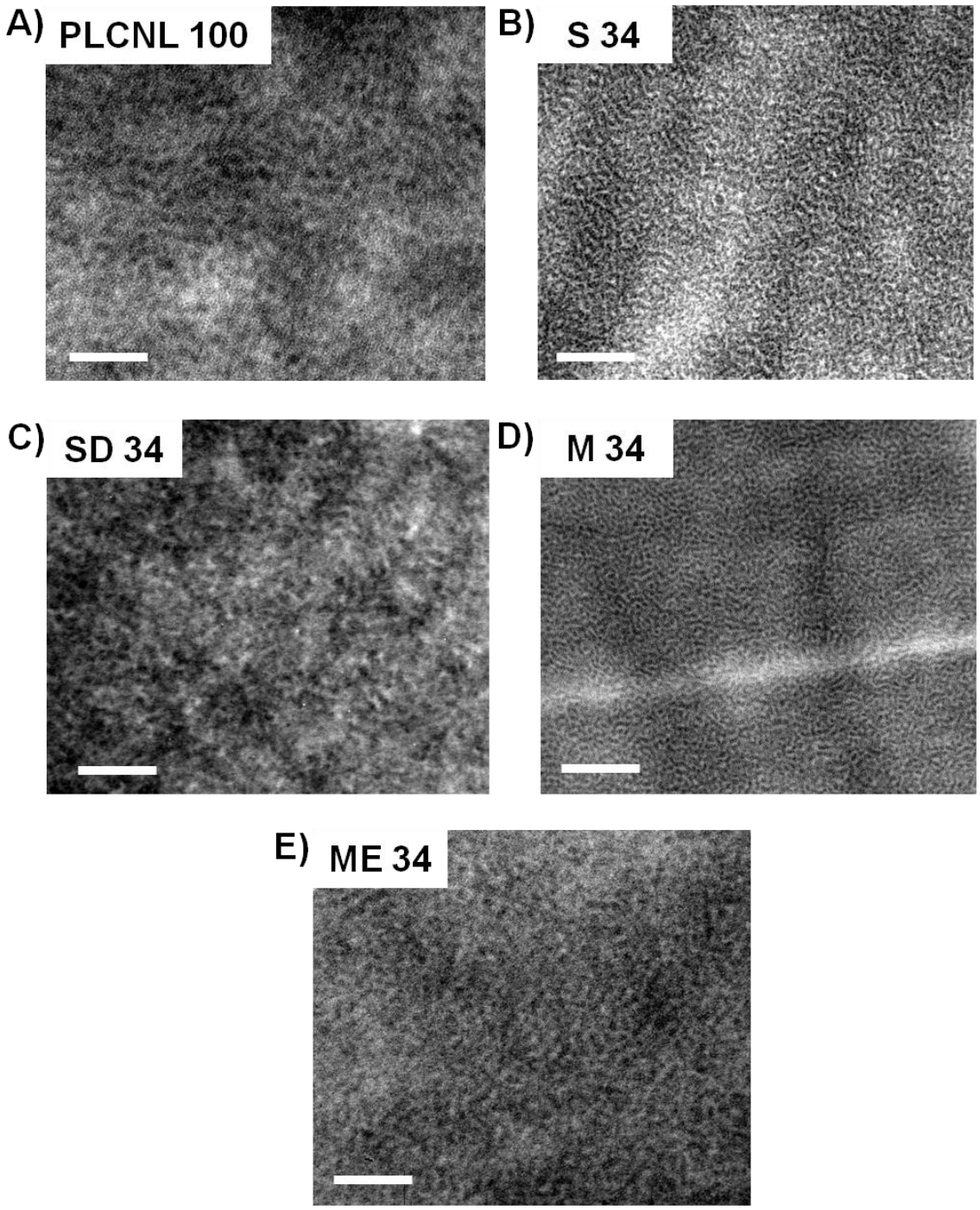

Figure 5.10. TEM micrographs of A) PLCNL 100 B) S 34, C) SD 34, D) M 34, and E) ME 34. Samples were microtomed and then stained with osmium tetroxide prior to imaging. The white scale bar in each image is 100 nm.

TEM of higher composition S and SD films reveal the compositional effects on morphology (Figure 5.11). Micrographs of S 50 revealed a structure similar to S 34, while S 66 exhibited a four layer lamellar morphology with a thin dark phase, a thin light phase a thin dark phase and a thick light phase. In contrast to the S films, SD 66 did not indicate any definitive morphology in agreement with a lack of SAXS scattering.

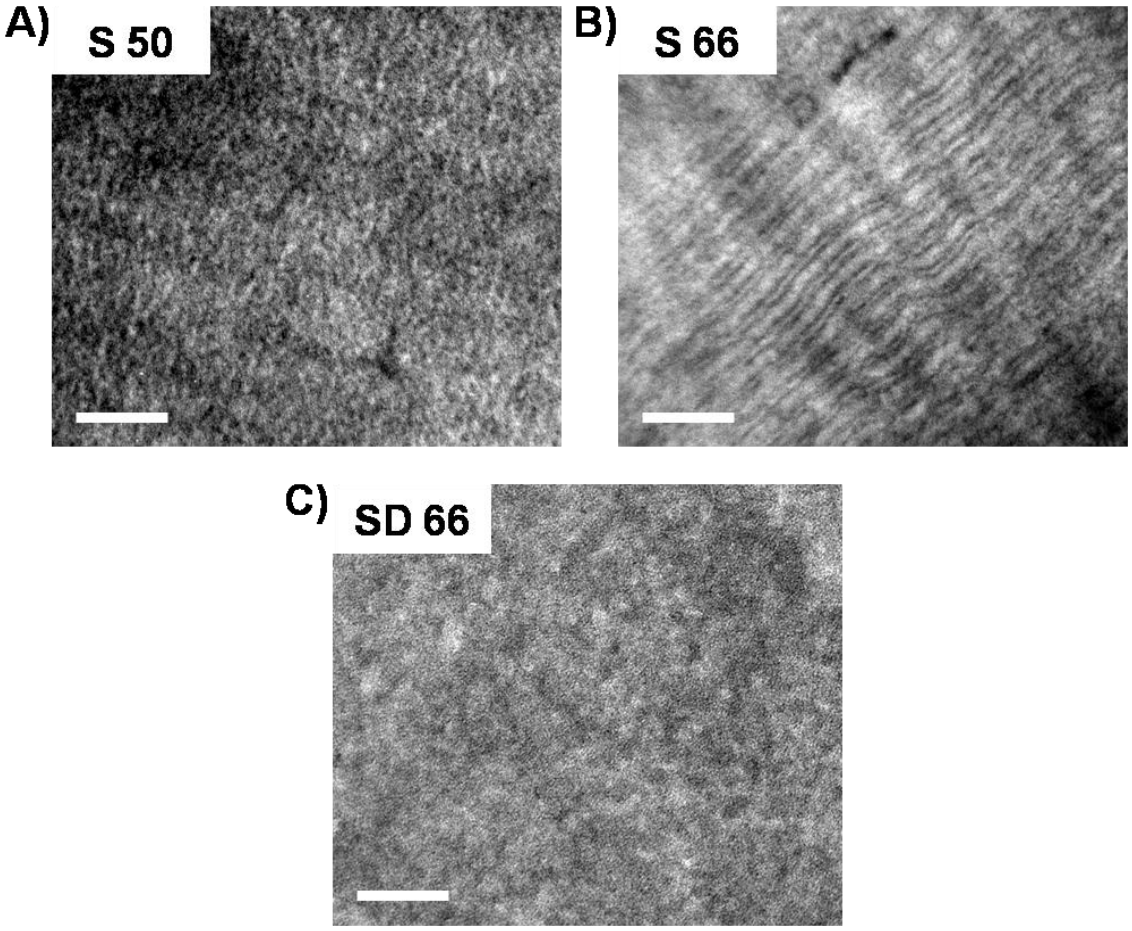

Figure 5.11. TEM micrographs of A) S 50 B) S 66, and C) SD 66. Samples were microtomed and then stained with osmium tetroxide prior to imaging. The white scale bar in each image is 100 nm.

The increase in domain spacing observed for S 50 (15 nm) and S 66 (28 nm) was in agreement with the trend in SAXS, but as in the case for the S 34 films the values were smaller than the calculated SAXS values. The reason for these discrepancies is unknown at this time and under further investigation. In addition to the overall domain spacing, sizes of the individual lamellar phases for S 66 were determined to be 10 nm for the thick light phase and 18 nm as the size of the thin dark, light, dark phases combined. Size estimates for the individual phases can be calculated from the component volume fractions and the overall domain spacing and are 10 nm for polylactide, 4 nm for PCN and 14 nm for styrene. These values suggest that polylactide is the thick light phase, PCN is the thin dark phases, and styrene spans the thin dark and light phases as it is crosslinked with PCN. The presence of a pure styrene phase for S 66 also corroborates DSC data, which indicated a T_g likely associated with styrene at 82 °C.

5.3.4. Mechanism of Nanostructure Formation.

The morphological variations of the films provide some insight into the mechanism of structure formation. For the S series of films, SAXS indicated a scattering peak for all films, and bicontinuous structures were observed for S 34 and S 50, while a lamellar structure was observed in S 66. These morphological differences are likely due to the timing of phase separation relative to gelation. As the amount of styrene increases, the amount of the multifunctional crosslinking agent, PLCNL[16-11-16], is reduced thereby delaying gelation. For the S 34 and S 50 films, the timing of gelation relative to phase separation is sufficiently close that the bicontinuous morphology is kinetically

trapped shortly after forming in both films. Gelation would be further delayed for S 66, which provides the material time to further organize after phase separation leading to the lamellar morphology observed.

The morphological differences between the S X and SD X films are also likely due to the reactivity differences during crosslinking. As previously discussed, the SD 34 film gelled in approximately half the time of the S 34 film. As S and D composition increases, the onset of gelation for the SD films would likely be even earlier relative to the S films as both PLCNL[16-11-16] and D act as crosslinking agents. This is reflected by both the increased mass retained upon curing and the increased gel fraction of the SD films (Table 5.1). The increased reactivity of the SD series would also affect the timing of phase separation relative to gelation. For SD 50, gelation is likely occurring closer to phase separation than for S 50, which limits polylactide mobility. The limited mobility of polylactide leads to a larger distribution in domain sizes and the broader SAXS pattern observed. For SD 66 and SD 84, gelation likely occurs prior to phase separation; thus phase separation is prevented altogether as supported by the lack of scattering patterns for SD 66 and SD 84 and the more homogenous TEM micrograph for SD 66. Similar structures and trends were observed for films crosslinked with M, and ME, although the miscibility of M and L further complicates structure formation at higher M compositions.

Figure 5.12 outlines how the timing of phase separation and gelation affects the final morphology in the films based on the morphologies observed. If gelation occurs well after phase separation a more ordered morphology would result as the material has

additional time to organize/self-assemble. If gelation occurs just after phase separation, a bicontinuous morphology is kinetically trapped in the material. Finally, if gelation occurs before phase separation a homogenous morphology is observed.

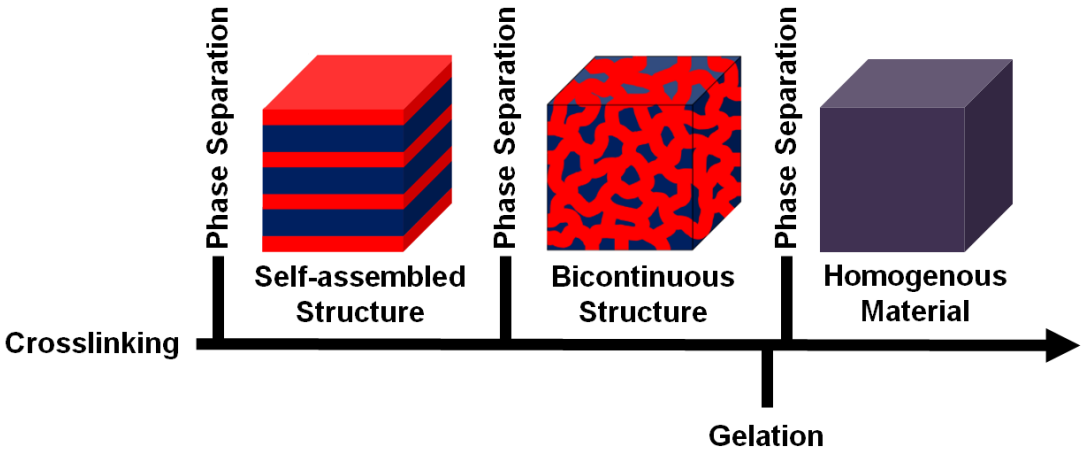

Figure 5.12. Scheme showing how the timing of gelation and phase separation affects the final morphology of the crosslinked material.

5.3.5. Etching of Nanostructured Films.

Taking advantage of the hydrolytic degradability of polylactide, we attempted to etch the nanostructured films to create nanoporous films. All R 34 and R 50 films were submersed in a 0.5 M NaOH 40/60 (v/v) methanol/water solution for 3 days at 70 °C, 7 days at 45 °C and 10 days at 25 °C, and the mass after etching was compared to the original film mass (Table 5.2).

Table 5.2. Mass loss of samples upon etching.

Sample	PLA (wt %)[a]	70 °C mass loss (wt%)[b]	45 °C mass loss (wt%) [b]	25 °C mass loss (wt%) [b]
LCNL 100	78	73	-	-
S 34	53	12	29	27
S 50	39	7	26	32
SD 34	52	55	54	52
SD 50	39	41	48	46
M 34	52	43	57	65
M 50	39	32	56	62
ME 34	50	52	58	56
ME 50	39	43	48	46

[a] PLA wt % based on the film composition prior to crosslinking and does not account for the loss of monomer during curing. [b] Mass loss corresponds to the total percentage of mass loss upon etching the sample.

The difunctional monomer containing films (i.e. SD and ME series) lost wt % greater than or equal to the lactide composition in all trials while the monofunctional monomer containing films lost variable amounts depending on the conditions used. The S X series did not lose masses equivalent to the lactide content in any trial, but the M X films lost masses equivalent to the lactide content when etched at 45 and 25 °C but not 70 °C. In all cases where the wt % lost was equivalent to the lactide wt %, the film nanostructure was lost as evidenced by a loss of scattering by SAXS as can be seen in Figure 5.13 for samples etched at 70 °C.

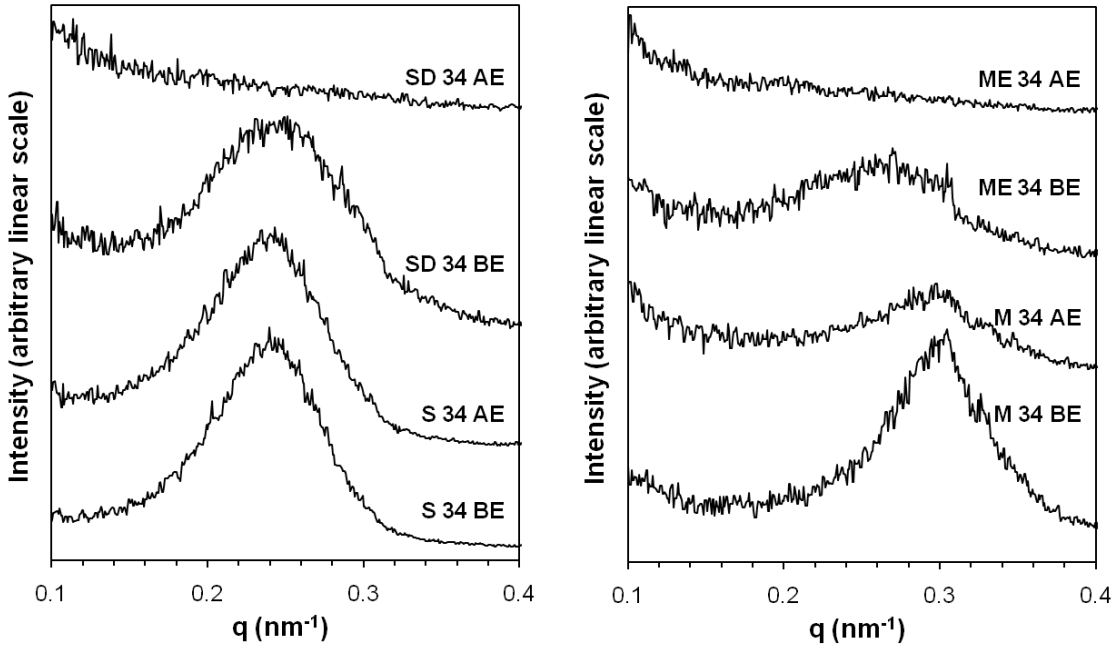

Figure 5.13. One-dimensional SAXS profiles for select PLCNL films at room temperature both before (BE) and after (AE) etching at 70 °C. The profiles have been vertically shifted for clarity.

The loss of structure upon lactide removal indicates that the soft nature of the PCN/monomer matrix leads to collapse of any developing pores. A stronger/higher T_g reactive backbone might be able to support the developing porous structure, and alternatives to the PCN reactive block are explored in Appendix B.

5.4. Conclusions

A reactive triblock terpolymer, PLCNL, was synthesized by the combination of ROMP of **C** and **N** followed by the ROP of d,l-lactide. Nanostructured bicontinuous thermosets were formed by crosslinking PLCNL with a variety of vinyl monomers as evidenced by SAXS, DSC and TEM. Thermosets composed of PLCNL and styrene were

nanostructured at all compositions investigated including bicontinuous and lamellar morphologies. Films crosslinked with styrene and divinyl benzene at 34 and 50 wt % were also nanostructured, but films with 66 and 84 wt% styrene and divinyl benzene were not as the timing of gelation likely prevented phase separation during crosslinking. Similar structures and trends were observed for M X and ME X films, although the miscibility of poly(methyl methacrylate) and polylactide prevented formation of nanostructures at higher methyl methacrylate compositions. Although the selective etching of polylactide from the structured thermosets was unsuccessful due to the soft nature of the PCN block, these systems could potentially be useful for the formation of nonporous separation membranes such as for gas separations if an appropriate block is substituted for polylactide.

5.5. Acknowledgments.

Louis Pitet took the TEM micrographs shown. This work was largely supported by CIE Polymers. M. A. A. acknowledges financial support from the U. S. Air Force. Parts of this work were carried out in the College of Science and Engineering Characterization Facility, University of Minnesota, a member of the NSF-funded Materials Research Facilities Network (www.mrfn.org).

5.6. References

(1) Friedrich, K.; Fakirov, S.; Zhang, Z., Eds.; In *Polymer Composites: From Nano-to-Macro-Scale;* Springer: New York, NY, 2005

(2) Jordan, J.; Jacob, K. I.; Tannenbaum, R.; Sharaf, M. A.; Jasiuk, I. *Mater. Sci. Eng., A* **2005**, *393*, 1-11.

(3) Ruiz-Pérez, L.; Royston, G. J.; Fairclough, J. P. A.; Ryan, A. J. *Polymer* **2008**, *49*, 4475-4488.

(4) Hillmyer, M. A.; Lipic, P. M.; Hajduk, D. A.; Almdal K.; Bates, F. S. *J. Am. Chem. Soc.* **1997**, *119*, 2749.

(5) Lipic, P. M.; Bates, F. S.; Hillmyer, M. A. *J. Am. Chem. Soc.* **1998**, *120*, 8963-8970.

(6) Meng, F.; Zheng, S.; Zhang, W.; Li, H.; Liang, Q. *Macromolecules* **2006**, *39*, 711-719.

(7) Meng, F.; Zheng, S.; Li, H.; Liang, Q.; Liu, T. *Macromolecules* **2006**, *39*, 5072-5080.

(8) Grubbs, R. B.; Dean, J. M.; Broz, M. E.; Bates, F. S. *Macromolecules* **2000**, *33*, 9522-9534.

(9) Grubbs, R. B.; Dean, J. M.; Bates, F. S. *Macromolecules* **2001**, *34*, 8593-8595.

(10) Dean, J. M.; Verghese, N. E.; Pham, H. Q.; Bates, F. S. *Macromolecules* **2003**, *36*, 9267-9270.

(11) Dean, J. M.; Grubbs, R. B.; Saad, W.; Cook, R. F.; Bates, F. S. *J. Polym. Sci., Part B: Polym. Phys.* **2003**, *41*, 2444-2456.

(12) Rebizant, V.; Abetz, V.; Tournilhac, F.; Court, F.; Leibler, L. *Macromolecules* **2003**, *36*, 9889-9896.

(13) Rebizant, V.; Venet, A. -.; Tournilhac, F.; Girard-Reydet, E.; Navarro, C.; Pascault, J. -.; Leibler, L. *Macromolecules* **2004**, *37*, 8017-8027.

(14) Serrano, E.; Larrañaga, M.; Remiro, P. M.; Mondragon, I.; Carrasco, P. M.; Pomposo, J. A.; Mecerreyes, D. *Macromol. Chem. Phys.* **2004**, *205*, 987-996.

(15) Serrano, E.; Martin, M. D.; Tercjak, A.; Pomposo, J. A.; Mecerreyes, D.; Mondragon, I. *Macromol. Rapid Commun.* **2005**, *26*, 982-985.

(16) Serrano, E.; Tercjak, A.; Kortaberria, G.; Pomposo, J. A.; Mecerreyes, D.; Zafeiropoulos, N. E.; Stamm, M.; Mondragon, I. *Macromolecules* **2006**, *39*, 2254-2261.

(17) Serrano, E.; Tercjak, A.; Ocando, C.; Larrañaga, M.; Parellada, M. D.; Corona-Galván, S.; Mecerreyes, D.; Zafeiropoulos, N. E.; Stamm, M.; Mondragon, I. *Macromol. Chem. Phys.* **2007**, *208*, 2281-2292.

(18) Ocando, C.; Tercjak, A.; Serrano, E.; Ramos, J. A.; Corona-Galván, S.; Parellada, M. D.; Fernández-Berridi, M. J.; Mondragon, I. *Polym. Int.* **2008**, *57*, 1333-1342.

(19) Ocando, C.; Tercjak, A.; MartiÌ⍰n, M. D.; Ramos, J. A.; Campo, M.; Mondragon, I. *Macromolecules* **2009**, *42*, 6215-6224.

(20) Chen, L.; Hillmyer, M. A. *Macromolecules* **2009**, *42*, 4237-4243.

(21) Chen, L.; Phillip, W. A.; Cussler, E. L.; Hillmyer, M. A. *J. Am. Chem. Soc.* **2007**, *129*, 13786-13787.

22 Phillip, W. A.; Amendt, M.; O'Neill, B.; Chen, L.; Hillmyer, M. A.; Cussler, E. L. *ACS Appl. Mater. Interfaces* **2009**, *1*, 472-480.

(23) Chen, L.; Hallinan, D. T.; Elabd, Y. A.; Hillmyer, M. A. *Macromolecules* **2009**, 42 6075-6085.

(24) Phillip, W. A.; Martono, E.; Chen, L.; Hillmyer, M. A.; Cussler, E. L. *J. Membr. Sci.* **2009**, *337*, 39-46.

(25) Querelle S. et al submitted.

(26) Pitet L. M. et al submitted.

(27) Pratt, R. C.; Lohmeijer, B. G. G.; Long, D. A.; Waymouth, R. M.; Hedrick, J. L. *J. Am. Chem. Soc.* **2006**, *128*, 4556-4557.

(28) Amendt, M. A.; Chen, L.; Hillmyer, M. A. *Macromolecules* **2010**, 43, 3924-3934.

(29) Preishuber-Pflügl, P.; Podolan, R.; Stelzer, F. *J. Mol. Catal. A: Chem.* **2000**, *160*, 53-61.

(30) Schitter, R. M. E.; Jocham, D.; Stelzer, F.; Moszner, N.; Völkel, T. *J. Appl. Polym. Sci.* **2000**, *78*, 47-60.

(31) Kumar, A.; Jang, S.; Padilla, J.; Otero, T. F.; Sotzing, G. A. *Polymer* **2008**, *49*, 3686-3692.

(32) Li, A.; Ma, J.; Wooley, K. L. *Macromolecules* **2009**, *42*, 5433-5436.

(33) Bielawski, C. W.; Hillmyer, M. A. In *Handbook of Metathesis*; Grubbs, R. H., Ed.; Wiley-VCH: Weinham, Germany, 2003; Vol. 3, pp 255-282.

(34) Bielawski, C. W.; Morita, T.; Grubbs, R. H. *Macromolecules* **2000**, *33*, 678-680.

(35) Xie, M.; Kong, Y.; Han, H.; Shi, J.; Ding, L.; Song, C.; Zhang, Y. *React. Funct. Polym.* **2008**, *68*, 1601-1608.

(36) Mahanthappa, M. K.; Bates, F. S.; Hillmyer, M. A. *Macromolecules* **2005**, *38*, 7890-7894.

(37) Chung, T. C.; Chasmawala, M. *Macromolecules* **1992**, *25*, 5137-5144.

(38) Hillmyer, M. A.; Grubbs, R. H. *Macromolecules* **1993**, *26*, 872-874.

(39) Hillmyer, M. A.; Grubbs, R. H. *Macromolecules* **1995**, *28*, 8662-8667.

(40) Hillmyer, M. A.; Nguyen, S. T.; Grubbs, R. H. *Macromolecules* **1997**, *30*, 718-721.

(41) Bielawski, C. W.; Benitez, D.; Morita, T.; Grubbs, R. H. *Macromolecules* **2001**, *34*, 8610-8618.

(42) Bielawski, C. W.; Scherman, O. A.; Grubbs, R. H. *Polymer* **2001**, *42*, 4939-4945.

(43) Pitet, L. M.; Hillmyer, M. A. *Macromolecules* **2009**, *42*, 3674-3680.

(44) Pitet, L. M.; Amendt, M. A.; Hillmyer, M. A. *J. Am. Chem. Soc.* **2010**, *132*, 8230-8231.

(45) Pratt, R. C.; Lohmeijer, B. G. G.; Long, D. A.; Waymouth, R. M.; Hedrick, J. L. *J. Am. Chem. Soc.* **2006**, *128*, 4556-4557.

(46) Eguiburu, J. L.; Iruin, J. J.; Fernandez-Berridi, M. J.; San Román, J. *Polymer* **1998**, *39*, 6891-6897.

(47) Zhang, G.; Zhang, J.; Wang, S.; Shen, D. *J. Polym. Sci., Part B: Polym. Phys.* **2003**, *41*, 23-30.

(48) Rzayev, J.; Hillmyer, M. A. *J. Am. Chem. Soc.* **2005**, *127*, 13373-13379.

(49) Teubner, M.; Strey, R. *J. Chem. Phys.* **1987**, *87*, 3195.

(50) Xu, Z.; Zheng, S. *Macromolecules* **2007**, *40*, 2548–2558.

Bibliography

Abetz, V.; Simon, Peter F. W. *Adv. Polym.Sci.* **2005**, *189*, 125–212.

Akthakul, A.; Salinaro, R. F.; Mayes, A. M. *Macromolecules* **2004**, *37*, 7663-7668.

Alarcon, C. d. l. H.; Pennadam, S.; Alexander, C. *Chem. Soc. Rev.* **2005**, *34*, 276-285.

Amendt, M. A.; Chen, L.; Hillmyer, M. A. *Macromolecules* **2010**, 43, 3924-3934.

Aptel, P.; Buckley, C. A. In "Chapter 2 Categories of Membrane Operations"; Mallevialle, J., Odendaal, P. E. and Wiesner, M. R., Eds.; *Water Treatment Membrane Processes*; McGraw-Hill: New York, **1996**; 2.1–2.24.

Asatekin, A.; Kang, S.; Elimelech, M.; Mayes, A. M. *J. Membr. Sci.* **2007**, *298*, 136-146.

Asatekin, A.; Menniti, A.; Kang, S.; Elimelech, M.; Morgenroth, E.; Mayes, A. M. *J. Membr. Sci.* **2006**, *285*, 81-89.

Bagheri, R.; Marouf, B. T.; Pearson, R. A. *Polym. Rev.* **2009**, *49*, 201.

Bailey, T. S.; Rzayev, J.; Hillmyer, M. A. *Macromolecules* **2006**, *39*, 8772-8781.

Baker, R. W. *Membrane technology and applications*, 2nd Ed. John Wiley & Sons Ltd, West Sussex, England, **2004**.

Barrett, E. P.; Joyner, L. G.; Halenda, P. P. *J. Am. Chem. Soc.* **1951**, *73*, 373–380.

Bates, F. S. *Science* **1991**, *251*, 898-905.

Bates, F. S.; Fredrickson, G. H. *Annu. Rev. Phys. Chem.* **1990**, *41*, 525-557.

Bates, F. S.; Fredrickson, G. H. *Phys. Today* **1999**, *52*, 32.

Bates, F. S.; Schulz, M. F.; Khandpur, A. K.; Forster, S.; Rosedale, J., H.; Almdal, K.; Mortensen, K. *Faraday Discuss.* **1994**, *98*, 7–18.

Battisti, A.; Skordos, A. A.; Partridge, I. K. *Composites Sci. Technol.* **2010**, *70*, 633-637.

Bauhofer, W.; Kovacs, J. Z. *Composites Sci. Technol.* **2009**, *69*, 1486-1498.

Bielawski, C. W.; Benitez, D.; Morita, T.; Grubbs, R. H. *Macromolecules* **2001**, *34*, 8610-8618.

Bielawski, C. W.; Hillmyer, M. A. In *Handbook of Metathesis*; Grubbs, R. H., Ed.; Wiley-VCH: Weinham, Germany, **2003**; Vol. 3, pp 255-282.

Bielawski, C. W.; Morita, T.; Grubbs, R. H. *Macromolecules* **2000**, *33*, 678-680.

Bielawski, C. W.; Scherman, O. A.; Grubbs, R. H. *Polymer* **2001**, *42*, 4939-4945.

Bird, R.; Stewart, W. E.; Lightfoot, E. N. In *Transport Phenomena*; J. Wiley & Sons, Inc: New York, **2007**.

Biron, M. In *Thermosets and Composites: Technical Information for Plastics Users*; Elsevier: Kidlington, United Kingdom, **2004**; pp 501.

Brunauer, S.; Emmett, P. H.; Teller, E. *J. Am. Chem. Soc*. **1938**, *60*, 309–319.

Buchholz, U.; Mülhaupt, R. *Polym. Preprints* **1992**, *33*, 205-206.

Chen, J.; Fetters, L. *J. Polym. Bull*. **1981**, *4*, 275–280.

Chen, L.; Hallinan, D. T.; Elabd, Y. A.; Hillmyer, M. A. *Macromolecules* **2009**, *42* 6075-6085.

Chen, L.; Hillmyer, M. A. *Macromolecules* **2009**, *42*, 4237-4243.

Chen, L.; Phillip, W. A.; Cussler, E. L.; Hillmyer, M. A. *J. Am. Chem. Soc*. **2007**, *129*, 13786–13787.

Chen, S.; Chang, S.; Strey, R. *Prog. Colloid Polym. Sci*. **1990**, *81*, 30-35.

Chung, T. C.; Chasmawala, M. *Macromolecules* **1992**, *25*, 5137-5144.

Cochran, E. W.; Garcia-Cervera, C. J.; Fredrickson, G. H. *Macromolecules* **2006**, *39*, 2449–2451.

Cooney, D. T.; Hillmyer, M. A.; Cussler, E. L.; Moggridge, G. D. *Crystallogr. Rev*. **2006**, *12*, 13-24.

Coover, H. W.,Jr.; Shields, D. J. *J. Polym. Sci*. **1959**, *39*, 532-533.

Cussler, E. L. In *Diffusion Mass Transfer in Fluid Systems Second Edition*; Cambridge University Press: New York, **2005**.

Darling, S. B. *Prog. Polym. Sci*. **2007**, *32*, 1152–1204.

Dean, J. M.; Grubbs, R. B.; Saad, W.; Cook, R. F.; Bates, F. S. *J. Polym. Sci. Part B: Polym. Phys.* **2003**, *41*, 2444-2456.

Dean, J. M.; Lipic, P. M.; Grubbs, R. B.; Cook, R. F.; Bates, F. S. J. *Polym. Sci., Part B: Polym. Phys*. **2001**, *39*, 2996–3010.

Dean, J. M.; Verghese, N. E.; Pham, H. Q.; Bates, F. S. *Macromolecules* **2003**, *36*, 9267-9270.

Douglas, E. P. *Polym. Rev*. **2006**, *46*, 127–141.

Drockenmuller, E.; Li, L. Y. T.; Ryu, D. Y.; Harth, E.; Russell, T. P.; Kim, H.; Hawker, C. J. *J. Polym. Sci., Part A: Polym. Chem*. **2005**, *43*, 1028–1037.

Du, P.; Li, M.; Douki, K.; Li, X.; Garcia, C. B. W.; Jain, A.; Smilgies, D. -.; Fetters, L. J.; Gruner, S. M.; Wiesner, U.; Ober, C. K. *Adv. Mater*. **2004**, *16*, 953–957.

Duval, M.; Haida, H.; Lingelser, J. P.; Gallot, Y. *Macromolecules* **1991**, *24*, 6867–6869.

Eguiburu, J. L.; Iruin, J. J.; Fernandez-Berridi, M. J.; San Román, *J. Polymer* **1998**, *39*, 6891-6897.

Eykamp, W. In "Chapter 1 Microfiltration and Ultrafiltration"; Noble, R. D., Stern, S. A., Eds.; *Membrane Separations Technology Principles and Applications*; Elsevier: Amsterdam, **1995**; 1–43.

Fan, W.; Wang, L.; Zheng, S. *Macromolecules* **2009**, *42*, 327–336.

Fan, W.; Zheng, S. *Polymer*, **2008**, *49*, 3157–3167.

Fasolka, M. J.; Mayes, A. M. *Annu. Rev. Mater. Res*. **2001**, *31*, 323-355.

Friedrich, K.; Fakirov, S.; Zhang, Z., Eds.; In *Polymer Composites: From Nano-to-Macro-Scale*; Springer: New York, NY, **2005**

Fukunaga, K.; Elbs, H.; Magerle, R.; Krausch, G. *Macromolecules* **2000**, *33*, 947-953.

Gawenda, M.; Sperschneider, A.; Schacher, F.; Krausch, G.; Müller, A.; Ulbricht, M. *Desalination* **2006**, *200*, 29-31.

Girard-Reydet, E.; Pascault, J.; Bonnet, A.; Court, F.; Leibler, L. *Macromol. Symp*. **2003**, *198*, 309–322.

Goldbach, J. T.; Lavery, K. A.; Penelle, J.; Russell, T. P. *Macromolecules* **2004**, *37*, 9639–9645.

González-Campo, A.; Orchard, K. L.; Sato, N.; Shaffer, M. S. P.; Williams, C. K. *Chem. Commun*. **2009**, *27*, 4034-4036.

Grubbs, R. B.; Broz, M. E.; Dean, J. M.; Bates, F. S. *Macromolecules* **2000**, *33*, 2308–2310.

Grubbs, R. B.; Dean, J. M.; Bates, F. S. *Macromolecules* **2001**, *34*, 8593–8595.

Grubbs, R. B.; Dean, J. M.; Broz, M. E.; Bates, F. S. *Macromolecules* **2000**, *33*, 9522-9534.

Guo, F.; Andreasen, J. W.; Vigild, M. E.; Ndoni, S. *Macromolecules* **2007**, *40*, 3669-3675.

Guo, F.; Jankova, K.; Schulte, L.; Vigild, M. E.; Ndoni, S. *Macromolecules* **2008**, *41*, 1486-1493.

Guo, Q.; Dean, J. M.; Grubbs, R. B.; Bates, F. S. *J. Polym. Sci. Part B: Polym. Phys.* **2003**, *41*, 1994-2003.

Guo, Q.; Liu, J.; Chen, L.; Wang, K. *Polymer* **2008**, *49*, 1737-1742.

Guo, Q.; Thomann, R.; Gronski, W.; Staneva, R.; Ivanova, R.; Stuhn, B. *Macromolecules* **2003**, *36*, 3635-3645.

Guo, Q.; Thomann, R.; Gronski, W.; Thurn-Albrecht, T. *Macromolecules* **2002**, *35*, 3133–3144.

Hadjichristidis, N. *J. Polym. Sci. Part A: Polym. Chem*. **1999**, *37*, 857–871.

Hadjichristidis, N.; Iatrou, H.; Pitsikalis, M.; Pispas, S.; Avgeropoulos, A. *Prog. Polym. Sci*. **2005**, *30*, 725-782.

Hadjichristidis, N.; Pitsikalis, M.; Iatrou, H. *Adv. Polym. Sci*. **2005**, *189*, 1–124.

Hadjichristidis, N.; Pitsikalis, M.; Pispas, S.; Iatrou, H. *Chem. Rev*. **2001**, *101*, 3747–3792.

Hahm, J.; Sibener, S. J. *Langmuir* **2000**, *16*, 4766-4769.

Hajduk, D. A.; Takenouchi, H.; Hillmyer, M. A.; Bates, F. S.; Vigild, M. E.; Almdal, K. *Macromolecules* **1997**, *30*, 3788–3795.

Hamley, I. W. J. Phys. *Condens. Matter* **2001**, *13*, R643–R671.

Hancock, L. F. *J. Appl. Polym. Sci*. **1997**, *66*, 1353-1358.

Hancock, L. F.; Fagan, S. M.; Ziolo, M. S. *Biomaterials* **2000**, *21*, 725-733.

Hansen, M. S.; Vigild, M. E.; Berg, R. H.; Ndoni, S. *Polym. Bull*. **2004**, *51*, 403–409.

Hawker, C. J.; Russell, T. P. *MRS Bull*. **2005**, *30*, 952-966.

Hedrick, J. L.; Yilgör, I.; Wilkes, G. L.; McGrath, J. E. *Polym. Bull*. **1985**, *13*, 201-208.

Hedrick, J.; Labadie, J.; Russell, T.; Hofer, D.; Wakharker, V. *Polymer* **1993**, *34*, 4717–4726.

Henk, P. O.; Kortsen, T. W.; Kvarts, T. *High Perform. Polym*. **1999**, *11*, 281-296.

Hermel-Davidock, T. J.; Tang, H. S.; Murray, D. J.; Hahn, S. F. *J. Polym. Sci., Part B: Polym. Phys*. **2007**, *45*, 3338–3348.

Hester, J. F.; Banerjee, P.; Mayes, A. M. *Macromolecules* **1999**, *32*, 1643-1650.

Hester, J. F.; Banerjee, P.; Won, Y.; Akthakul, A.; Acar, M. H.; Mayes, A. M. *Macromolecules* **2002**, *35*, 7652-7661.

Hester, J. F.; Mayes, A. M. *J. Membr. Sci*. **2002**, 2*02*, 119-135.

Hiemenz, P. C.; Lodge, T. P. In *Polymer Chemistry*; CRC Press: Boca Raton, **2007**; Vol. 2nd Edition.

Hillmyer, M. A. *Adv. Polym. Sci.* **2005**, *190*, 137-181.

Hillmyer, M. A.; Bates, F. S. *Macromolecules* **1996**, *29*, 6994–7002.

Hillmyer, M. A.; Grubbs, R. H. *Macromolecules* **1993**, *26*, 872-874.

Hillmyer, M. A.; Grubbs, R. H. *Macromolecules* **1995**, *28*, 8662-8667.

Hillmyer, M. A.; Lipic, P. M.; Hajduk, D. A.; Almdal, K.; Bates, F. S. *J. Am. Chem. Soc*. **1997**, *119*, 2749–2750.

Hillmyer, M. A.; Nguyen, S. T.; Grubbs, R. H. *Macromolecules* **1997**, *30*, 718-721.

Hoek, Eric M. V.; Jawor, A. In "Nanofiltration Separations"; Schwarz, J. A., Contescu, C. I. and Putyera, K., Eds.; *Encyclopedia of Nanoscience and Nanotechnology*; Marcel Dekker: New York, **2004**; Vol. 1, pp 2399–2412.

Hsieh, H. L.; Quirk, R. P. In "Chapter 10: Copolymerization;" *Anionic Polymerization: Principles and Practical Applications*; Marcel Dekker, Inc.: New York, **1996**; pp 237.

Hu, D.; Xu, Z.; Zeng, K.; Zheng, S. *Macromolecules* **2010**, *43*, 2960-2969.

Huang, E.; Rockford, L.; Russell, T. P.; Hawker, C. J. *Nature* **1998**, 3*95*, 757-758.

Hunter, D. L.; Kamena, K. W.; Paul, D. R. *MRS Bull*. **2007**, *32*, 323-327.

Inoue, T. *Prog. Polym. Sci*., **1995**, *20*, 119-153.

Ishizu, K.; Uchida, S. *Prog. Polym. Sci*. **1999**, *24*, 1439–1480.

Jaffrennou, B.; Portal, J.; Méchin, F.; Pascault, J. *Eur. Polym. J*. **2008**, *44*, 3439-3455.

Jeong, U.; Kim, H.; Rodriguez, R. L.; Tsai, I. Y.; Stafford, C. M.; Kim, J. K.; Hawker, C. J.; Russell, T. P. *Adv. Mater*. **2002**, *14*, 274-276.

Jeong, U.; Ryu, D. Y.; Kho, D. H.; Lee, D. H.; Kim, J. K.; Russell, T. P. *Macromolecules* **2003**, *36*, 3626-3634.

Jeong, U.; Ryu, D. Y.; Kim, J. K.; Kim, D. H.; Russell, T. P.; Hawker, C. J. *Adv. Mater*. **2003**, *15*, 1247-1250.

Jeong, U.; Ryu, D. Y.; Kim, J. K.; Kim, D. H.; Wu, X.; Russell, T. P. *Macromolecules* **2003**, *36*, 10126-10129.

Jeong, W.; Kessler, M. R. *Chem. Mater*. **2008**, *20*, 7060–7068.

Jordan, J.; Jacob, K. I.; Tannenbaum, R.; Sharaf, M. A.; Jasiuk, I. *Mater. Sci. Eng., A* **2005**, *393*, 1-11.

Kang, S.; Asatekin, A.; Mayes, A. M.; Elimelech, M. *J. Membr. Sci*. **2007**, *296*, 42-50.

Khandpur, A. K.; Foerster, S.; Bates, F. S.; Hamley, I. W.; Ryan, A. J.; Bras, W.; Almdal, K.; Mortensen, K. *Macromolecules* **1995**, *28*, 8796–8806.

Kiefer, J.; Hedrick, J. L.; Hilborn, J. G. *Adv Polym Sci* **1999**, *147*, 161-247.

Kim, G.; Libera, M. *Macromolecules* **1998**, *31*, 2569-2577.

Kim, S. O.; Solak, H. H.; Stoykovich, M. P.; Ferrier, N. J.; de Pablo, J. J.; Nealey, P. F. *Nature* **2003**, *424*, 411-414.

Kim, S.; Misner, M.; Xu, T.; Kimura, M.; Russell, T. *Adv. Mater*. **2004**, *16*, 226-231.

Kim, Y. J.; Sung, Y. K.; Piao, A. Z.; Grainger, D. W.; Okano, T.; Kim, S. W. *J. Appl. Polym. Sci*. **1994**, *54*, 1863–1872.

Klouda, L.; Mikos, A. G. *Eur. J. Pharm. Biopharm*. **2008**, *68*, 34-45.

Koehler, R. D.; Schubert, K. -.; Strey, R.; Kaler, E. W. *J. Chem. Phys*. **1994**, *101*, 10843-10849.

Könczöl, L.; Döll, W.; Buchholz, U.; Mülhaupt, R. *J. Appl. Polym. Sci*. **1994**, 54, 815-826.

Koppi, K. A.; Tirrell, M.; Bates, F. S. *Phys. Rev. Lett*. **1993**, *70*, 1449.

Kosonen, H.; Ruokolainen, J.; Nyholm, P.; Ikkala, O. *Macromolecules* **2001**, *34*, 3046-3049.

Kosonen, H.; Ruokolainen, J.; Nyholm, P.; Ikkala, O. *Polymer*, **2001**, *42*, 9481–9486.

Kosonen, H.; Ruokolainen, J.; Torkkeli, M.; Serimaa, R.; Nyholm, P.; Ikkala, O. *Macromol. Chem. Phys*. **2002**, *203*, 388-392.

Kosonen, H.; Valkama, S.; Nykänen, A.; Toivanen, M.; ten Brinke, G.; Ruokolainen, J.; Ikkala, O. *Adv. Mater*. **2006**, *18*, 201-205.

Krausch, G.; Magerle, R. *Adv. Mater*. **2002**, *14*, 1579-1583.

Kumar, A.; Jang, S.; Padilla, J.; Otero, T. F.; Sotzing, G. A. *Polymer* **2008**, *49*, 3686-3692.

Kumar, A.; Srivastava, A.; Galaev, I. Y.; Mattiasson, B. *Prog. Polym. Sci*. **2007**, *32*, 1205-1237.

Lai, J. T.; Filla, D.; Shea, R. *Macromolecules* **2002**, *35*, 6754-6756.

Larrañaga, M.; Arruti, P.; Serrano, E.; de la Caba, K.; Remiro, P.; Riccardi, C.; Mondragon, I. *Colloid Polym. Sci*. **2006**, *284*, 1419-1430.

Larrañaga, M.; Gabilondo, N.; Kortaberria, G.; Serrano, E.; Remiro, P.; Riccardi, C. C.; Mondragon, I. *Polymer*, **2005**, *46*, 7082-7093.

Larrañaga, M.; Martín, M.; Gabilondo, N.; Kortaberria, G.; Corcuera, M.; Riccardi, C.; Mondragon, I. *Polym. Int*. **2004**, *53*, 1495-1502.

Larrañaga, M.; Martin, M.; Gabilondo, N.; Kortaberria, G.; Eceiza, A.; Riccardi, C.; Mondragon, I. *Colloid Polym. Sci*. **2006**, *284*, 1403-1410.

Larrañaga, M.; Serrano, E.; Martin, M. D.; Tercjak, A.; Kortaberria, G.; de la Caba, K.; Riccardi, C. C.; Mondragon, I. *Polym. Int*. **2007**, *56*, 1392-1403.

Lee, J. S.; Hirao, A.; Nakahama, S. *Macromolecules* **1988**, *21*, 274–276.

Lee, M.; Park, M.; Oh, N.; Zin, W.; Jung, H.; Yoon, D. K. *Angew. Chem. Int. Ed*. **2004**, *43*, 6465–6468.

Leibler, L. Macromo*l*ecules **1980**, *13*, 1602–1617.

Leiston-Belanger, J. M.; Russell, T. P.; Drockenmuller, E.; Hawker, C. J. *Macromolecules* **2005**, *38*, 7676-7683.

Li, A.; Ma, J.; Wooley, K. L. *Macromolecules* **2009**, *42*, 5433-5436.

Liang, C.; Hong, K.; Guiochon, G. A.; Mays, J. W.; Dai, S. *Angew. Chem. Int. Ed*. **2004**, *43*, 5785-5789.

Lichterfeld, F.; Schmeling, T.; Strey, R. *J. Phys. Chem*. **1986**, *90*, 5762-5766.

Lipic, P. M.; Bates, F. S.; Hillmyer, M. A. *J. Am. Chem. Soc*. **1998**, *120*, 8963–8970.

Liu, G.; Ding, J.; Hashimoto, T.; Kimishima, K.; Winnik, F. M.; Nigam, S. *Chem. Mater*. **1999**, *11*, 2233-2240.

Liu, G.; Ding, J.; Stewart, S. *Angew. Chem. Int. Ed*. 1999, *38*, 835-838.

Liu, J. ; Sue, H.; Thompson, Z. J.; Bates, F. S.; Dettloff, M.; Jacob, G.; Verghese, N.; Pham, H. *Macromolecules* **2008**, *41*, 7616–7624.

Lodge, T. P. Macromol. *Chem. Phy*. **2003**, *204*, 265–273.

Lowell, S. In *Introduction to Powder Surface Area*; John Wiley and Sons: New York, **1979**; pp 199.

Lue, S. J.; Hsu, J.; Chen, C.; Chen, B. *J. Membr. Sci*. **2007**, *301*, 142-150.

Lynd, N. A. *The Effects of Polydispersity on Block Copolymer Self-assembly*, University of Minnesota, Ann Arbor, MI, **2007**.

Mahanthappa, M. K.; Bates, F. S.; Hillmyer, M. A. *Macromolecules* **2005**, *38*, 7890-7894.

Mansky, P.; Liu, Y.; Huang, E.; Russell, T. P.; Hawker, C. *Science* **1997**, *275*, 1458-1460.

Mao, H.; Arrechea, P. L.; Bailey, T. S.; Johnson, B. J. S.; Hillmyer, M. A. *Faraday Discuss*. **2005**, *128*, 149-162.

Mao, H.; Hillmyer, M. A. *Soft Mater* **2006**, *2*, 57–59.

Matsen, M. W.; Bates, F. S. *Macromolecules* **1996**, *29*, 1091–1098.

Matsen, M. W.; Schick, M. *Phys. Rev. Lett*. **1994**, *72*, 2660.

Mehta, A.; Zydney, A. L. *J. Membr. Sci*. **2005**, *249*, 245-249.

Mendes, P. M. *Chem. Soc. Rev*. **2008**, *37*, 2512-2529.

Meng, F.; Xu, Z.; Zheng, S. *Macromolecules* **2008**, *41*, 1411-1420.

Meng, F.; Yi, F.; Zheng, S. *J. Macromol. Sci. Part B Phys*. **2008**, *47*, 450-462.

Meng, F.; Zheng, S.; Li, H.; Liang, Q.; Liu, T. *Macromolecules* **2006**, *39*, 5072-5080.

Meng, F.; Zheng, S.; Liu, T. *Polymer*, **2006**, *47*, 7590-7600.

Meng, F.; Zheng, S.; Zhang, W.; Li, H.; Liang, Q. *Macromolecules* **2006**, *39*, 711–719.

Mijovic, J.; Shen, M.; Sy, J. W.; Mondragon, I. *Macromolecules* **2000**, *33*, 5235–5244.

Miyaki, Y.; Iwata, M.; Fujita, Y.; Tanisugi, H.; Isono, Y.; Fujimoto, T. *Macromolecules* **1984**, *17*, 1907–1912.

Morkved, T. L.; Lu, M.; Urbas, A. M.; Ehrichs, E. E.; Jaeger, H. M.; Mansky, P.; Russell, T. P. *Science* **1996**, *273*, 931-933.

Morkved, T. L.; Stepanek, P.; Krishnan, K.; Bates, F. S.; Lodge, T. P. *J. Chem. Phys*. **2001**, *114*, 7247-7259.

Muller, A. J.; Balsamo, V.; Arnal, M. L. *Adv. Polym. Sci*. **2005**, *190*, 1–63.

Ndoni, S.; Vigild, M. E.; Berg, R. H. *J. Am. Chem. Soc*. **2003**, *125*, 13366–13367.

Nelson, J. K.; Hu, Y. *J. Phys. D* **2005**, *38*, 213-222.

Ni, Y.; Zheng, S. *Macromolecules* **2007**, *40*, 7009-7018.

Nunes, S. P.; Peinemann, K. V. In *Membrane Technology in the Chemcial Industry*, Second Edition; Wiley-VCH: Weinheim, Germany, **2006**.

Nuxoll, E. E.; Hillmyer, M. A.; Wang, R.; Leighton, C.; Siegel, R. A. A*CS Appl. Mater. Interfaces* **2009**, *1*, 888-893.

Ocando, C.; Serrano, E.; Tercjak, A.; Pena, C.; Kortaberria, G.; Calberg, C.; Grignard, B.; Jerome, R.; Carrasco, P. M.; Mecerreyes, D.; Mondragon, I. *Macromolecules* **2007**, *40*, 4068-4074.

Ocando, C.; Tercjak, A.; Martin, M. D.; Ramos, J. A.; Campo, M.; Mondragon, I. *Macromolecules* **2009**, *42*, 6215-6224.

Ocando, C.; Tercjak, A.; Serrano, E.; Ramos, J. A.; Corona-Galván, S.; Parellada, M. D.; Fernández-Berridi, M. J.; Mondragon, I. *Polym. Int*. **2008**, *57*, 1333–1342.

Olayo-Valles, R.; Lund, M. S.; Leighton, C.; Hillmyer, M. A. *J. Mater. Chem*. **2004**, *14*, 2729–2731.

Olson, D. A.; Chen, L.; Hillmyer, M. A. *Chem. Mater*. **2008**, *20*, 869-890.

Park, C.; Yoon, J.; Thomas, E. L. *Polymer* **2003**, *44*, 6725–6760.

Pascault, J.; Sautereau, H.; Verdu, J.; Williams, R. J. J. In *Thermosetting Polymers*; Marcel Dekker: New York, NY, **2002**; pp 485.

Peinemann, K.; Abetz, V.; Simon, P. F. W. *Nat. Mater*. **2007**, *6*, 992-996.

Phillip, W. A. *Block Polymer Membranes for Selective Separations*, University of Minnesota, Ann Arbor, MI, **2009**.

Phillip, W. A.; Amendt, M.; O'Neill, B.; Chen, L.; Hillmyer, M. A.; Cussler, E. L. *ACS Appl. Mater. Interfaces* **2009**, *1*, 472–480.

Phillip, W. A.; Martono, E.; Chen, L.; Hillmyer, M. A.; Cussler, E. L. *J. Membr. Sci.* **2009**, *337*, 39–46.

Phillip, W. A.; O'Neill, B.; Rodwogin, M.; Hillmyer, M. A.; Cussler, E. L. *ACS Appl. Mater. Interfaces* **2010**, *2*, 847-853.

Phillip, W. A.; Rzayev, J.; Hillmyer, M. A.; Cussler, E. L. *J. Membr. Sci*. **2006**, *286*, 144-152.

Pitet, L. M.; Amendt, M. A.; Hillmyer, M. A. *J. Am. Chem. Soc*. **2010**, *132*, 8230-8231.

Pitet, L. M.; Hillmyer, M. A. *Macromolecules* **2009**, *42*, 3674-3680.

Pitsikalis, M.; Pispas, S.; Mays, J. W.; Hadjichristidis, N. *Adv. Polym. Sci*. **1998**, *135*, 1–137.

Pratt, R. C.; Lohmeijer, B. G. G.; Long, D. A.; Waymouth, R. M.; Hedrick, J. L. *J. Am. Chem. Soc*. **2006**, *128*, 4556-4557.

Preishuber-Pflügl, P.; Podolan, R.; Stelzer, F. *J. Mol. Catal. A: Chem*. **2000**, *160*, 53-61.

Rana, D.; Matsuura, T. *Chem. Rev.* **2010**, *110*, 2448-2471.

Rebizant, V.; Abetz, V.; Tournilhac, F.; Court, F.; Leibler, L. *Macromolecules* **2003**, *36*, 9889-9896.

Rebizant, V.; Venet, A.; Tournilhac, F.; Girard-Reydet, E.; Navarro, C.; Pascault, J.; Leibler, L. *Macromolecules* **2004**, *37*, 8017–8027.

Riffle, J. S.; Steckle, W. P., Jr; White, K. A.; Ward, R. S. *Polym. Preprints* **1985**, *26*, 251-252.

Ritzenthaler, S.; Court, F.; David, L.; Girard-Reydet, E.; Leibler, L.; Pascault, J. P. *Macromolecules* **2002**, *35*, 6245-6254.

Ritzenthaler, S.; Court, F.; Girard-Reydet, E.; Leibler, L.; Pascault, J. P. *Macromolecules* **2003**, *36*, 118–126.

Roux, S. P.; Jacobs, E. P.; Reenen, A. J. v.; Morkel, C.; Meincken, M. *J. Membr. Sci*. **2006**, *276*, 8-15.

Ruiz-Pérez, L.; Royston, G. J.; Fairclough, J. P. A.; Ryan, A. J. *Polymer* **2008**, *49*, 4475-4488.

Rzayev, J.; Hillmyer, M. A. *J. Am. Chem. Soc*. **2005**, *127*, 13373-13379.

Rzayev, J.; Hillmyer, M. A. *Macromolecules* **2005**, *38*, 3–5.

Sandler, J.; Shaffer, M. S. P.; Prasse, T.; Bauhofer, W.; Schulte, K.; Windle, A. H. *Polymer* **1999**, *40*, 5967-5971.

Saxena, A.; Tripathi, B. P.; Kumar, M.; Shahi, V. K. *Adv. Colloid Interface Sci*. **2009**, *145*, 1-22.

Schellekens, M.; Klumperman, B. *J. Macromol. Sci., Rev. Macromol. Chem. Phys*. **2000**, *40*, 167.

Schild, H. G. *Prog. Polym. Sci*. **1992**, *17*, 163-249.

Schitter, R. M. E.; Jocham, D.; Stelzer, F.; Moszner, N.; Völkel, T. *J. Appl. Polym. Sci*. **2000**, *78*, 47-60.

Schmidt, S. C.; Hillmyer, M. A. *Macromolecules* **1999**, *32*, 4794–4801.

Schubert, K. -.; Strey, R.; Kline, S. R.; Kaler, E. W. *J. Chem. Phys*. **1994**, *101*, 5343-5355.

Schubert, K.; Strey, R. *J. Chem. Phys*. **1991**, *95*, 8532-8545.

Scriven, L. E. *Nature* **1976**, *263*, 123–125.

Serrano, E.; Gerard, P.; Lortie, F.; Pascault, J.; Portinha, D. *Macromol. Mater. Eng*. **2008**, *293*, 820–827.

Serrano, E.; Larrañaga, M.; Remiro, P. M.; Mondragon, I.; Carrasco, P. M.; Pomposo, J. A.; Mecerreyes, D. *Macromol. Chem. Phys*. **2004**, *205*, 987–996.

Serrano, E.; Martin, M. D.; Tercjak, A.; Pomposo, J. A.; Mecerreyes, D.; Mondragon, I. *Macromol. Rapid Commun*. **2005**, *26*, 982–985.

Serrano, E.; Tercjak, A.; Kortaberria, G.; Pomposo, J. A.; Mecerreyes, D.; Zafeiropoulos, N. E.; Stamm, M.; Mondragon, I. *Macromolecules* **2006**, *39*, 2254–2261.

Serrano, E.; Tercjak, A.; Ocando, C.; Larrañaga, M.; Parellada, M. D.; Corona-Galván, S.; Mecerreyes, D.; Zafeiropoulos, N. E.; Stamm, M.; Mondragon, I. *Macromol. Chem. Phys*. **2007**, *208*, 2281–2292.

Seyhan, A. T.; Gojny, F. H.; Tanoğlu, M.; Schulte, K. *Euro. Polym. J*. **2007**, *43*, 374-379.

Shannon, M. A.; Bohn, P. W.; Elimelech, M.; Georgiadis, J. G.; Marinas, B. J.; Mayes, A. M. *Nature* **2008**, *452*, 301-310.

Shannon, M. A.; Semiat, R. *MRS Bulletin* **2008**, *33*, 9–15.

Shtanko, N. I.; Kabanov, V. Y.; Apel, P. Y.; Yoshida, M.; Vilenskii, A. I. *J. Membr. Sci*. **2000**, *179*, 155-161.

Singh, R. In *Hybrid Membrane Systems for Water Purification*; Elsevier: Oxford, **2006**.

Sinturel, C.; Vayer, M.; Erre, R.; Amenitsch, H. *Macromolecules* **2007**, *40*, 2532-2538.

Sixun, Z.; Naibin, Z.; Xiaolie, L.; Dezhu, M. *Polymer* **1995**, *36*, 3609-3613.

Sperschneider, A.; Schacher, F.; Gawenda, M.; Tsarkova, L.; Müller, A. H.; Ulbricht, M.; Krausch, G.; Köhler, J. *Small* **2007**, *3*, 1056-1063.

Standard Test Method for Molecular Weight Cutoff Evaluation of Flat Sheet Ultrafiltration Membranes; ASTM-ASTM International, **2001**; ASTM E 1343-90 (reapproved 2001)

Storey, R. F.; Scheuer, A. D.; Achord, B. C. *Polymer* **2005**, 46, 2141-2152.

Strathmann, H. *AIChE Journal* **2001** *47*, 1077–1087.

Tang, H. S.; Hermel-Davidock, T. J.; Hahn, S. F.; Murray, D. J.; Cieslinski, R. C.; Verghese, N. E.; Pham, H. Q. *J. Polym. Sci., Part B: Polym. Phys*. **2009**, *47*, 393–406.

Teubner, M.; Strey, R. *J. Chem. Phys*. **1987**, *87*, 3195.

Thio, Y. S.; Wu, J.; Bates, F. S. *Macromolecules* **2006**, *39*, 7187-7189.

Thurman, E. M. In *Organic Geochemistry of Natural Waters*; Martinus Nighoff/Dr. W. Junk: Hingham, MA, **1985**; pp 497.

Thurn-Albrecht, T.; Schotter, J.; Kastle, G. A.; Emley, N.; Shibauchi, T.; Krusin-Elbaum, L.; Guarini, K.; Black, C. T.; Tuominen, M. T.; Russell, T. P. *Science* **2000**, *290*, 2126-2129.

Thurn-Albrecht, T.; Steiner, R.; DeRouchey, J.; Stafford, C. M.; Huang, E.; Bal, M.; Tuominen, M.; Hawker, C. J.; Russell, T. P. *Adv. Mater.* **2000**, *12*, 787–791.

Tobolsky, A. V.; Boudreau, R. J. *J. Polym. Sci*. **1961**, *51*, S53–S56.

Uehara, H.; Kakiage, M.; Sekiya, M.; Sakuma, D.; Yamonobe, T.; Takano, N.; Barraud, A.; Meurville, E.; Ryser, P. *ACS Nano* **2009**, *3*, 924-932.

Uehara, H.; Yoshida, T.; Kakiage, M.; Yamanobe, T.; Komoto, T.; Nomura, K.; Nakajima, K.; Matsuda, M. *Macromolecules* **2006**, *39*, 3971–3974.

Ulbricht, M. *Polymer* **2006**, *47*, 2217-2262.

UN Millennium Project Task Force on Water and Sanitation In *Health Dignity and Development: What Will It Take?* Earthscan: London, **2005**; Vol. Final Report.

United Nations Educational Scientific and Cultural Organization World Water Assessment Program In *Water for People, Water for Life—the United Nations World Water Development Report*; Berghahn Books: Barcelona, **2003**.

van de Witte, P.; Dijkstra, P. J.; van den Berg, J. W. A.; Feijen, J. *J. Membr. Sci*. **1996**, *117*, 1-31.

van der Bruggen, B.; Vandecasteele, C.; Van Gestel, T.; Doyen, W.; Leysen, R. *Environ. Prog*. **2003**, *22*, 46-56.

van Reis, R.; Zydney, A. *Curr. Opin. Biotechnol*. **2001**, *12*, 208-211.

van Reis, R.; Zydney, A. *J. Membr. Sci*. **2007**, *297*, 16-50.

Wang, S.; Zhu, Y. *Langmuir* **2009**, *25*, 13448-13455.

Wang, Y.; Hillmyer, M. A. *Macromolecules* **2000**, *33*, 7395–7403.

Wang, Y.; Wang, T.; Su, Y.; Peng, F.; Wu, H.; Jiang, Z. *Langmuir* **2005**, *21*, 11856-11862.

Williams, R. J. J.; Rozenberg, B. A.; Pascault, J. *Adv. Polym. Sci*. **1997**, *128*, 95-156.

Winey, K. I.; Kashiwagi, T.; Mu, M. *MRS Bull*. **2007**, *32*, 348-353.

Winter, H. H.; Scott, D. B.; Gronski, W.; Okamoto, S.; Hashimoto, T. *Macromolecules* **1993**, *26*, 7236-7244.

Wu, J.; Thio, Y. S.; Bates, F. S. *J. Polym. Sci. Part B: Polym. Phys*. **2005**, *43*, 1950-1965.

Xia, Y.; Yin, X.; Burke, N. A. D.; Stover, H. D. H. *Macromolecules* **2005**, *38*, 5937-5943.

Xie, M.; Kong, Y.; Han, H.; Shi, J.; Ding, L.; Song, C.; Zhang, Y. *React. Funct. Polym*. **2008**, *68*, 1601-1608.

Xu, Z.; Hameed, N.; Guo, Q.; Mai, Y. *J. Appl. Polym. Sci*. **2010**, *115*, 2110-2118.

Xu, Z.; Zheng, S. *Macromolecules* **2007**, *40*, 2548–2558.

Yang, S. Y.; Park, J.; Yoon, J.; Ree, M.; Jang, S. K.; Kim, J. K. *Adv. Funct. Mater*. **2008**, *18*, 1371-1377.

Yang, S. Y.; Ryu, I.; Kim, H. Y.; Kim, J. K.; Jang, S. K.; Russell, T. P. *Adv. Mater*. **2006**, *18*, 709-712.

Yi, F.; Zheng, S.; Liu, T. *J. Phys. Chem. B* **2009**, *113*, 1857-1868.

Yin, M.; Zheng, S. *Macromol. Chem. Phys*. **2005**, *206*, 929-937.

Zalusky, A. S.; Olayo-Valles, R.; Taylor, C. J.; Hillmyer, M. A. *J. Am. Chem. Soc*. **2001**, *123*, 1519-1520.

Zalusky, A. S.; Olayo-Valles, R.; Wolf, J. H.; Hillmyer, M. A. *J. Am. Chem. Soc*. **2002**, *124*, 12761–12773.

Zammarano, M.; Franceschi, M.; Bellayer, S.; Gilman, J. W.; Meriani, S. *Polymer* **2005**, *46*, 9314–9328.

Zeng, K.; Wang, L.; Zheng, S.; Qian, X. *Polymer* **2009**, *50*, 685-695.

Zeng, K.; Zheng, S. *J. Phys. Chem. B* **2007**, *111*, 13919-13928.

Zhang, G.; Zhang, J.; Wang, S.; Shen, D. *J. Polym. Sci., Part B: Polym. Phys*. **2003**, *41*, 23-30.

Zhang, M.; Yang, L.; Yurt, S.; Misner, M. J.; Chen, J.; Coughlin, E. B.; Venkataraman, D.; Russell, T. P. *Adv. Mater*. **2007**, *19*, 1571–1576.

Zhong, Z.; Guo, Q. *Polymer* **1998**, *39*, 517-523.

Zhou, G.; Movva, S.; Lee, L. J. *J Appl. Polym. Sci*. **2008**, *108*, 3720-3726.

Zhou, N.; Bates, F. S.; Lodge, T. P. *Nano Lett*. **2006**, *6*, 2354–2357.

Appendix A.

Nanoporous poly(dicyclopentadiene) membranes for virus filtrations

This appendix reports on initial investigations into the potential of poly(norbornenylethyl styrene-*s*-styrene)-*b*-poly(lactide) (PNS-PLA) templated poly(dicyclopentadiene) membranes for virus filtrations. Two sets of filtrations of minute virus of mice with membranes 100 and 30 μm thick were performed with varying degrees of success. Overall, the experiments were hindered by slow fluxes due to the thicknesses of the membranes, which prevented fully vetting the virus rejection behavior of the membrane.

A.1. Introduction

The separation and purification of cells, bacteria, DNA, proteins and viruses is of critical importance to developing and producing biological materials, and the diverse array of membrane based filtration technologies has lent itself well to the challenge of separating biomolecules.[1,2,3] For example microfiltration is often used for the separation of proteins from bacteria or cells,[2] while ultrafiltration can be used to concentrate and purify a protein of interest.[3]

A critical consideration for any membrane based filtration is the permeability and selectivity of the membrane,[1] which ultimately must be matched to the purification and throughput requirements for the final biological material.[2] Mehta and Zydney compiled an analysis of the separation efficiencies for a variety of commercially available ultrafiltration membranes for isolating the protein bovine serum albumin.[4] Their analysis indicated an upper limit of membrane performance due to the tradeoffs between permeability and selectivity. Specifically, in order to realize higher selectivities, membranes with smaller pore sizes are required leading to lower permeabilities, while higher permeabilities are achieved at the cost of the selectivity. Breaking through this apparent performance barrier would further increase the efficiency of membrane based filtrations allowing for higher throughput while maintaining high selectivities during the purification process.

Materials recently investigated as an alternative to current ultrafiltration membranes with the potential for achieving higher permeabilities and selectivities[5] are

nanoporous materials derived from block polymers. Block polymers are composed of two or more segments of chemically distinct monomers covalently bound that self-assemble into phase separated morphologies with nanometer length scales.[6,7,8,9] Selective removal of one of the polymeric segments renders the material nanoporous, and since the pores are templated by the self-assembled structure (typically a cylindrical morphology) a narrow pore size distribution results.[10,11]

Block polymer derived membranes have been produced by different techniques to evaluate their potential for separating biomaterials. Composite membranes with pore sizes of 15 and 17 nm formed by removing the cylindrical domains from a block polymer thin film supported by a microfiltration membrane, demonstrated excellent removal of human rhinovirus 14 with fluxes of 30-50 L/m^2 hr at 0.1 bar.[12,13] An asymmetric membrane with an ordered separation layer and a highly porous substructure resulting from the non-solvent induced phase separation of a block polymer with hydrophobic and hydrophilic segments exhibited 82% rejection of bovine serum albumin with a flux of 20 L/m^2 hr at 0.5 bar.[14] While these examples demonstrate the promise of block polymer membranes one of the challenges associated with these materials is the matrix component is poly(styrene), which is inherently a brittle polymer possibly limiting the operating pressure ranges of these materials.

More robust block polymer based membranes formed by the reaction induced phase separation of a doubly reactive block polymer, poly(norbornenylethylstyrene-*s*-styrene)-*b*-poly(lactide) (PNS-PLA) and dicyclopentadiene (DCPD) were recently

reported.[15] The resulting microphase separated structure is bicontinuous, so subsequent removal of the PLA component results in the formation of a nanoporous bicontinuous structure which precludes the need for alignment to achieve continuous pores through the material. Having already reported the flux and MWCO characteristics of the PNS-PLA/PDCPD membranes in Chapter 3,[16] this appendix reports on initial investigations into virus filtrations using the PNS-PLA/PDCPD membranes. This work was done in collaboration with Justin Weaver in Professor Ranil Wickramasinghe's research group at Colorado State University.

A.2. Results and Discussion

A.2.1. Membrane formation

Two films for membranes were templated by a PNS-PLA block polymer with a molecular weight of 69 kg/mol and a PLA weight fraction of 61%. Films were formed by dissolving the block polymer (67 wt %) and DCPD (33 wt %) in THF; to the casting solution, a second solution of second-generation Grubbs catalyst (0.5 wt %) was added, and the solutions were stirred for 5 seconds before being cast onto a glass plate using a doctors blade. The solutions were cast at two concentrations to attain different film thicknesses. Specifically, film F100 was cast at 25 wt % and was 100μm thick, while film F30 was cast at 15 wt % and had a thickness of 30μm. The cast membranes were cured overnight, removed from the glass, and the PLA portion was selectively removed by mild basic hydrolysis. Removal of the PLA component was confirmed by the percent mass loss of the film and by fourier transfer infrared-spectroscopy (FT-IR) of the films both

before and after etching. IR of the film (see Figure A.1) shows almost complete disappearance of the peak at 1750 cm^{-1} indicative of the loss of the carbonyl stretch of the PLA. Table A.1summarizes the film compositions used for these studies, and Figure A.1 shows the FT-IR for film F100.

Table A.1. Composition and mass loss data for the two crosslinked films

Film	PNS-PLA (wt %)	DCPD (wt %)	Casting Concentration (wt %)	PLA (wt %)	mass loss (wt %)
F100	67	33	25	41	51
F30	67	33	15	41	52

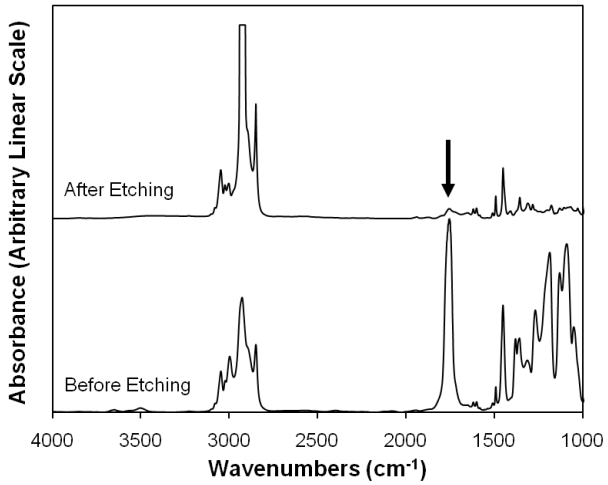

Figure A.1. FT-IR spectra of the F100 film before (lower) and after (upper) etching. The peat at1755 cm^{-1} (arrow) indicates the position of the PLA carbonyl stretch which is practically absent after etching.

The morphology of the films was investigated using small-angle X-ray scattering (SAXS) and scanning electron microscopy (SEM). Scattering patterns of the films both before and after etching (see Figure A.2) revealed a single broad scattering peak

indicative of a microphase separated but disordered structure. The increased scattering intensity of the etched film is consistent with the creation a nanoporous material.

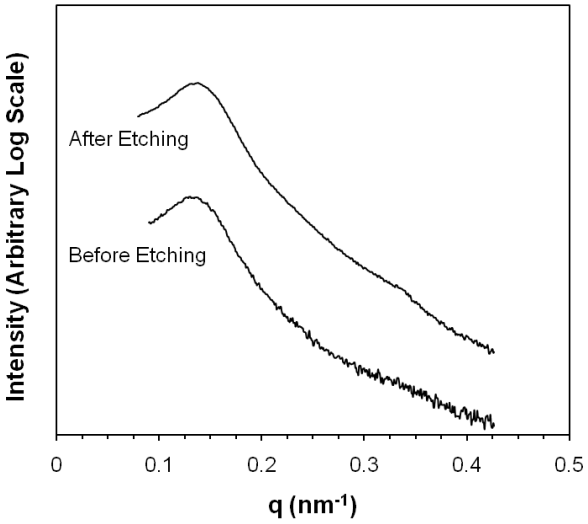

Figure A.2. One-dimensional SAXS profiles for the F100 film both before and after etching acquired at room temperature.

The scattering patterns were fit using the Teubner-Strey microemulsion model (equation A.1)[17] as the films exhibited a bicontinuous structure (see Figure A.3).

$$I(q) \sim \frac{1}{a_2 + c_1 q^2 + c_2 q^4} \qquad (A.1)$$

In equation A.1 *I(q)* is the scattering intensity, q the principle scattering vector, and a_2, c_1 and c_2 are fitting constants. The principal domain spacing (D) can be determined from the fitting constants using equation A.2.[18]

$$D = 2\pi \left[\frac{1}{2} \left(\frac{a_2}{c_2} \right)^{1/2} - \frac{1}{4} \frac{c_1}{c_2} \right]^{-1/2} \qquad (A.2)$$

The domain spacing for the F100 film was 46.1 and 45.3 nm before and after etching respectively indicating preservation nanostructure. Scattering was not observed for the F30 film most likely due to how thin it was, but it is expected to have the same domain spacing as F100 since it was templated by the same block polymer.

Prior to SEM, the film surfaces were etched using an oxygen reactive ion etch to remove a thin nonporous PDCPD "skin" that forms during curing.[15] SEM micrographs of the film surfaces (Figure A.3) revealed a bicontinuous structure of pores and matrix material for both the F100 and F30 films.

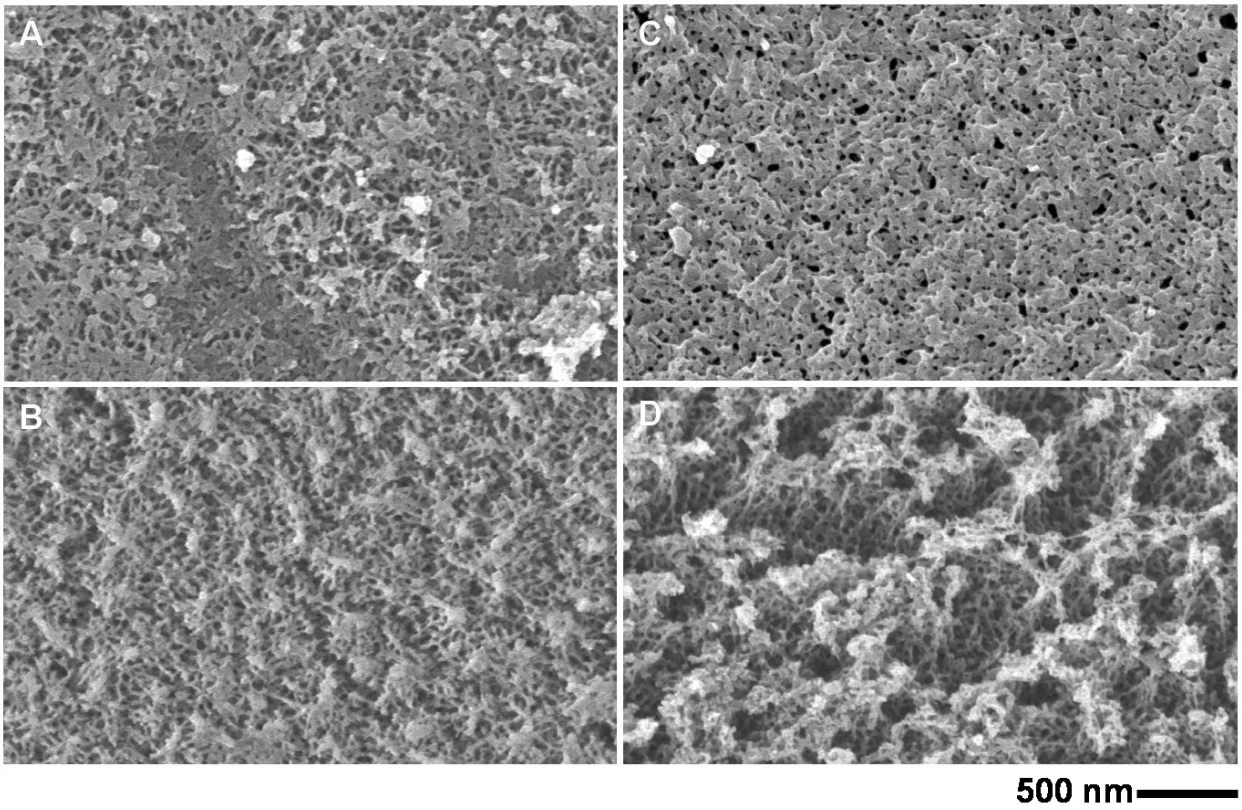

Figure A.3. SEM micrographs of both sides of the F100 (A and B) and F30 (C and D) films.

A.2.2. Virus Filtrations

The potential for virus filtration was examined by filtering solutions of minute virus of mice (MVM) using a normal flow filtration stirred cell. The membranes were tested by first monitoring the flux of either an acetate-buffered solution (pH 6.0) or a tris-buffered solution (pH 9.0) across the membrane. After establishing a baseline flux, the feed solution was exchanged with a buffered solution with a virus concentration around 10^{10} particles/mL and fractions were collected periodically while the flux was monitored. The virus particle concentration in the permeate fractions was then determined by quantitative polymerase chain reaction (QPCR) and compared to the virus concentration in the feed solution.

The F100 membrane was initially challenged using both the acetate-buffered (pH 6.0) and tris-buffered (pH 9.0) solutions at a pressure of 15 PSI. Under both conditions, the flux across the membrane differed only slightly with an average flux of 3.8 LMH and 3.6 LMH for the acetate and tris-buffered solutions respectively. Minimal variations in the flux throughout each trial were observed as can be seen in Figure A.4. For the acetate-buffered trial 6 fractions were collected and analyzed by QPCR for the presence of virus titer, while two fractions were analyzed from the tris-buffered trial. For all the permeate fractions, the concentration of virus particles was at or below the limit of detection for the QPCR assay (14 virus eq./μL) corresponding to a concentration in the fraction of 1.40 x 10^5 virus eq./mL or less, which corresponds to at least a log reduction value (LRV) of 5.5

when compared to the initial concentration (5.26 x 10^{10} virus eq./mL) of the feed solution.

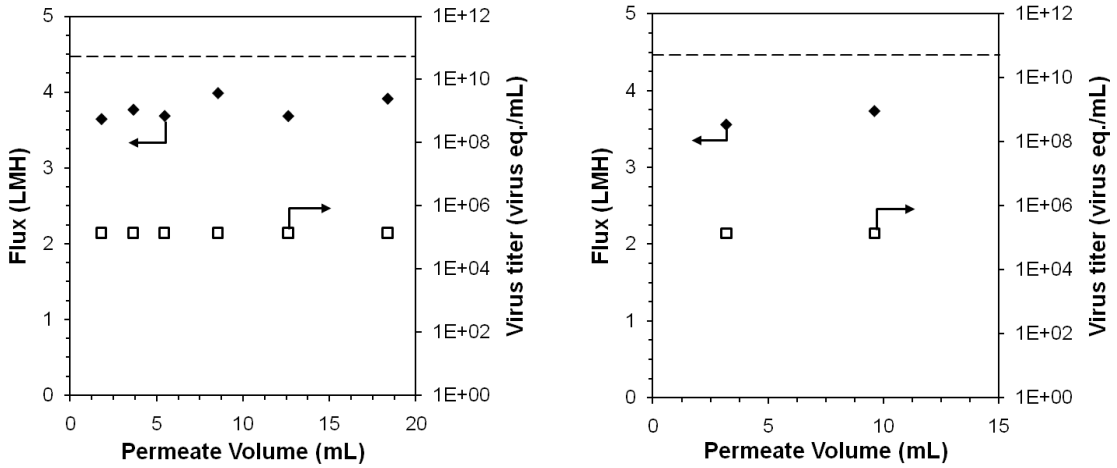

Figure A.4. Flux and virus titer concentrations for the initial acetate-buffered (pH 6.0) filtration, (left) and the tris-buffered (pH 9.0) filtration (right). The open squares denote the virus titer concentration in virus equivalents per mL and the filled diamonds denote the flux across the membrane in LMH at a pressure of 15 PSI. The dashed line in the figures denotes the initial virus concentration in the feed solution.

To further investigate the rejection, a third filtration experiment on the F100 membrane was conducted over 60 hours. In this trial the tris-buffer (pH 9.0) feed solution was spiked with 1 g/L of the protein bovine serum albumin to investigate whether the membrane was susceptible to fouling during the filtration. Overall, the flux was slightly less than the first two trials as the average flux was 2.9 LMH, but the flux did not appear to be as steady in this trial as the first two. Initially, the flux increased around 14% during the first 5 hours of the experiment, but it then slowly declined corresponding to an 18% drop from the highest to the lowest flux values. A larger flux decline would be expected if fouling were a major factor during the experiment, so the origin of this minor flux decline is unknown at this time. A total of 14 fractions were analyzed from this

experiment and again the concentration of virus particles for each fraction was at or below the limit of detection for the QPCR assay corresponding to a LRV of 5.5. Figure A.5 depicts the flux and virus concentration plotted as a function of the permeate volume.

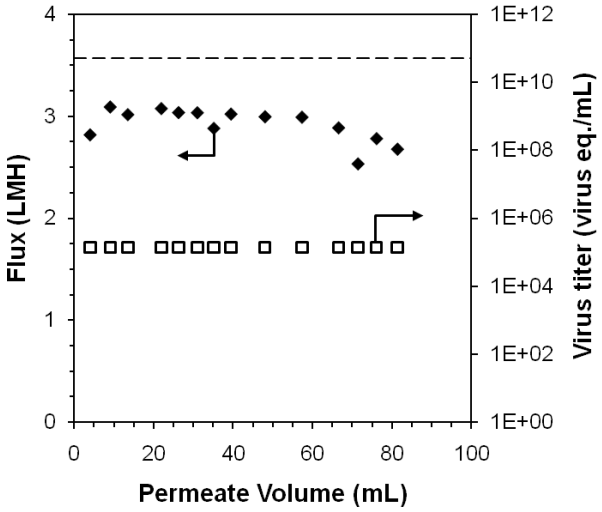

Figure A.5. Flux and virus titer concentrations for the extended tris-buffered (pH 9.0) filtration. The open squares denote the virus titer concentration in virus equivalents per mL and the filled diamonds denote the flux across the membrane in LMH at a pressure of 15 PSI. The dashed line in the figures denotes the initial virus concentration in the feed solution.

While near complete virus removal by the F100 membrane was evident, the low flux prevented complete investigation of the rejection mechanism and fouling characteristics. Since flux is inversely related to a thickness, a thinner membrane, F30, was cast to try to realize faster fluxes. The F30 membrane was approximately 30% the thickness of the F100 membrane and should have flux values around 3x the F100 membrane. An initial experiment using the tris-buffer (pH 9.0) feed solution was conducted at 15 PSI. Figure A.6 depicts the flux and virus concentration plotted as a function of the permeate volume.

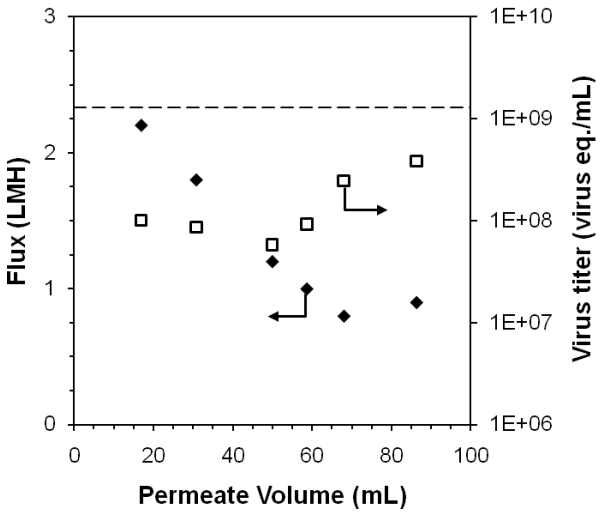

Figure A.6. Flux and virus titer concentrations for filtration with the F30 membrane. The open squares denote the virus titer concentration in virus equivalents per mL and the filled diamonds denote the flux across the membrane in LMH at a pressure of 15 PSI. The dashed line in the figures denotes the initial virus concentration in the feed solution.

Flux values observed for the F30 membrane were lower than the F100 membrane and decreased over time. Additionally, the initial wetting of the membrane with a 50/50 methanol/water (v/v) was also more difficult than wetting the F100 membrane. Together the difficulties in wetting and lower flux values possibly indicate incomplete removal of the nonporous PDCPD skin layer at the surface of the membrane.

Rejection of the virus particles was also significantly less than the F100 membrane as a LRV of 0.9 was observed. While a defect in the membrane such as a crack or much larger pores could be the reason for less rejection, a higher flux would be expected, which was not observed. Another possibility is that if the prime mechanism of virus rejection is pore plugging, decreasing the thickness of the active layer (i.e. membrane) may allow virus particles to pass through as opposed by being trapped. Thus far, the low fluxes observed prevented gathering sufficient data to observe any fouling

and determine whether a pore plugging or a cake layer type rejection mechanism is active based on changes in flux.

A.3. Conclusions and Outlook

Initial explorations into the performance of these block polymer templated membranes for filtering MVM found mixed results. While experiments with a 100 μm thick membrane consistently exhibited a LRV of 5.5 indicating virtually complete rejection, a similar experiment with a 30 μm thick membrane demonstrated very little rejection as a LRV of 0.9 was observed. The low fluxes observed for both membranes inhibited the ability to collect sufficient data to and determine the rejection mechanism and fouling characteristics of the membrane. Overall, these initial results indicate the need to develop membranes with higher fluxes in order to fully evaluate the performance of these block polymer templated membrane in virus filtrations.

A.4. References

(1) van Reis, R.; Zydney, A. *Curr. Opin. Biotechnol.* **2001**, *12*, 208-211.

(2) van Reis, R.; Zydney, A. *J. Membr. Sci.* **2007**, *297*, 16-50.

(3) Saxena, A.; Tripathi, B. P.; Kumar, M.; Shahi, V. K. *Adv. Colloid Interface Sci.* **2009**, *145*, 1-22.

(4) Mehta, A.; Zydney, A. L. *J. Membr. Sci.* **2005**, *249*, 245-249.

(5) Phillip, W. A.; Rzayev, J.; Hillmyer, M. A.; Cussler, E. L. *J. Membr. Sci.*, **2006**, *286*, 144-152.

(6) Bates, F. S.; Fredrickson, G. H. *Annu. Rev. Phys. Chem.* **1990**, *41*, 525-557.

(7) Bates, F. S. *Science* **1991**, *251*, 898-905.

(8) Bates, F. S.; Fredrickson, G. H. *Phys. Today* **1999**, *52*, 32.

(9) Lodge, T. P. *Macromol. Chem. Phys.* **2003**, 204, 265-273.

(10) Hillmyer, M. A. *Adv. Polym. Sci.* **2005**, *190*, 137-181.

(11) Olson, D. A.; Chen, L.; Hillmyer, M. A. *Chem. Mater.* **2008**, *20*, 869-890.

(12) Yang, S. Y.; Ryu, I.; Kim, H. Y.; Kim, J. K.; Jang, S. K.; Russell, T. P. *Adv. Mater.* **2006**, *18*, 709-712.

(13) Yang, S. Y.; Park, J.; Yoon, J.; Ree, M.; Jang, S. K.; Kim, J. K. *Adv. Funct. Mater.* **2008**, *18*, 1371-1377.

(14) Peinemann, K.; Abetz, V.; Simon, P. F. W. *Nat. Mater.* **2007**, *6*, 992-996.

(15) Chen, L.; Phillip, W. A.; Cussler, E. L.; Hillmyer, M. A. *J. Am. Chem. Soc.* **2007**, *129*, 13786-13787.

(16) Phillip, W. A.; Amendt, M.; O'Neill, B.; Chen, L.; Hillmyer, M. A.; Cussler, E. L. *ACS Appl. Mater. Interfaces* **2009**, *1*, 472-480.

(17) Lichterfeld, F.; Schmeling, T.; Strey, R. *J. Phys. Chem.* **1986**, *90*, 5762-5766.

(18) Teubner, M.; Strey, R. *J. Chem. Phys.* **1987**, *87*, 3195.

Appendix B.

Nanoporous Vinyl Thermosets

This appendix describes the formation of nanoporous vinyl thermosets templated by a new reactive block polymer, polylactide-*b*-poly(styrene-*s*-hydroxyethyl methacrylate-*s*-ethylene glycol dimetacrylate). Crosslinking the block polymer with styrene and divinyl benzene resulted in nanostructured thermosets. The more rigid poly(styrene) matrix component facilitated removal of the poly(lactide) in comparison to the poly(cyclooctene) based matrixies which collapsed upon poly(latcide) removal as discussed in Chapter 5.

B.1. Introduction

Nanoporous materials[1] derived from self-assembled block polymers[2] have been explored for a variety of applications including inorganic templating, nanoparticle formation, nanolithography, photonic crystals, high-density storage media, and separation membranes.[3,4,5,6] A variety of block polymers have been investigated as templates, but most matrix structures are composed of thermoplastic polymers that are often brittle, susceptible to solvent dissolution and have modest range of use temperatures.[1] Improvements in the thermal stability, solvent resistance and mechanical toughness of block polymer templated nanoporous materials could not only enhance their performance in current applications but also expand their utilization to new technologies.

A variety of approaches have been employed to form more robust nanoporous materials by focusing on improving individual properties such as the thermal stability, but crosslinking the matrix component has the potential to simultaneously improve thermal, solvent and mechanical stability. Hawker and coworkers reported the use of a thermally crosslinked benzocyclobutene/styrene copolymer matrix, which resulted in nanoporous thin films stable in a variety of solvents and at temperatures up to 200 °C.[7,8] Ndoni and coworkers crosslinked polyisoprene or polybutadiene matrixes using dicumyl peroxide and formed solvent resistive nanoporous materials,[9,10] and Zhou et al. described the formation of nanoporous polyisoprene crosslinked using sulfur monochloride as part of a bicontinuous microemulsion that was thermally stable up to 200 °C and resistant to a variety of solvents.[11]

Another class of materials with the potential for achieving more robust matrixes is thermosetting polymers. Thermosets are formed by crosslinking multifunctional monomers into network structures and exhibit excellent thermal and solvent stabilities. Thermosets have been nanostructured by incorporating block polymers that self assemble into microphase separated domains either before or during curing based on the individual blocks affinity for the thermoset.[12] Recently, nanoporous thermosets have been formed from nanostructured thermosets by selective removal of one of the self-assembled blocks. Removal of polyisoprene by ozonolysis from a polyisoprene-*b*-poly(4-vinyl pyridine) templated nanostructured epoxy resulted in a nanoporous epoxy thermoset.[13] Phenolic thermosets templated by a variety of block polymers have been used as precursors to nanoporous carbon formed by pyrolysis of the nanostructured thermoset.[14,15,16] Finally, mechanically robust nanoporous polydicyclopentadiene (PDCPD) thermosets have been templated by a doubly reactive block polymer.[17,18]

The formation of nanostructured vinyl thermosets using a polylactide-*b*-poly(cyclooctene-*s*-5-norbornene-2-methacrylate)-*b*-polylactide reactive triblock polymer was discussed in Chapter 5, but attempts to render the material nanoporous by selectively etching the polylactide component were unsuccessful due to the soft nature of the polycyclooctene component of the matrix. This appendix describes the formation of nanoporous vinyl thermosets using a more mechanically rigid reactive block polymer, polylactide-*b*-poly(styrene-*s*-hydroxyethyl methacrylate-*s*-ethylene glycol dimetacrylate)

(PLSHE), formed by the post polymerization functionalization of polylactide-*b*-poly(styrene-*s*-hydroxyethyl methacrylate) (PLSH) with methacryloyl chloride.

B.2. Experimental

B.2.1. Materials.

Unless specifically noted, all chemicals were used as received from Aldrich. All vinyl monomers were passed through a basic alumina column to remove any inhibitors prior to use. d,l-lactide (99%) from Purac was recrystallized twice from toluene and stored under N_2 atmosphere. 2,2'-azobis(isobutyronitrile) (AIBN) from Aldrich was purified by recrystallization from methanol. Degassed toluene, was purified by passage over an activated alumina column. *S*-1-Dodecyl-*S'*-(α,α'-dimethyl-α''-acetic acid)trithiocarbonate was following a reported procedure.[19]

B.2.2. Characterization.

$CDCl_3$ (Cambridge Isotope Laboratories) solutions at approximately 10 mg/mL of sample were analyzed by ^1H nuclear magnetic resonance (NMR) spectroscopy on a Varian Inova 500 instrument operating at 500 MHz. All spectra were obtained at 20 °C after 64 transients using a relaxation delay of 5 s with chemical shifts reported as δ (ppm) relative to the ^1H signals from hydrogenous solvent (7.26 ppm for $CHCl_3$).

Molecular weight evolution and polydispersity indicies of the polymers were determined using size exclusion chromatography (SEC). Samples were prepared at concentrations near 5 mg/mL in $CHCl_3$. The instrument operates at 35 °C with three

PLgel 5μm Mixed-C columns in series covering the molecular weight range of 400–400000 g mol^{-1}. The columns are housed in a Hewlett-Packard (Agilent Technologies) 1100 series liquid chromatograph equipped with a Hewlett-Packard 1047A refractive index detector. PDIs are reported with respect to polystyrene standards (Polymer Laboratories).

Small angle X-ray scattering (SAXS) of the crosslinked films was performed on a custom beam line at the University of Minnesota. X-rays (CuKα, λ=1.542 Å) were generated by a Rigaku RU-200BVH rotating anode with Franks mirror optics and a 0.2 x 2 mm^2 microfocus cathode. Two-dimensional (2-D) diffraction patters were recorded for 300 s using a Siemens area detector and corrected for detector response before analysis. In both cases, the 2-D images were azimuthally integrated to a 1-D plot of intensity versus scattering vector, $q = 4\pi \sin(\theta/2)/\lambda$ [θ is scattering angle; λ is wavelength].

Differential scanning calorimetry (DSC) was performed on a TA instruments DSC Q-1000 calorimeter calibrated with an internal indium standard. Samples were sealed inside hermetic aluminum pans and were heated to and annealed at 150 °C for 5 minutes prior to being cooled to 0 °C to standardize the thermal history. The samples were then analyzed by heating at 10 °C /min to 150 °C.

Fourier transfer infrared spectroscopy (FT-IR) was performed using a Nicolet Magna-IR spectrometer 550. All spectra were recorded using a total of 32 scans, and the background was collected prior to each sample for performing background subtractions. Samples were prepared and analyzed as salt pellets using potassium bromide.

SEM images were obtained on a Hitachi S-900 FE-SEM instrument using a 3.0 kV accelerating voltage. Prior to SEM analysis, cryo fractured monoliths were coated with a 1.5 nm thick platinum layer via direct platinum sputtering using a VCR Ion Beam Sputter Coater.

B.2.3. Synthesis.

Synthesis of polylactide-poly(styrene-stat-2-hydroxyethyl methacrylate) (PLSH). PLSH was synthesized by the reversible addition-fragmentation chain transfer (RAFT) copolymerization of styrene and 2-hydroxyethyl methacrylate (HEMA) using a trithiocarbonate functionalized polylactide (27 kg/mol) prepared by previously reported methods.[20] A description of an example polymerization follows. 5.01 g (0.19 mmol) of a trithiocarbonate polylactide, 6.92 g (66.5 mmol) of styrene, 1.03 g (7.9 mmol) of HEMA and 4 mg (0.02 mmol) of AIBN were dissolved in 10 mL of dry toluene in a 48 mL pressure vessel with a side arm. The flask was degassed with argone for 10 minutes before three freeze pump thaw cycles were performed. The flask was then heated in a 70 °C oil bath for 20 hours. The polymer solution was precipitated in pentane, redissolved in methylene chloride and reprecipitated in pentane. The polymer was recovered by vacuum filtration and dried under vacuum for 24 hours. The recovered yield was 5.74 g (44%). The number average molecular weight of the polymer was 36.8 kg/mol with w_L = 0.73, w_S = 0.20 and w_{HEMA} = 0.07 by ^{1}H NMR. The PDI of the polymer was 1.09 as determined by SEC relative to polystyrene standards.

Functionalization of PLSH with methacryloyl chloride. 3.01 g (0.08 mmol) of PLSH was dissolved in 50 mL of dry THF, and then transferred to a round bottom flask with a side arm flame dried under argon. To the flask 0.34 mL (4.2 mmol) of pyridine and a stir bar was added before the flask was capped with a rubber septum. 1.4 mL (14.3 mmol) of methacryloyl chloride was added dropwise via a syringe through the septum, and the solution was allowed to stir for 48 hours. The resulting polymer was run through a small alumina column before being precipitated in pentane. The recovered polymer was redissolved in methylene chloride and reprecipitated in pentane. The polymer was recovered through vacuum filtration and dried under vacuum for 16 hours. Conversion = 42%.

Preparation of Nanoporous Films. In a small vial, the PLSHE block polymer, and vinyl monomer were added at the desired composition (300 mg in total) before adding 1 mg of AIBN, 1 mL of toluene and a small stir bar. Once a homogenous solution was obtained, the capped vial was then placed in an oven initially at room temperature that was warmed to 100 °C over 1 h. The sample was cured for 16 h, before being placed under vacuum for 2 h. The resulting transparent films had contracted from the sides of the vial and were slightly yellow in color. In order to remove the polylactide, the films were etched in a 0.5 M NaOH solution (40/60 methanol/water by volume) at 70 for 3 d. After etching, the films were rinsed with methanol and vacuum dried for 16 h.

B.3. Results and Discussion

B.3.1. Synthesis and Characterization of PLSHE Block Polymers.

As discussed in Chapter 5, attempts to selectively remove polylactide from vinyl thermosets nanostructured with a polylactide-*b*-poly(cyclooctene-*s*-5-norbornene-2-methacrylate)-*b*-polylactide triblock copolymer were unsuccessful as the matrix collapsed due to the soft polycyclooctene compoenent. Hence a more rigid reactive block with a higher glass transition temperature was needed.

Polystyrene has been a block commonly explored for forming nanoporous materials,[21,22] and while it is quite brittle, it was pursued as an initial proof of concept for forming nanoporous vinyl thermosets. Since styrene is polymerized by anionic or radical polymerizations, imparting the necessary reactive vinyl functionality would have to be done through a post polymerization modification to avoid crosslinking of the polymer template. Incorporation of hydroxyl functionality through RAFT copolymerization of styrene and HEMA using a trithiocarobonate functionalized polylactide[20] (PL) was thus pursued as functionalization of HEMA could potentially be achieved by esterificaiton with methacryloyl chloride. Figure B.1 outlines the polymerization of polylactide-*b*-poly(styrene-*s*-hydroxyethyl methacrylate) (PLSH) and its functionalization to PLSHE.

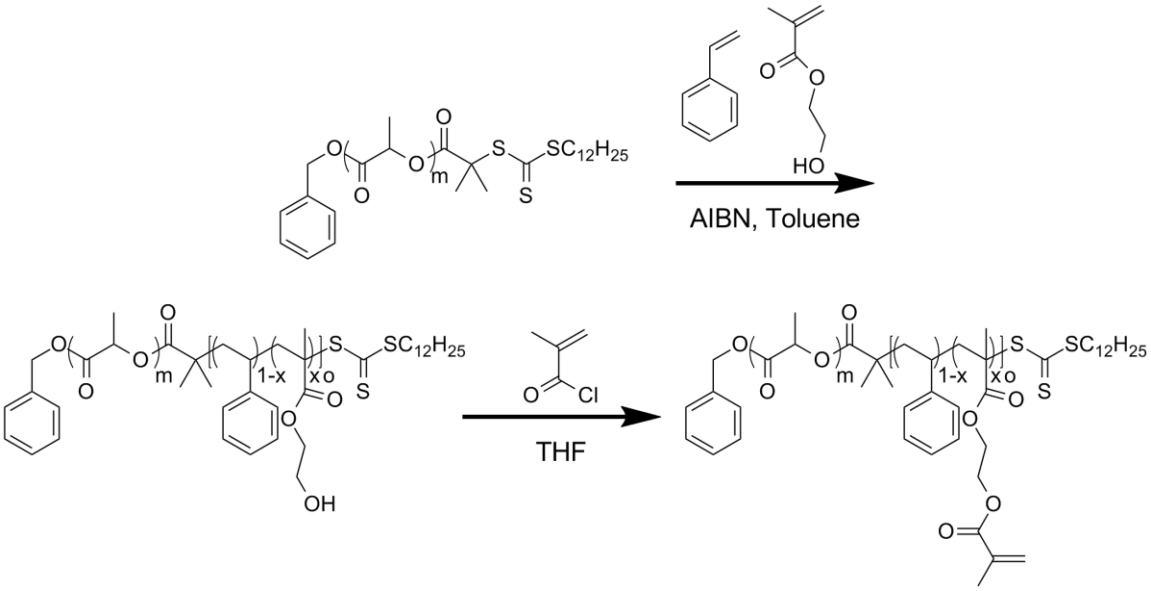

Figure B.1. Scheme for the polymerization of PLSH and its functionalization to PLSHE.

A series of RAFT copolymerizations of styrene and HEMA for various times using a 27.0 kg/mol PL resulted in PLSH block polymers with varied molecular weights and compositions (Table B.1) based on ^{1}H NMR. As can be seen in Figure B.2, the conversion of HEMA over time was greater than that of styrene, so the polymer HEMA composition was enriched relative to the monomer feed.

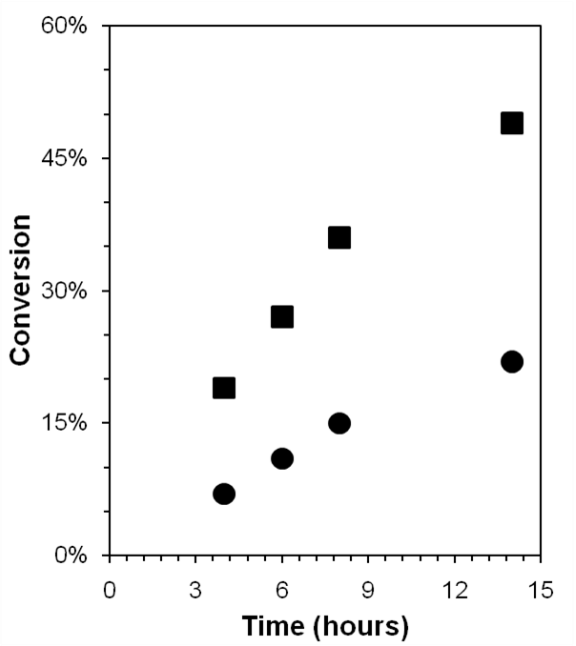

Figure B.2. Conversion of styrene (circles) and HEMA (squares) overtime.

Based on conversion overtime, a PLSH block polymer with a 10 kg/mol PSH block and 15 mol % HEMA was targeted. Copolymerization of styrene and HEMA for 20 hours at more diluted conditions than the initial time series resulted in a 9.8 kg/mol PSH block with 19 mol % HEMA. SEC traces of the PL macro-RAFT agent and the PLSH block polymer in Figure B.3 clearly demonstrate a shift to lower retention volumes upon addition of the PSH block consistent with an increase in molecular weight. PDIs of the initial PL block and the PLSH block polymer was 1.10 and 1.09 respectively.

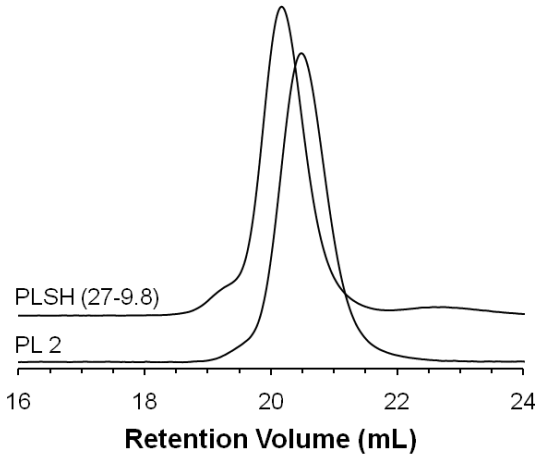

Figure B.3. SEC trace for the PL 2 homopolymer and PLSH (27-9.8) block polymer.

Table B.1 provides the characterization data for the PLSH block polymers. In addition to the PLSH block polymer a PSH homopolymer was synthesized by the RAFT copolymerization of styrene and HEMA in toluene using the same trithiocarbonate chain transfer agent.

Table B.1. Molecular characteristics of the PLSH block polymers.

Polymer[a]	$M_{n,\ PLA}$ (kg/mol)[b]	$M_{n,\ PSH}$ (kg/mol)[b]	x_H[c]	PDI[d]	w_{PLA}[e]
PL 1	27	-	-	1.23	1.00
PLSH (27-4.8)[f]	27	4.8	0.33	1.30	0.85
PLSH (27-7.3)[f]	27	7.3	0.31	1.34	0.79
PLSH (27-9.6)[f]	27	9.6	0.30	1.38	0.74
PLSH (27-13.5)[f]	27	13.5	0.28	1.43	0.67
PL 2	27	-	-	1.10	1.00
PLSH (27-9.8)[g]	27	9.8	0.19	1.09	0.73
PSH (7.9)	-	7.9	0.12	1.18	-

[a]The block polymers are named PLSH(X-Y) where X is the molecular weight of the PL block and Y is the molecular weight of the PSH block. [b]Molecular weights were determined by ^{1}H NMR end group analysis. [c]Mole fraction of H in the PSH block was determined by ^{1}H NMR spectroscopy. [d]PDI determined by size exclusion chromatography based on poly(styrene) standards. [e]Weight fraction of PLA ($w_{PLA} = M_{n,\ PLA}/(M_{n,\ PSH} + M_{n,\ PLA})$). [f]PL 1 was used as the initial block for this polymer. [g]PL 2 was used as the initial block for this polymer.

Functionalization of the PLSH block polymer to PLSHE via esterification of the hydroxyl group with methacryloyl chloride was initially done in the presence of triethyl amine. The ^{1}H NMR spectrum (Figure B.4) after the reaction exhibited additional peaks at 5.5 and 6.1 ppm consistent with addition of the methacrylate vinyl protons, but the emergence of a peak at 4.35 consistent with a methine proton at the end of a polylactide chain indicates that at least a portion of the PL block had hydrolyzed. This was confirmed by the emergence of a shoulder at higher retention volumes in an SEC chromatograph of the polymer indicating the presence of lower molecular weight chains.

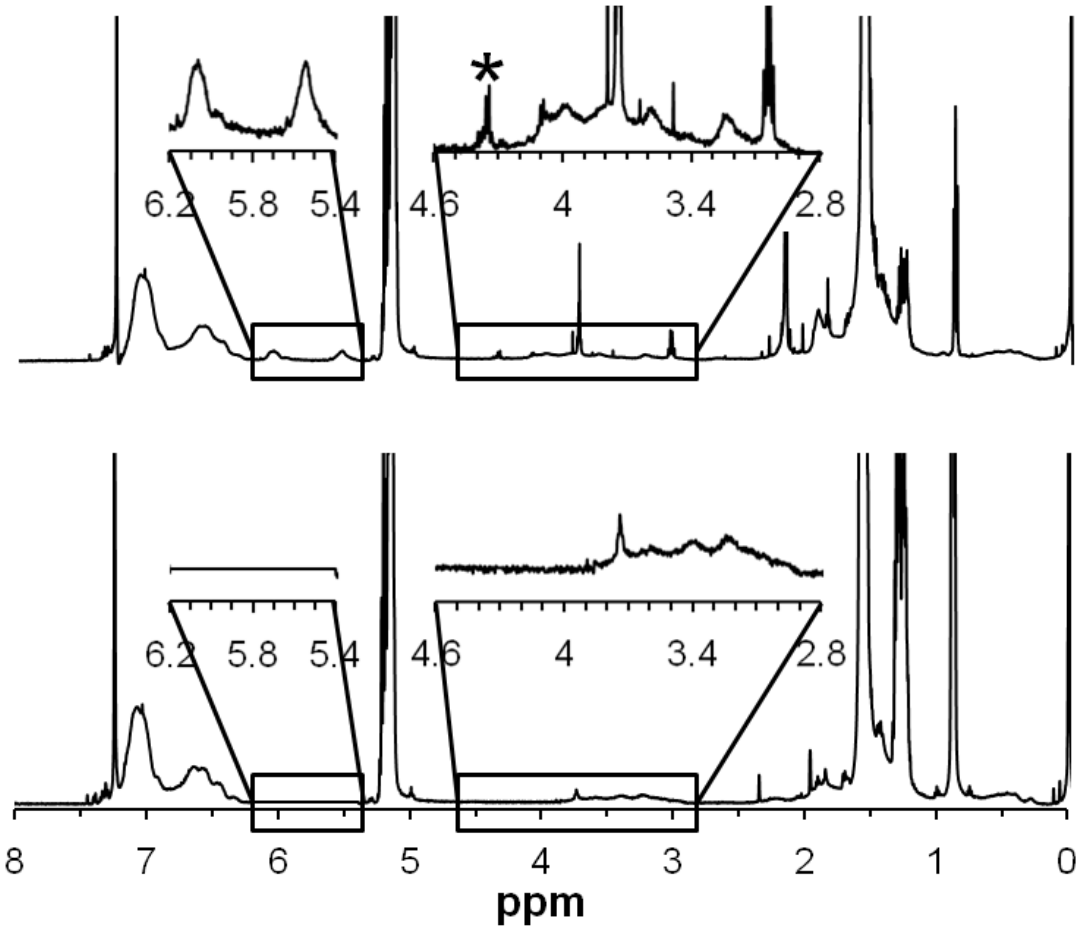

Figure B.4. ^{1}H NMR spectra of PLSH before (bottom) and after (top) functionalization with methacryloyl chloride using triethyl amine. The peak with the * in the top spectrum is consistent with the methine proton at the end of a polylactide chain.

Additional attempts to convert PLSH to PLSHE by reducing the relative amount of triethyl amine, shortening the reaction time or changing the order of addition were all unsuccessful. Acidic conditions using hydrochloric acid were also used without success. Finally, substitution of the weaker base pyridine for triethyl amine successfully esterified some of the HEMA groups without hydrolyzing the PL block. ^{1}H NMR of the polymer after functionalization indicated 42% of the HEMA groups had been converted after 24

hours. Additional reactions for 48 and 72 hours did not significantly increase conversion. **Figure B.5** shows the ^{1}H NMR of a PLSHE block polymer.

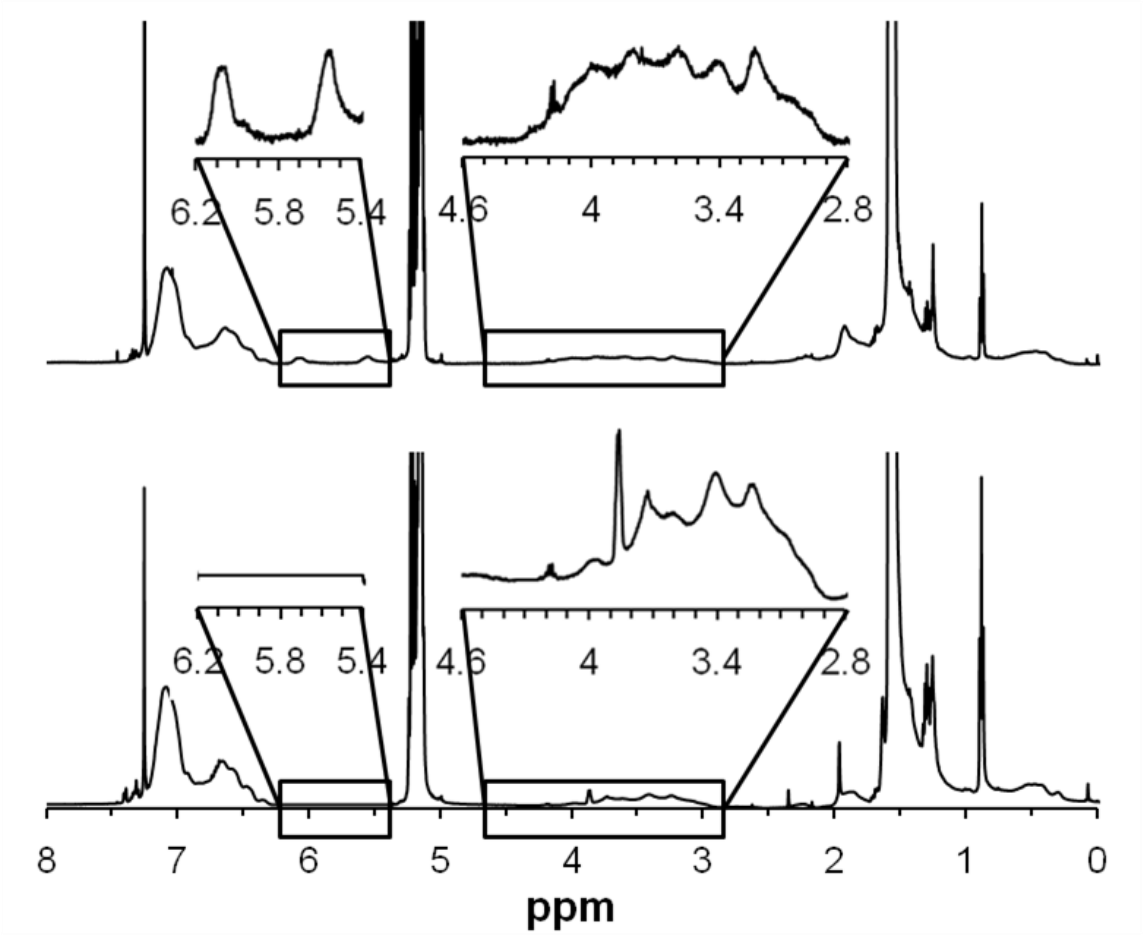

Figure B.5. ^{1}H NMR spectra of PLSH before (bottom) and after (top) functionalization with methacryloyl chloride using pyridine.

B.3.2. Formation of Nanoporous Films.

Prior to crosslinking the PLSHE block polymer with different vinyl monomers, potential matrix materials were investigated by crosslinking PSHE (7.9) with styrene (S), styrene and divinyl benzene (SD), methyl methacrylate (M), and methyl methacrylate and ethylene glycol dimethacrylate (ME). Films were crosslinked by heating the PSHE

homopolymer (5 wt %) with the monomer(s) (10 wt %) in toluene (79.9 wt %) with AIBN (0.1 wt %). The film composition was set to mimic the final matrix composition after lactide removal from a PLSHE crosslinked films.

The transparent to transluscent crosslinked films varied in rigidity based on qualitative analysis. The PSHE/S and PSHE/M films were extremely brittle and fell apart after being removed from their vials. The PSHE/ME film was very hard and stiff but was cracked throughout. The PSHE/SD film was the most promising as it was a smooth, hard but somewhat pliable. Thermal analysis by DSC indicated that the films had glass transition termperatures (T_g) above 80 °C (Figure B.6) indicating that the matrix might be robust enough to support a porous structure upon PLA removal.

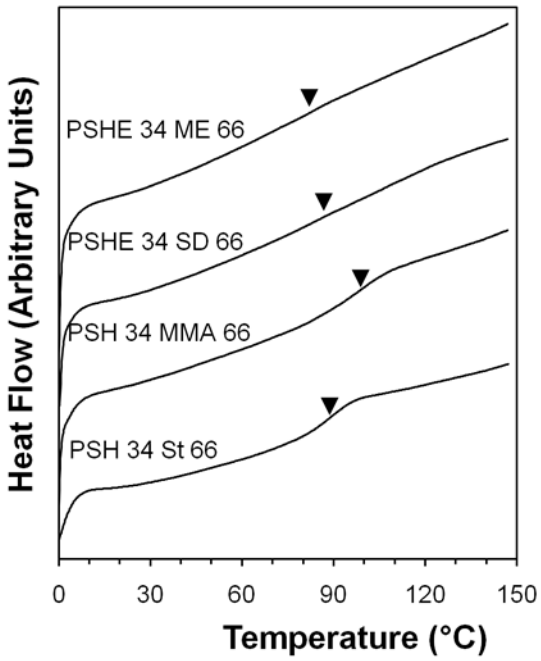

Figure B.6. DSC traces for crosslinked PSHE films. Traces represent the second heating at a rate of 10 °C/min after annealing at 150 °C for 5 min before cooling to 0 °C. The traces have been vertically shifted for clarity.

Based on the analysis of the PSHE films, the PSHE/SD film seemed to be the most promising matrix material due to its physical properties and T_g. PLSHE/SD films were then crosslinked by heating a toluene (74.9 wt %) solution of the PLSHE and monomers (25 wt %) and AIBN (0.1 wt %) at 100 °C for 16 hours in a glass vial. The transparent, yellow films were smooth and hard. Table B.2 has the characterization data for the films. The films are named PLSHE X SD Y where X denotes the PLSHE wt % while Y denotes the SD wt % in the film.

Table B.2. Composition and characterization data for PLSHE SD films.

Film[a]	PLA (wt %)	Mass Loss[b] (wt %)	Domain Spacing (nm)[c]		Pore size[d] (nm)
			BE	AE	
PLSHE 66 SD 34	49	54	20	21	14.0
PLSHE 50 SD 50	37	49	23	22	12.3

[a]The name of the film is PLSHE X SD Y where X refers to the wt % of PLSHE and Y the wt % of SD. [b]Mass loss corresponds to the total percentage of mass loss upon etching the sample. [c]Domain spacings were determined from SAXS at room temperature using the Teubner-Strey microemulsion model. [d]The pore size was estimated from SEM micrographs.

The polylactide block was selectively removed from the films by submersing the films in a 0.5 M NaOH solution in methanol/water (40/60 by volume). The mass loss of each film due to etching calculated as a percentage of the original mass of the cured sample (Table B.2) was greater than the initial polylactide composition suggesting that matrix portions of the film not completely integrated into the final network were also lost during etching. FT-IR of the samples before and after etching demonstrated loss of the lactide carbonyl stretch at 1750 cm^{-1} (Figure B.**7**).

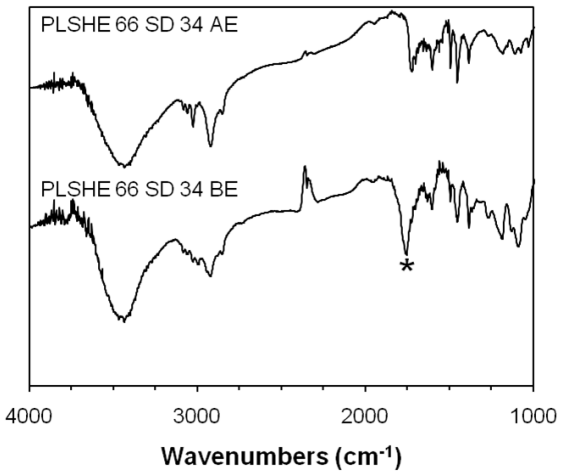

Figure B.7. FT-IR spectra of the PLSHE 66 SD 34 film both before and after etching showing the loss of the lactide carbonyl peak at 1750 cm^{-1}. The broad peak observed at 3500 cm^{-1} is due to the water in the potassium bromide salt pellet.

B.3.3. Characterization of Nanoporous Films.

One-dimensional SAXS patterns of the films both before and after etching can be seen in Figure B.8. Both samples exhibited a single broad peak characteristic of a microphase separated but disordered structure. After etching, the scattering intensity increased significantly consistent with the increased electron contrast between the matrix and the voids created upon removal of the polylactide. The scattering patterns were fit using the Teubner-Strey microemulsion model, and the domain spacing was calculated for each sample. The PLSHE 66 SD 34 samples had domain spacings of 20 and 21 nm both before and after etching while the PLSHE 50 SD 50 domain spacings were 23 and 22 nm. The increased domain spacing with increased vinyl monomer composition is consistent with an enlarged matrix component.

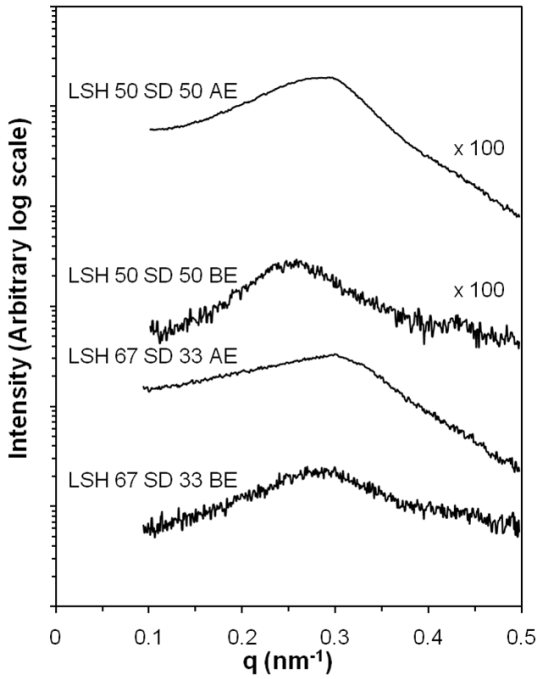

Figure B.8. One dimensional SAXS profiles for the PLSHE/SD films. The PLSHE 50 SD 50 films both before and after etching were vertically shifted by 100x for clarity.

The etched samples were also imaged by SEM. SEM micrographs of cryo-fractured surfaces coated with 1.5 nm of platinum (Figure B.9) revealed a nanoporous bicontinuous structure. The pore sizes estimated to be 14.0 and 12.3 nm for the PLSHE 66 SD 34 and PLSHE 50 SD 50 samples respectively.

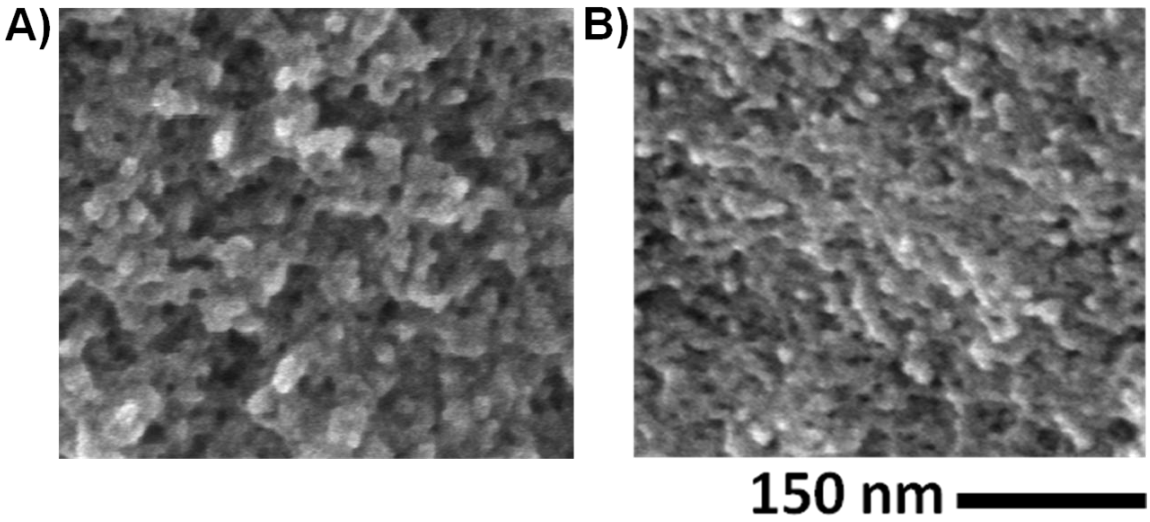

Figure B.9. SEM micrographs of freeze fractured surfaces of the **A)** PLSHE 66 SD 34 and **B)** PLSHE 50 SD 50 films after etching. The samples were coated with 1.5 nm of platinum prior to imaging to prevent charging.

B.4. Conclusions

A reactive PLSHE block polymer synthesized by the RAFT copolymerization of styrene and HEMA followed by functionalization with methacryloyl chloride was crosslinked with styrene and divinyl benzene to form nanostructured vinyl thermosets as evidenced by SAXS. Subsequent removal of the poly(lactide) component confirmed by mass loss, FT-IR, SAXS and SEM resulted in the formation of a nanoporous bicontinuous structure. Successful templating of nanoporous structures using a vinyl reactive block polymer indicates the general applicability of using reactive block polymers in thermosetting systems for forming nanoporous structures.

B.5. Acknowledgements

This work was largely supported by CIE Polymers. M. A. A. acknowledges financial support from the U. S. Air Force. Parts of this work were carried out in the College of Science and Engineering Characterization Facility, University of Minnesota, a member of the NSF-funded Materials Research Facilities Network (www.mrfn.org).

B.6. References

(1) Hillmyer, M. A. *Adv. Polym. Sci.* **2005**, *190*, 137-181.

(2) Bates, F. S. *Science* **1991**, *251*, 898-905.

(3) Fasolka, M. J.; Mayes, A. M. *Annu. Rev. Mater. Res.* **2001**, *31*, 323-355.

(4) Park, C.; Yoon, J.; Thomas, E. L. *Polymer*, **2003**, *44*, 6725-6760.

(5) Hawker, C. J.; Russell, T. P. *MRS Bull.* **2005**, *30*, 952-966.

(6) Olson, D. A.; Chen, L.; Hillmyer, M. A. *Chem. Mater.* **2008**, *20*, 869-890.

(7) Drockenmuller, E.; Li, L. Y. T.; Ryu, D. Y.; Harth, E.; Russell, T. P.; Kim, H.; Hawker, C. J. *J. Polym. Sci. Part A: Polym. Chem.* **2005**, *43*, 1028-1037.

(8) Leiston-Belanger, J. M.; Russell, T. P.; Drockenmuller, E.; Hawker, C. J. *Macromolecules* **2005**, *38*, 7676-7683.

(9) Hansen, M. S.; Vigild, M. E.; Berg, R. H.; Ndoni, S. *Polym Bull* **2004**, *51*, 403-409.

(10) Guo, F.; Andreasen, J. W.; Vigild, M. E.; Ndoni, S. *Macromolecules* **2007**, *40*, 3669-3675.

(11) Zhou, N.; Bates, F. S.; Lodge, T. P. *Nano Lett.* **2006**, *6*, 2354-2357.

(12) Ruiz-Pérez, L.; Royston, G. J.; Fairclough, J. P. A.; Ryan, A. J. *Polymer* **2008**, *49*, 4475-4488.

(13) Guo, Q.; Liu, J.; Chen, L.; Wang, K. *Polymer* **2008**, *49*, 1737-1742.

(14) Liang, C.; Hong, K.; Guiochon, G. A.; Mays, J. W.; Dai, S. *Angew. Chem. Int. Ed.* **2004**, *43*, 5785-5789.

(15) Kosonen, H.; Valkama, S.; Nykänen, A.; Toivanen, M.; ten Brinke, G.; Ruokolainen, J.; Ikkala, O. *Adv. Mater.* **2006**, *18*, 201-205.

(16) Hu, D.; Xu, Z.; Zeng, K.; Zheng, S. *Macromolecules* **2010**, *43*, 2960-2969.

(17) Chen, L.; Phillip, W. A.; Cussler, E. L.; Hillmyer, M. A. *J. Am. Chem. Soc.* **2007**, *129*, 13786-13787.

(18) Chen, L.; Hillmyer, M. A. *Macromolecules* **2009**, *42*, 4237-4243.

(19) Lai, J. T.; Filla, D.; Shea, R. *Macromolecules* **2002**, *35*, 6754-6756.

(20) Rzayev, J.; Hillmyer, M. A. *J. Am. Chem. Soc.* **2005**, *127*, 13373-13379.

(21) Thurn-Albrecht, T.; Steiner, R.; DeRouchey, J.; Stafford, C. M.; Huang, E.; Bal, M.; Tuominen, M.; Hawker, C. J.; Russell, T. P. *Adv. Mater.* **2000**, *12*, 787-791.

(22) Zalusky, A. S.; Olayo-Valles, R.; Taylor, C. J.; Hillmyer, M. A. *J. Am. Chem. Soc.* **2001**, *123*, 1519-1520.